Experimental Investigation and Modeling of Lithium-ion Battery Cells and Packs for Electric Vehicles

By

Satyam Panchal

A Thesis Submitted in Partial Fulfillment

of the Requirements for the Degree of

Doctor of Philosophy

in

Mechanical Engineering

Faculty of Engineering and Applied Science

University of Ontario Institute of Technology

Oshawa, Ontario, Canada

Abstract

The greatest challenge in the production of future generation electric and hybrid vehicle (EV and HEV) technology is the control and management of operating temperatures and heat generation. Vehicle performance, reliability and ultimately consumer market adoption are dependent on the successful design of the thermal management system. In addition, accurate battery thermal models capable of predicting the behavior of lithium-ion batteries under various operating conditions are necessary. Therefore, this work presents the thermal characterization of a prismatic lithium-ion battery cell and pack comprised of $LiFePO_4$ electrode material. Thermal characterization is performed via experiments that enable the development of an empirical battery thermal model.

This work starts with the design and development of an apparatus to measure the surface temperature profiles, heat flux, and heat generation from a lithium-ion battery cell and pack at different discharge rates of 1C, 2C, 3C, and 4C and varying operating temperature/boundary conditions (BCs) of 5ºC, 15°C, 25°C, and 35°C for water cooling and ~22°C for air cooling. For this, a large sized prismatic $LiFePO_4$ battery is cooled by two cold plates and nineteen thermocouples and three heat flux sensors are applied to the battery at distributed locations. The experimental results show that the temperature distribution is greatly affected by both the discharge rate and BCs. The developed experimental facility can be used for the measurement of heat generation from any prismatic battery, regardless of chemistry. In addition, thermal images are obtained at different discharge rates to enable visualization of the temperature distribution.

In the second part of the research, an empirical battery thermal model is developed at the above mentioned discharge rates and varying BCs based on the acquired data using a neural network approach. The simulated data from the developed model is validated with experimental data in terms of the discharge temperature, discharge voltage, heat flux profiles, and the rate of heat generation profile. It is noted that the lowest temperature is 7.11°C observed for 1C-5°C and the highest temperature is observed to be 41.11°C at the end of discharge for 4C-35°C for cell level testing. The proposed battery thermal model can be used for any kind of Lithium-ion battery. An example of this use is demonstrated by validating the thermal performance of a realistic drive cycle collected from an EV at different environment temperatures.

In the third part of the research, an electrochemical battery thermal model is developed for a large sized prismatic lithium-ion battery under different C-rates. This model is based on the principles of transport phenomena, electrochemistry, and thermodynamics presented by coupled nonlinear partial differential equations (PDEs) in x, r, and t. The developed model is validated with an experimental data and IR imaging obtained for this particular battery. It is seen that the surface temperature increases faster at a higher discharge rate and a higher temperature distribution is noted near electrodes.

In the fourth part of the research, temperature and velocity contours are studied using a computational approach for mini-channel cold plates used for a water cooled large sized prismatic lithium-ion battery at different C-rates and BCs. Computationally, a high-fidelity turbulence model is also developed using ANSYS Fluent for a mini-channel cold plate, and the simulated data are then validated with the experimental data for temperature profiles. The present results show that increased discharge rates and increased operating temperature results in increased temperature at the cold plates.

In the last part of this research, a battery degradation model of a lithium-ion battery, using real world drive cycles collected from an EV, is presented. For this, a data logger is installed in the EV and real world drive cycle data are collected. The vehicle is driven in the province of Ontario, Canada, and several drive cycles were recorded over a three-month period. A Thevenin battery model is developed in MATLAB along with an empirical degradation model. The model is validated in terms of voltage and state of charge (SOC) for all collected drive cycles. The presented model closely estimates the profiles observed in the experimental data. Data collected from the drive cycles show that a 4.60% capacity fade occurred over 3 months of driving.

Acknowledgements

The journey through my PhD studies and the process of writing this thesis have been nothing short of amazing. This has resulted from many experiences I have encountered at the University of Ontario Institute of Technology and the University of Waterloo from dozens of remarkable individuals whom I also wish to acknowledge.

I would first like to express my deep and sincere gratitude to my supervisor, Dr. Ibrahim Dincer, the Director of the University of Ontario Institute of Technology Clean Energy Research Laboratory, and my co-supervisor, Dr. Martin Agelin-Chaab, for their support during this research. Dr. Dincer has a great vision and clear mind and he has shown me what I could achieve. This PhD would not be possible without the guidance, patience, understanding, motivation, and support from both Dr. Dincer and Dr. Agelin-Chaab. They also helped with their insightful comments as well as the challenging questions and great discussions which incented me to widen my research from various perspectives. I hope to keep working with Dr. Dincer and Dr. Agelin-Chaab in the future and I know that I will always be proud to have studied for my PhD under their supervision.

Besides my advisors, my special thanks go to Dr. Roydon Fraser and Dr. Michael Fowler for allowing me to work in the Electrochemical Energy Storage Laboratory at the University of Waterloo. It is thanks to them that I was provided with the opportunity to work in their labs, and it would not have been possible to finish my PhD without their support.

I would like to thank Dr. John McPhee, Director of the Green and Intelligent Automotive (GAIA) Research Lab, and Professor of System Design Engineering, at the University of Waterloo for allowing me to work in the GAIA Lab for battery pack testing. I would also like to extend my thanks to Miss Stefanie Bruinsma, Manager at the GAIA Lab, for her help in setting up equipment. We (I and my colleague, Mr Monu Malik) were the first persons to be allowed to work at the GAIA Lab and special thanks for this go to Dr. John McPhee.

I would also like to thank Dr. Richard Culham, Vice Dean, Faculty of Engineering, Associate Dean International, Professor, Mechanical and Mechatronics Engineering, University of Waterloo, for allowing me to work in his Microelectronics Heat Transfer Laboratory (MHTL) and Dr. Elizabeth Weckman, Professor and Head of the Building Fire Research Group for providing an IR camera.

I also thank Dr. Pearl Sullivan, Dean, Faculty of Engineering, University of Waterloo, and Dr. Eric Croiset, Chair and Professor, Chemical Engineering Department, University of Waterloo, for a letter of offer as a full-time visiting scholar in the Department of Chemical Engineering, Faculty of Engineering, to conduct battery thermal experiments and analysis with Dr. Michael Fowler.

I would like to extend my appreciation to my committee members: Dr. Wey Leong, Dr. Ghauz Rizvi, Dr. Sheldon Williamson and Dr. Ahmad Barari, for their valuable time in reading and providing their comments to improve the content of my thesis.

Moreover, I offer my deepest thanks to Bharat Solanki, Rocky Khasow, Seham Sahid and Dr. Ehsan Samadani for all their assistance and constructive feedback. Bharat is one of the nicest people I have ever seen in my life. Also, I must express my gratitude to Manoj Matthew and co-op students, Jackson McGrory and John Kong, at the University of Waterloo, for their help throughout my research.

Last but not least, I would like to thank my father and my great friend, Professor Jashubhai Panchal. He is one of the nicest people I have known without whose constant moral support it would not have been possible to finish my Ph.D. I would also like to thank my mother, Sushilaben Panchal. I am very lucky to have such great parents who raised me with a love of science and supported me in all my pursuits and my life in general. My sisters, Swati Panchal and Kirti Panchal, have turned out to be my best friends, and their understanding and encouragement has been present throughout my education. Lastly, I would like to thank my wife, Jolly Panchal, and my dear twins, Dev Panchal and Dwij Panchal, for their constant support.

Table of Contents

List of Figures

List of Tables

Nomenclature

a_s : solid/electrolyte interfacial area per unit volume or active surface area per electrode unit volume for electron transfer reactions [1/cm]

A : area [m^2]

c_p : specific heat capacity [J/kg°C]

$C_{p,p}$: specific heat for positive tab [J/kg-K]

$C_{p,n}$: specific heat for negative tab [J/kg-K]

$C_{p,a}$: specific heat for active zone [J/kg-K]

$C_{1\varepsilon}$: model constants

$C_{2\varepsilon}$: model constants

$C_{3\varepsilon}$: model constants

C_{μ} : constant

C_e : concentration of lithium in electrolyte phase [mol/m^3]

C_s : concentration of lithium in solid phase [mol/m^3]

$C_{s,p,max}$: maximum solid Li$^+$ Concentration for positive electrode [mol/m^3]

$C_{s,n,max}$: maximum solid Li$^+$ Concentration for negative electrode [mol/m^3]

D_s : mass diffusion coefficient of lithium-ion in electrolyte

$D_{s,p}$: reference diffusivity for positive electrode [m^2/s]

$D_{s,n}$: reference diffusivity for negative electrode [m^2/s]

$D_{s,ref}$: reference solid diffusion coefficient

${D_e}^{eff}$: effective diffusion coefficient

E : open-circuit potential [V]

E_d : activation energy that controls temperature sensitivity of $\mathrm{D_s}$ [kJ/mol]

E_r : activation energy that controls temperature sensitivity of k_m [kJ/mol]

$f_{\pm}$: molecular activity coefficient of the electrolyte also called electrolyte activity coefficient

F : Faraday`s constant [96485 Columb/mol]

G : Gibb’s free energy

G_k : the generation of turbulence kinetic energy due to the mean velocity gradients

G_b : the generation of turbulence kinetic energy due to buoyancy

H : hidden layer neurons

h : heat transfer coefficient [W/m^2 °C]

i_0 : exchange current density [A/m^2]

I : current [A]

j^{Li} : transfer current resulting from lithium insertion/de-insertion at the electrode/electrolyte interface [A/m^2]

k : ionic conductivity of electrolyte [S/m] or turbulent kinetic energy [J]

k_p : reference rate constant for positive electrode [mol/m^{2}s/(mol/m^3)$^{1.5}$]

k_n : reference rate constant for negative electrode [mol/m^{2}s/(mol/m^3)$^{1.5}$]

$k_{m,ref}$: reference reaction rate coefficient

k^{eff} : effective diffusional conductivity [S/m]

${k_D}^{eff}$: effective ionic conductivity [S/m]

l_n : length of negative electrode [µm]

l_s : length of separator [µm]

l_p : length of the positive electrode [µm]

L : overall length ($L = l_n + l_s + l_p$) in [µm]

m : mass [kg]

$\dot{m}$: mass flow rate [kg/s]

n : number of electrons

N_T : number of temperature readings in the summation

N_C : total number of coulombs transported into or out of the battery

P : pressure [Pa]

Pr : Prandtl number

Pr_t : turbulent Prandtl number

Q : heat [kJ]

$\dot{Q}$: heat generation rate [W]

q : heat flux [W/m^2]

r : radial coordinate along active material particle

R : universal gas constant [8.3143 kJ/kg mole. K] or resistance [Ω]
R^2 : coefficient of determination
R_e : Reynold’s number
R_t : terminal resistor [Ω]
R_s : radius of solid active material particle [µm]
$R_{s,p}$: particle radius for positive electrode [µm]
$R_{s,n}$: particle radius for negative electrode [µm]
S : entropy [kJ/kg K]
S_k : user-defined source terms
S_ε : user-defined source terms
T : temperature [°C or K]
${t_+}^0$: transfer number of lithium-ion
t : time [s]
U : electrode potential of the reaction or thermodynamic open circuit potential [V]
V : cell voltage [V] or speed [m/s]
$\bar{V}$: average velocity [m/s]
X : net rate of energy change through conduction (heat) [kW]
Y : net rate of energy change through convection (fluid flow) [kW]
Y_M : the contribution of the fluctuating dilatation in compressible turbulence to the overall dissipation rate
Z : net rate of work by body forces and surface forces [kW]
dE/dT : temperature coefficient [V/°C]
dT/dx : temperature gradient [°C/m]
$y+$: enhanced wall treatment
$\bar{Y}$: mean of all observations
Y_i : actual observations
$\hat{Y}_i$: estimated observation at time i

Greek Symbols

α : thermal diffusivity [m^2/s]
φ : energy dissipation rate

β : thermal expansion coefficient or bias or Burggeman porosity exponent
i : layer index
ρ : density [kg/m^3]
μ : dynamic viscosity [Ns/m^2]
μ_t : turbulent or eddy viscosity
ν : kinematic viscosity [m^2/s]
ν_s : mean fluid velocity [m/s]
∇ : gradient operator
λ : Reynold’s stress
Γ : average surface temperature of a battery [°C or K]
θ_k : discharge/charge current [A] or Ah capacity of battery
ξ_k : boundary conditions [°C or K]
ω : weights
$\emptyset_s$: solid phase potential [V]
$\emptyset_e$: electrolyte phase potential [V]
σ^{eff} : effective conductivity [S/m]
σ_+ : effective electrical conductivity for positive electrode [S/m]
σ_- : effective electrical conductivity for negative electrode [S/m]
σ_k : turbulent Prandtl numbers for k
ε_k : turbulent Prandtl numbers for ε
ϵ_e : volume fraction of electrolyte phase in electrode
ϵ_s : volume fraction of solid particle (active material) in electrode
ϵ_f : volume fraction of filler material in electrode
$\propto_a$: transfer coefficient of anode
$\propto_c$: transfer coefficient of the cathode
ω : turbulent eddy frequency [1/s]

Subscripts

∞ : ambient
$_0$: initial

act : actual

avg : average

b : battery

bs : battery surface

c : cell

cp : cooling plate

chg : charging

conv : convection

dchg : discharging

e : environment

exp : experimental

f : fluid

gen : generated

i : layer index

in : inlet

int : internal

max : maximum

n : negative electrode

oc : open circuit

out : outlet or output

p : positive electrode

rev : reversible

s/c : surface

sim : simulated

tot : total

th : thermal

thk : thickness

w : water

w,o : outlet water

w,i : inlet water

x,y,z : cartesian coordinate directions

Superscripts

$^{\circ}$: degree

$^{+}$: related to wall treatment

eff : effective value

Acronyms

A123	A lithium-ion pouch cell manufactured by A123. It is obtained after market.
ANSYS Inc.	American computer-aided engineering software developer
ANSYS-CFX	A computation fluid dynamics software tools
APS	Accelerator pedal position
ARC	Accelerated rate calorimeter
BC	Boundary condition
BAS	Belt-alternator-starter
BPS	Brake pedal position
BEV	Battery electric vehicle
BOL	Beginning of life
BMS	Battery management system
BTMS	Battery thermal management system
C	Capacity
CC	Constant current
CD	Charge depleting
CV	Constant voltage
CAD	Computer aided design
CFD	Computational fluid dynamics
CNTs	Carbon nanotubes
DP	Dual polarization
DAQ	Data acquisition
DOD	Depth of discharge
DEC	Diethyl carbonate
DMC	Dimethyl carbonate
DES	Detached eddy simulation

DRU	Data recording unit
EC	Ethylene carbonate
ECT	Electrochemical thermal
ECM	Equivalent circuit-based modeling
ESS	Energy storage system
EPA	Environment protection agency
EMC	Ethyl-methyl carbonate
EV	Electric vehicle
EOL	End of life
EOD	End of discharge
E-stop	Emergency shut down
FCV	Fuel cell vehicle
FEA	Finite element analysis
FEM	Finite element method
FSP	Field synergy principle
FUDS	Federal urban driving schedule
GM	General motors
GHG	Greenhouse gas
GUI	Graphical user interface
GPS	Global positioning system
HEV	Hybrid electric vehicle
HFS	Heat flux sensor
HPPC	Hybrid pulse power characterization
HWFET	Highway fuel economy cycle
I/O	Input/output
ICE	Internal combustion engine
ICEM-CFD	Popular proprietary software package used for CAD and mesh generation
IHC	Isothermal heat conduction calorimeter
IMA	Integrated motor assist
IR	Infra-red
Li-ion	Lithium ion

$LiCoO_2$	Lithium cobalt oxide
$LiMn_2O_4$	Lithium manganese oxide
$LiNiMnCoO_2$	Lithium manganese cobalt oxide
$LiFePO_4$	Lithium iron phosphate
LCC	Liquid cooled cylinder
LCM	Lumped capacitance model
LCP	Liquid cold plate
LCO	Lithium cobalt oxide
LFP	Lithium phosphate
LPM	Lumped parameter model
LPV	Linear parameter varying
LES	Large eddy simulation
LiBOB	Lithium bis (oxalate) borate
MATLAB	Matrix laboratory
LabVIEW	Laboratory virtual instrument engineering workbench
MSE	Mean square error
MLP	Multilayer perceptron
MSMD	Multi scale multi domain
NN	Neural network
NI	National Instrument
NMC	Lithium manganese cobalt oxide
NYCC	New York city cycle
NiMH	Nickel metal hydride
NiCad	Nickel cadmium
OCV/OCP	Open circuit voltage/Open circuit potential
PC	Personal computer
P2D	Pseudo two dimensional
PDE	Partial differential equation
PHEV	Plug-in hybrid electric vehicle
PVC	Polyvinyl chloride
PE	Polyethylene

PP	Polypropylene
RC	Resistance capacitance
RBF	Radial basis function
RANS	Reynolds-averaged Navier-Stokes
RNG	Renormalization group
RPM	Revolution per minute
RS-232	Recommend standard number 232
SEI	Solid electrolyte interface
SPI	Solid permeable interphase
SOC	State of charge
SOD	Start of discharge
SOH	State of health
SLE	Special limit of errors
SST	Shear stress transport
$tansig$	Tan sigmoid function
TC	Thermocouple
TDR	Turbulent dissipation rate
TKE	Turbulent kinetic energy
TMS	Thermal management system
US06	United States of America 06 drive cycle
UDDS	Urban dynamometer driving schedule
UQM	Power phase motor developed by UQM
WNN	Wavelet neural networks
1D	One-dimensional
2D	Two-dimensional
3D	Three-dimensional

Chapter 1

Introduction

Energy and the environment are current key issues due to limited fossil fuels sources and concerns over greenhouse emissions [1, 2, 3]. Therefore, car manufacturers are under extreme pressure to improve the fuel economy and emission performance of their cars. In Canada, the transportation sector is the largest contributor to greenhouse gases (GHG) and air pollution in Canada [4]. Subsequently, automobile manufacturers have to create and apply recent advancements to meet their objectives. Electric vehicles (EVs), along with fuel cell vehicles (FCVs), hybrid electric vehicles (HEVs), and also plug-in hybrid electric vehicles (PHEVs), are answers to energy and environmental issues and have recently received much attention due to their "zero emission" label as well as being more energy proficient [5, 6]. Therefore, demand for EVs and HEVs has significantly increased due to rising costs and environmental concerns [7].

The heart of EVs is the battery or battery pack because batteries, a major powertrain component of EVs and HEVs, will undergo thousands of charge/discharge cycles during the life-time of a vehicle. Over this lifetime, a battery degrades potentially to the point of requiring replacement. Given the high cost of batteries and their importance in determining electric vehicle range, it is very desirable to extend battery degradation as long as possible. One element of controlling battery degradation is controlling the battery temperature [8, 9]. Among accessible technologies, the lithium-ion battery plays a key part in the improvement of EVs, HEVs, and PHEVs [10] as a result of their broad use because of :1) high specific energy and power densities [11, 12]; 2) high nominal voltage and low self-discharge rate [13]; and 3) long cycle-life and no memory effect [14]. However, lithium-ion batteries must be precisely observed and managed (electrically and thermally) to avoid safety (inflammability) and performance related issues [15, 16, 17]. Understanding vehicle battery temperatures and heat generations both with experimental and modeling during discharge is the focus of this research. In order to better understand the battery thermal problem, it is useful to first understand the basic vehicle applications for large battery packs. Electrified vehicles are classified in three groups: 1) Hybrid electric vehicles (HEVs); 2) Plug-in hybrid electric vehicles (PHEVs); and 3) Electric vehicles (EVs).

1.1 Hybrid Electric Vehicles (HEVs)

A hybrid electric vehicle has one or more power sources, such as an internal combustion engine and an electric motor [18, 19]. In a hybrid vehicle, the engine is smaller so consequently gives better mileage. These vehicles utilize less fuel and produce less pollution. Modern produced hybrids vehicles prolong the charge on their batteries by taking kinetic energy through regenerative braking. During cruising or idling where only a light thrust is required, "full" hybrids can use the internal combustion engine to generate power by spinning an electric generator in order to recharge the battery or to feed power to an electric motor which drives the vehicle. Almost all hybrids still require gas and diesel as a source of fuel and other fuels for example, ethanol or occasionally plant based oils. There are three principle types of hybrid configurations [20] available on the market: 1) parallel hybrid vehicle arrangement; 2) series hybrid vehicle arrangement; and 3) series-parallel hybrid vehicle arrangement.

1.1.1 Parallel Hybrid Vehicle Arrangement

A parallel hybrid vehicle arrangement is shown in Figure 1.1. In this arrangement, power to the wheels can be simultaneously supplied by the engine and the electric motor. The electric motor and internal combustion engine drive shafts are coupled together on either side of the transmission. Electric motors are powered from the batteries and the motor running backward can likewise be utilized to charge the battery through the regenerative braking system. In a parallel hybrid, for short in city driving, it is also possible to turn off the engine and run the electric motor from the battery pack. In such a case, the parallel hybrid works as a fully electric vehicle and becomes emission free [21, 22, 23]. The driving range is up to 400 miles or more for a parallel hybrid. Parallel hybrids are usually lower power vehicles, such as passenger cars, whereas a hybrid system is utilized to enhance performance. Examples of this type of arrangement can be found in Honda's Integrated Motor Assist (IMA) system used in Civic, Accord, Insight and the Belt-Alternator-Starter (BAS) system used in the Chevrolet Malibu.

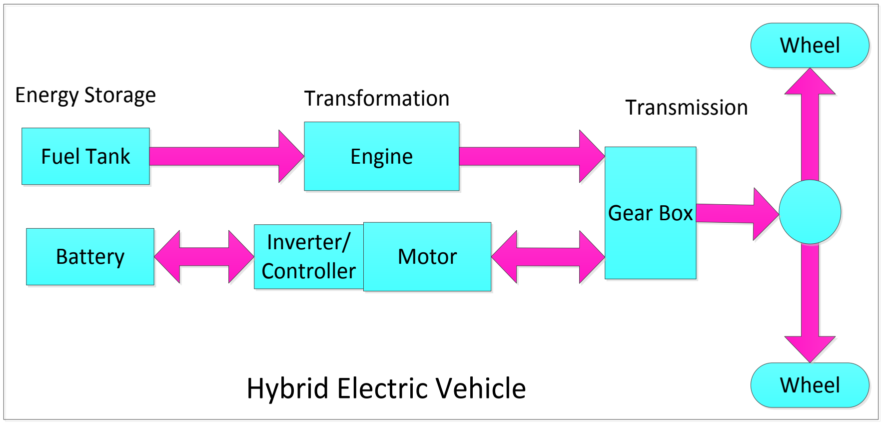

Figure 1.1: Schematic of parallel hybrid vehicle arrangement (modified from [19]).

1.1.2 Series Hybrid Vehicle Arrangement

An arrangement of a series hybrid vehicle is shown in Figure 1.2. Here, the electric motor gives power to the wheels. That is, the engine does not directly provide power to the wheels, but rather the wheels are completely powered by the electric motor. An internal combustion engine drives a generator which produces power that can be stored in the battery and delivered to the electric motor to drive the wheels [21, 22, 23]. Series hybrids are generally higher power systems, sometimes even using a gas turbine between 150 kW and 1000 kW. Series hybrids have a small combustion engine and a large battery pack when contrasted with parallel hybrids. Because of this, series hybrids are more costly than parallel hybrids. This makes series hybrids more efficient in city driving [24]. The Chevrolet Volt developed by General Motors is the best example of this type of vehicle.

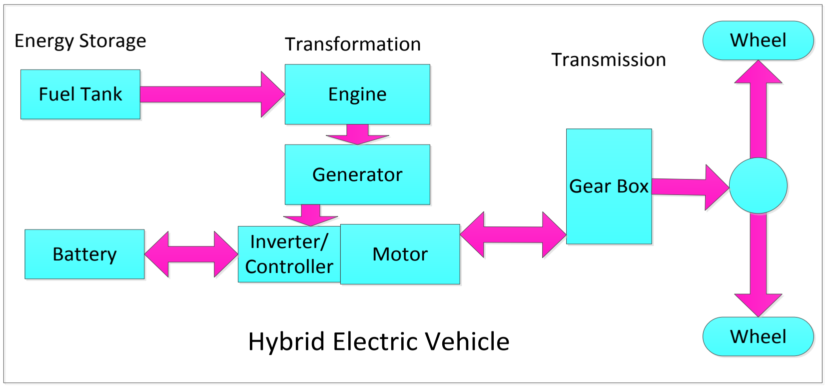

Figure 1.2: Schematic of series hybrid vehicle arrangement (modified from [19]).

1.1.3 Series-Parallel (Power Split) Hybrid Vehicle Configuration

An arrangement of a series-parallel hybrid system is shown in Figure 1.3. This is a most complicated design. In this type of system, power to the wheels can be delivered by the engine and it can power a generator which supplies power/electricity to the battery. This battery supplies power to the motor and then gives power to the wheels [21, 22, 23]. The regenerative braking energy to the battery for later utilization can be delivered by an electric motor. This is similarly called a "power-split" hybrid system in which the hybrid makes use of a power splitting device, typically a planetary gear mechanism and has turned into a prominent design because of its unique modes of operation as well as its use in the successful Toyota Prius. Toyota's hybrid system is able to function as a continuously variable transmission and provide smooth power delivery and very efficient operation. One of the greatest advantages of this kind of hybrid system is the great potential reduction in vehicle emission. Examples of such a system are Toyota's Hybrid Synergy Drive [25] (as used, for example, in the Camry hybrid and Prius), Ford's Escape/Mariner hybrid system, and the GM two mode hybrid system (used in the Chevrolet Tahoe).

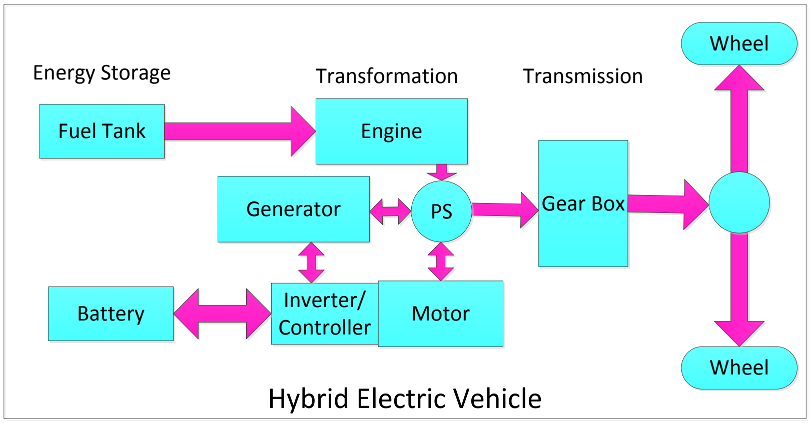

Figure 1.3: Schematic of series-parallel hybrid vehicle arrangement (modified from [19]).

1.2 Plug-In-Hybrid Electric Vehicles (PHEVs)

Plug-in-hybrid electric vehicles may comprise of any of three hybrid systems (series hybrid, parallel hybrid or series-parallel hybrid). Plug-in-hybrids have a large battery pack capacity that can be charged from electrical power output. They can drive a specific distance in an all-electric mode, after which the vehicles works like a non-plug-in-hybrid. This means that while driving in all electric modes, the PHEV consumes no fuel and there is zero emission [26, 27, 28, 29]. PHEVs are classified by their Charge-Depleting (CD) range. For example, a PHEV10 has a charge-depleting range of 10 miles (16 km) and a PHEV40 has a charge-depleting range of 40 miles (64 km). If you drive less than 64 km a day, the PHEV40 would normally operate in charge-depleting mode [30].

1.3 Electric Vehicles (EVs)

Electric Vehicles (EVs) do not utilize an internal combustion engine to supply energy to the wheels and drivetrain. However, they depend on an electric motor to supply the power to the wheels [31, 19, 17, 32]. Most EVs have a more elaborate method to control the amount of electricity going to the motor and an arrangement of gears to drive the wheels in a most effective way. The high price of oil and increased concern over the environmental impact of gasoline-based transportation has led to renewed interest in electric transportation [33, 34]. EVs vary from fossil fuel powered vehicles in that the power they consume is produced from various sources, such as solar power, wind power, and tidal power, or any combination of those energies [35]. The electricity can be stored on board the vehicle utilizing a battery, flywheel or a capacitor. The main benefit of EVs and HEVs is regenerative braking and the capability to recover the lost energy during braking as electricity stored in the on-board battery. Gas and diesel engines are just 30% to 40% productive at transferring fuel energy into kinetic energy (i.e. as work on driveshaft or as motion), while electric motors can convert more than 94% of electrical energy supplied into useful work. EVs can be a substantially more proficient method for transportation, provided that the electricity can be efficiently stored and provided to the motor.

1.4 Drive Cycle

A drive cycle is basically a series of data points of vehicle speed versus time. The use for drive cycles is in vehicle simulations. More precisely, they are utilized in propulsion system simulations to obtain the performance of internal combustion engines, electric drive systems, batteries, transmissions, and fuel cell systems. The dominant standards within the United States and Canada are the UDDS (Urban Dynamometer Driving Schedule) and HWFET (Highway Fuel Economy Test) drive cycles. While the EPA (Environmental Protection Agency) label mentions two drive cycles, there are numerous others. These cycles intend to compare other aspects of the vehicle; for example, efficiency while using accessories such as air conditioning (SC03) or during low speed stop-and-go traffic conditions (NYCC-New York City Cycle). UDDS and HWFET remain dominant as with US06 as a possible addition, which is depicted as a “high acceleration and aggressive” driving schedule. The trace speed and time correlation for these cycles (UDDS, HWFET, and US06) are shown in Figure 1.4 (a, b, and c) for EVs.

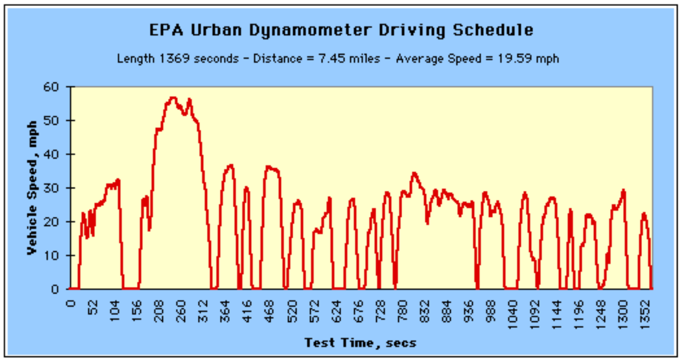

(a) UDDS drive schedule

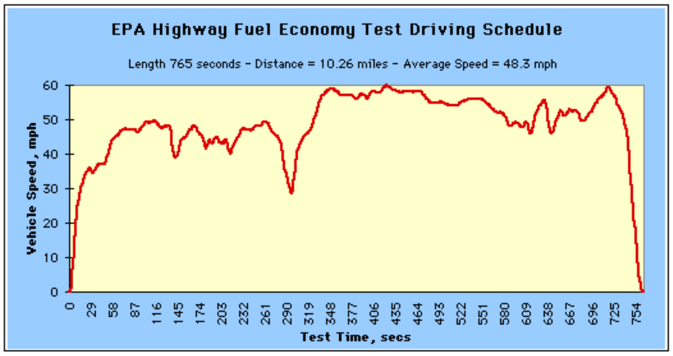

(b) HWFET drive schedule

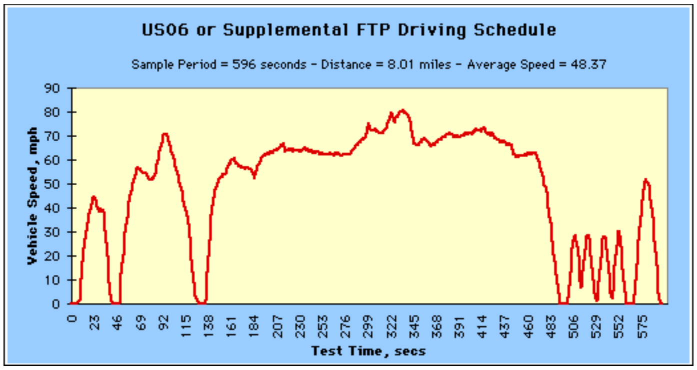

(C) US06 drive schedule

Figure 1.4: (a) UDDS (b) HWFET, (c) US06 drive schedule for EV [36].

1.5 Motivation

Lithium-ion battery packs for EVs and HEVs are greatly influenced by the battery operating temperatures [8, 9] as discussed below. In order to understand the thermal behaviour of batteries and its impact on battery performance and life, the first step experimentally is to study the battery temperature distributions and the heat generation profiles at different charge and discharge rates. To make this study relevant to EVs and HEVs, the charge and discharge rates must be typical to those seen and expected in vehicles. Figure 1.5 shows the surface temperature of a lithium-ion battery cell at different discharge rates of 1C, 2C, 3C and 4C (C-rate is the measurement of the charge and discharge current of a battery), on the order of those seen in vehicles. The charge rate between discharges in all cases is 1C.

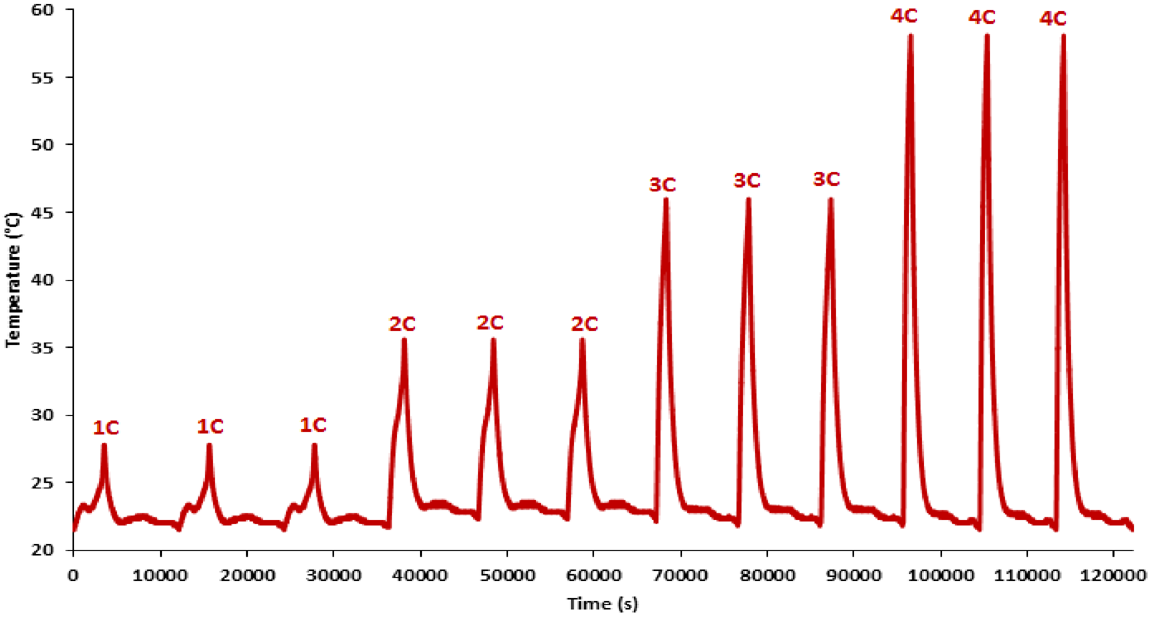

Figure 1.5: Surface temperature profile of a $LiFePO_4$ battery cell during 1C, 2C, 3C and 4C discharge rates and 1C charge rate.

The figure illustrates the large thermal spikes that can accompany discharge. Over a short 15-minute time period (short from a vehicle operation viewpoint) for 4C and 20-minute time period for 3C discharge, enough heat is generated to increase the cell temperature to 58°C (for 4C) and 46°C (for 3C) from a 22°C start condition. This value is only for a single lithium-ion battery cell with free convection boundary condition, so even a greater temperature can result when extrapolated to approximately 300 lithium-ion battery cells in a pack of EVs and HEVs, where there is no free boundary convection, but only conduction between pouch cells. This problem is explained in more detail subsequently.

Operating lithium-ion batteries above 50°C can accelerate the aging process and lead to significant degradation of battery capacity and electric range reduction [37]. As illustrated in Figure 1.5 battery cell temperatures above 50°C are very possible, especially when cells are stacked in modules and packs, and if the ambient temperature is closer to 50°C than the 22°C used in Figure 1.5. The possibility of fire is also a major issue with a high operating temperature, where thermal runaway is a possibility [38]. Thus, adequate battery cooling and thermal management are an integral part of the vehicle operation during electric mode operation. EVs and HEVs require a robust battery thermal management system in order to ensure optimal (safe, good performance, and long battery life) vehicle operation.

Experimental data on the thermal characteristics of batteries is important not only to the battery pack designers and modellers, but also to those looking more fundamentally at electrochemical battery models. Battery modeling gives very important information on battery charging/discharging, SOC, SOH, and temperature. There are different methods for modeling batteries, for example: 1) neural network modeling; 2) electrochemical modeling; 3) turbulence modeling; and 4) equivalent circuit modeling. Electrochemical modeling provides a deep understanding of the chemical and physical process inside the battery and is useful when building a cell or pouch cell, but high computational time makes this approach impractical for applications that involve multiple pouch cells, such as vehicle battery packs. On the other hand, in equivalent circuit modeling, battery losses are represented in terms of electrical circuit components, making this method more efficient in terms of computation.

1.6 Objectives

Given the problems of 1) poor battery thermal performance, 2) aging or degradation of batteries, and 3) fire issues, all due to high battery operating temperature, as identified in the previous section, and given our limited knowledge of the thermal behaviour of vehicle batteries [9, 8], it is important to conduct further research into the performance of EV and HEV batteries undergoing realistic vehicle charge and discharge cycles. To date, significant work has been performed on battery modeling [39, 40, 41, 42, 43, 44, 45] but limited published work exists experimentally with varying boundary conditions. Therefore, one of the key objectives in this research is to characterize the thermal behavior of a vehicle suitable lithium-ion battery pouch cells and packs using cold plates to provide a large range of boundary conditions. Based on the above reasons, the specific objectives along with their sub objectives/experimental milestones of the thesis research are listed as follows:

a) To characterise the thermal behavior of a lithium-ion battery cell undergoing various charge and discharge rates with a wide range of boundary conditions.
b) To develop and validate a battery thermal model at different discharge rates (1C, 2C, 3C, and 4C) and different ambient/cooling/boundary conditions (5ºC, 15°C, 25°C, and 35°C). The developed model should be scaled up to vehicle battery pack level and validated with a real world drive cycle.
c) To examine the effect of discharge rate and operating temperature on battery cell and pack discharge capacity.

   In order to fulfill the above mentioned objectives, empirical data, including battery voltage, current, temperature, heat flux, and heat generation, are required. A thermal boundary condition test apparatus is designed and developed for a $LiFePO_4$ prismatic battery cell with a dual cold plate approach to generate the data of interest. The data from each part is used in the development of battery models. Some specific sub objectives/experimental milestones for the above stated objectives are:

   To design an apparatus that directly measures:

   - The surface temperature distribution of prismatic batteries undergoing discharge and charge cycles.
   - The surface heat flux near the anode, the cathode, and at the center of the prismatic lithium-ion pouch cell.
   - The heat rejection to the dual cold plates at different discharge rates, with varying boundary conditions.

d) To characterise the thermal behavior of a lithium-ion battery pack undergoing various charge and discharge rates with a wide range of boundary conditions.

In order to fulfill the above mentioned objective, empirical data, including battery pack voltage, pack current and temperature are required; for this, a thermal boundary condition test apparatus is designed and developed for a pack to generate the data of interest. A battery pack is designed and developed with three lithium-ion battery cells connected in series and 18 thermocouples that directly measure the surface temperature distribution on all prismatic batteries undergoing discharge and charge cycles.

e) To identify and quantify the locations of highest heat generation using IR imaging techniques.

For the IR images of a lithium-ion battery cell, a thermo-graphic camera is used to produce images of the principal battery surface to visually observe temperature distribution and heat generation. This is an effective tool for finding temperature distribution or hot spots on the surface of an object without using any intrusive temperature sensors.

f) To develop and validate an electrochemical thermal (ECT) model for a large sized prismatic lithium-ion battery.

For this ECT modeling, a commercial software, ANSYS Fluent, is used and the developed electrochemical-thermal model can be used to analyze the effect of different parameters on the electrochemical and thermal characteristics of batteries. These parameters may include charge/discharge rates and geometric design of the battery cells. From these studies, the model design can be optimized, contributing to a more uniform electrochemical reaction and temperature distributions. The developed model should be validated against the experiment results for the thermal profiles on the surface of the battery along with IR images. This validation ensures that the model is correctly developed and can be used in different studies such as battery design.

g) To develop and validate a numerical model for mini channel cold plates placed on the top and bottom surface of a lithium-ion battery.

For the numerical modeling, the flow in the cold plates is considered to be turbulent. Although analytical solutions for these flows are not accurate, on the basis of the continuum fluid assumption, the dynamics of turbulence is adequately described by the continuity and Navier-Stokes equations. The solutions of the Navier-Stokes equations are solved numerically. The solution is implemented by generating a mesh of the region of interest or domain. The governing equations are then discretized yielding a system of algebraic equations which can be solved at each point within the domain. This study provides results showing the temperature and velocity distributions at different C-rates and BCs. The physical insight of this kind of study will provide more information to improve the design of an effective battery cooling system.

h) To perform cycling degradation testing and modeling of a lithium-ion battery in real life conditions.

For this degradation study, in-situ vehicle data is collected to enable characterization of vehicle batteries undergoing real-world drive cycles by outfitting an electric vehicle with data loggers and a data reporting infrastructure. The data from each part is used in the development of battery models. Some specific experimental milestones/sub objectives for above stated objectives are:

- To install a data logger in an EV.
- To collect driving and battery data from an EV, in order to analyze the battery performance.
- To do performance assessment and evaluations under various drive cycles in terms of temperature, voltage, and SOC from lab battery versus vehicle battery, using real drive cycles from an EV.
- To develop the Thevenin battery model utilizing MATLAB along with an empirical degradation model and validate in terms of the battery SOC and voltage.
- To characterize the lithium-ion battery using different discharge-charge cycles with hybrid pulse power characterization (HPPC).

1.7 Thesis Structure

This thesis is organized into seven chapters as follows:

Chapter 2 presents the background and literature reviews related to the lithium-ion battery used in electric vehicles. Battery definitions, lithium-ion cell operation, insertion process, materials for anode, cathode, and separator, types of lithium-ion batteries, thermal management of batteries (air cooling and liquid cooling), thermal study via thermocouples and calorimeters, heat generation and thermal runaway are explained. In addition to this, battery thermal modeling with different approaches, such as electrochemical modeling, equivalent circuit modeling, neural network modeling, ANSYS modeling, and battery degradation modeling and mechanism, is presented.

Chapter 3 introduces an experimental study in which Experiment 1 includes an experimental set-up, procedure and plan for the thermal characterization of a battery cell. It also provides an explanation of thermocouple and heat flux sensors locations on the principle surface of the battery, governing equations, and the data analysis method. Experiment 2 includes the battery pack testing with all thermocouple locations. Experiment 3 focuses on degradation testing for capacity fade measurement and includes a data logger installation in EVs, data collection and data analysis method.

Chapter 4 presents the modeling of a lithium-ion battery. The first model deals with the thermal behavior of a lithium-ion battery using a neural network approach. It includes input training data, output training data, training performance plot, training state plot, error histogram, regression plot, and mean square error. Finally, the mathematical functions are presented along weights and bias. The second model focuses on the electrochemical thermal model for a large sized prismatic lithium-ion battery. This includes all governing equations with boundary conditions for charge conservation in the solid phase, charge conservation in the electrolyte phase, lithium conservation in the solid phase, and lithium conservation in the electrolyte phase. To conclude, the Butler-Volmer equation is used to couple the charge-species governing equation. The third model deals with ANSYS Fluent turbulence modeling for mini-channel cold plates. The water flow in the cold plates is turbulent and therefore the flow is modeled using the Reynolds-Averaged Navier-Stokes Equations (RANS). It also includes the governing equations, geometry and boundary conditions, design of the set-up in NX8.5, mesh generation in ICEM CFD, and finally a grid independence study. The fourth model considers battery degradation based on the Thevenin model for drive cycles obtained from an EV.

Chapter 5 presents the results and discussion. The first part explains experimental results obtained from the battery cell and pack level testing in terms of surface temperature distribution, discharge voltage profiles and heat generation profiles. The second part includes the battery thermal model validation, while the third part includes the electro chemical thermal model validation. The fourth part of this chapter discusses the CFD analysis for a mini channel cold plate, and the fifth part includes the degradation results obtained from an EV and validation. Finally, capacity fade measurement over three months of driving is presented.

Chapter 6 presents conclusions and recommendations for future work.

Chapter 2

Background and Literature Review

This chapter reviews background information about the battery, including: chemistry and definitions; lithium-ion battery operation; insertion process; thermal management of batteries; thermal measurements via thermocouples and calorimeters; battery thermal modeling; and battery degradation mechanism.

2.1 Batteries

Moving from conventional vehicles to EVs and HEVs, the heart of the vehicle moves from the engine to the battery. In the nineties, developed EVs utilized lead-acid batteries. The typical range was around 100 kilometers. However because lead-acid batteries have a low energy density, the weight of the vehicle was large, hence different chemistries were utilized in subsequent years [46]. Because of the higher power and energy density and improved cycle life, EVs began to utilize nickel metal hydrate (NiMH). Today NiMH batteries are still utilized in HEVs and PHEVs for their low cost per watt. However, because of high self-discharge, limited SOC operating limit and low energy density, these batteries are unsuitable for EVs. ZEBRA or molten salt batteries are likewise utilized in EVs. These batteries have a low cost and high safety, but because the operating temperature is too high (270-350˚C) and power density is too low, they are not very popular in EV applications [46]. Table 2.1 presents the characteristics of various types of batteries used in EVs.

Today, the lithium-ion battery is considered as an appropriate energy storage device for alternative energy sources, such as wind and solar, and has numerous advantages: i) high specific energy and power densities [11, 47]; ii) high nominal voltage and low self-release rate [13] ; and iii) long cycle-life and no memory effect [14]. For these reasons, the lithium-ion battery is the most advanced battery technology for EVs, HEVs, and PHEVs. The disadvantages of lithium-ion batteries also include the high cost and safety issues. It can be said that the battery performance, cost and life directly affect the life and performance of the EVs. Subsequently, the need to extend the battery lifetime and to utilize it at their full capacity is of the utmost importance. Figure 2.1

represents various storage devices with different energy and power. Despite these positive aspects that legitimize the recent spread of this technology, it is vital to notice that, during operation, lithium-ion polymer batteries must be deliberately checked and managed (electrically and thermally) to avoid issues related to safety (inflammability) and performance [15].

Table 2.1: Characteristics of battery types used in EVs [46].

Characteristic	Lead Acid	NiMH	ZEBRA	Li-ion
Nominal cell voltage	2 V	1.2 V	2.58 V	2.5 V/ 3.3 V/ 3.6-3.7 V
Specific energy	30-45 Wh/kg	30-80 Wh/kg	90-100 Wh/kg	90-220 Wh/kg
Energy density	60-75 Wh/L	140-300 Wh/L	160 Wh/L	280-400 Wh/L
Specific power	180 Wh/kg	250-1000 Wh/kg	150 Wh/kg	600-3400 Wh/kg
Cycle life	500-800	500-1000	1000	1000-8000
Self-discharge	2-4% /month	20-30% /month	0% /month	2-5% /month
Temperature range	-20-60℃	-20-60℃	270-350℃	-20-60℃
Relative costs	Low	Moderate	Low	High

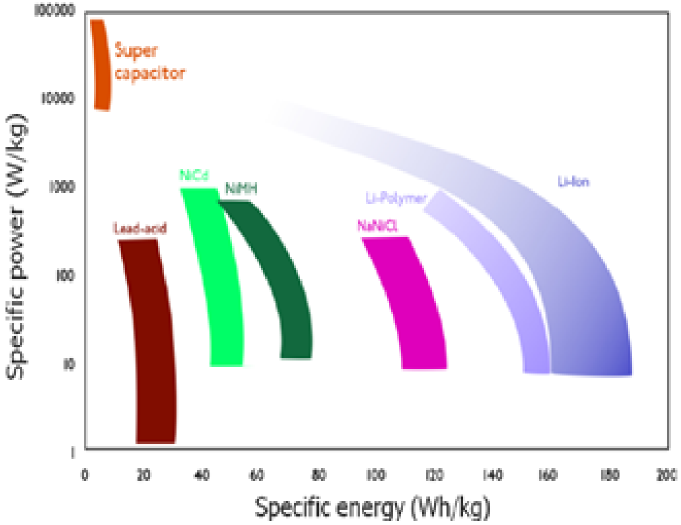

Figure 2.1: Ragone plot [48].

A comparison between the best EV suitable lithium-ion batteries is presented in Figure 2.2. The more the colored shape extends along a given axis, the better the execution in that direction. For instance, lithium-iron-phosphate ($LiFePO_4$/LFP) does not experience thermal runaway and has no fire hazards, since no oxygen is released at high temperatures [49]. $LiFePO_4$ cells have the lowest costs per

Ah and kW [50], great life expectancy, good power abilities and are extremely safe, yet they have lower specific energy and poor performance at low temperatures.

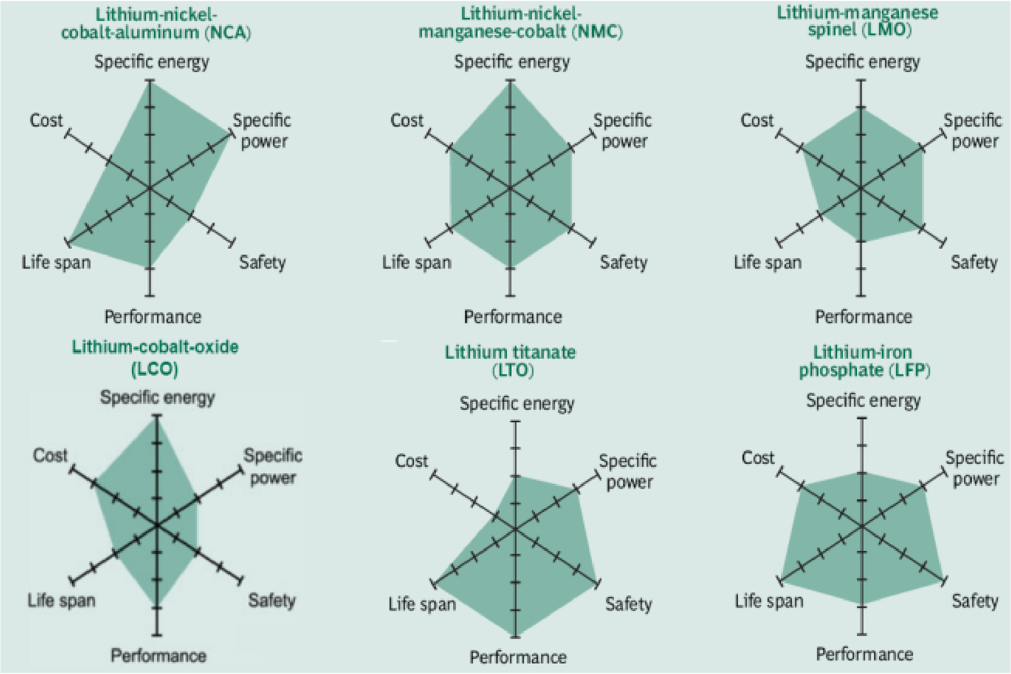

Figure 2.2: Comparison of suitable lithium ions for EVs [51].

The most well-known lithium-ion type battery used in small consumer electronics such as laptops and cell phones, is the lithium-cobalt-oxide ($LiCoO_2$/LCO) because of its high specific energy. Tesla Motors utilizes laptop sized LCO battery cells in their EVs in combination with a liquid cooling system safety issues. However, low specific power and life span prevents this type from being a good choice for EVs [46]. Lithium-iron-phosphate ($LiFePO_4$/LFP) on the other hand does not experience thermal runaway and experiences no fire hazards, since of no oxygen is released at the higher temperature side [49]. $LiFePO_4$ cells have good life span, low costs per Ah and kW [49] and great power abilities, and are extremely safe, yet the specific energy is low and the performance is poor at low temperatures. The batteries can either be of high power density type or high energy density type. Power density gives a good measure of how much energy can be released due to discharge at a given time with regards to kilograms or liters. Energy density is the amount of energy with regards to kg or liters. A high energy density battery is useful in applications where a longer driving distance is required, such as in a PHEV which is intended to be driven on pure electricity for longer distances.

2.2 Battery Definitions

Some basic definitions related to the lithium-ion battery are presented in this section [52].

Cell, modules, and packs – Electric and hybrid vehicles have a high voltage battery pack that comprises individual modules and battery cells arranged either in series or parallel. A cell is the smallest, packaged form a battery can take and is usually in the order of one to six volts. A module comprises several cells generally connected in a series or parallel arrangement. A battery pack is then assembled by joining the modules together, again either in series or parallel [52]. An exploded view of a A123 prismatic battery module and pack is presented in Figure 2.3 (a). A battery pack comprised of A123 modules is appears in Figure 2.3 (b).

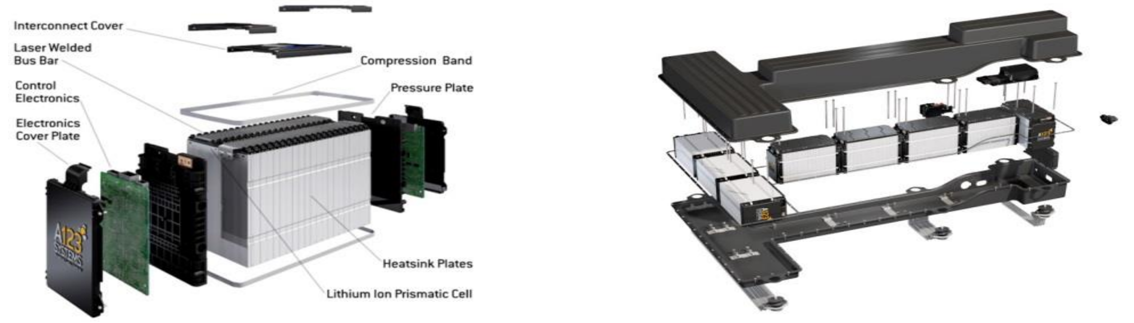

a) Exploded view of A123 25S2P prismatic module **b) Battery pack comprised of A123 modules**

Figure 2.3: a) Exploded view of A123 25S2P prismatic module [53], b) Battery pack comprised of A123 modules [54].

Secondary and Primary Cells – Batteries for electric and hybrid vehicles are all secondary batteries. A primary battery is one that cannot be recharged. A secondary battery is one that is rechargeable [52].

C and E-rates - The discharge and charge current of a battery is measured in C-rate. The majority of small batteries are rated at 1C, which means that a 100 Ah battery would provide 100A for 1 hour if discharged at 1C rate. The same battery discharged at 0.5C (1/2C) would give 50A (100 x 0.5=50) for 2 hours. At 2C, the 100Ah battery can deliver 200A for half an hour (30 minutes). 1C is also referred to as a 1 hour discharge; a 0.5C would be a 2 hour and 0.1C a 10 hour discharge.

Similarly, E-rate describes the discharge power. A 1E-rate is the discharge power to discharge the entire battery in 60 minutes (1 hour). It is also given by:

$$C - rate = \frac{I}{Q_{max}} \tag{2.1}$$

State of charge (SOC) - The state of charge (SOC) is a percentage measure of charge remaining in a battery relative to its predefined "full" and "empty" states. Manufacturers typically provide voltages that indicate when the battery is empty (0% SOC) and full (100% SOC). SOC is generally calculated using current integration to determine the change in battery capacity over time. The most widely recognized and simplest SOC estimation strategy depends on the notion that one can count the coulombs entering and leaving the battery. Since current, I, can be expressed in coulombs per second, the integration of that current with respect to time, t , gives the aggregate number of coulombs, N_C , transported into or out of the battery.

$$N_C = \int_{t_0}^{t} I \, dt \tag{2.2}$$

The total number of coulombs can be expressed as a capacity, Q, following a simple unit conversion.

$$Q = \int_{t_0}^{t} \frac{I}{3600} \, dt \tag{2.3}$$

Thus SOC can be estimated by considering the initial SOC, SOC_0 as well as the capacity processed during usage as a percentage of the maximum battery capacity, Q_{max}.

$$SOC = SOC_0 - \frac{Q}{Q_{max}} \times \ 100 \ \% \tag{2.4}$$

However, the limitation of this method is that it requires the initial SOC of the time period; which may be unavailable. Fortunately, current levels of vehicle technology, memory, and processing power make this form of SOC estimation an appropriate choice.

Depth of discharge (DOD) – This is a percentage measure of the amount of energy extracted during a discharge process, compared to a fully charged state. For instance, a 100 Ah battery from which 40 Ah has been withdrawn has undergone a 40% depth of discharge (DOD). Depth of discharge is the opposite of state of charge (SOC). A battery at 60% SOC is also at 40% DOD [52].

State of health (SOH) - The state of health (SOH) is a measurement of the battery condition compared to its initial or ideal state, measured in percentage points; i.e. the state of the battery between the beginning of life (BOL) and end of life (EOL) expressed as a percentage. The EOL of a battery is reached when the battery cannot perform according to the minimum requirement. There is no universally accepted technique for describing SOH. Any of the following, in single or in combination form, might be used: internal resistance; impedance/conductance; capacity; voltage; ability to accept charge; and number of charge/discharge cycles [52].

Cycle life - Cycle life alludes to the number of times a battery must be discharged and charged before its nominal capacity goes down below 80% (or some other predetermined threshold) of its rated value. Cycle life is given for a particular DOD and determined under particular charge and discharge conditions. Typically, higher DOD translates to a lower life cycle [52].

Open Circuit Voltage (OCV or Voc) - The open circuit voltage (OCV) is the voltage when there is no current passing in or out from the battery, and, subsequently no chemical reactions occur within the battery. It is a function of SOC and is expected to remain the same during the life-time of the battery. Moreover, with the change in time, other battery characteristics will also change, e.g. capacity gradually decreases as a function of the number of discharge-charge cycles [52].

Terminal Voltage (V) - The voltage between the battery terminals when load connected. Terminal voltage fluctuates with SOC and discharge/charge current [52].

Nominal Voltage (V) – Nominal voltage is the reference voltage or reported voltage of the battery. It also sometimes thought of as the “normal” voltage of the battery [52].

Cut-off Voltage (V) – Cut-off voltage is the minimum allowable voltage. It is this voltage that generally defines the “empty” state of the battery [52].

Charge Voltage (V) - The voltage to which the battery is charged when charged to full capacity. Charging schemes usually consist of a constant current charge until the cell voltage has reached the charge voltage, then constant voltage charge, which allows the charge current to taper until it is very small [52].

Float Voltage (V) - The voltage at which the battery is maintained after being charged to 100% SOC to maintain that capacity by compensating for self-discharge of the battery [52].

Capacity or Nominal Capacity (Ah for a specific C-rate) – The coulometric capacity, the total Amp-hours available when the battery is discharged at a certain discharge current (specified as a C-rate) from 100% SOC to the cut-off voltage. Capacity is calculated by multiplying the discharge current (in Amps) by the discharge time (in hours) and decreases with increasing C-rate [52].

Energy or Nominal Energy (Wh (for a specific C-rate)) – The "energy capacity" of the battery, the total Watt-hours available when the battery is discharged at a certain discharge current (specified as a C-rate) from 100% SOC to the cut-off voltage. Energy is calculated by multiplying the discharge power (in Watts) by the discharge time (in hours). As with capacity, energy decreases with increase in C-rate [52].

Specific Energy (Wh/kg) - The specific energy of a battery is expressed as a nominal energy per unit mass, such as Wh/kg. It is highly dependent on the battery chemistry and packaging [52].

Specific Power (W/kg) - The specific power of a battery is expressed as a nominal power per unit mass, such as W/kg or kW/kg. It is highly dependent on the battery chemistry and packaging [52].

Energy Density (Wh/L) - The energy density of a battery is expressed as a nominal energy per unit volume, such as Wh/L. It is highly dependent on the battery chemistry and packaging [52].

Power Density (W/L) - The power density of a battery is expressed as a nominal power per unit volume, such as W/L or kW/L. It is highly dependent on the battery chemistry and packaging [52].

Internal resistance- The internal resistance is sometimes considered as the ohmic resistance of the cell, which is the immediate voltage change after use of a current step on a cell in equilibrium. In other words, the internal resistance is the summation of the ohmic, activation and diffusion polarization resistances [55, 52], which is the greatest possible voltage drop in the cell. Nevertheless, power dissipation in the form of heat will result because of the entire voltage drop. The voltage drop can be generally characterized as:

- IR drop is a direct result of the current flowing across the internal resistance of the battery, by ohmic resistance.

- Activation polarization alludes to the different retarding factors inherent in the kinetics of an electrochemical reaction, similar to the work function that ions must overcome at the junction between the electrodes and the electrolyte.
- Concentration polarization considers the resistance faced by the mass transfer (e.g. diffusion) process by which ions are transported across the electrolyte from one electrode to another.

Figure 2.4 represents the typical polarization curve of a battery with the contributions of all three above mentioned components exhibited as a function of the current withdrawn from the battery. Since these components are current-dependent, the voltage drop caused by them usually increases with increasing output current. The internal resistance of a battery relies on temperature, SOC, and C-rate. Different values for the internal resistance can be discovered depending on the measurement strategy.

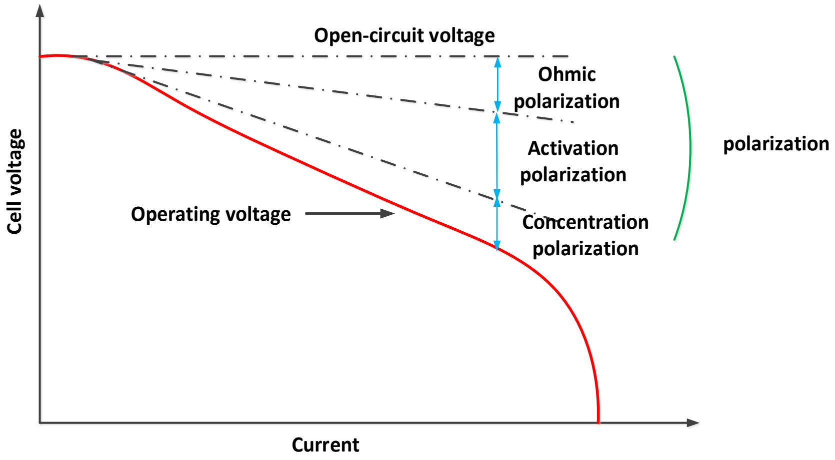

Figure 2.4: Ohmic, activation, and concentration polarization of a battery (modified from [56]).

2.3 Lithium-Ion Cell Operation

A lithium-ion battery cell usually consists of five distinctive layers: two current collectors (the negative current collector and positive current collector); a negative electrode (anode); a separator; and a positive electrode (cathode). The cathode is made of a composite material and defines the name of the lithium-ion battery cell. There are generally four types of positive electrode materials [8, 57]: 1) a metal oxide with a layered structure, such as, Lithium cobalt oxide ($LiCoO_2$ / LCO)

[58]; 2) a metal with a three dimensional spinel structure, such as, Lithium manganese oxide ($LiMn_2O_4$) [59]; 3) Lithium nickel manganese cobalt oxide ($LiNiMnCoO_2$/NMC); and 4) a metal with an olivine structure, such as Lithium iron phosphate ($LiFePO_4$/LFP) [60]. The anode is generally made of graphite or a metal oxide. The electrolyte can be liquid, polymer or solid. Figure 2.5 (a) shows the composition of a lithium-ion battery.

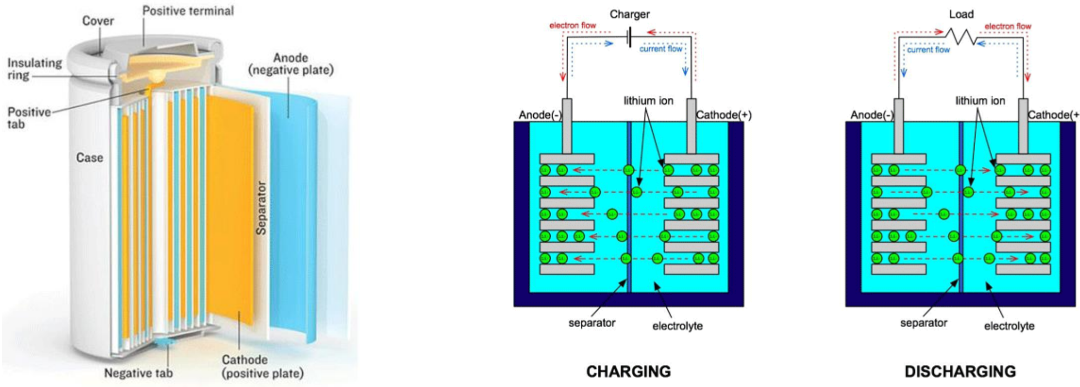

a) A schematic of lithium-ion battery [61] **b) Charge/discharge mechanism of lithium-ion battery [61]**

Figure 2.5: Lithium-ion battery structure and charge/discharge mechanism.

The lithium ions diffuse from the anode towards the cathode via the electrolyte during the discharge process. The lithium ions will intercalate (Intercalation alludes a reversible chemical process of binding a molecule between other molecules. Deintercalation is the opposite process, causing the cathode to become more positive). Because of the potential difference between the cathode and anode, an electric current will pass through the external circuit, supplying power to the load. During charging, the opposite mechanism occurs. The current will cause the lithium ions to deintercalate from the cathode and diffuse to the anode. At the anode intercalation of the lithium ions occurs, charging the battery. The charge and discharge mechanism of a lithium-ion battery is shown in Figure 2.5 (b).

2.4 Insertion Process

Heat generation within the battery cell is a complex process and is dependent on the electrochemical reaction rates; it changes with time and temperature. As shown in Figure 2.6, the active materials in both electrodes (positive and negative electrode) behave like an important element for the lithium content of the battery in a lithium-ion cell. The lithium ions can be removed from or inserted into active material particles without significant change of the structure of the element. This process, called the exchange process, forms the basis of lithium-ion batteries. During the charging process, lithium-ion removed from the active side in the positive electrode and inserted into the negative electrode.

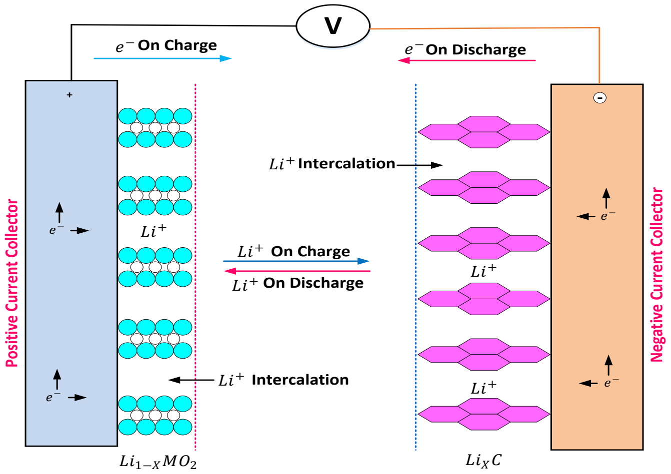

Figure 2.6: Charge and discharge mechanism in lithium-ion battery (modified from [56]).

In Figure 2.6 [56], $LiMO_2$ is a metal oxide material used in the positive electrode and C is a carbonaceous material used in the negative electrode. In the discharge process, lithium-ion travels via the electrolyte to the positive electrode. The electrochemical reactions for the positive electrode, negative electrode, and the overall reaction are given by [47, 62]:

Positive electrode :
$$LiMO_2 \underset{Discharge}{\overset{Charge}{\rightleftarrows}} Li_{1-x}MO_2 + x\,Li^+ + xe^- \tag{2.5}$$

Negative electrode :
$$C + x\,Li^+ + xe^- + LiMO_2 \underset{Discharge}{\overset{Charge}{\rightleftarrows}} Li_xC \tag{2.6}$$

Overall :
$$LiMO_2 + C \underset{Discharge}{\overset{Charge}{\rightleftarrows}} Li_xC + Li_{1-x}MO_2 \tag{2.7}$$

2.5 Anode

Anode materials are typically carbonaceous in nature. It is important for the anode, and similarly the cathode, to have the following: capacity to hold large amounts of lithium without significant change in structure; good chemical and electrochemical stability with the electrolyte; a good electrical and ionic conductor; and low cost.

Graphite: Today, graphite is one of the most commonly utilized anode materials in lithium-ion batteries, stacked in layers. It undergoes a reversible lithium-intercalation reaction from 0 to 0.2 V vs Li/Li+ and is favoured for its small volume change during lithiation and delithiation [63]. With graphite anodes, high coulombic efficiencies of over 95% have been achieved, but they have a relatively low theoretical specific capacity of 372 mAh/g [64]. Although this is already higher than the specific capacity of the commonly used cathode materials, higher specific capacity anodes are still desirable because they contribute to a lower overall battery density. Among carbonaceous materials, CNTs (carbon nano tubes) are the most promising materials being developed. Purified CNTs of the single walled variety can reversibly intercalate lithium ions with a maximum composition of $Li_{1.7}C_6$, equivalent to 632 mAh/g. Etching can increase the reversible capacity to 744 mAh/g, and capacities as high as 1000 mAh/g have been reported using ball milling treatments [65]. Multiwalled CNTs have a reported reversible capacity of up to 640 mAh/g. Although CNTs have high reversible capacities, they also have large irreversible capacities as high as 1488 mAh/g for purified single walled CNTs [65]. This lithium, which cannot be cycled, causes growth of SEI (solid electrolyte interface) and reduces overall capacity. Two major issues that must be solved before CNT anodes can be widely adopted are excessive irreversible capacity and methods of large-scale fabrication [66].

Silicon: Silicon is another leading alternative anode material to carbon and has been extensively researched. Pure Si anodes readily alloy with lithium and have an extremely large theoretical capacity of 4200 mAh/g, but are impractical as they undergo great volumetric changes and thus have poor cycleability. Composite materials have been developed to mitigate the effects of the mechanical stresses of lithiation and delithiation. One method is to house the active silicon material in inert matrices made of materials such as C (e.g. graphite, pitch, CNTs), TiC, SiC, TiN, or Cu/C. The inactive matrix absorbs the mechanical stresses and strains experienced by the active phase, resulting in improved cycleability. Nanowires have also been proposed as an anode material because lithium diffusion occurs only in one dimension and mechanical stresses can be well accommodated. Low cycleability even at small currents and significant irreversible capacities remain challenges in the development of silicon based anodes [66].

2.6 Cathode

A cathode material is usually a metal oxide capable of intercalating lithium ions. It is important that the cathode be able to hold a large amount of lithium without significant change in structure, have a good chemical and electrochemical stability with the electrolyte, be a good electrical conductor and diffuser of lithium ions, and be of low cost. The thermal stability and the rate capability of the battery is also largely dependent on the cathode material [67]. A layered structure of $LiCoO_2$, $LiMn_2O_4$, and $LiFePO_4$, is shown in Figure 2.7.

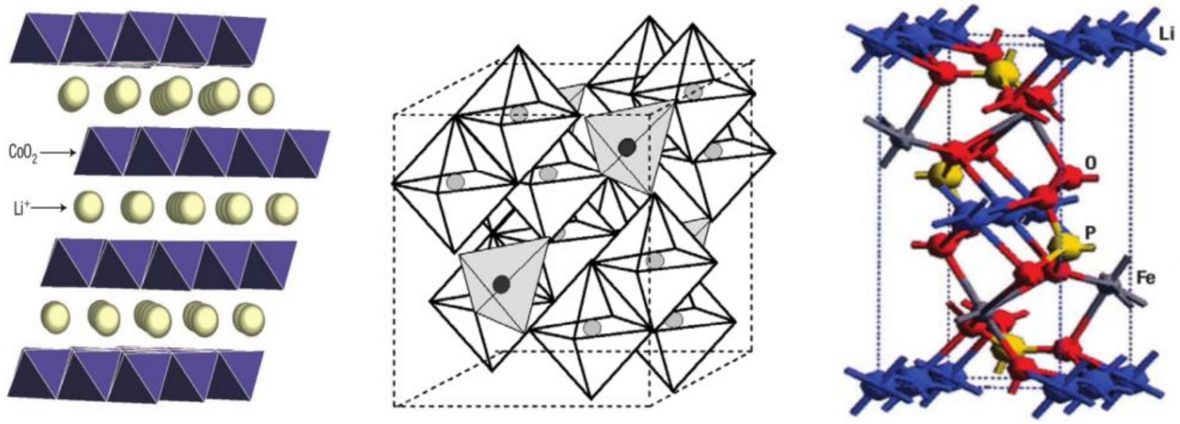

a) Layered structure of $LiCoO_2$ **b) Cubic crystal structure of $LiMn_2O_4$** **c) Olivine structure of $LiFePO_4$**

Figure 2.7: a) Layered structure of $LiCoO_2$ [58], b) Cubic crystal structure of $LiMn_2O_4$ [59], and c) Olivine structure of $LiFePO_4$ [60].

$LiCoO_2$: $LiCoO_2$ is most the most commonly used cathode material [68], shown in Figure 2.7 (a). LCO batteries are widely used in portable applications. Lithium ions are intercalated between sheets of CoO_2 274 mAh/g, but an anisotropic structural change occurs at $Li_{0.5}CoO_2$, so the realizable capacity is limited to about 140-160 mAh/g [69, 70, 71, 72]. Coatings such as $AlPO_4$ have been developed to improve capacity retention and thermal stability [67]. The discharge capacity of $LiCoO_2$ is good; 136 mAh/g at a 5C rate has been demonstrated with multiwalled carbon nanotube (CNT) augmented cathodes. However, cobalt is relatively expensive as compared to other transition metals, such as, manganese and iron, despite the attractive electrical properties of $LiCoO_2$ cathodes.

$LiMn_2O_4$: $LiMn_2O_4$ is a promising cathode material with a cubic spinel structure, as shown in Figure 2.7 (b), where the corners of each tetrahedral and octahedral are oxygen atoms. The theoretical specific capacity is 148 mAh/g. Current designs achieve between 115 and 130 mAh/g at modest discharge rates of 1C or less [73, 74, 75]. $LiMn_2O_4$ nanowire cathodes have demonstrated to possess excellent high power capabilities of 107 and 102 mAh/g at 5C and 10C, respectively and with virtually no capacity loss after 100 cycles. Other transition metals such as Ni, Co, and Fe can also be added to $LiMn_2O_4$ in varying amounts to increase capacity and improve capacity retention during cycling [68].

$LiFePO_4$: $LiFePO_4$ is one of the most recent cathode materials to be introduced. Its olivine structure, as shown in Figure 2.7 (c), is very different from the layered and spinel structures of other lithium-ion chemistries, and its intercalation mechanism is also different, involving phase changes. It has a theoretical specific capacity of 170 mAh/g, a figure which has been approached by recent advances [76]. A composite material such as $LiFePO_4/C$ with a nano-carbon wire network has been shown to have excellent high rate performance, achieving 129 mAh/g at a 10C rate and retaining over 90% of its capacity after 400 cycles at 10C [77]. $LiFePO_4$ has the added advantage of being inexpensive and environmentally friendly.

2.7 Separator

Lithium-ion cells use a separator known as microporous film to prevent physical contact between the cathode and anode while permitting free ion flow. The battery performance can be adversely affected by the presence of separator material as it increases electrical resistance as well as battery density [78]. Therefore, care must be taken in order to select an appropriate material. Commercially available liquid electrolyte cells utilize microporous polyolefin materials, such as polyethylene (PE) or polypropylene (PP). Pore sizes of 0.03 to 0.1 μm, and 30 to 50% porosity are commercially available [79]. The separator films form an important element of the battery in an over-temperature scenario. The low melting point of polyethylene (PE) materials allows their use as a thermal fuse. As the temperature rises to the softening point of the polymer, the membrane begins to shrink, and consequently pore size is reduced. The flow of Li+ ions is disrupted and the reaction rate is decreased. If the temperature continues to rise, the separator is required to be capable of shutting down the reaction entirely, below the thermal runaway threshold. For currently utilized PE-PP bilayer separators shutdown occurs at about 130°C and melting occurs at about 165°C [78].

2.8 Types of Lithium-ion Batteries

Lithium-ion batteries are available in various forms. The internal structure of the different types of batteries is shown in Figure 2.8. The cylindrical and prismatic batteries are built from wound electrodes and separators, immersed in electrolyte, containing several electrochemical cells within. The coin battery is a small flat construction containing a single electrochemical cell within it, while the pouch battery is also a flat construction, but containing several electrochemical cells within. Cylindrical, prismatic, and pouch packaging are often used in automotive applications because of the larger surface areas of the positive and negative electrodes. The intended operating conditions for the battery determine which packaging is selected by the automotive manufacturer. For example, the Chevrolet Volt and Nissan Leaf use pouch batteries while the Tesla Model S uses cylindrical batteries. Usually, cylindrical cells designs are limited to below 4 Ah while prismatic cells designs are used for higher capacity ratings [79].

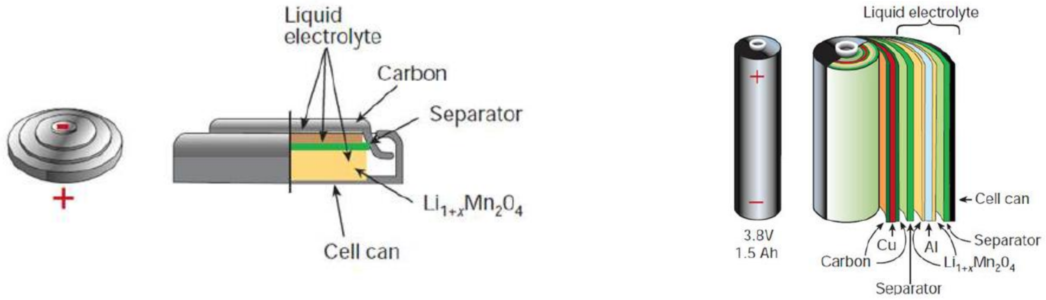

(a) Coin Battery **(b) Cylindrical Battery**

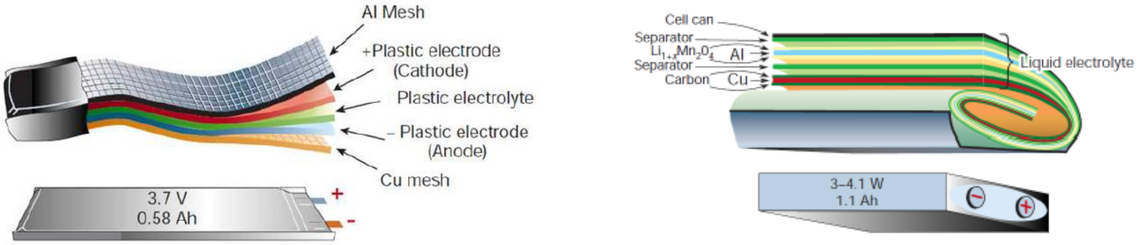

(c) Pouch Battery **(d) Prismatic Battery**

Figure 2.8: Internal structure of different types of battery [80].

2.9 Thermal Management of Batteries

Thermal management of batteries is crucial in acquiring the required performance at a lower environmental temperature and the desired life at a higher environmental temperature. Lithium-ion batteries degrade quickly at high temperatures, while cold temperatures diminish power and energy output, in this manner limiting their driving range or performance capabilities [39, 81]. The heat produced within a battery must be dissipated to improve reliability and prevent failure [82, 83, 84]. A thermal management system is necessary in transportation applications in order to regulate the batteries to operate within the required temperature range; and to decrease uneven distribution of temperature [82]. In a battery pack, uneven temperature variations may lead to electrically unbalanced modules which bring down the required performance of the pack and vehicle [85, 86, 87, 88, 89].

There are two principle sorts of cooling: i) air cooling, and ii) liquid cooling. The liquid cooling option appears to be more compelling, because of higher specific heat content contrasted with air cooling. It occupies less volume, yet brings more complexities and additionally high cost and weight [90]. The temperature increase in a lithium-ion battery during charging/discharging follows three processes: 1) the rate at which heat is produced within the cell; 2) the rate at which heat conducts from inside the cell to the external surface; and 3) the rate at which heat is removed from the cell's external surface to the environment. Many cooling systems, especially those which are active, require heat to be rejected outside the vehicle, which requires additional flow ducting and a heat exchanger. Vehicles have limited physical space available and packaging can become an issue. Some air cooling methods, such as those in the Toyota Prius, pass cooled cabin air (cooled by the vehicle’s air conditioner) through the battery pack. In liquid or fin cooling systems, a secondary refrigeration loop to remove the heat may be needed [82]. Battery pack thermal management and control systems have been demonstrated, commercially and in the literature utilizing: air or liquid systems, insulation, and phase-change materials, within both active and passive approaches. Several papers that investigate these various strategies are presented in the following section.

2.9.1 Air Cooling

The main advantage of air cooling systems is their simplicity over liquid coolant systems. Another advantage is electrical safety. However, air cooling systems have a lower heat transfer coefficient, making it more difficult to achieve a uniform temperature on the pack. There are various papers available in open literature for air cooling.

Pesaran [90] described a systematic approach with a detailed schematic of a battery thermal management system using air as a coolant fluid. He divided the design process of a BTMS into seven general steps:

1. To define the objective and constraints of a BTMS is to identify the specification of the desired system. (As an example, a few key considerations, including the temperature range of safe operation, space and ventilation requirements of the battery pack, need to be considered in case of release of hazardous gases).
2. To measure or estimate the module/pack heat dissipation rate and heat capacity. The heat generated over a period of time is measured experimentally e.g. calorimetry method.
3. To carry out a first-order BTMS evaluation. To select the heat carrying fluid the battery pack and modules are tested for their steady state and transient response. This step also tests the flow models; e.g. parallel, series and combination.
4. To characterize the module and battery pack heat transfer behaviour. The overall thermal conductivity of the system is defined and software is employed to predict the heat transfer rate between the battery pack and the environment.
5. To design a basic BTMS.
6. To construct, install and test the BTMS. Based on the basic design a BTMS prototype is built and tested under predefined operational conditions.
7. To optimize the BTMS.

Pesaran [90] also described the pros and cons of different BTMSs, such as a cooling system with series or parallel air distribution. He claimed that for parallel cooling, where the total air flow is split into equal portions, more uniform temperature distribution in the pack is achievable. Parallel configurations, however, require very careful design of air manifolds. Hence, large battery packs usually use a series-parallel configuration.

In a cooling channels approach, Sun et al. [91] modeled a battery pack to optimize cooling channel configuration. The pack was composed of stacks which were assembled beside each other. The air enters and exits the pack using the lower and upper ducts, respectively, and flows between the stacks to cool them down. The simulations showed that the average temperature of the stacks close to the inlet and outlet of the pack is lower compared to the farther locations. This was due to the uneven flow rate in the channels that resulted from the pressure drops in the ducts. Therefore, the uniformity of flow rates was improved by tapering the upper duct. In this way, the temperature difference across the pack was reduced from 4°C to 1.3°C. The method presented in [91] is a good example of utilizing thermal models in BTMS development.

Yeow et al. [92] also conducted a series of studies to improve cooling lithium-ion batteries using indirect methods. In the indirect method, the cooling fluid is not in direct contact with the battery while in the direct method the coolant flows over the surface of the battery. In this method, the coolant moves through a series of tubes embedded in a cold plate which is in contact with the battery or thermal fins. In their work, stacks were cooled using a thin aluminum plate in contact with the surface. The thermal fins extract heat from the stack and transfer it to the liquid cooled cold plates at the side of the stacks. Some parametric studies, such as the effect of employing one or two cold plates, were conducted on this BTMS [8, 92]. The results of their study showed that the dual cold plate cooling had about twice the cooling capacity of the single cold plate cooling. It was also concluded that the cell temperature distribution can be significantly influenced by the location of the cold plate. Furthermore, they proposed a thermal fin which can rapidly conduct heat to the cold plates. These fins contain embedded heat spreaders that improve the uniformity of temperature distribution on the stack surface.

2.9.2 Liquid Cooling

Active thermal management methods utilize forced fluid convection to absorb heat from individual batteries or subgroups of batteries within a pack. The work of Karimi and Dehghen [93] evaluated thermal management using both air and liquid cooling. A pack consisting of twenty, prismatic $LiCoO_2$-20 Ah batteries were modeled with a battery thermal model based on 1) ohmic heating and, 2) reaction entropy changes alone. A flow network model was used to determine the effect of several coolant flows on the final temperature distribution of a pack undergoing constant current discharge. Air and silicon oil were chosen as a cooling medium in a battery pack. Two flow configurations were modeled: a U-configuration, where flow enters and exits the same side of the pack casing, and a Z-configuration where the inlet and outlet are at opposite ends of the pack and on opposite sides of each end. The aim is to evaluate thermal distribution in the pack by measuring the standard deviation of temperature. Numerical results from the temperature distributions show that for both air and silicon oil, the Z-configuration for flow results in a more uniform temperature distribution than the U-configuration. Furthermore, silicon oil results in a much smaller temperature deviation (0.15°C vs.7.33°C after 2C discharge). The authors conclude that the penalty for the improved thermal control is that parasitic power is much higher for silicon oil, due to the high viscosity.

In addition to this study, the tab location and tab size are important and should be optimized for effective thermal management of batteries and cooling of the battery pack. Kim et al. [94] examined four different cell designs with different aspect ratios, as well as tab size and location. They showed that some measurable responses, such as output potential, do not vary between cell designs. However, the internal kinetics and temperature distribution of the battery is significantly influenced. The author also found that the width of tabs has a minor effect on temperature distribution, while increasing the surface area of the cells significantly raises the temperature non-uniformities on the battery surface.

2.9.3 Thermal Analysis of Batteries

Temperature estimations and the prediction of the lithium-ion battery cell are addressed by various papers including analytical and numerical modeling [95, 96, 97, 98, 99, 100, 101, 102, 45].

Ye et al. [103] developed and validated a thermal model based on battery surface temperature measurements using thermocouples. The experiment consisted of measurement of the surface temperature of a prismatic battery (11.5 Ah) at a single location, the center of the battery's largest surface. The battery was discharged at various rates of 0.2C, 0.5C, 1C, and 2C inside a temperature-controlled box with several initial temperatures (0°C, 10°C, 25°C, and 55°C). To minimize heat transfer to the box and ambient air, insulation was wrapped around the battery. The quasi-insulation allows the assumption that all generated heat remains within the battery, and the resulting measured temperature represents the total heat generated during the operation.

Mi et al. [104] presented numerical and analytical thermal results for a pack consisting of 48 batteries. The thermal response of an individual cell with a single thermocouple was measured as the battery underwent discharge. The measured response was used as an input heat term to a commercial FEA code. In the physical experiment, the battery was placed in a test chamber in a vertical position with natural convection cooling. A single thermocouple was used to measure the surface temperature of the battery, while another thermocouple monitored ambient temperature. This difference between the battery surface temperature and ambient temperature was used to quantify the heat dissipation by radiation and natural convection means.

Wiliford et al. [105] used distributed thermocouples (16 K-type thermocouples) on a prismatic $LiCoO_2$-4.5 Ah battery with C/3, 1C, 2C, and 4C discharge rates. The battery was suspended in a Plexiglas frame for natural convection cooling. The experiment was performed to provide validation of a thermal model based on electrode entropy changes. The surface temperature variation was measured during each discharge. Temperatures around the positive, aluminum tab were found to be consistently higher (about 5°C) than those at the negative, copper tab. In comparing experimental and model results, the authors only utilize point 14 in defining the battery temperature. For this work, the author used the below Equation (2.8) for the heat generation rate.

$$\dot{Q} = I^2 R \; - T \, \Delta S \left[\frac{I}{n\,F} \right] \tag{2.8}$$

where, I is the current density (A/cm^2), R is the material resistivity (Ω-cm), T is temperature (K), ΔS is entropy change (J/mole K), n equals one electron per reaction, and F is the Faraday's constant.

In **calorimetric methods**, two approaches are used to measure the heat generation rates of lithium-ion batteries: 1) Accelerated rate calorimeter (ARC) and 2) Isothermal heat conduction calorimeter (IHC), both apply a control volume around the battery and calculate the heat generation rate $\dot{Q}$ [106] by using:

$$\dot{Q} = m \, C_p \, \frac{dT}{dt} + h \, A \, (T_{surf} - T_{sink}) \tag{2.9}$$

where m is the mass of the battery (kg), C_p is the heat capacity of the battery (J/kg K), dT/dt is the change in battery temperature with respect to time (K/s), hA is the calorimeter constant (W/K), T_{surf} is the surface temperature of the battery (K), and T_{sink} is the sink temperature surrounding the battery (K).

The ARC method measures the rate of heat generation by measuring the temperature increase in the battery and heat rejected from the battery to the surroundings, according to Equation (2.9).

Hong et al. [107] used an accelerated rate calorimeter to measure the heat generation rate, and a 1.35Ah Sony 18650 cylindrical battery at 308 K and discharge rates of C/3, C/2, and C/1 with maximum measured rate of heat generation of 1.63 (W/L) [107]. Al Hallaj et al. [108] conducted some experiments on 18650 cylindrical batteries and found a maximum heat generation rate of 0.26 W/L for less than C/10 discharge and charge rate of C/3 [108].

Eddahech et al. [109] performed an analysis of the thermal behaviour of high-powered lithium-ion cells using an ARC calorimeter in order to measure the heat produced by the lithium battery cell during the discharging and charging processes at several current rates. Basically overall heat generation in a battery is connected to both joule heating and entropy change. The electrochemical reactions that happen during charging and discharging, changes battery entropy leads to heat generation, while joule heating takes place due to internal resistance to current flow. From this study, it is found that at the higher current rate the effect of change in entropy is negligible, which leads to a larger irreversible heat component during the charging and discharging.

The IHC method uses a large heat sink in contact with the battery surface in order to keep the battery at steady temperature (isothermal) operation during measurements, therefore eliminating the first term in Equation (2.9). This method restricted the estimations to low discharge rates, since the fast discharge rates of the battery prompts higher heat generation rates which the heat sink cannot extract, resulting in temperature gradient within the battery [106].

Kim et al. [110] used a three-cell isothermal micro calorimeter to examine the dependence of thermal behavior on the discharge/charge rate with $Li_xMn_2O_4$ coin cells of 2016 size (20 mm diameter and 1.6 mm height). The rate of heat generation of the battery was measured utilizing temperature sensors placed between the battery and the heat sink, with selected discharge rates of C/10, C/5, C/2, and 1C from 300 to 308 K. The corresponding maximum heat generation rates were 0.82 W/L between C/10 and C/5 discharge rates, 0.97 W/L for a discharge rate of C/5 to C/2, and 3.21 W/L for a discharge rate of C/2 to 1C [110].

Kobayashi et al. [111] measured the rate of heat generation of Sony 18650 lithium-ion batteries using a calvet type conduction micro-calorimeter, which contains an isothermal aluminium vessel in contact with a test battery. A thermocouple was utilized to measure the amount of heat transfer from the battery to the heat sink. The battery was discharged at 1/50C and 1/10C with an ambient temperature of 300 K, and the measured maximum rate of heat generation was 0.97 W/L for a discharge rate between C/10 and C/5.

Keller et al. [112] studied the effect of battery operation in extreme temperature conditions over the characteristics of a vehicle, such as the range of Griffon electric vehicles equipped with a CMP 3ET205 lead-acid battery. In order to conduct a comparison, tests have been conducted on a vehicle without TMS and with air and liquid TMS and it is found that the vehicle range decreased in the absence of TMS due to the high ambient temperatures and heat spread across the battery pack. This can lead to a premature cell failure and seasonal driving variability. From the study, it is also found that the mileage of a vehicle can be increased up to 20% by using TMS. In addition, with the use of TMS, the temperature distribution can be reduced to 4.0ºC and 2.3ºC compared to 11.6ºC for the non-managed pack, by circulating-air and circulating-liquid, respectively.

Kuper et al. [113] examined different active cooling systems with air, liquid and refrigerant cooling mediums as well as heat generation in battery cells. The increase in battery temperature over time based on internal heating and cooling rates has been formulated. The study shows that maximum and minimum cell temperatures should be maintained within a 3 – 5 K range, in order to prevent 25% acceleration of the aging kinetics and up to 50% variance in power capability. It is also recommended that the coolant inlet and outlet temperature difference be kept at less than 3 K in order to maintain a uniform cell temperature.

Fathabadi [114] proposed a novel design of a lithium-ion battery pack including hybrid active passive TMS for EVs and HEVs. In the suggested distributed ducts and PCM/EG composite, airflow was used as active as well as passive cooling/heating components, respectively. Thermal investigation of the suggested battery pack, consisting of 20 battery units, 19 distributed ducts and PCM/EG composite, was carried out and calculations were performed for the temperature distribution by numerically solving the related partial differential equations. Results show a high thermal performance of the battery pack for ambient temperatures up to 55°C and for battery temperature remaining in the recommended temperature range (below 60°C).

Liu et al. [115] developed and simulated a two-dimensional and transient model for the thermal management of a 20-flat-plate lithium-ion battery stack in order to investigate the effect of the Reynolds number, discharge rate and ambient temperature over the temperature distribution in the battery stack by using different cooling materials. Results shows that, in the case of mild ambient temperature, liquid cooling is most effective in decreasing the temperature inside the battery compared to PCM. It is also advised to avoid fast and deep discharge in order to keep the temperature within an acceptable range. The study shows that air cooling is more preferred at a zero or sub-zero ambient temperature because, at such a temperature, heat needs to be retained rather than removed. There is minor difference between the effect of using air and liquid cooling material when SOC is high and ambient temperature is mild. The effect of change in the Reynolds number is present in the case of liquid cooling while it is negligible in air cooling. Also, selections of a suitable cooling material have a significant effect in the case of fast discharge and low ambient temperature.

2.9.4 Thermal Imaging of Lithium-ion Battery

IR (Infra-red) imaging technique is an excellent tool for the temperature measurement on the surface of an object. It provides several advantages over other types of temperature sensors. It is basically non-contact and also gives very helpful details of the surface being studied [116]. Some examples are:

Niculuta et al. [117] used this technique to measure the surface temperature profile with a discharge current of 14A and 35A, of a 70 Ah $LiFePO_4$ battery. This enabled visual determination of the spatial temperature distribution, and resulted in validation of a three-dimensional electro-thermal model. They compared images and it was found that the maximum surface temperature measured during the experiment was 32.1°C and the model gave a maximum temperature of 33.5°C. The authors found that when currents of 35A (C/2) or higher are used to charge/discharge the cell, the temperature profile is not uniform.

Streza et al. [118] used an IR camera (FLIR 7200 series) to capture the thermal images of lead-acid batteries to investigate the distribution of current in the electrodes. They designed a special cell (14 cm x 14 cm) with electrodes in direct contact with an air. The information was extracted during the discharge process by analysis of the heat dissipation in the electrode. The effect of the current in the metallic grid can be de-convoluted by the total heat generated in the electrode by numerical processing of the temperature profile on the surface of an electrode. Their proposed method had the potential to become an important tool in optimising electrode geometry because of its simplicity and effectiveness.

Keyser et al. [119] used utilize thermal images of Generation I (4.5 Ah), Generation II (5 Ah), Generation III (8 Ah) lithium polymer cells to measure heat generation and temperature distribution. It was found that, during the discharge process, the first and second generation cells demonstrated signs of localized heat during IR imaging below the positive electrode, while the Gen III cell remained generally uniform in temperature. As the cell was improved and better electrodes designed, the Gen III turned into the most efficient of the cells that were tried. It surpassed an efficiency of 91% for all currents under 48 amps. In contrast, the Gen II cell was just 78% effective at 30 amps. Moreover, the Gen III cell presented signs of being slightly endothermic during the initial 2 hours at a discharge of C/5 and demonstrated that the heat generation at C/5 discharge is not consistent and highly reliant on the SOC of the cell.

Bazinski et al. [120] also utilized a combined method of thermography technique along with a closed-form lumped capacitance model (LCM) in order to predict the heat generation inside the 14.5 Ah lithium-ion phosphate pouch cell. They used a FLIR A320 Infrared thermal camera to capture the images at high discharge rates of 1C, 2C, 3C, and 5C, as well as at a low discharge rate of C/4. The authors found that, at lower C-rate, the temperature is uniform while at higher C-rates the localized hot spots developed in the cell and the spatial temperatures were not uniform.

2.10 Heat Generation and Thermal Runaway

Heat is generated within a battery cell by (1) ohmic heating (or Joule's effect) due to transfer of the current across internal resistances and over potential (2) entropy change from electrochemical reactions (i.e., reversible endothermic/exothermic part of the reaction). For some electrochemical pairs, another electrical energy loss (and thus heat generation) could result from overcharging a fully charged battery cell. The rate of heat generation within a battery cell can be calculated by [39, 121, 122, 123, 124, 125] :

$$\dot{Q} = I\,(E - V) - I\left[T\left(\frac{dE}{dT}\right)\right] \tag{2.10}$$

The first term, $I\ (E - V)$, is heat generation due to internal resistance (irreversible heat dissipation) while the second term, $-I[T(dE/dT)]$, is known as reversible heat resulting from changes in open circuit potentials with respect to the temperature at the two electrodes. At practical EV and HEV rates, the second term is usually smaller as compared to the first term. Hence, the heat is generated and released from the cell during both charging and discharging [122]. Thermal runaway can occur if this heat is not properly removed, as elevated temperatures trigger additional heat generating exothermic reactions [38, 126, 127, 128]. These reactions then further increase the battery temperature; creating a positive feedback mechanism that causes the battery temperature to climb sharply if the heat is not well dissipated. As a result, thermal runaway can occur, resulting in complete cell failure accompanied by fire or explosive gas release. Furthermore, even if thermal runaway does not occur, significant degradation of battery capacity can take place by consistent operation at an elevated temperature (>50°C) [37]. The rate of heat generation was later reformulated by Fathabadi [129] and is given by:

$$\dot{Q} = I^2 R - T\ \Delta S\ \left[\frac{I}{n\ F}\right] \tag{2.11}$$

where, I is the current and $I > 0$ for discharge, $I < 0$ for charge, (i.e. +ve value is taken for discharging and –ve value is taken for charging), R is the resistance, ΔS is the change in entropy, n is the number of flow of electrons, and F is the Faraday's constant (96485 Columb/mol).

Current collectors create additional Ohmic heating due to the high current densities that occur in planar prismatic type batteries. In another work, Equation (2.12) was developed to include two added terms that account for heat generated in the current collector tabs [130, 131, 132]:

$$\dot{Q} = I\left(E - V - T\left(\frac{dE}{dT}\right)\right) + A_p R_p I_p^2 + A_n R_n I_n^2 \tag{2.12}$$

As heat is generated in the cell during both charge and discharge, the need for adequate cooling arises. The temperature of the cell will continue to increase without adequate processes to remove the heat. The heat generation of cell stacks and the collection of stacks into a pack lead to the need for battery pack thermal management. Researchers have examined achieving thermal control with air or liquid systems, thermal insulation, thermal storage (phase-change material), active or passive techniques, or a combination [133].

2.11 Battery Modeling

A major obstacle in PHEV, EV, and HEV commercialization is the high cost of the battery pack. To address this issue, different solutions, such as energy density improvements and reduction of material cost, could be considered. To come up with an optimal solution, one approach is to develop battery models. Battery simulation has been conducted on different scales, namely: cells, stacks, modules, and packs. There are various papers in the open literature available for battery thermal modeling, using different approaches such as: an artificial neural network [134, 135, 136, 137]; a finite element model (FEM) [138, 139] or lumped parameter model (LPM) [140]; a linear parameter varying (LPV) model [141]; or a partial differential equation (PDE) model [142]. Many researchers [39, 40, 41, 42, 43, 44, 45, 143] investigated the thermal behavior of lithium-ion batteries only for a single cell.

Battery modeling, in fact, provides valuable information on battery discharging/charging and transient behavior as well as SOH status of the battery (battery degradation) as a function of different parameters (such as temperature and discharge rate). EV designers use battery models for sizing the required battery and predict the battery performance. Battery models are also used for on-line self-learning performance and SOC estimation in BMS [144, 145, 146]. Common battery models used in the automotive applications are reviewed in the following sections. There are two basic types of modeling.1) Electrochemical modeling and 2) equivalent circuit modeling.

2.11.1 Electrochemical Modeling

Battery modeling based on electrochemical equations provides a deep understanding of the physical and chemical process inside the battery which makes it useful when designing a cell, but high computational time makes these models improper for applications with high dynamics. The first electrochemical modeling approach to porous electrodes with battery applications was presented by Newman and Tiedemann in 1975 [147]. In the porous electrode theory, the electrode is treated as a superposition between the electrolytic solution and solid matrix; the matrix itself is modeled as microscopic spherical particles where lithium ions diffuse and react on the surface of the sphere. This approach was expanded to include two composite models and a separator by Fuller et al. in 1994 [148]. This model was later adapted for Ni-MH batteries [149] , and then lithium-ion batteries [150].

Li et al. [151] studied physics-based CFD simulation of a lithium-ion battery with the drive cycle of Federal Urban Driving Schedule (FUDS) and used Newman's pseudo-2D (P2D) porous electrode model for a large sized lithium-ion battery. They also addressed two major problems to implement such models in the electrochemical-thermal coupled battery simulation. The first was how to use such an electrode-scale model in a large scale simulation and the second was how to make the physics-based model cost-efficient in a CFD simulation. In their study, to address the first technical issue, they used the multi-scale multi-dimensional approach (MSMD), and to address the second issue, they used a linear approximation.

Majdabadi et al. [152] built up a physics-based model to anticipate the thermal and electrical performance of a $LiFePO_4$ battery under different operating conditions. They simplified Newman's full-order porous-electrode model at the electrode-level by using polynomial approximations for electrolyte variables, while at the molecule level, a multi-particle model featuring variable solid-state diffusivity was utilized. The computational time was reduced by almost one order of magnitude when contrasted with the full-order model without sacrificing the preciseness of the results. Their model was general and can be utilized to expedite the simulation of any composite electrode with active-material particles of non-uniform properties (e.g., contact resistance, size).

Mastali et al. [153] similarly created an electrochemical-thermal model of a commercial Graphite/$LiFePO_4$ prismatic cell (20 Ah capacity) using FORTRAN code. They conducted the validation against the experimental data for charge/discharge rates varying from 1C to 5C. Physics-based one-dimensional electrochemical models were coupled with charge conservation and heat diffusion equations to describe the electrochemical and thermal variable distributions throughout the battery domain. All the electrochemical properties of the graphite and LiFePO4 electrodes were obtained from half-cell simulations performed on the same electrode materials.

Xu et al. [154] built up a pseudo 3D electro-chemical-thermal model for a large sized prismatic $LiFePO_4$ battery during the discharge process by coupling the mass, charge, and energy conservations, and the cell electrochemical kinetics. They studied both the electrochemical and thermal performance of the battery. Their model treated the battery with the current collecting tabs as 3D and the local cell units as 1D. They also introduced a consistency index describing the SOC distributions among 1D cell units. This index was utilized to explore the effects of the tab arrangement on the consistency of the battery cell. They similarly found that the location of the current collecting tabs (of the negative and positive) on the prismatic battery had a great impact on the distributions of its potential and local reaction rates, which therefore affect the rate of heat generation, and subsequently the distribution of temperature inside the battery.

Vyroubal et al. [62] studied an analysis of the temperature field in a lithium-ion battery during discharging. They used a Kokam prismatic battery with 4000 mAh capacity, and prepared a numerical model by utilizing SolidWorks and ANSYS Fluent software. This was later matched by real measurement utilizing electrical impedance spectroscopy and thermal imaging.

Yang et al. [155] similarly performed an examination of the uneven discharging and aging as a result of the difference in temperature among the parallel-connected battery cells. They built a thermal–electrochemical model for the parallel-connected battery pack and found that, at a higher temperature, the cell encounters a bigger current in the early discharging process before around 75% of DOD for the parallel-connected cells. They additionally reported that the changes in the discharging current through the cell at a lower temperature were inverse to that of the cell at a higher temperature. Their simulations also demonstrated that the temperature difference between the parallel-connected battery cells incredibly aggravates the irregularity discharge between the cells, which accelerated the losses of the battery pack capacity. For the pack with parallel-connected batteries, the rate of capacity loss approximately increased linearly as the difference in temperature between each cell increased.

Huo et al. [156] also presented a 3D model of the thermal performance of a lithium-ion battery. The effect of the discharge conditions on the thermal behavior was determined by utilizing the FEM. They analyzed the dynamic thermal behavior by utilizing UDDS, HWFET, and US06 drive cycles and concluded that the temperature increase was rapid under the US06 drive cycle as compared to UDDS and HWFET drive cycles. In less aggressive driving conditions for UDDS and HWFET, natural convection was adequate to keep a secure temperature range at 25°C.

Lastly, Lai et al. [2] also built up a pseudo two-dimension (P2D) electrochemical model combined with a 3D heat transfer model. Their numerical model solved conservation of energy throughout the battery by considering the sources of heat generation; for example, electrochemical reactions, active polarization, and ohmic losses. Their outcomes showed an identical behavior of the temperature profile with thermal imaging and voltage distribution. They additionally found that the heat generation of the current collectors and separator was generally lower in magnitude, demonstrating little effect on temperature changes. The reversible heat variations on the positive side affected the aggregate reversible heat, while the negative irreversible heat had a predominant position in the total irreversible heat.

2.11.2 Equivalent Circuit Modeling

Equivalent circuit-based modeling (ECM) is suitable for automotive real time applications (such as BMS design), since it does not need deep understanding of the electrochemistry of the cell and at the same time is well capable of simulating the battery dynamics. ECMs simulate the battery as a circuit often composed of resistors and capacitors, as well as other elements. There is a wide selection of models depending on trade-offs of accuracy and time required. Ideal voltage source or a large capacitor is selected to represent the open-circuit voltage (OCV), with the remainder of the circuit representing battery internal resistance and dynamic effects (e.g. terminal voltage relaxation). Generally, each observed phenomena is modeled with an individual circuit component. For example, the bulk electrolyte resistance is represented with a simple resistor, R_0. To keep the model simple, similar phenomena (e.g. concentration and electrochemical polarization effects) could be grouped, although this decreases model accuracy. Resistances of other components, such as electrodes and separator, are additive and included in R_0. Other phenomena, including the polarization effect of the battery, are usually represented by capacitors and resistors in parallel. In addition, diffusion effects are represented by a Warburg element. In the following section, common ECMs used in PHEV applications are presented.

2.11.2.1 R_{int} model

The R_{int} model, as shown in Figure 2.9, is one of the simplest models. The model consists of an OCV (V_{OC}), and resistor (R_0) to account for different resistance values under discharging and charging, respectively [157]. These two parameters model all forms of internal resistance, including internal ohmic and polarization resistances. I_L is the load current with a positive sign at discharging and a negative sign at charging. The battery terminal voltage (V_L) is represented in Equation (2.13) as the OCV plus the voltage rise or drop across the resistor. Finally, the R_{int} model can be parameterized directly from the experimental data and is very efficient as there is no need to evaluate the differential equations. However, the model is unable to provide a simulation of transient or time-variant behaviour [158].

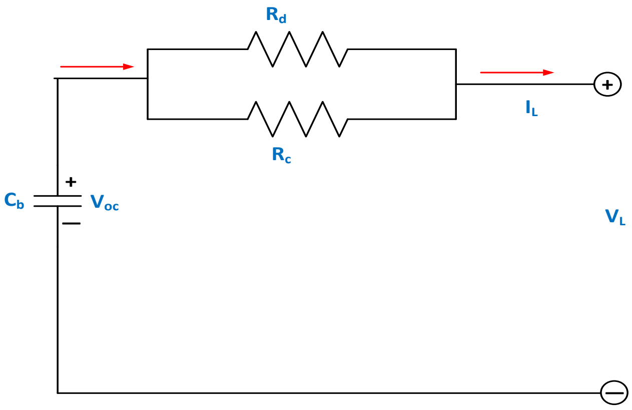

Figure 2.9: Line diagram of R_{int} model (modified from [157]).

$$V_L = V_{oc} - I_L R_0 \tag{2.13}$$

2.11.2.2 The RC model

The resistor capacitor (RC) model is presented in Figure 2.10. It has two capacitors (C_c, C_b) and three resistors (R_t,R_e,R_c). The capacitor C_c, that has a small capacitance and generally presents the surface effects of a battery, is named the surface capacitor [157]. The capacitor C_b, which has an extensive capacitance and represents the battery's ample capability to store charge chemically, is known as a bulk capacitor. SOC can be calculated by the voltage across the bulk capacitor. Three resistors R_t,R_e,R_c are known as the terminal resistor, end resistor and capacitor resistor, respectively. V_b and V_c are the voltages across C_b and C_c, respectively. The electrical behaviour [157] of the circuit can be presented by:

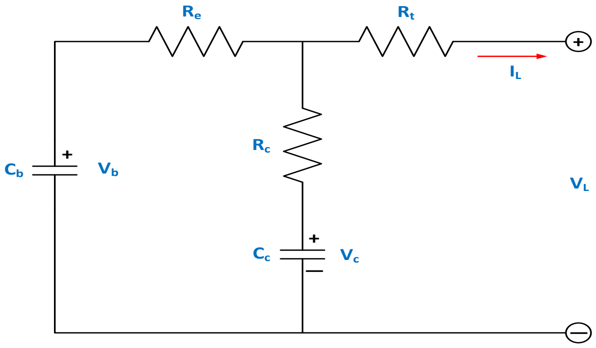

Figure 2.10: Line diagram of RC model (modified from [157]).

$$\begin{bmatrix} V_b \\ V_c \end{bmatrix} = \begin{bmatrix} \dfrac{-1}{C_b(R_e + R_c)} & \dfrac{1}{C_b(R_e + R_c)} \\ \dfrac{1}{C_c(R_e + R_c)} & \dfrac{-1}{C_c(R_e + R_c)} \end{bmatrix} \begin{bmatrix} V_b \\ V_c \end{bmatrix} + \begin{bmatrix} \dfrac{-R_e}{C_b(R_e + R_c)} \\ \dfrac{-R_e}{C_c(R_e + R_c)} \end{bmatrix} [I_L] \tag{2.14}$$

$$[V_L] = \begin{bmatrix} \dfrac{R_c}{(R_e + R_c)} & \dfrac{R_e}{(R_e + R_c)} \end{bmatrix} \begin{bmatrix} V_b \\ V_c \end{bmatrix} + \begin{bmatrix} -R_t - \dfrac{R_e\, R_c}{(R_e + R_c)} \end{bmatrix} [I_L] \tag{2.15}$$

2.11.2.3 Thevenin model:

The Thevenin model connects a parallel RC network in series based on the R_{int} model, presenting the dynamic characteristics of the battery [157, 158]. As appeared in Figure 2.11, it mainly consists of three parts; an open-circuit voltage V_{oc}, internal resistances and equivalent capacitances. The internal resistances incorporate the ohmic resistance R_o and the polarization resistance R_{Th}. The equivalent capacitance C_{Th} is used to describe the transient response during both discharging and charging. V_{Th} represents the voltages across C_{Th}. I_{Th} is the outflow current of C_{Th}. The electrical behavior of the Thevenin model can be represented by:

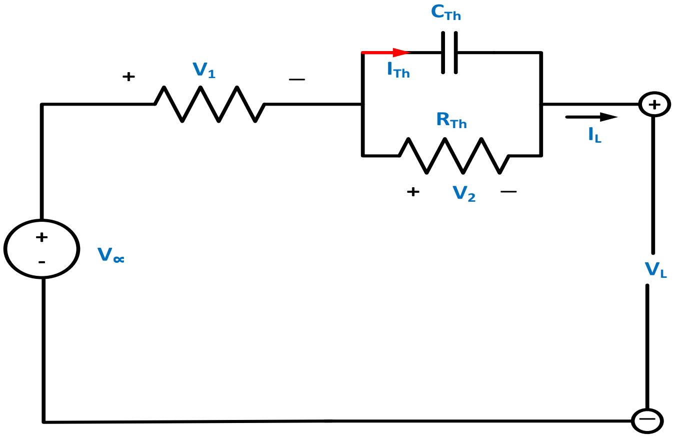

Figure 2.11: Line diagram of Thevenin model (modified from [157]).

$$V_{Th} = -\frac{V_{Th}}{R_{Th}C_{Th}} + \frac{I_L}{C_{Th}} \tag{2.16}$$

$$V_L = V_{oc} - V_{Th} - I_L R_o \tag{2.17}$$

2.11.2.4 DP model:

Based on the test analysis of the characteristics of a lithium-ion power battery, an obvious polarization can be observed. The polarization characteristic could be simulated by the Thevenin model to some degree. However, the difference between the concentration polarization and electrochemical polarization leads to an inaccurate simulation in the moments at the end of the charge or discharge. An improved circuit model is introduced in Figure 2.12, which is characterized as a dual polarization (DP) model, to refine the description of polarization characteristics and independently simulate the concentration polarization and the electrochemical polarization [157].

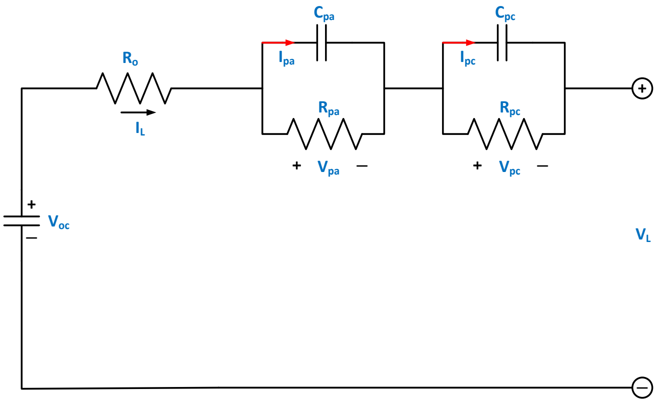

Figure 2.12: Line diagram of DP model (modified from [157]).

The DP model [157] is made out of three parts: (1) Open-circuit voltage V_{oc}; (2) Internal resistances, such as the ohmic resistance R_o and the polarization resistances, which join R_{pa} to represent the effective resistance characterizing electrochemical polarization and R_{pc} to represent the effective resistance characterizing concentration polarization; and (3) The effective capacitances such as C_{pa} and C_{pc}, which are used to characterize the transient response during transfer of power to/from the battery and to depict the electrochemical polarization and the concentration polarization independently. V_{pa} and V_{pc} are the voltages across C_{pa} and C_{pc} respectively. I_{pa} and I_{pc} are the outflow currents of C_{pa} and C_{pc} respectively. The electrical behavior of the circuit can be represented by:

$$V_{pa} = -\frac{V_{pa}}{R_{pa}C_{pa}} + \frac{I_L}{C_{pa}} \tag{2.18}$$

$$V_{pc} = -\frac{V_{pc}}{R_{pc}C_{pc}} + \frac{I_L}{C_{pc}} \tag{2.19}$$

$$V_L = V_{oc} - V_{pa} - V_{pc} - I_L R_o \tag{2.20}$$

2.11.3 Neural Network Modeling

In this research, a neural network is used for the battery thermal modeling. The neural network (NN) or artificial neural network (ANN) is defined as a computational model made up of a number of simple, highly interconnected processing elements, which process information by their dynamic state response to external inputs. Neural networks can be used to model the complex relation between the input and output data using a relatively simple construction and algorithm. Neural networks have a relatively high tolerance limit to noisy data as well as the ability to discern a pattern even for the data that have not been initially used to train the model. This is one of the main advantages of using neural networks. The correctness of the model output function depends extensively on the goodness of the input data being fed into the model; this is one of the essential characteristic of neural networks. Therefore, learning about the network can be impaired if the input data does not contain enough information representing the output [159].

Neural networks are usually organized in layers with nodes or neurons that connect different layers through an activation function. Data or patterns are presented at the input layer which travels to the hidden layers through weighted connections and is finally processed at the output layer which represents the output of the network. Different neural network structures, such as multilayer perceptron (MLP), radial basis function (RBF) and wavelet neural networks (WNN), have been designed and applied to specific applications, as summarized in [160]. MLP is the most widely used neural network architecture and the same has been applied in this work. In what follows, a brief description of the MLP architecture, its components and training function has been presented. A general structure of MLP is shown in Figure 2.13. MLP [161] belongs to a general class of neural networks, called feed forward networks, with one or more layers between the input and the output capable of the approximating generic class of functions, including continuous and integrable functions. Here, the first layer is called the input layer. This is a layer that receives a stimulus from outside of the neural network. Every other subsequent layer receives stimuli from its preceding layer. For example, from Figure 2.13, a layer l receives stimuli from its preceding layer $l-1$. The neurons, which receive stimuli from the previous layer's neurons and the output of which is used as stimuli for the outer layer neurons, constitute the hidden layer neurons. Neurons, whose outputs are used external to the network, are called the output layer neurons. The term stimuli in this context refers to a weighted sum of the inputs passed through an activation function to form an output function.

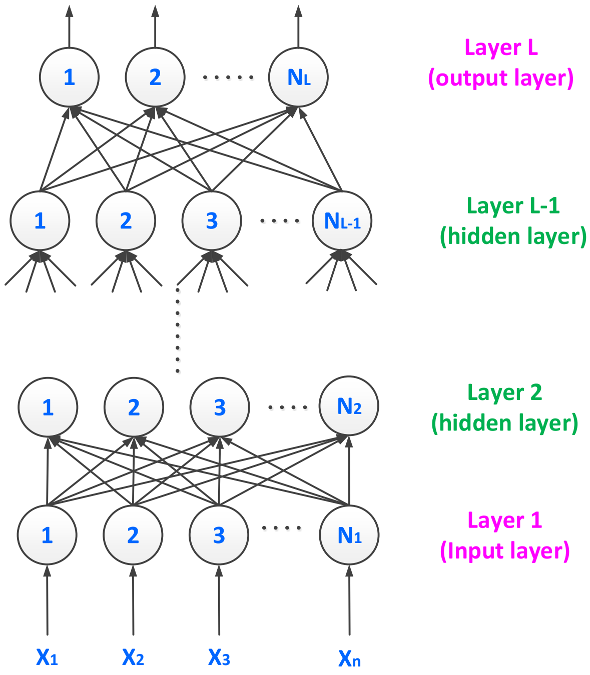

Figure 2.13: MLP architecture (modified from [162]).

Activation functions are used in the network to scale the data output from a layer [163]. Some commonly used activation functions in neural networks are described in the following section:

Log sigmoid function: The sigmoid function is given below. The function is real valued and differentiable, characterized by horizontal asymptotes as $x \rightarrow \pm \infty$

$$\sigma\,(x) = \frac{1}{1+e^{-x}} \tag{2.21}$$

$$\sigma\,(x) = \ 0 \text{ when } x \rightarrow -\infty$$

$$\sigma\,(x) = \ 1 \text{ when } x \rightarrow \ \infty$$

where $\sigma\,(.)$ is the activation function and x is the weighted sum of inputs from the preceding layers.

Tan sigmoid function: This function is represented by:

$$\sigma\,(x) = \frac{2}{1 + e^{-2x}} - 1 \tag{2.22}$$

$$\sigma\,(x) = -1 \text{ when } x \rightarrow -\infty$$

$$\sigma\,(x) = 1 \text{ when } x \rightarrow \infty$$

This function can also be represented by a hyperbolic tan function

$$tan\,(h)\ or\ \sigma\,(x) = \frac{e^{x} + e^{-x}}{e^{x} - e^{-x}} \tag{2.23}$$

The previous equation can also be represented as:

$$tan\,(h)\ or\ \sigma\,(x) = \frac{2}{\pi}\,arctan\,(x) \tag{2.24}$$

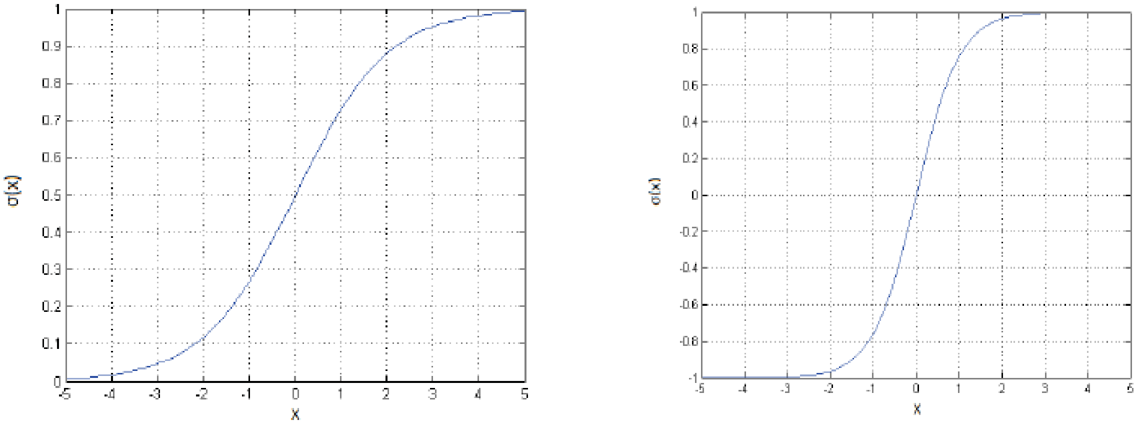

a) Log sigmoid function **b) Tan hyperbolic function**

Figure 2.14: Log sigmoid and tan hyperbolic function [163].

Levenberg–Marquardt is the default training algorithm for the feed-forward network in many commercial solvers including MATLAB, due to its robust nature. According to the universal approximation theorem of the feed-forward neural networks [160], a single hidden layer can approximate any measurable function regardless of the activation function and input space with desired accuracy. Theoretically, there seems to be no constraint on the success of the feed-forward networks. However, it must be noted that the universal approximation theorem does not fix the number of neurons in a layer to guarantee success. In fact, in many black-box models which seldom have any information about the functional relationship and parameters, the number of neurons is selected by trial and error with an objective to minimize the error gradient. A balance has to be struck between an increase in the number of neurons of the hidden layer and the convergence rate for a given accuracy, since either of them is directly proportional. Failure to obtain a good model could be attributed to inadequate learning, too few hidden layer neurons or the presence of a stochastic relation between the input and output functions.

Once the network has been trained to deduce the weights and biases, the next step is to be tested and validated to ascertain the quality of the model. Typically, based on the size of the input data set, the data is divided to perform training, testing and validation analysis. Testing of a model is carried out only once against the trained model to obtain the predicted error using non-training data. This gives an indication of the performance of the model against unseen data. Once the model testing has been completed, the model is subjected to validation tests. A good model is expected to produce a generalized functional relationship between the input and the output. Cross validation of the model is essential to check the generalization of the estimated model. Unlike the test data, the validation data is generally used repeatedly to minimize the non-training performance function such as the mean square error (MSE) of the model. Training can be stopped once the validation error performance function stops decreasing or once it reaches the tolerance. Training, along with testing and validation concludes the overlying process in developing a neural network model. There are four functions available in MATLAB^{TM} for dividing the data set into training, validation and test sets, namely: dividerand, divideblock, divideint, and divideind, which have the following characteristics [164, 159]:

- dividerand: This function divides the data set into three subsets using random indices.
- divideblock: This function divides the data set into three subsets using blocks of indices.
- divideint: This function divides the data set into three subsets using interleaved indices.
- divideind: This function divides the data set into three subsets using specified indices.

2.11.4 ANSYS Modeling

In this research, the flow inside the cold plates is turbulent and therefore for numerical modeling, the ANSYS is used. The turbulent flow is characterized by chaotic property changes or by irregular movement of fluid within a flow region in fluid dynamics. Non-turbulent flow is basically a laminar or streamline flow where the fluid is flowing in parallel layers with no interruption between each layer. In order to exhibit whether a flow is treated as laminar or turbulent, the Reynolds number is used. This is the proportion of inertia forces to viscous forces and given by:

$$R_e = \frac{\rho {v_s}^2/L}{\mu v_s/L^2} = \frac{v_s L}{\nu} \tag{2.25}$$

where, v_s is the mean fluid velocity (m/s), L is the characteristic dimension (m), μ is the dynamic fluid viscosity (Ns/m^2), ν is the kinematic fluid viscosity (m^2/s) also defined as $\frac{\mu}{\rho}$, and ρ is the fluid density (kg/m^3). The transition from laminar to turbulent flow relies on flow configuration. The transition occurs at the Reynolds number of the order of 10^5 to 10^6 for the flow over a flat plate. For flows in circular pipes, the critical Reynolds number are between 2000 to 3000.

Two methods are available for the solution of the Navier-Stokes equations without directly simulating the fluctuations in small scale turbulent: Reynolds Averaging (ensemble averaging) and filtering. The Reynolds-averaged Navier-Stokes (RANS) based modeling approach decreases the computational times and resources by time averaging the flow quantities for an entire range of scales of the turbulence being modeled. Two main RANS based turbulence models are available: (1) K-Epsilon and (2) K-Omega.

2.11.4.1 K-Epsilon Turbulence Model

The K-Epsilon model is a standout amongst the most broadly utilized turbulence models as it gives robustness, economy and precision for an extensive range of turbulent flows. Upgrades have been made to the standard model which improves its execution. Two variations are accessible in Fluent; the RNG (renormalization group) model and the realizable model. The standard, RNG, and realizable models have the same transport equations for k and ϵ. The two transport equations separately solve for the turbulent velocity and length scales. The principle contrasts between the three models are as per the following:

- The turbulent Prandtl numbers representing the turbulent diffusion of k and ϵ.
- The generation and destruction terms in the equation for ϵ.
- The technique of calculating turbulent viscosity.

2.11.4.2 K-Omega Turbulence Model

The K-Omega turbulence model, which is the second turbulence model, demonstrates two variations: the standard K-Omega model, and the shear stress transport (SST) model. Both of these models use the same transport equations for k-ε. However, the SST model varies from the standard model as follows:

- There is a slow change in the inner region of the boundary layer to the outer part of the boundary layer from the standard k-omega model to the k-epsilon model.
- The transport effects of the principal turbulent shear stress the SST model includes a modified turbulent viscosity equation.

There are different papers in the open literature accessible for battery thermal modeling, utilizing CFD models [165, 151, 62, 166, 167, 8]. A liquid cooling system, with two cold plates set one on the top and the other at the bottom of the battery, rejects heat produced within the lithium-ion battery using a structure of a metal thin-wall with various channels. This kind of system is able to reduce the operating temperature, which keeps consistent temperature distributions.

Jarrett et al. [168] designed and modeled a battery cooling plate using CFD. Basically, a liquid cooling system model employed a serpentine channel and used CFD simulation to optimize the model. It is based on weighted average pressure drop, and the mean and standard deviation of the cold plate temperature. A numerical optimization was applied to improve its design. Their results indicate that a single design can satisfy both the average temperature and pressure objectives, but at the expense of temperature consistency.

Zhao et al. [169] proposed another sort of cooling strategy for cylindrical batteries based on a mini-channel liquid cooled cylinder (LCC) to maintain the maximum temperature and local temperature difference within an appropriate range. The heat dissipation performance was numerically investigated by varying the effects of channel quantity, mass flow rate, flow direction and entrance size. Their outcome demonstrated that the most extreme temperature can be controlled under 40°C for 42,110 cylindrical batteries when the inlet mass flow rate is 1×10^{-3} kg/s and the number of mini-channels is also limited to four. They additionally found that the cooling style by a LCC can exhibit favorable circumstances contrasting with free convection cooling just when the channel number is higher than eight.

Saw et al. [170] considered CFD analysis in order to explore the air cooling method for a battery pack with 38,120 cells. With an accelerating rate calorimeter, they additionally measured the heat generated by the cell while charging. Utilizing steady state simulation, the thermal performances of the battery pack were analyzed with various mass flow rates of cooling air. The correlation between the Nusselt number and Reynolds number was derived from the numerical modeling results. Also, an experimental testing of the battery pack at different charging rates validated the correlation. Their strategy provided a basic approach to estimate the thermal performance of a battery pack when the battery pack is large and full transient simulation is not feasible.

In another study, Jin et al. [167] composed an oblique fin cold plate to cool down the batteries of an EV. In their outline, a basic configuration of oblique cuts across the straight fins of a conventional straight channel design was created, to enhance the performance of the conventional channel with minimal pressure penalty. These oblique cuts across the straight fins formed an oblique fin array. The composed liquid cold plate (LCP) contained these simple oblique fins with optimized angle and width. This segmentation of the continuous fin into oblique sections led to the re-initialization of boundary layers, giving an answer for the elevated temperatures caused by a thick boundary layer in the fully developed region. Their test results demonstrated that the heat transfer coefficients of an oblique minichannel were higher than those of a conventional straight minichannel. The oblique LCP can keep the battery surface average temperature below 50°C for 1240 W heat load at lower than 0.9 l/min flow rate.

Mohammadian et al. [171] reviewed internal and external cooling methods for thermal management of lithium-ion battery packs using 2D and 3D transient thermal analysis. For this, water and liquid electrolytes have been used as coolants for external and internal cooling, respectively. They also examined the effects of the techniques on diminishing the temperature inside the battery and temperature consistency. Their outcomes demonstrated that, at the same pumping power, utilizing internal cooling not only reduces the bulk temperature inside the battery more than external cooling, but also significantly decreases the standard deviation of the temperature field inside the battery. In conclusion, using internal cooling decreased the intersection angle between the velocity vector and the temperature gradient which, according to the field synergy principle (FSP), caused an increase the convection heat transfer.

Lastly, Huo et al. [172] similarly designed a battery thermal management system based on a minichannel cold plate. Their design was to cool a rectangular lithium-ion battery. In their study, they developed a 3D thermal model of the cooling system and studied the effects of flow direction, inlet mass flow rate, number of channels and ambient temperature on temperature increase and distribution of the battery during the discharge process. The authors found that the most extreme temperature of the battery decreases with increases in the number of channels and the rate of inlet mass flow. They also concluded that the effect of flow direction on cooling performance was smaller after mass flow rate increased, and that, with the increase of inlet mass flow rate, the cooling execution improved but the increasing trend became smaller, and the mass flow rate as 5×10^{-4} kg/s was optimal.

2.12 Battery Degradation Modeling and Mechanism

Modeling of degradation is mainly based on the aging experiments and measurements and the complexity of the model depends on the various factors and degradation mechanisms to be incorporated in the modeling. It is worth specifying that each type of battery experiences a particular degradation mechanism and not all stress factors have comparable impact on various battery chemistries. To date, understanding and assessment of battery performance in EVs essentially depends on lab testing. As with standard driving schedule tests and analyses, these tests and duty cycle analyses have constraints in their validity to real-life operation. A key issue in both cases is that even under particular driving cycles, consumption of energy strongly depends on uncontrolled surrounding working conditions. On the other hand, conducting drive cycle analysis using trip data collected from real-life vehicle operation is a challenging task [173, 174]. Although quite helpful in evaluating SOH, very limited effort has been put into field testing with the collection of data and statistical analysis, mainly because such experiments are expensive and there is virtually no control [175, 176, 177].

It is important to study the various types of degradation mechanisms of lithium-ion cells because the heat generation from the cell/module/pack is directly related to the degradation and life of the battery. Lithium-ion cells undergo degradation in terms of capacity and power capability during usage and storage. The degradation of a cell occurs much faster during cycling than storage under the same conditions. The normal and accelerated degradation mechanisms for cycling and storage are described in the following subsections.

2.12.1 Degradation of Lithium-ion Cell due to Storage

During storage, the active anode material is exposed to the electrolyte through the porous solid electrolyte interphase (SEI) layer, and side reactions enhance this SEI layer [174]. High temperatures or high SOCs result in more severe capacity fading as well as resistance growth (power fading) in the cell. Therefore, to improve battery life and to slow down the electrochemical processes, lithium-ion cells should be stored with less than 100% SOC and around 15°C (optimal conditions 40% SOC and 15°C) [178]. This will allow a lithium-ion cell to last many times longer than one stored at 100% charge, particularly at high temperature.

2.12.2 Normal Degradation of Lithium-ion Cell due to Cycling

Capacity fade primarily occurs on the electrode/electrolyte interphase under the influence of intercalation and deintercalation of lithium ions. Ideally, loss of lithium ions and active materials are the only mechanisms that degrade a lithium-ion cell. However, in practice, other degradation mechanisms accelerate the capacity fading. Power fade is also coupled to capacity fading. The growth of the SEI layer results in the internal impedance rise of the battery cell and the deformation of the electrodes in a lower conductivity. As a result, due to the loss of active material, the power fading occurs. Capacity fading can be divided into four stages as shown in Figure 2.15 [179, 180, 174].

Stage-A: During stage A, on the interphase of the anode with the electrolyte of the separator, a SEI film will form as a side reaction; as a result, there is a fast decrease in capacity. This stage does not last for many cycles because, as the cell is cycled more, the side reaction rate will gradually decay [181] . A schematic of a SEI film layer in a lithium-ion cell is given in Figure 2.16.

Stage-B: In stage B, the anode is the limiting electrode [181]. Because of the SEI film layer formed on the anode, less active material is available and fewer lithium ions are intercalated into the anode during charging. As a result, the loss rate of lithium ions will be slower, and the SEI layer protects the anode from reduction reactions with the electrolyte. During continuous intercalation and deintercalation the SEI layer cracks and more active material will be exposed. This will cause more side reactions and the SEI layer will continue to grow, leading to a less porous SEI layer and loss of lithium ions [182].

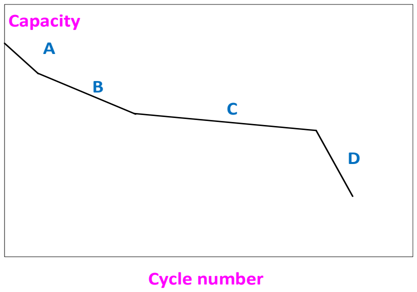

Figure 2.15: The general shape for capacity versus cycle number (modified from [179]).

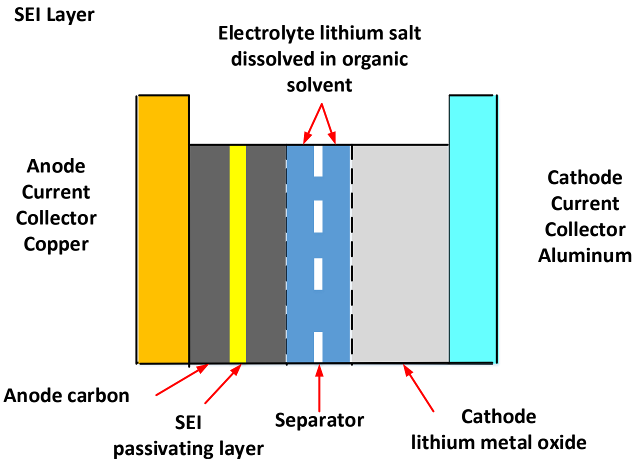

Figure 2.16: Schematic of SEI film layer in lithium-ion battery (modified from [180]).

Stage-C: In stage C, the degradation rate of the active cathode material is higher than the loss of lithium ions. On the cathode/electrolyte interphase, a layer similar to the SEI layer is formed, which is named the solid permeable interphase (SPI) [183]. Due to cycling, this layer will also grow and limit the active cathode material. The anode is however still the limiting electrode in this stage, as there is still more active cathode material available than lithium ions.

Stage-D: In stage D, the cathode becomes the limiting electrode due to the high degradation rate of the cathode. Less active cathode material is available than the number of ‘cycle able’ lithium ions [181]. Not all the lithium ions that were intercalated into the anode during charging can be intercalated into the cathode during discharge. Hence, more and more lithium ions are stuck inside the anode. The cathode will be fully intercalated during discharge, which raises the active cathode material loss rate. These added effects cause an accelerated capacity fading and the capacity will rapidly decrease.

The severity of these stages is not the same for different types of lithium-ion cells. For example, for $LiFePO_4$, the main capacity fading mechanism of cells is the loss of lithium ions by the later lithium-ion consuming SEI film formation, which also results in a loss of active anode material [184]. Loss of cathode material happens at a lower rate for $LiFePO_4$ cells, since neither cycling nor temperature change enhances the formation of the SPI layer [183]. This causes $LiFePO_4$ cells to have a much higher cycling life compared to other chemistries.

2.12.3 Accelerated Degradation of Lithium-ion Cell due to Cycling

In real life applications, lithium-ion cells experience accelerated degradation due to certain stress factors. Stress factors such as deep DODs, elevated C-rates, high or low temperatures, and operating at high SOCs can have negative impact on the cell capacity and cause accelerated degradation. These stress factors are described in the following subsections.

2.12.3.1 Depth of Discharge (DOD)

The cycle life of a cell strongly depends on the DOD. Figure 2.17 shows cycle life versus DOD curve for different battery cell chemistries (NiMH, Li-ion, Lead-Acid AGM/Gel, and Lead-Acid flooded).

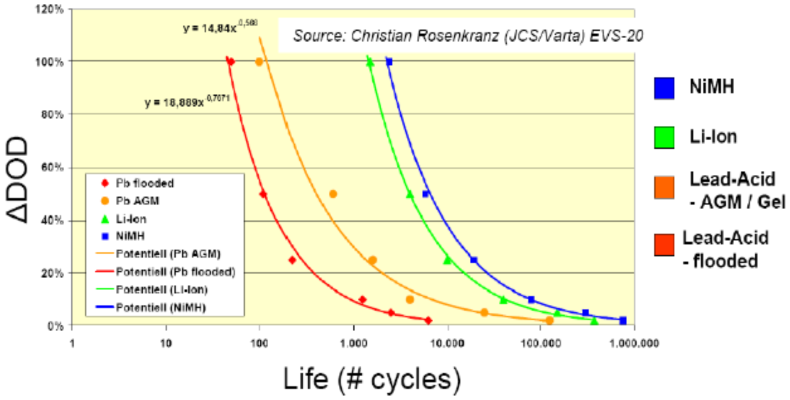

Source: Christian Rosenkranz (JCS/Varta) EVS-20

Figure 2.17: Cycle life vs. ΔDOD curve for different battery cell [185].

More intercalation and deintercalation takes place in the electrodes due to deeper discharge. The loss of lithium ions and active electrode material is higher for larger DOD cycles. At high DODs, additional degradation mechanisms can occur resulting in decomposition and dissolution of cathode material and capacity fading [186]. DOD has no influence on the capacity fading of $LiFePO_4$ cells, but the charge or energy processed is the determining factor [187].

2.12.3.2 Elevated C-rate Effect

High C-rates generate more heat and cause the temperature of the cell to rise invoking the high temperature degradation mechanisms. High currents also cause local over potential of the electrodes' earlier stage at certain areas of the cell. High C-rates will also cause the SEI layer on the anode to crack faster. More active anode material is exposed and the SEI layer will restore itself, reducing lithium ions from the battery cell process. High C-rates will cause additional strain on the electrode materials, resulting in increased deformation and loss of active material [186]. These effects will result in power fading and capacity fading.

2.12.3.3 Temperature Effect

The discharge capacity of lithium-ion cells is strongly influenced by temperature. Lithium-ion cells have an optimal temperature operating range, outside of which the battery cell undergoes severe loss of capacity. A typical operating temperature range is between 20°C and 40°C [188] for lithium-ion batteries, while an extended range is between -10°C and +50°C [189, 190]. Higher and lower temperatures have different effect on the life of the battery. In Figure 2.18, an example of the temperature range for an optimal life cycle is shown. It can be seen that the decay of cycle life is different for high and low temperatures, as different degradation mechanisms deteriorate the battery.

At the **lower temperature side**, due to the higher activation energy needed for the chemical reactions and lower ion diffusion, there will be a loss of capacity and deliverable power. However, when the temperature is restored to nominal level, the capacity and power capabilities will be recovered. Under normal discharge, low temperature on its own does not have any permanent influence on capacity fading but, during charging, lithium plating is likely to happen because the intercalation rate at the anode is inherently slower than the deintercalation rate [191].

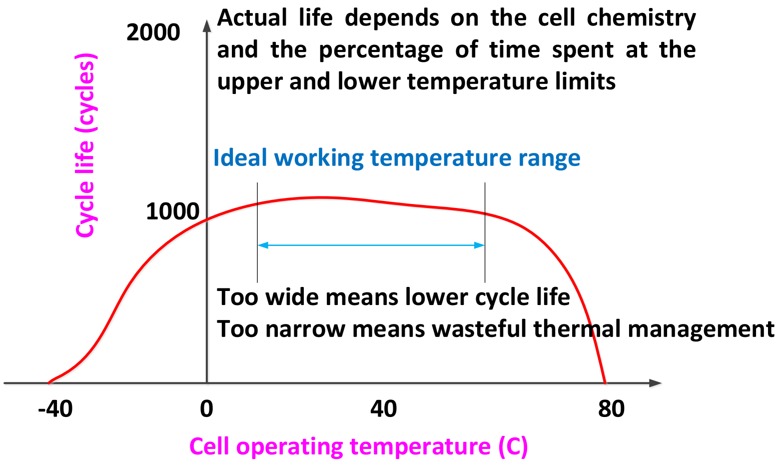

Figure 2.18: A battery cell's temperature range for optimal cycle life (modified from [192]).

In the long term operating at the **higher temperature side** can cause severe damage to the cell [193]. As shown in Figure 2.19, increase in temperatures results in higher capacity fading. Due to high temperature, the SEI layer will slowly break down and dissolve into the electrolyte. The active material of the anode will be partly exposed to the electrolyte again, causing side reactions. The damaged SEI layer will be restored due to the side reactions or a precipitation of the dissolved SEI particles will take place. In addition, parts of the cathode can dissolve into the electrolyte and become incorporated into the SEI layer. As a result, the intercalation at the anode will be more difficult and the ionic conductivity will be lowered. The same degradation mechanism happens at the cathode side with the SPI layer. Another degradation mechanism is the deformation of the anode and cathode.

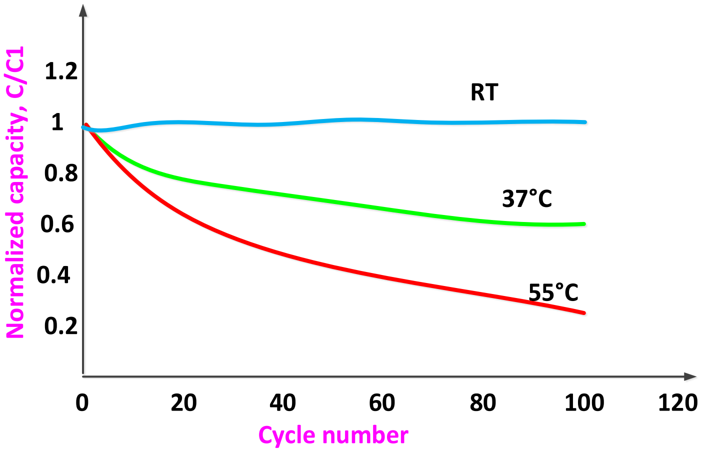

Figure 2.19: The accelerated capacity fading due to high temperatures (modified from [193]).

2.12.3.4 State of Charge (SOC)

At higher SOC, a battery cell is more reactive, which will accelerate degradation of the cell. At high SOC, the anode will be highly energized, self-discharge will also be higher and the SEI layer will grow faster. Furthermore, electrolyte oxidation occurs at high SOC, leading to impedance increase [194]. These effects result in capacity and power fading. During storage for a long time, a high SOC will have a more profound effect. In case of overcharge or over discharge, other degradation mechanisms come into play as follows:

2.12.3.5 Overcharge

When the cell is charged over the specified voltage, a small increase in capacity is initially obtained, but the cycle life is strongly reduced. This effect is stronger as the end of charge voltage increases. During overcharge, electrical energy is pumped into the battery, but more intercalation cannot take place. This will be represented by a sharp increase of internal resistance and the temperature [195]. Decomposition of the binder and electrolyte, forming insoluble products, blocking the pores of the electrodes and causing gas generation, may subsequently take place [196].

2.12.3.6 Over Discharge

When the cell is discharged under the specified cut-off voltage, two degradation mechanisms severely damage the cell. 1) Corrosion of the copper current collectors and dissolution into the electrolyte resulting in loss of contact with anode and power fade [197]. 2) Decomposition of the SEI layer on the anode. The high anode potential will cause dissolution of the SEI layer. Upon recharge the exposed active material will cause side reactions to restore the SEI layer and reduce lithium ions, causing capacity fading [198].

Chapter 3

Experimental Studies

The focus of this chapter is on experimental set-up, procedure, and data analysis. The first experiment focuses on thermal characterization of a lithium-ion battery cell. The experiment measures the temperature and heat flux on the surface of the lithium-ion battery cell at various discharge and charge rates in four discharge conditions with five different cooling conditions/boundary conditions (four for water cooling and one for air cooling). The heat generated in the four discharge conditions with four different cooling conditions is also determined. A special apparatus is developed to enable this experiment. In addition to this, thermal imaging of the principle surface of the battery cell while undergoing discharging are presented. The second experiment deals with thermal characterization of a lithium-ion battery pack with the above mentioned C-rates and BCs while the focus of the third experiment is a battery degradation test based on actual drive cycles from an EV.

3.1 Experiment 1 : Battery Cell Thermal Characterization

Depending on ambient conditions, there may be a need to remove or add heat to the battery in order to maintain the optimal temperature range and distribution. Non-uniform temperature distribution results over time in low charge and discharge performance and cell unbalancing. Existing thermal management techniques include applying liquids, insulations and phase-change-materials. Therefore, this experiment consists of measurement of the surface temperature distribution and heat flux on the principle surface of the battery cell. The experimental set-up, procedure, and data analysis method for this experiment are presented in the following sections.

3.1.1 Experimental Set-up

The thermodynamics of lithium-ion cells is complicated due to the complexity and diversity of the material involved. To obtain a reliable prediction of the temperature profile, the total heat generation must be evaluated. Therefore, the temperature variation and heat dissipation of cells under a variety of loading conditions must be measured to provide a baseline for simple but high fidelity of batteries at higher scales (module, packs) [109]. In this study, a large sized prismatic lithium-ion battery cell utilized in EVs and HEVs is characterized. The 20Ah $LiFePO_4$ lithium-ion prismatic cell is shown in Figure 3.1. The cell's specifications are described in Table 3.1.

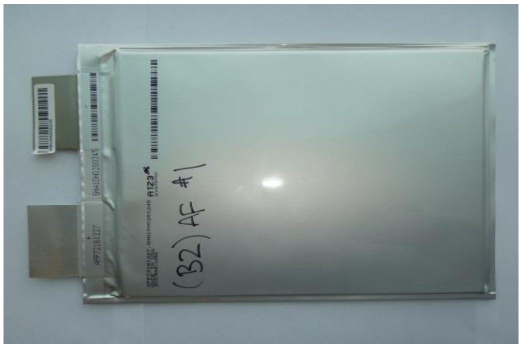

Figure 3.1: 20Ah $LiFePO_4$ lithium-ion prismatic cells.

Table 3.1: $LiFePO_4$- 20Ah lithium-ion prismatic pouch cell specifications [199].

Specification	Value	Unit
Cathode Material	$LiFePO_4$	-
Anode Material	Graphite	-
Electrolyte	Carbonate based	-
Nominal Capacity	~20	Ah
Nominal Voltage	3.3	V
Nominal Energy	65	Wh
Energy Density	247	Wh/L
Mass	496	g
Discharge Power	1200	W
Dimensions	7.25 x 160 x 227	mm
Specific Power	2400	W/kg
Specific Energy	131	Wh/kg
Operating Temperature	- 30 to 55	°C
Storage Temperature	- 40 to 60	°C
Volume	0.263	L
Number of Cycles	Min. 300, approx. 2000	Cycles
Max Discharge	300	A
Max Charge	300	A
Internal resistance	0.5	mΩ

The experiments for thermal characterization of lithium-ion battery cells were performed at the University of Waterloo's Green Electrochemical Energy Storage Laboratory. The schematic of the hybrid test bench for thermal management is shown in Figure 3.2. The hybrid test bench was originally designed and built to test various hybrid technologies and assess their usefulness in vehicle design. However, the hybrid test bench has been modified to test batteries on different duty cycles and to measure battery thermal performance and degradation. It provides an overview of the hardware and connections installed on the bench.

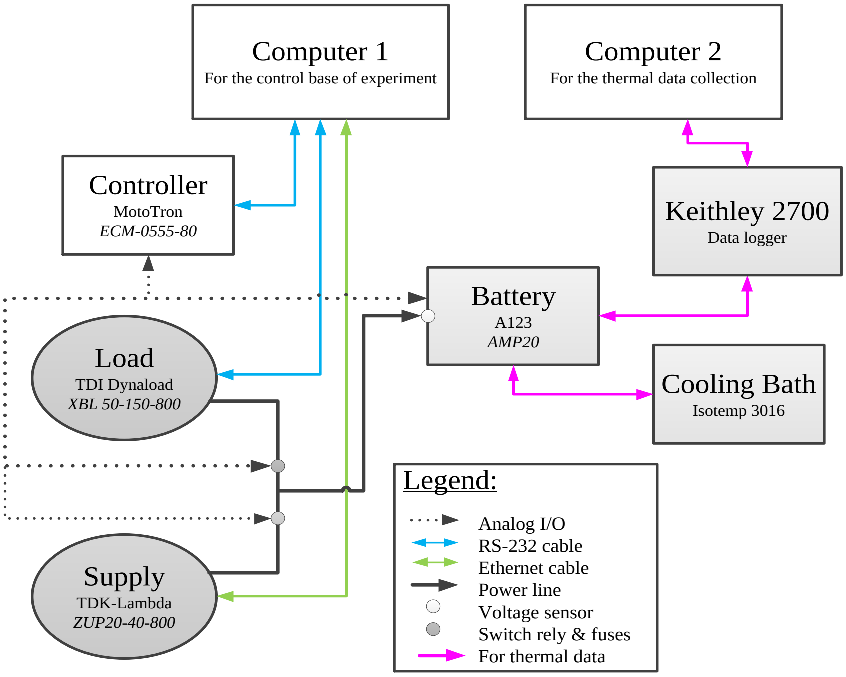

Figure 3.2: Schematic of the hybrid test bench.

The Computer-1 provides the basic controls using LabVIEW VI to the controller and load box via RS-232 cables, and the power supply with an ethernet cable. The computer also offers a GUI for the user to monitor the progress of the experiment. The controller uses analog I/O signal wiring to communicate with the relays and measure the battery voltage, and transmits the measured battery voltage back to the Computer-1. The Computer-1 sets the current or voltage values on the load box and power supply depending on the experiment. The current measured internally of the load box and power supply is transmitted back to the Computer-1. Depending on the Computer-1 requests, the power supply or load box will provide power to or draw power from the battery, respectively. The image with detailed components of the experimental set-up for battery cell thermal characterization is shown in Figure 3.3.

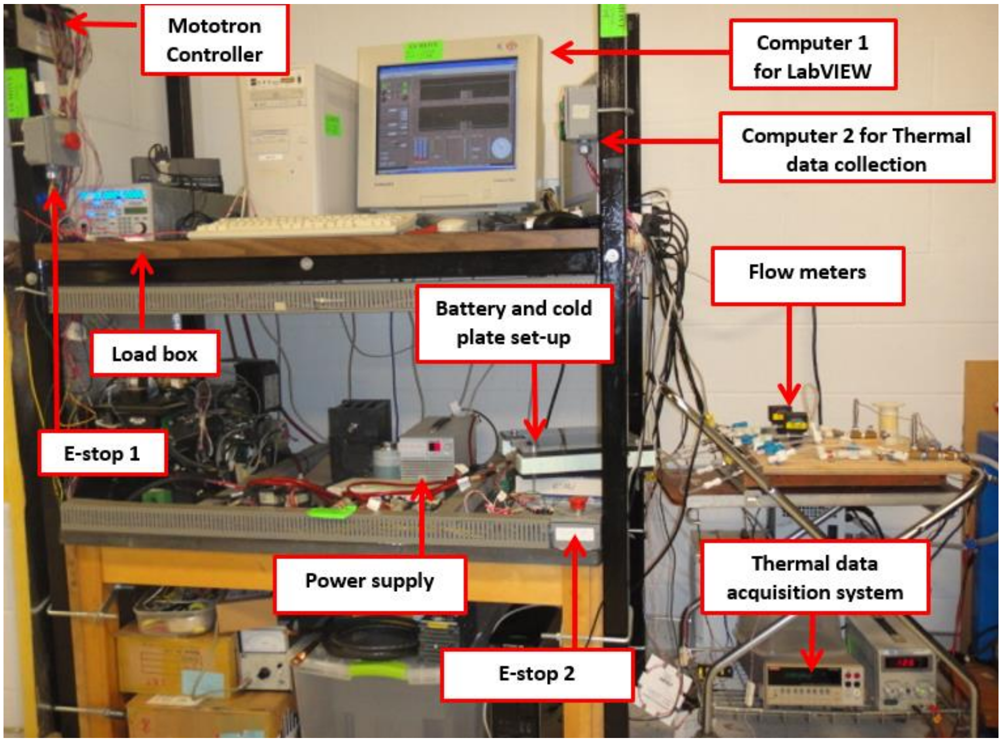

Figure 3.3: Experimental set-up for battery cell thermal characterization.

Test stand Computer-2 manages the Keithley-2700 (Data Acquisition) program used for the measurements of battery cell surface temperature, heat flux, and water inlet and outlet temperature for the top and bottom cold plates. There are two E-stop (Emergency shutdown) buttons in the test stand; one is near the MotoTron controller and the other is near the cell housing. The E-stop circuit controls the 12V supply to the normally-open contactors, subsequently acting in series arrangement with the MotoTron control circuit that usually controls the ground path of the contractor control circuit. The E-stop circuit was coordinated to cause a prompt opening of the contactors on the power lines if one of two E-stop buttons was hit.

The screen capture of LabVIEW interface is shown in Figure 3.4. It represents the real parameters taken during these experiments, for example, battery voltage, charge current, discharge current, and temperature. In the top left corner, there are three battery voltage windows: battery A, B and C, in other words, there is a possibility to connect three lithium-ion batteries together in series.

Here, but for the current experimental work, we used only one battery, therefore, the solid green light is seen only for battery A. The maximum voltage was set to 3.6 V and the over voltage protection was set to a value of 4.2 V. The battery temperature rise measured by thermocouples can also be seen for battery A. One can also run a different drive cycle which is also shown in the bottom right corner in Figure 3.4. The voltage and current (charge and discharge) window, which states that once the voltage reaches to cut-off voltage then the cycle changes from discharging to charging cycle. Figure 3.4 also displays the corresponding current window in which, the red color line is for discharging current and the white color line is for charging current.

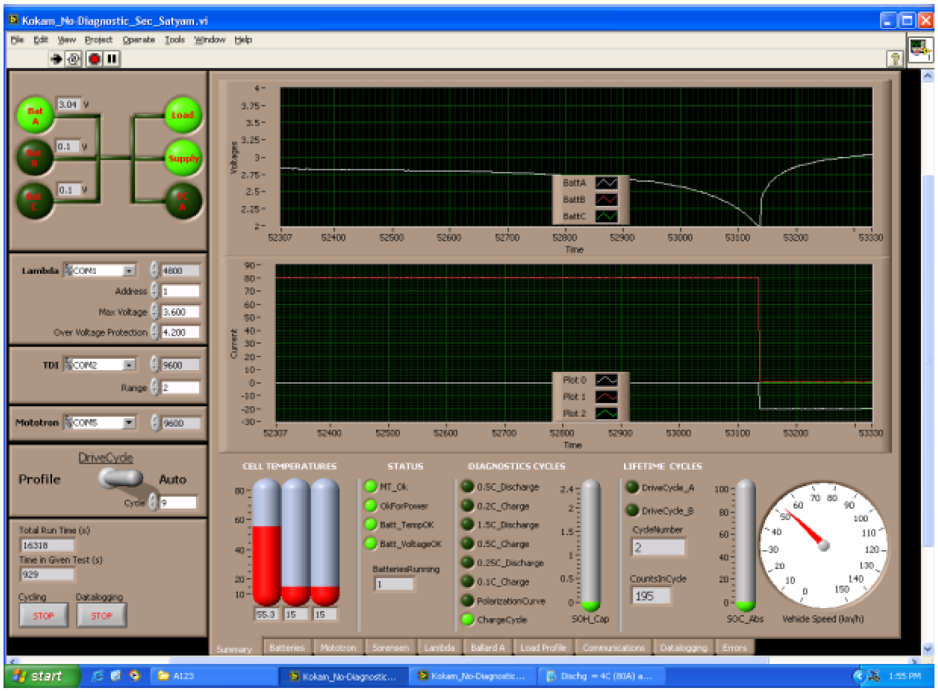

Bat A: 3.04 V
Bat B: 0.1 V
Bat C: 0.1 V
Lambda: COM1, 4800
Address: 1
Max Voltage: 3.600
Over Voltage Protection: 4.200
TDI: COM2, 9600
Range: 2
Mototron: COM5, 9600
Cycle: 9
Total Run Time (s): 16318
Time in Given Test (s): 929
Cell temperatures: 55.3, 15, 15
BatteriesRunning: 1
CycleNumber: 2
CountsInCycle: 195

Figure 3.4: Screen capture of LabVIEW interface

The commercial cooling plates were selected from industry (Dana Holdings Inc., Oakville, Ontario, Canada) to remove heat from the battery. The coolant plates were manufactured from two stamped aluminum plates that are joined in a nickel-brazing process. The plate tested was the “zig-zag” plate. This plate was characterized as having a single flow channel with one inlet and one outlet placed on the top and bottom of the battery. The single flow channel runs down the length of the plate before turning back on itself, stepping one channel width across the plate with each turn. This flow pattern results in a thermal profile where coolant temperature gradient is largest across the width of the plate. The water cooling set-up along with cold is shown in Figure 3.5 (a).

For air cooling, the battery was placed in a vertical position fixed in a wooden stand and is appeared in Figure 3.5 (b), where the free air convection was considered. The environment was controlled by lab temperature for air cooling.

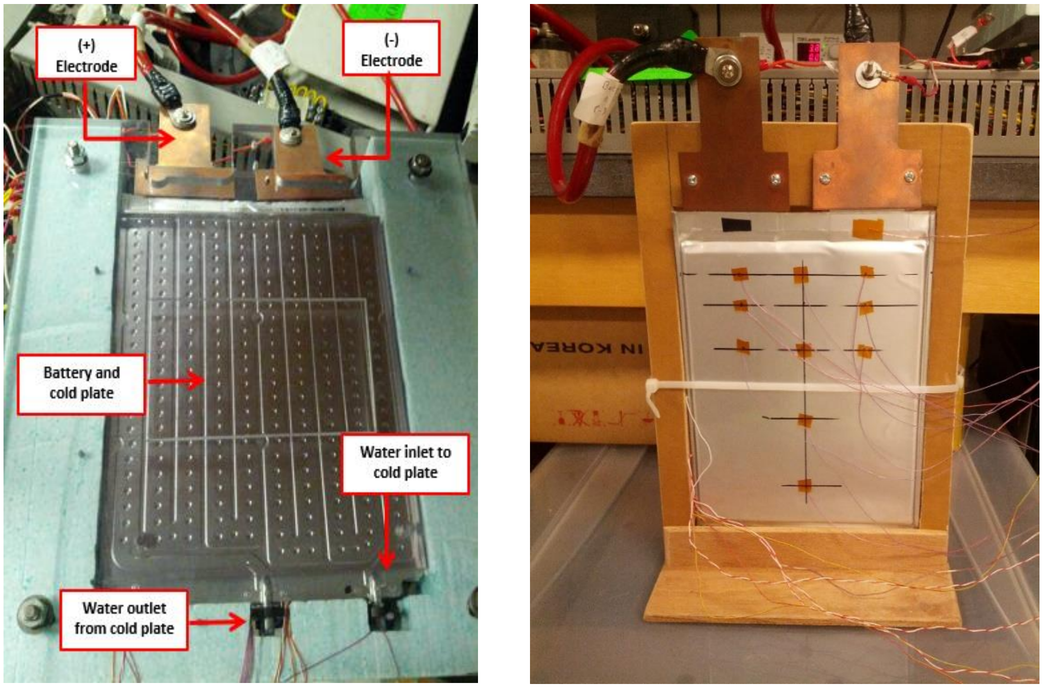

a) Water cooling **b) Air cooling**

Figure 3.5: Water and air cooling set-up.

3.1.2 Experimental Procedure and Plan

In this experiment, two different cooling types are tested: air cooling and water cooling. For air cooling ~22°C boundary condition is selected. For water cooling, four different coolant temperatures or boundary conditions are selected: 5°C, 15°C, 25°C, and 35°C. Four different discharge rates are selected: 1C, 2C, 3C, and 4C. The charge rate is 1C. The flow chart for experimental procedure is shown in Figure 3.6. The charge/discharge rate and their corresponding current is shown in Table 3.2.

This procedure was followed to initiate battery cycling and the thermal data collection, but it does not directly describe the procedure for assembling the battery and cooling/instrumentation components within the compression rig. As such, this procedure assumes the cell and cooling components are correctly installed and fully connected to all other components as required.

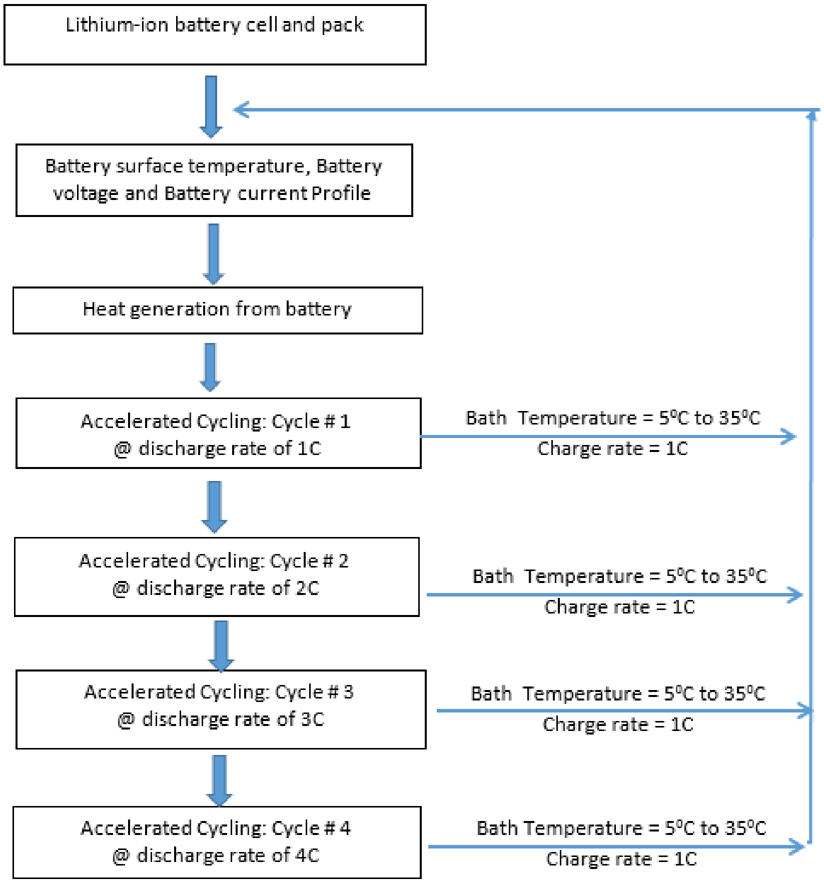

Figure 3.6: Flow chart for experimental procedure.

Table 3.2: Discharge rates and equivalent current values.

Discharge Rate	Constant Current
1C	20 A
2C	40 A
3C	60 A
4C	80 A

1. The isothermal fluid bath and pump was turned on for a minimum 3 hours prior to beginning cycling in order to bring the battery cell/pack, bath and cooling apparatus to a steady state temperature. The valves leading to the cold plates were observed and set to open. The isothermal fluid bath was set to the desired cooling temperature or boundary conditions of 5°C, 15°C, 25°C, and 35°C for the test.

2. The LabVIEW code for the charge discharge stand was started and relevant test parameters were input to the LabVIEW program. Relevant test parameters include:
    a. Discharge current
    b. Charge current
    c. Number of cycles
    d. Drive cycle (charge and discharge cycle)
    e. Maximum voltage at end of charge
    f. Minimum voltage at end of discharge
    g. Measurement sample rate
3. The thermal data acquisition PC and Keithly 2700 were turned on and allowed to initialize. On the PC, ExcelLink recording software was prepared for data acquisition. The following parameters were recorded within the recording software:
    a. Battery surface temperature (top and bottom surface of the $LiFePO_4$ battery cell)
    b. Heat flux at the top surface of the battery: near the electrodes (positive and negative electrode) and the middle of the battery cell
    c. Water inlet and outlet temperature at the top and bottom cold plates.
4. The internal clocks on both PCs were synchronized to the same time to allow combining data files.
5. The charge-discharge test stand and thermal data acquisition were then activated at the same time, such that charging/discharging and data acquisition begin at the same instant.
6. The test continued until the desired number of battery cycles was completed.
7. Two files were created for each test:
    a. Data from the thermal data acquisition PC
    b. Electrical charge discharge data.

3.1.3 Thermocouple Locations

Thermocouples were installed on the principal surface of the battery to measure the surface temperatures at ten discrete points. The majority of the thermocouples were located near the electrodes because the heat generation is higher near the electrodes. On one side, T-type 30 gauge, special limits of error (SLE) thermocouple wire was used and, on the other side, three additional K-type thermocouples integral to the heat flux sensors were present. The K-type thermocouple locations are discussed in the next section. The location of T-type thermocouples is shown in Figure 3.7 and listed in Table 3.3. Kapton backed adhesive tape was used to adhere the thermocouples to the battery cell surface.

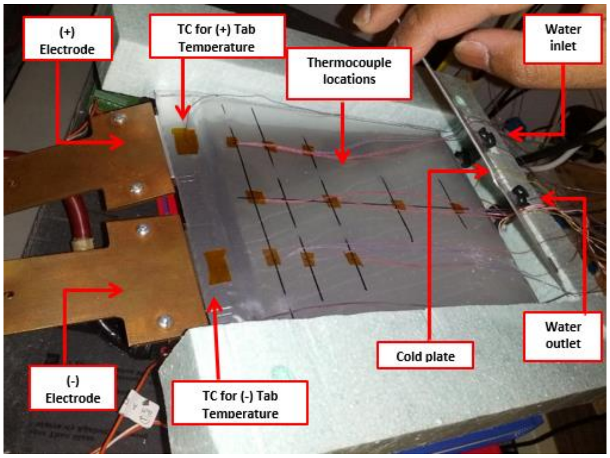

Figure 3.7: Thermocouple placement.

Table 3.3 : Distance of thermocouple locations from bottom left corner of the cell surface.

Thermocouple	X [cm]	Y [cm]
1,1	2.65	19.4
1,2	7.85	19.4
1,3	13.05	19.4
2,1	2.65	16.9
2,2	13.05	16.9
3,1	2.65	13.0
3,2	7.85	13.0
3,3	13.05	13.0
4,1	7.85	7.0
5,1	7.85	3.5

Finally, total nineteen thermocouples were used for this experimental work, out of which ten were places on the principle surface of the battery, two were placed for tab temperature measurement, three were placed on the another surface of the battery, and four were used for the water inlet and outlet temperature measurement for the top and bottom cold plates.

3.1.4 Heat Flux Sensors Locations

Three thin-film heat flux sensors were located on the surface opposite to the locations of the thermocouples. These heat flux sensors were located near the electrodes because the heat generation is higher near the electrodes. The heat flux sensors were selected because it directly provided heat flux in W/m^2. The locations of these three sensors are shown in Figure 3.8 and the corresponding x and y coordinates of HFS center points are given in Table 3.4.

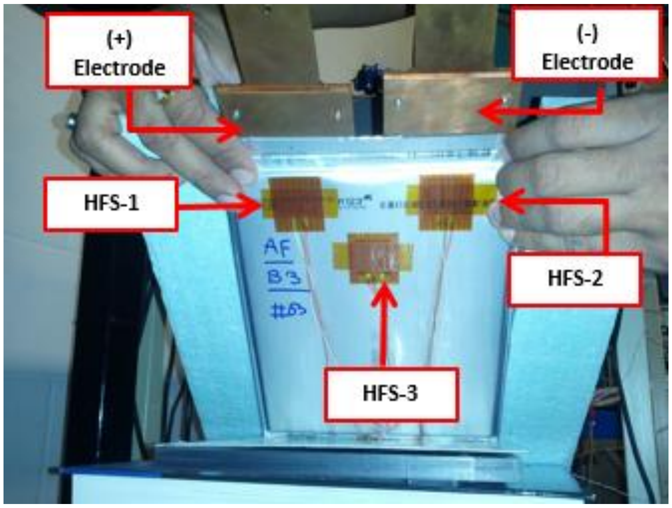

Figure 3.8: Heat flux sensors placement.

Table 3.4 : Locations of heat flux sensor centre-points distance from bottom left corner of the cell surface.

Heat Flux Sensor	Location	Type of HFS	X [cm]	Y [cm]
1	(+) Electrode	HFS-1	5.43	16.98
2	(-) Electrode	HFS-2	10.47	16.98
3	Mid-surface	HFS-3	7.85	12.27

These sensors function as a self-generating thermopile transducer. They require no special wiring, reference junctions or signal conditioning. The HFS utilizes a multi-junction thermopile construction on a polyimide film laminate. The output of the sensors provides an average measurement of surface heat flux in a 25.4 x 25.4 mm area (1 $inch^2$). Kapton backed adhesive tape was used to adhere the thermocouples to the battery surface.

3.2 Experiment 2 : Battery Pack Thermal Characterization

In EV applications, the battery system consists of a number of single cells connected either in series or in parallel in order to achieve the power and capacity requirements. In these experiments, the surface temperature and voltage distributions are measured for a lithium-ion battery pack with three $LiFePO_4$ battery cells. The pack thermal characterization testing was performed at Green and Intelligent Automotive (GAIA) Laboratory at the University of Waterloo and the experimental set-up is shown in Figure 3.9.

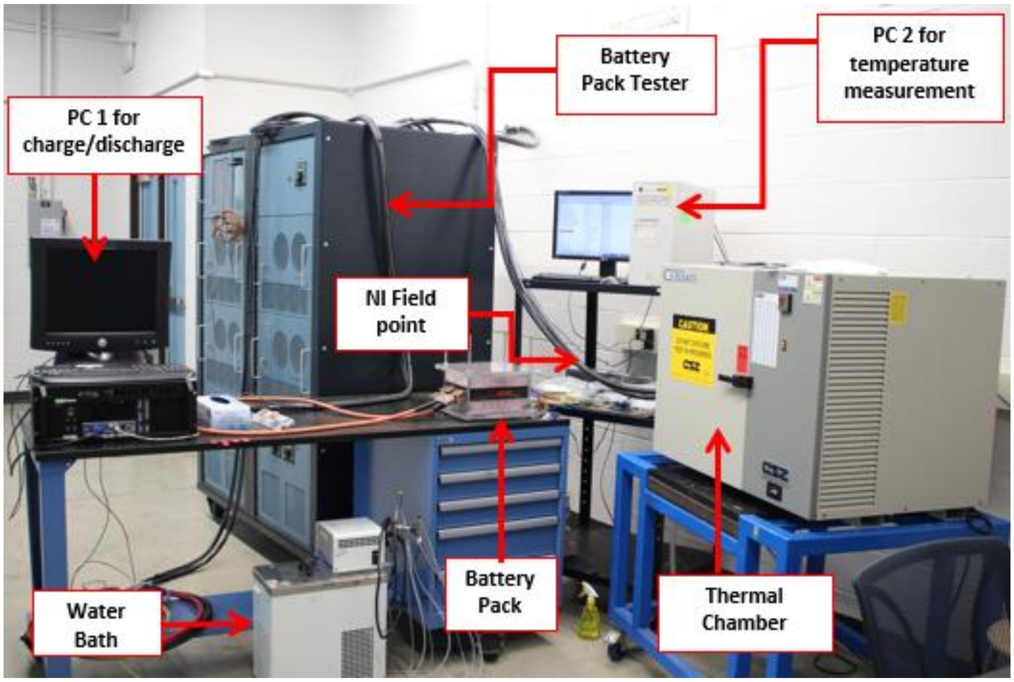

Figure 3.9: Experimental set-up for battery pack thermal characterization.

This test bench consists of mainly five components: A & D cell cycler, National Instrument (NI) field point, battery pack, Computer-1 and Computer-2. T-type thermocouple used to measure the temperature is connected to NI temperature measurement device, which is further connected to Computer-2. LabVIEW 8.2 software is used to control and operate the NI temperature measurement device through Computer-2. Computer-1 is used to measure the battery pack voltage, current, SOC at one second intervals. A & D cell cycler (Bitrode) having a maximum capacity to charge/discharge up to 20V and 1200 A, is used to charge and discharge the battery pack. The cell cycler is controlled by Computer-1 through VisuaLCN software. Heavy duty copper cables are used to connect battery pack with cell cycler. To charge and discharge the battery pack at different rates, a profile is created using VisuaLCN program editor. An exploded view of the battery pack appears in Figure 3.10 and different views (front view, side view, and top view) of battery pack are shown in Figure 3.11.

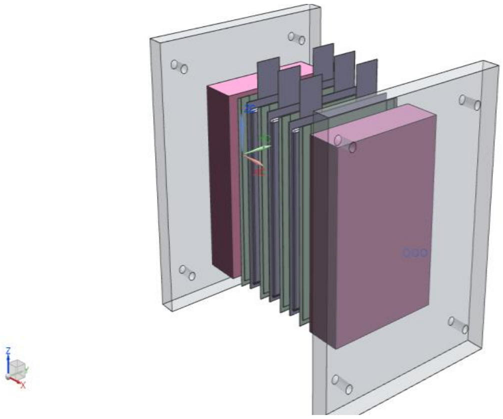

Figure 3.10: An exploded view of three lithium-ion battery cells with four cold plates in a pack.

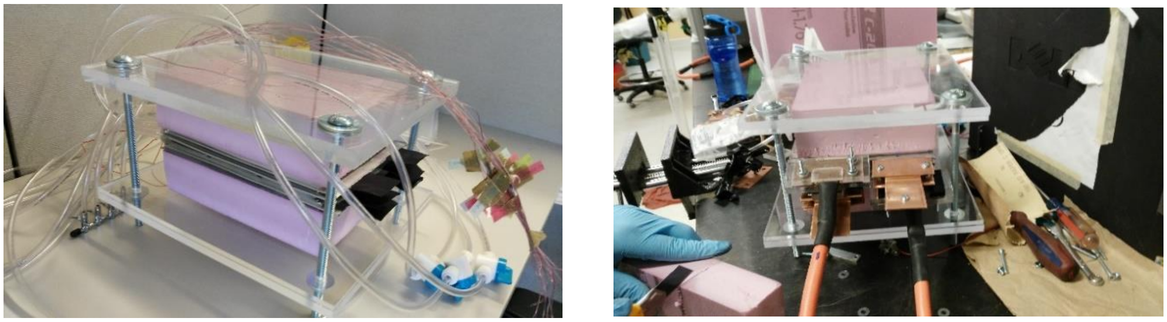

a) Picture of battery pack

b) Front view

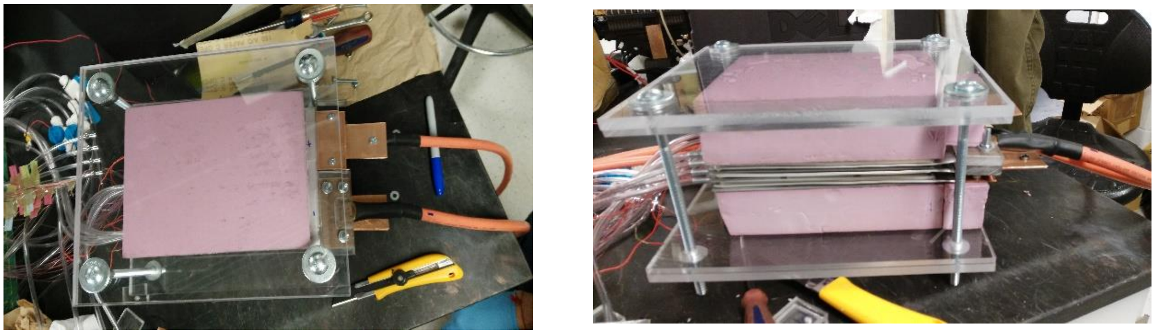

a) Top view

b) Side view

Figure 3.11: Different views of battery pack.

The pack consists of three prismatic lithium-ion cells electrically connected in series. A $LiFePO_4$ battery cell as shown in Figure 3.1 is used and the cell's specifications are described in Table 3.1.

The tab extensions were also made from copper plates and can be seen in top and front view in Figure 3.11. The pack was sandwiched between two-inch-thick insulation foam to prevent heat loss to surrounding. Same insulation foam is used in both sides and at the back to insure proper insulation. To make secure and tight connection, cells along with insulation foam were tightened in 12 mm thick Acrylic sheet by using ½ × 8 inch nuts and bolts.

3.2.1 Thermocouple Locations

To measure the temperature variations, the pack was instrumented with eighteen thermocouples (specification: T-type 30 gauge, special limits of error thermocouple wire with uncertainty of 0.5°C according to manufacturer's specifications). Out of eighteen, six thermocouples were installed on each cell: three on each side. Out of three thermocouples, the first thermocouple was placed near the cathode, the second near the anode, and the third at the mid surface of the cell as shown in Figure 3.12. A special thermal tape was used to attach the thermocouple to all three cell's surface.

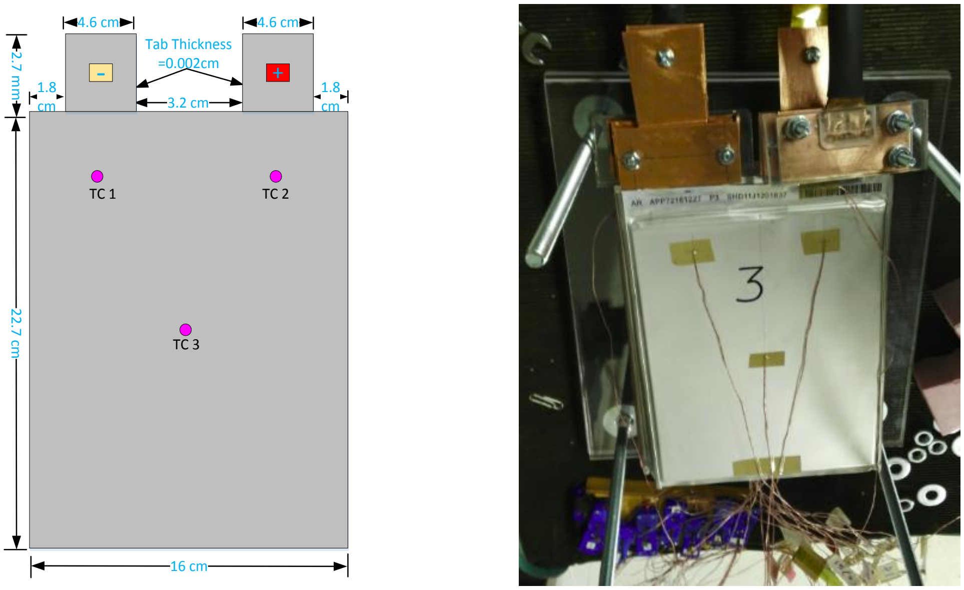

a) Drawing with dimensions **b) Picture of actual cell with thermocouple**

Figure 3.12: Thermocouple locations; (a) drawing with dimensions, (b) picture of actual cell with thermocouple.

The pack was also made with individual cell voltage sensors and current sensors for three cells. In this series, each battery cell is experimentally characterized, in order to predict the cell voltage and capacity during discharging and charging operations at an ambient temperature (~22°C). In all the experiments conducted, the cells are initially charged, then utilized until completely discharged. It is very well known that the temperature distribution is not uniform in a battery pack. Therefore, the operating temperature of the cells are different from each other. The output voltage of the series connected cells and the discharge current is given by:

$$V_{out} = V_{cell\,1} + V_{cell\,2} + \cdots + V_{cell\,n} \tag{3.1}$$

$$I_{out} = I_{cell\,1} = I_{cell\,2} = \cdots = I_{cell\,n} \tag{3.2}$$

In the experimental measurements, four different discharge rates are selected: 1C, 2C, 3C, and 4C. The charge rate is 1C. The internal resistance is calculated based on Ohm's law (covering the voltage drop is divided by current values) and the voltage drop is the difference between the open circuit voltage and the actual or measured terminal voltage. The internal resistance is calculated by:

$$r_{int} = \frac{\Delta V}{I} = \frac{V_{oc} - V_{act}}{I} \tag{3.3}$$

Figure 3.13 shows four cold plates used for this experimental work. The flow rate of water to all the cold plates is 150 mL/min. The pack is insulated by all five sides (left, right, back, top, and bottom of the pack along the height of the lithium-ion battery cell) using thermocol sheet in order to prevent heat loss from the pack to the surrounding sides. In addition to eighteen, two additional thermocouples were used to measure the temperature of the water inlet and outlet at the cold plates. The same experimental procedure and plan was followed for pack testing, as described in the previous Section 3.1.2.

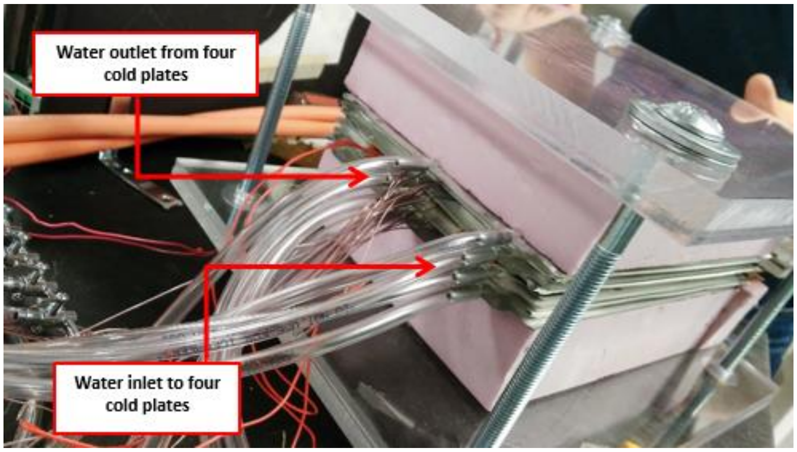

Figure 3.13: Four cold plates with three battery cells.

3.2.2 Temperature Measurement with NI Field Point

Three NI field point (NI-FP-TC-120) with 8-channel thermocouple input modules were used to measure the temperature of the battery pack. These three modules were connected together through a terminal base to form a 24 channel thermocouple input module as shown in Figure 3.14. Each field Point thermocouple input module has eight thermocouple or millivolt inputs. These modules have inbuilt linearization and cold-junction compensation for eight type of thermocouple (J, K, R, S, T, N, E, and B). These modules can operate between –40 to 70°C.

Figure 3.14: NI field point for temperature recording.

To operate all three modules, a code has been developing in LabVIEW software with a capability to measure and record temperature from all 24 thermocouples connected to modules. A user interface has been also created in LabVIEW software to observe the temperature and control the test as shown in Figure 3.15 .

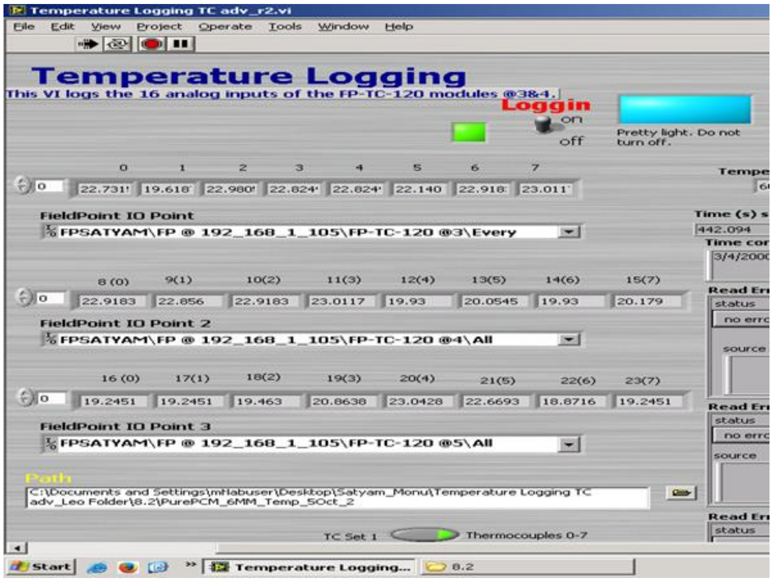

Temperature Logging

This VI logs the 16 analog inputs of the FP-TC-120 modules @3&4.

Pretty light. Do not turn off.

0	1	2	3	4	5	6	7
22.731	19.618	22.980	22.824	22.824	22.140	22.918	23.011

FieldPoint IO Point: FPSATYAM\FP @ 192_168_1_105\FP-TC-120 @3\Every

Time (s): 442.094

3/4/200

8 (0)	9(1)	10(2)	11(3)	12(4)	13(5)	14(6)	15(7)
22.9183	22.856	22.9183	23.0117	19.93	20.0545	19.93	20.179

FieldPoint IO Point 2: FPSATYAM\FP @ 192_168_1_105\FP-TC-120 @4\All

16 (0)	17(1)	18(2)	19(3)	20(4)	21(5)	22(6)	23(7)
19.2451	19.2451	19.463	20.8638	23.0428	22.6693	18.8716	19.2451

FieldPoint IO Point 3: FPSATYAM\FP @ 192_168_1_105\FP-TC-120 @5\All

Path: C:\Documents and Settings\mHabuser\Desktop\Satyam_Monu\Temperature Logging TC adv_Leo Folder\8.2\PurePCM_6MM_Temp_5Oct_2

Figure 3.15: LabVIEW for NI field point.

3.3 Experiment 3 : Battery Degradation

Although lithium-ion batteries have many advantages as explained in the literature review, their thermal and electrical performance as well as reliability with an actual EV requires further study. For this, a data logger is installed in an EV and different drive cycles are collected at different ambient temperatures of -6°C, 2°C, 10°C, and 23°C. The vehicle is driven in the province of Ontario, Canada and several drive cycles are collected. The collected drive cycles consist of different modes: acceleration, constant speed, and deceleration in both highway and city driving at the above mentioned ambient temperatures, turning on all electrical accessories such as radio, air conditioning and heater. In addition, a comprehensive investigation and simulation is conducted on the lithium-ion battery performance under different drive cycles with various ambient temperatures.

3.3.1 Data Collection

The EV used for this work is shown in Figure 3.16 (a) and the main features of the EV are : (i) mass 1814 kg; (ii) total battery pack energy capacity 25kWh; (iii) battery module nominal voltage 19.2 V; (iv) battery module nominal capacity 69 Ah; (v) battery module energy density 89 Wh/kg. There are three packs of lithium-ion batteries installed on the vehicle, including a total of 20 battery modules. The first six modules are associated in series arrangement and are shown in Figure 3.16 (b).

a) The EV **b) First six modules connected in series**

Figure 3.16: The EV and first six modules connected in series.

Every module contains 6 series × 49 parallel IFR 18650 cylindrical valence cells (“I” stands for Li-ion rechargeable, “F” stands for the element “Fe” which is Iron, “R” just means the cell is round, 18650 means 18 mm diameter and 650 means 65 mm height); i.e., every battery module incorporates 6 strings of battery cells in series and each string contains 49 cells in parallel, resulting in an aggregate of 294 cells in every battery module. The cells utilized as a part of this EV are 18650 cylindrical cells in configuration; their specifications are displayed in Table 3.5.

Table 3.5: EV cell specification.

ESS Specification, Valence IFR18650e	Value
Number of Battery Packs	3
Number of Modules	20
Number of cell per module	6 in series
Charge Voltage	3.65V Standard (3.4V Float, 4.2V Max)
Nominal Operating Voltage	3.2 V
Nominal Rated capacity (C/5)	1350 mAh (1.4 Ah)
Discharge Cur-off Voltage	2.5 V
Cell Dimensions	Length: 65mm , Diameter :18.2 mm
Cell Weight	40 g

The ISAAC data logger, as shown in Figure 3.17 (a), is installed in the vehicle underneath the front passenger seat and appears in Figure 3.17 (b). The cellular antenna enables wireless data transmission and is located on top of the car. The data logger is powered by the existing 12V battery in the vehicle and the shutdown wire. The EV has a 125 kW UQM power phase electric motor beneath the front battery pack.

a) Data logger connection and shutdown wire

b) The data logger installation beneath passenger seat

Figure 3.17: ISAAC data logger installation beneath passenger seat and shut down wire.

3.3.2 Hybrid Pulse Power Test

A prismatic lithium-ion battery, as shown in Figure 3.1, was characterized for this work. It was chosen because it is suitable as a basic block for a large battery pack for commercial automotive vehicle applications. The basic specifications of the cell are displayed in Table 3.1. Figure 3.18 shows the HPPC cell testing for resistance measurement, consisting of a Biologic VMP 3B-100 load box, which works during charging and discharging of the cell. Data acquisition was conducted in the EC Lab software.

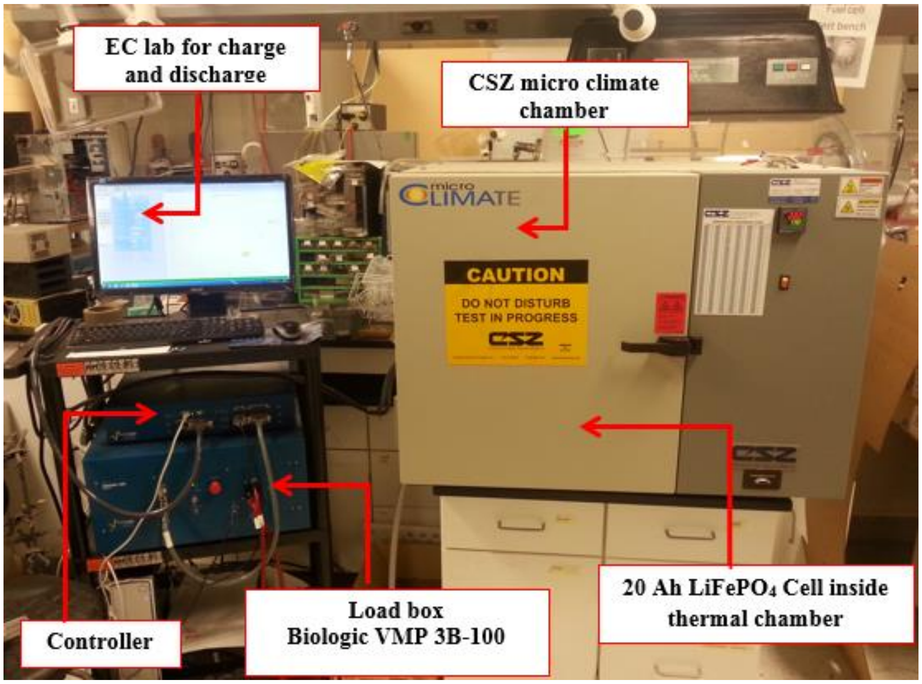

Figure 3.18: HPPC cell testing for resistance measurement.

The controller is utilized to log the battery electrical data, including time, charge current, discharge current, charge voltage, and discharge voltage. Cell cycling included charge-discharge cycles at 1C (20A), C/2 (10A) and C/25 (0.8A), all following a constant current, constant voltage (CCCV) protocol. Electrical data was recorded at regular intervals of one second. The battery cell was experimentally characterized, so as to predict the cell voltage and capacity during discharging and charging operations at an ambient temperature (~22°C). In all the conducted tests, the cells were first fully charged, and then used until totally discharged. Later, the A CSZ Micro Climate chamber was used to maintain the temperature of the cell during HPPC, in order to estimate the resistance at different conditions. The temperatures tested were 5°C, 10°C, 15°C, 20°C, 25°C, 30°C, 35°C, 40°C, 45°C, and 50°C. The discharges between pulses to reach the next lowest SOC value were 6 minutes long at 1C. An hour of rest followed each of these discharges, in order to assure that the battery's temperature had equilibrated at the ambient temperature before each pulse. It was assumed that the battery's internal temperature did not change during the HPPC, due to the low current and very short time.

3.4 Data Analysis Method for Cell and Pack Testing

In this section, the data analysis method is presented for the total heat generation from battery including heat stored in the battery, heat removed from the cold plates, and heat from environment are presented. In addition, the experimental uncertainty analysis is presented.

The total heat generation rate is calculated by:

$$\dot{Q}_{tot} = \dot{Q}_b + \dot{Q}_{cp} + \dot{Q}_e \tag{3.4}$$

where, $\dot{Q}_b$ is the heat stored in the battery, $\dot{Q}_{cp}$ is the heat from cold plates, and $\dot{Q}_e$ is the heat from environment and are explained with details in below subsections.

3.4.1 Sensible Heat

The heat stored in the battery is termed Q_{stored}. It is calculated based on the change in the temperature of the battery in conjunction with the specific heat value. Equation (3.5) is used to evaluate the stored heat energy in the battery when the battery temperature changes from some initial temperature to a final temperature.

$$\underset{t_1\ to\ t_2}{Q_{stored}} = m_b c_{p,b}(T_{t_2} - T_{t_1}) \tag{3.5}$$

A standard method of determining the average temperature across the entire battery surface has been devised to enable stored heat calculations. For each thermocouple, it is assumed that the measured temperature represents the average of an area extending around the sensor. The areas are determined by defining each area boundary by calculating the x and y midpoint distance between adjacent sensors. Equation (3.6) is used to evaluate the average battery surface temperature by summing the temperature-area products and dividing by the total area of the surface.

$$T_{\underset{avg}{s/c}} = \frac{\sum(T_{ij}A_{ij})}{A_{total}} \tag{3.6}$$

The ten thermocouples measuring the surface temperatures shown in Figure 3.7 are each assigned the areas that correspond to their locations. In Table 3.6, the physical size of the thermocouple areas is presented.

Table 3.6: X and Y component lengths of thermocouple areas.

Thermocouple	Area	X [cm]	Y [cm]	Area [m^2] (x10^{-3})
1,1	$A_{1,1}$	5.25	2.55	1.34
1,2	$A_{1,2}$	5.2	2.55	1.33
1,3	$A_{1,3}$	5.25	2.55	1.34
2,1	$A_{2,1}$	7.85	3.2	2.51
2,2	$A_{2,2}$	7.85	3.2	2.51
3,1	$A_{3,1}$	5.25	4.95	2.60
3,2	$A_{3,2}$	5.2	4.95	2.57
3,3	$A_{3,3}$	5.25	4.95	2.60
4,1	$A_{4,1}$	15.7	4.75	7.46
5,1	$A_{5,1}$	15.7	5.25	8.24

The rate of sensible heat accumulation is directly influenced by the battery heat generation rate and the heat transfer coefficient out of the system. The temperature of the battery increases as heat is generated due to the finite heat transfer coefficient to the surrounding. The rate of sensible heat accumulation is determined from Equation (3.7), where $\frac{dT}{dt}$ is the rate at which the battery temperature changes.

$$\dot{Q}_{stored} \ or \ \dot{Q}_b = m_b c_{p,b} \frac{dT}{dt} \tag{3.7}$$

The rate of temperature change is evaluated by measuring the temperature at two times and is calculated by:

$$\frac{dT}{dt} = \frac{(T_{t_2} - T_{t_1})}{t_2 - t_1} \tag{3.8}$$

The rate of stored heat accumulation can then be determined as follows:

$$\dot{Q}_{\substack{stored \\ t_1\ to\ t_2}} = m_b\ c_{p,b}\ \frac{(T_{t_2} - T_{t_1})}{t_2 - t_1} \tag{3.9}$$

3.4.2 Heat from Cooling Plates

Cooling plate heat removal rate is determined by the inlet and outlet thermocouple data, in conjunction with the recorded flow rates. The difference in inlet and outlet temperatures is due to heat conducted from the battery surface. The heat removed by a single cooling plate is calculated by using:

$$\dot{Q}_{CP} = \dot{m}_w C_{p,w}\left(T_{w,o} - T_{w,i}\right) \tag{3.10}$$

The total amount of heat removed by the cooling plates for a time period Δt can be determined using the following:

$$Q_{CP} = \dot{m}_w\ C_{p,w}\ \left(T_{w,out,avg} - T_{w,in,avg}\right)\Delta t \tag{3.11}$$

The term $T_{w,out,avg}$ is the average measured outlet temperature during the period Δt, as in Equation (3.12). N_T represents the number of temperature readings in the summation.

$$T_{w,out,avg} = \frac{\sum T_{w,o}}{N_T} \tag{3.12}$$

3.4.3 Heat from Environment

The compression rig is not perfectly insulated and, as such, cooling plate measurements incorporate a component of heat gain or loss from the environment ($\dot{Q}_e$). When the cooling is set to 5°C, a temperature difference of approximately 17°C is established between the inside surface of the compression rig and the ambient air. This results in heat transfer between the ambient environment and the cooling fluid. This additional heat is measured as an increased temperature difference between the inlets and outlets. For tests above the ambient temperature, the opposite occurs. This additional heat affects the temperature difference between the inlets and outlets.

In order to evaluate this effect, the cooling system and thermal data acquisition was activated with the battery in place but no charging or discharging occurring. In this way, the temperature difference between the inlet and outlet of each cooling plate could be recorded. The average difference for each plate, along with the respective flow rates, were used to quantify the heat removed or added by the environment using the method presented in the above section on cooling plates. The heat removed or added by the environment for different coolant temperatures is shown in Figure 3.19.

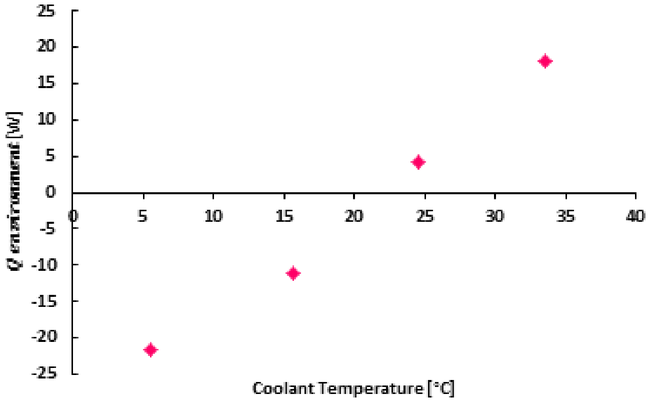

Figure 3.19: Ambient heat flow to compression rig for four coolant temperatures.

3.5 Experimental Uncertainty Analysis

In this section, the uncertainty analysis of the experimental measurements and derived correlations is presented. The accuracy of the measurement equipment is determined and used to establish the uncertainty of calculated relationships and properties.

The overall uncertainty of the experimental results and theoretical predictions will be calculated using the method described by Moffat in [200]. In this method, the result R of an experiment is determined from a set of measurements as:

$$R = R(X_1, X_2, X_3, \dots, X_N) \tag{3.13}$$

Each measurement can be represented as $X_i \pm \delta X_i$ where δX_i is the uncertainty. The effect of each measurement error on the calculated result is determined as follows:

$$\delta R_{X_i} = \frac{\delta R}{\delta X_i}\delta X_i \tag{3.14}$$

Hence the overall uncertainty of the result is determined by:

$$\delta R = \left\{\sum_{i=1}^{N}\left(\frac{\delta R}{\delta X_i}\delta X_i\right)^2\right\}^{1/2} \tag{3.15}$$

If R is described by an equation of the form $R = X_1^a\, X_2^b\, X_3^c \cdots\cdots X_N^m$ then the overall uncertainty of the result can be directly determined from the set of individual measurement uncertainties as:

$$\frac{\delta R}{R} = \left\{\left(a\frac{\delta X_1}{X_1}\right)^2 + \left(b\frac{\delta X_2}{X_1}\right)^2 + \cdots + \left(m\frac{\delta X_N}{X_1}\right)^2\right\}^{1/2} \tag{3.16}$$

The average battery surface temperature is evaluated using:

$$T_{\substack{surface\\average}} = \frac{\sum(T_{ij}A_{ij})}{A_{total}} \tag{3.17}$$

Evaluating the uncertainty of surface temperature measurements and area measurements was required to determine the overall uncertainty of the average surface temperature measurement. The uncertainties are as follows:

a) Surface Temperature, T_{ij}

Surface temperature measurements were made with T-type SLE (special limits of error) thermocouples and recorded with a Keithley 2700 data acquisition system. The uncertainty due to the thermocouple readout is 1°C [201], according to manufacturer’s specifications. The uncertainty is shown as:

$$\frac{\delta T}{T} = \pm\frac{1℃}{T[℃]} \tag{3.18}$$

b) Area, A_{ij}

An electronic digital caliper with a resolution of 0.005 was used to measure the positions of the thermocouples as installed on the battery surface. As $A_{ij} = lw$, Equation (3.19) was used to determine the uncertainty in each area.

$$\frac{\delta A}{A} = \pm\left\{\left(\frac{\delta l}{l}\right)^2 + \left(\frac{\delta w}{w}\right)^2\right\}^{1/2} \tag{3.19}$$

For the purpose of evaluating uncertainty in the average surface temperature, let $P_{i,j}$ represent the individual $T_{ij}A_{ij}/A_{total}$ components of the surface temperature average, where i and j subscripts describe the particular thermocouple. Equation (3.20) was used to determine the error in each $P_{i,j}$ product.

$$\frac{\delta P_{i,j}}{P_{i,j}} = \pm\left\{\left(\frac{\delta T_{ij}}{T_{ij}}\right)^2 + \left(\frac{\delta A_{ij}}{A_{ij}}\right)^2 + \left(\frac{\delta A_{total}}{A_{total}}\right)^2\right\}^{1/2} \tag{3.20}$$

A relative uncertainty for the average surface temperature was established via Equation (3.21). The highest surface temperature absolute error occurs when the surface temperature is smallest. The range of relative uncertainty is large and thus was calculated for each operating temperature. These values are summarized in Table 3.7.

$$\frac{\delta T_{\substack{surface\\average}}}{T_{\substack{surface\\average}}} = \pm\left\{\left(\frac{\delta P_{1,1}}{P_{1,1}}\right)^2 + \left(\frac{\delta P_{1,2}}{P_{1,2}}\right)^2 + \cdots + \left(\frac{\delta P_{5,1}}{P_{5,1}}\right)^2\right\}^{1/2} \tag{3.21}$$

Table 3.7: Average uncertainty in surface temperature for five operating temperatures.

Operating Temperature [°C]	± Relative Uncertainty (%)	± Absolute Uncertainty [°C]
5	20.3	1.5
15	2.6	0.5
25	1.2	0.4
35	0.7	0.3
~22	1.1	0.4

The uncertainty analysis explained above was also used for measuring the uncertainty in mass flow rate of water to the cold plates, temperature of the cold plates, heat from battery, heat from cold plates, heat from environment, total heat generated, and heat flux distributions. They are presented in Table 3.8.

Table 3.8: Summary of uncertainty.

Variable	Range	Temperature [°C]	± Relative Uncertainty (%)
$\dot{m}$ [mL/min]	170 mL/min – 218 mL/min	–	8.3% - 10.2%
ΔT_w[°C]	0.1°C – 2.6°C	–	0 % – 21.9%
$T_{i,j}$[°C]	5.6°C – 47°C	–	2.1% - 17.8%
$T_{\substack{surface\\average}}$[°C]	5.6°C – 44.5°C	–	0.48 % - 28.5%
$\dot{Q}_b$ [W]	0.51 W – 24.08 W	5	28.7 %
		15	3.69 %
		25	1.71 %
		35	1.02 %
$\dot{Q}_{cp}$ [W]	2.91 W – 50.61 W	–	24.4 %
$\dot{Q}_e$[W]	4.13 W – 21.60 W	–	24.4 %
$\dot{Q}_{tot}$ [W]	2.321 W – 58.558 W	5	44.9 %
		15	34.7 %
		25	34.5 %
		35	34.5 %
q_{HFS}[W/m^2]	0 W/m^2 - 4994 W/m^2	–	0% - 0.04%

Chapter 4

Model Development

In this chapter, four different types of models for prismatic lithium-ion battery are developed and discussed in detail. The first model is about a mathematical model for a lithium-ion battery based on experiments performed at different discharge rates and varying BCs using a neural network approach. The second model is an electrochemical thermal model for a large sized prismatic lithium-ion battery, and it is basically a Newman's Pseudo two dimensional (P2D) model. The third model is a turbulence model for mini channel cold plates using ANSYS Fluent. The fourth model is a battery degradation model based on actual drive cycles collected from an EV.

4.1 Model 1 : Battery Thermal Model

Here, a detailed mathematical model demonstrating the fundamental governing relationship between charge/discharge current, boundary conditions, and battery capacity (Ah) on the surface temperature prediction is presented. This model is estimated using a novel approach known as a neural network, which is trained by supervised learning. The proposed battery thermal model can be used for any kind of lithium-ion battery. The neural network architecture is shown in Figure 4.1.

4.1.1 Input and Output Training Data

- **Boundary Conditions (BCs) or Temperature**: The external temperature has a great effect on battery performance. Therefore, to increase the accuracy of the modeling, the BCs or temperature have been considered over the same time period and granularity as in the output. Here, the selected thermal boundary conditions or operating temperature are 5°C, 15°C, 25°C, 35°C (for water cooling), and 22°C (for air cooling).
- **Charge/Discharge Current:** This is basically the charge and discharge rate for the battery that is being discharged at a constant current. This rate basically increases the battery

surface temperatures as discharge progresses. The charge rate is 1C while the discharge rates are 1C, 2C, 3C, and 4C.

- **Battery Capacity (Ah):** The battery discharge capacity is measured over the entire time period which measures the capacity of the battery. This typically measures the discharge current multiplied by the time in hours over the entire discharge of the battery for the above mentioned discharge rates. The capacity is the time integral of the current and is calculated by:

$$C = \int_0^t (i)dt \tag{4.1}$$

- **Battery Surface Temperature:** The average surface temperature of the battery is simulated based on the target. The data is measured with a sampling period of 1 second over a time horizon of 24 hours.

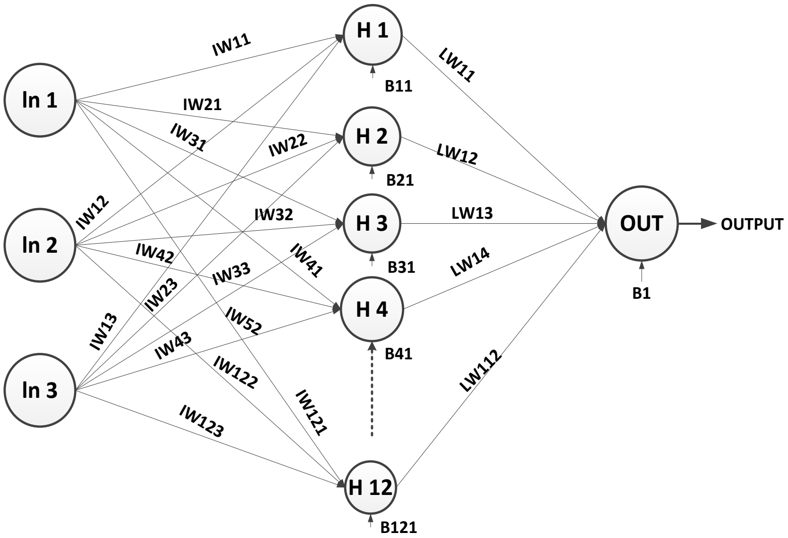

Figure 4.1: Neural network architecture for battery thermal model.

The output from the model is the simulated average temperature distributions on the principle surface of the battery. The same procedure was followed for the voltage simulations and the outputs are discussed in detail in the results and discussion section. The internal resistance is calculated by:

$$R_{int} = (V_{oc} - V_{act})/I_{dchg} \tag{4.2}$$

The model was trained by selecting the number of hidden neurons starting from one to twelve. There are three methods for training the algorithm: 1) the Levenberg-Marquardt Method; 2) the Bayesian Regularization Method; and 3) the Scaled Conjugate Gradient. For training the model, the Levenberg-Marquardt Method was selected. This algorithm typically takes more memory but less time. It automatically trains when generalization stops improving, as indicated by an increase in the mean square error (MSE) of the validation samples. As mentioned in the above paragraph, the model was trained several times, until the regression value (R) is close to one and the MSE is close to minimum. The R value close to one means a close relationship between outputs and targets.

The network performance plot is shown in Figure 4.2. It shows the MSE for all datasets on a logarithmic scale as a function of epoch, where epoch refers to the number of training trials. Validation and test performance are the points of interest, and the plot shows the iteration at which the validation performance function reaches minimum even as the training is continued for 6 more epochs. The best validation has been depicted in Figure 4.2, which corresponds to an MSE = 0.48955.

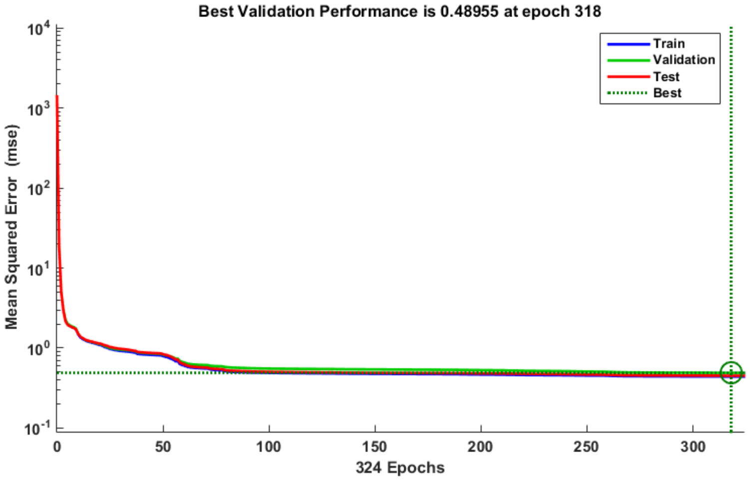

Figure 4.2: Neural network performance plot showing best validation.

The training state plot is shown in Figure 4.3. It comprises three subplots, the first of which is the backpropagation gradient expressed in logarithmic scale. It shows the gradient descent across the iterations and arrives at a gradient value of 0.21586 at epoch 324 where the training has stopped. The second subplot shows the scalar μ dynamics across the epochs, where μ corresponds to the scalar in the Levenberg-Marquardt algorithm at the update step. A small value of μ leads to Newton’s method, while a large μ leads to the gradient descent method. This scalar value is decreased when the performance function decreases, resulting in a faster and accurate Newton’s method. The value of μ increases when the performance function is expected to increase, thus switching to the gradient method as the minimum error is far. At the stopping condition, the scalar magnitude is 0.001. The third subplot shows the validation failure count. As can be seen at epoch 324, the stipulated count of the maximum number of validation fail is reached and the training has stopped.

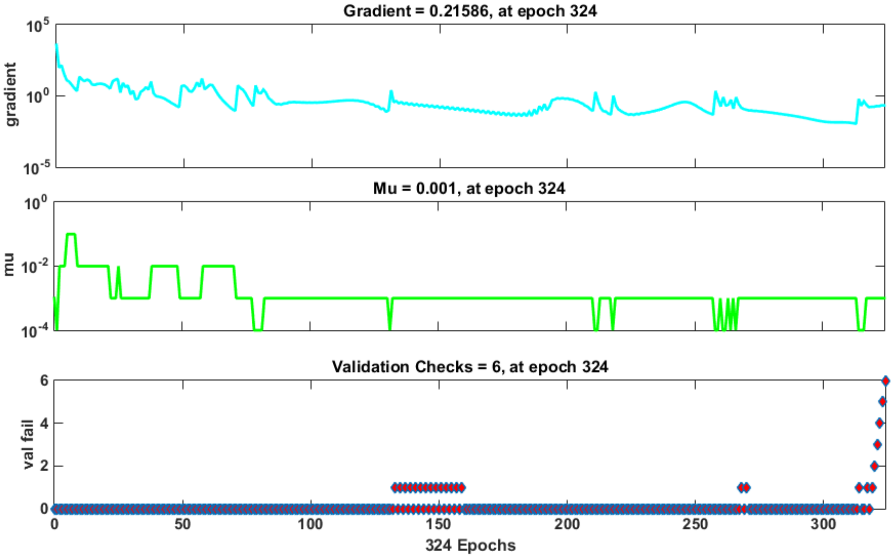

Figure 4.3: Training state plot comprises gradient, scalar μ, and validation check.

At the end of the training procedure, it is propagative to compare the actual model output with the target system output. In the study, a total of 117,344 samples obtained from experiments are considered, out of which 70% samples (82,141) were used for training the model. Also, 15% samples (17,601) were used for validation and, finally, 15% samples (17,601) were used for testing the model. These data should be sufficient for training, validation, and testing of the model. In order to unambiguously illustrate the fit, 1473 data points for 1C, 689 data points for 2C, 434 data points for 3C, and 373 data points for 4C are considered.

The neural network inherently subjects the trained model with test and validation datasets to evaluate its flexibility and outputs the best validation performance model. Randomness can be introduced into this model to visualize the model behavior under constrained random data. In this case, the model is subjected to uniformly distributed random in [0, 1] data at the input and the estimated target output obtained has been plotted. It is noted that with constrained random input data, i.e., noise, the neural network performance does not deteriorate and thus indicates a fair degree of robustness.

A histogram showing the difference between the actual and the target output is plotted in Figure 4.4 and, as noted, among the total samples considered, the majority of the errors lie in the range of -0.3823 to 0.5251.

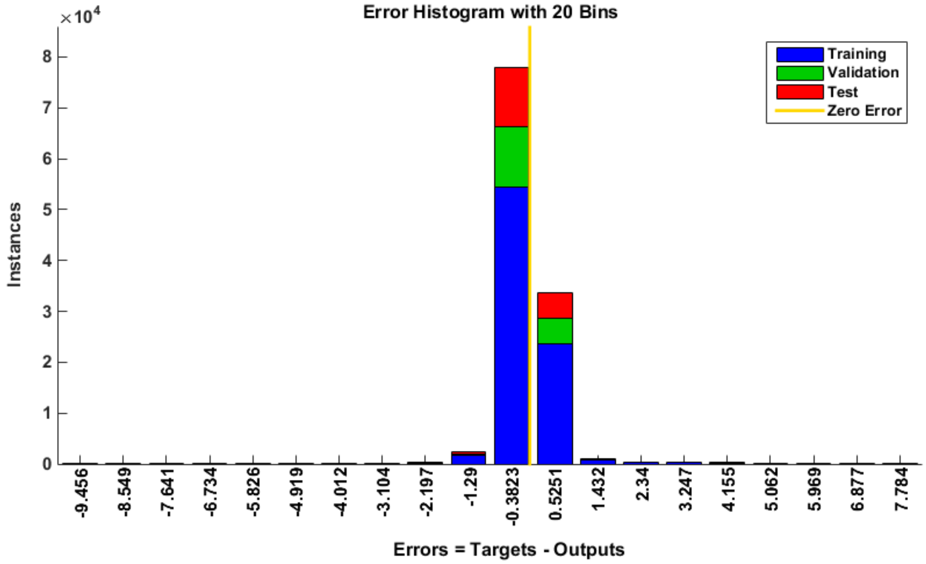

Figure 4.4: Error histogram showing the difference between the actual and the target output.

A regression plot is shown in Figure 4.5. It plots the regression relation between the actual output and the targets. The sampled output is essentially a binary signal in the sense that it has a fixed amplitude touching zero over few alternating sample sizes. The neural network reproduces this behavior in the actual output and in the process the network output lags as the target output slightly shifts at the end. When MSE is low, the model is better. The corresponding table for MSE, R, and R^2 for all outputs is shown in Table 4.1. The coefficient of determination (R^2) is the ratio between both the expected and total variations and is a measure of better observation. It is given by:

$$R^2 = \frac{Sum\ of\ expected\ variations}{sum\ of\ total\ variations} = \frac{\sum(\hat{Y}_i - \bar{Y})^2}{\sum(Y_i - \bar{Y})^2}, \tag{4.3}$$

where $\bar{Y}$ is the mean of all observations, $\hat{Y}_i$ is the estimated observation at time i and Y_i is the actual observations. The value of R^2 ranges from 0 to 1. The nearer the value of R^2 is to 1, the better the observations fit with the selected forecasting model.

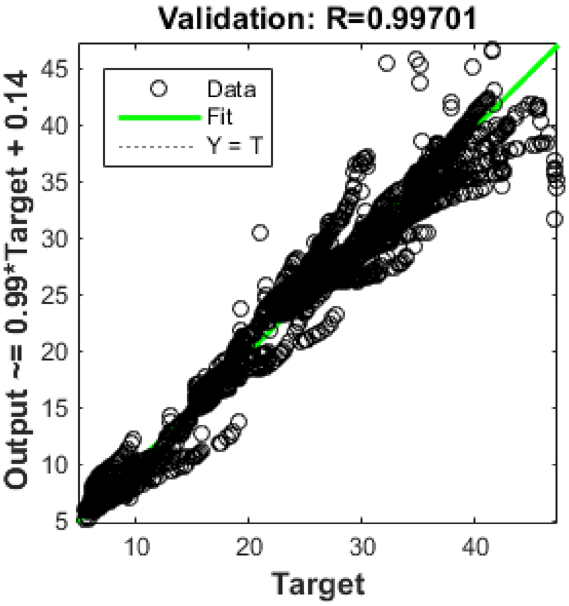

Figure 4.5: Regression plot showing regression relation between the actual output and the targets.

Table 4.1: Mean square error and regression.

Outputs	MSE	R	R^2
0	2.3524	0.9887	0.9776
1	1.6191	0.9922	0.9845
2	0.7937	0.9962	0.9924
3	0.8192	0.9961	0.9922
4	1.2981	0.9938	0.9876
5	0.5859	0.9972	0.9944
6	0.8319	0.9960	0.9920
7	0.4470	0.9978	0.9957
8	0.4236	0.9979	0.9959
9	0.3782	0.9982	0.9964
10	0.2738	0.9987	0.9974
11	0.4570	0.9978	0.9956
12	0.4655	0.9977	0.9955

4.1.2 Mathematical Functions of NN Model

In order to obtain a mathematical function of the average surface temperature of the battery, Γ from the trained NN, the output from each hidden layer neuron $H_k^1 \ to \ H_k^{12}$ is first determined. Here, the average surface temperature of a battery is a function of time (t), discharge/charge current (or Ah capacity) (θ_k) and boundary conditions (ξ_k), given by:

$$\Gamma = f\ (t, \theta_k, \xi_k\ ) \tag{4.4}$$

The incoming inputs with suitable weights $\omega_{i,j}\ \forall_i \in 1,\ldots, N_H, J \in 1,\ldots, N_I$, are summed up at each hidden layer neuron. Moreover, each hidden layer neuron has additional input, the bias $\beta_1 \ to \ \beta_{12}$, which is used in the network to generalize the solution and to avoid a zero value of the output, even when an input is zero. This summed signal is passed through an activation function (tansig) associated with each hidden layer neuron, which transforms the net weighted sum of all incoming signals into an output signal from the hidden layer neuron. $H_k^1 \ to \ H_k^{12}$ are given by:

$$H_k^1 = tansig(\omega_{1,1}\theta_k + \omega_{1,2}\,\xi_k + \omega_{1,3}\,t + \beta_1) \tag{4.5}$$

$$H_k^2 = tansig(\omega_{2,1}\theta_k + \omega_{2,2}\,\xi_k + \omega_{2,3}\,t + \beta_2) \tag{4.6}$$

$$H_k^3 = tansig(\omega_{3,1}\theta_k + \omega_{3,2}\,\xi_k + \omega_{3,3}\,t + \beta_3) \tag{4.7}$$

$$H_k^4 = tansig(\omega_{4,1}\theta_k + \omega_{4,2}\,\xi_k + \omega_{4,3}\,t + \beta_4) \tag{4.8}$$

$$H_k^5 = tansig(\omega_{5,1}\theta_k + \omega_{5,2}\,\xi_k + \omega_{5,3}\,t + \beta_5) \tag{4.9}$$

$$H_k^6 = tansig(\omega_{6,1}\theta_k + \omega_{6,2}\,\xi_k + \omega_{6,3}\,t + \beta_6) \tag{4.10}$$

$$H_k^7 = tansig(\omega_{7,1}\theta_k + \omega_{7,2}\,\xi_k + \omega_{7,3}\,t + \beta_7) \tag{4.11}$$

$$H_k^8 = tansig(\omega_{8,1}\theta_k + \omega_{8,2}\,\xi_k + \omega_{8,3}\,t + \beta_8) \tag{4.12}$$

$$H_k^9 = tansig(\omega_{9,1}\theta_k + \omega_{9,2}\,\xi_k + \omega_{9,3}\,t + \beta_9) \tag{4.13}$$

$$H_k^{10} = tansig(\omega_{10,1}\theta_k + \omega_{10,2}\,\xi_k + \omega_{10,3}\,t + \beta_{10}) \tag{4.14}$$

$$H_k^{11} = tansig(\omega_{11,1}\theta_k + \omega_{11,2}\,\xi_k + \omega_{11,3}\,t + \beta_{11}) \tag{4.15}$$

$$H_k^{12} = tansig(\omega_{12,1}\theta_k + \omega_{12,2}\,\xi_k + \omega_{12,3}\,t + \beta_{12}) \tag{4.16}$$

The weight matrix connecting the input layer neurons to the hidden layer neurons, i.e. $\omega_{i,j}\ \forall_i \in 1,\ldots, N_H, J \in 1,\ldots, N_I$ is given by:

$$\omega_{i,j} = \begin{bmatrix} 0.0880 & 1.6015 & 0.3962 \\ -1.9281 & -16.1589 & 0.4249 \\ -0.9256 & 0.3153 & -0.2344 \\ -0.7129 & -4.1500 & 4.4583 \\ 0.8469 & -0.3717 & 0.3060 \\ 6.9040 & 21.0847 & -3.9349 \\ 3.7381 & -0.3359 & -0.3849 \\ -8.0748 & -11.7963 & -9.8208 \\ 1.8059 & 0.9240 & -3.6318 \\ 5.3002 & -0.3394 & -0.3483 \\ -0.0341 & -0.9251 & 0.9361 \\ -0.6990 & -3.7963 & 4.2202 \end{bmatrix} \tag{4.17}$$

The bias β_i $\forall_i \in 1,\ldots, N_H$, associated with each hidden layer neuron, is given by:

$$\beta_i = [-0.8333 \;\; -14.4060 \;\; 0.0762 \;\; -6.9389 \;\; 0.0146 \;\; 10.6084 \;\; 1.2144 \;\; -4.9179 \;\; 3.7398 \;\; 1.7859 \;\; 1.5864 \;\; -6.5392]^T \tag{4.18}$$

Finally, Γ can be obtained from the output neuron of the trained NN by:

$$\Gamma = purelin\,(H_k^1\, W_{1,1} + H_k^2\, W_{1,2} + H_k^3\, W_{1,3} + H_k^4\, W_{1,4} + H_k^5\, W_{1,5} + H_k^6\, W_{1,6} + H_k^7\, W_{1,7} + H_k^8\, W_{1,8} + H_k^9\, W_{1,9} + H_k^{10}\, W_{1,10} + H_k^{11}\, W_{1,11} + H_k^{12}\, W_{1,12} + \mu) \tag{4.19}$$

where $purelin$ is a linear transfer function available in MATLAB. The weight matrix connecting the hidden layer neurons with the single output neuron $W_{i,l}$ $\forall_i \in 1,\ldots, N_H$, $l \in 1,\ldots, N_o$ is given by:

$$W_{i,l} = [0.2020 \;\; 0.5385 \;\; -5.4995 \;\; 7.0429 \;\; -4.9519 \;\; -0.0193 \;\; -5.7628 \;\; -0.0096 \;\; -0.1831 \;\; 5.7932 \;\; 0.5029 \;\; -7.7780] \tag{4.20}$$

The bias associated with the output layer neuron is given by:

$$\mu = -\,0.2929 \tag{4.21}$$

4.2 Model 2 : Electrochemical Thermal (ECT) Model

This section describes a coupled electrochemical-thermal model for a commercial 20 Ah prismatic cell that considers all the electrochemical-geometrical details of the cell. This model is basically a Newman's pseudo two dimensional (P2D) for a large sized prismatic lithium-ion battery. In this model, the physics-based two-dimensional electrochemical models are combined with the charge conservation and heat diffusion equations throughout the battery domain in order to calculate the temperature distributions. The governing equations and boundary conditions, along with the parameters used for the model development and material properties, are presented. The utilized physics-based two-dimensional models accurately predict the behavior of the negative and positive electrodes considering the material phase-change inside the active electrode particles and the particle-size distribution observed in scanning electron microscope (SEM) images of electrodes. This approach provides the opportunity of precisely studying even the particle-level phenomena effects on the prismatic cell electrochemical-thermal behaviors. The developed model for the 20 Ah prismatic battery cell is compared against the experimental data for the temperature distribution on the surface of the prismatic cell during discharge at 2C, 3C, and 4C. Good agreement between the simulation results and experimental data shows that the approach utilized in this section can also be implemented for the other battery materials and geometries.

4.2.1 Model Development

The Newman pseudo-two dimensional (P2D) model, initially presented by Doyle at el. [40, 148] and utilized by different researchers [202, 203], separates the battery into the particle and electrode domains. In the particle domain, the conservation of lithium is solved. The particles are usually considered to be spherical and Fick's law governs the particle lithium diffusion. In the electrode domain, the conservation of charge in the solid-phase and electrolyte, as well as the conservation of mass in the electrolyte, is solved. This model, based on the principles of transport phenomena, electrochemistry, and thermodynamics, is introduced by couples nonlinear partial differential equation (PDEs) in x, r, and t that can take from a second to a minute for simulation. This model expands on the ohmic porous-electrode model by including diffusion in electrolyte and solid phases, as well as Butler-Volmer kinetics. Doyle created a P2D model based on a concentrated solution theory to describe the internal behavior of a lithium-ion sandwich consisting of positive

(+) and negative (-) electrodes, a separator and current collector. This physics-based model is by far the most used by battery researchers and solves for the electrolyte concentration, electrolyte potential, solid state potential, and solid state concentration within the porous electrodes and electrolyte concentration, and electrolyte potential within the separator. A large sized 20 Ah-$LiFePO_4$ battery is used to verify the model results. The geometry of the battery is shown in Figure 4.6 and the actual cell is presented in Figure 3.1.

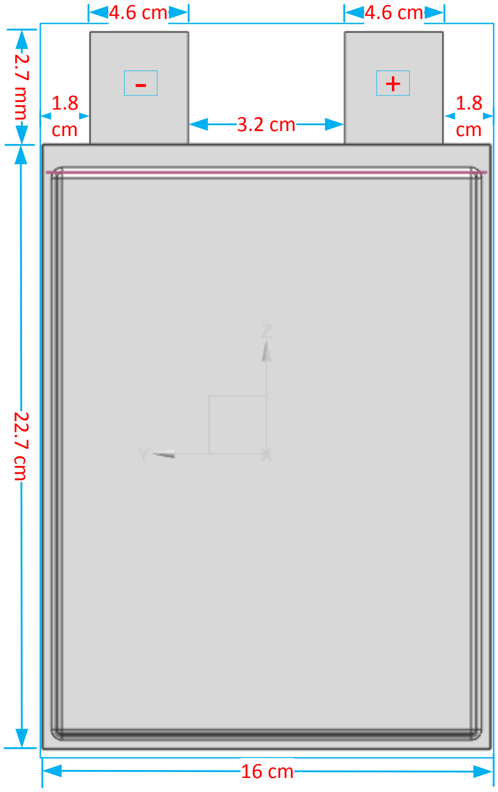

Figure 4.6: Lithium-ion prismatic cell geometry for ECT model.

The current collecting tabs of the prismatic battery cell are also considered and the dimensions of the battery cell along with tabs also appears in Figure 4.6. The studied prismatic cell includes a number of individual cells connected in parallel. Each cell contains a negative electrode, a separator, and a positive electrode, surrounded on either side by the current collectors. In the prismatic cell studied in this model, the negative and positive electrodes active materials are made from graphite and $LiFePO_4$, respectively. Copper is used as the negative current collector and aluminum as the positive current collector. This cell includes 48 individual cells, resulting in a 20 Ah nominal capacity. In order to decrease the material demand and reduce the electrical losses, current collectors are covered by electrode materials on both sides. Therefore, the number of aluminum current collectors for 48 cells is 24, while there are 25 copper collectors since copper collectors are on each end of the stack. All the layers are then enclosed in a separator sheet and a casing covers all. Figure 4.7 is a schematic diagram of lithium-ion battery cell configuration for the pseudo-two dimensional multi-particle model [154].

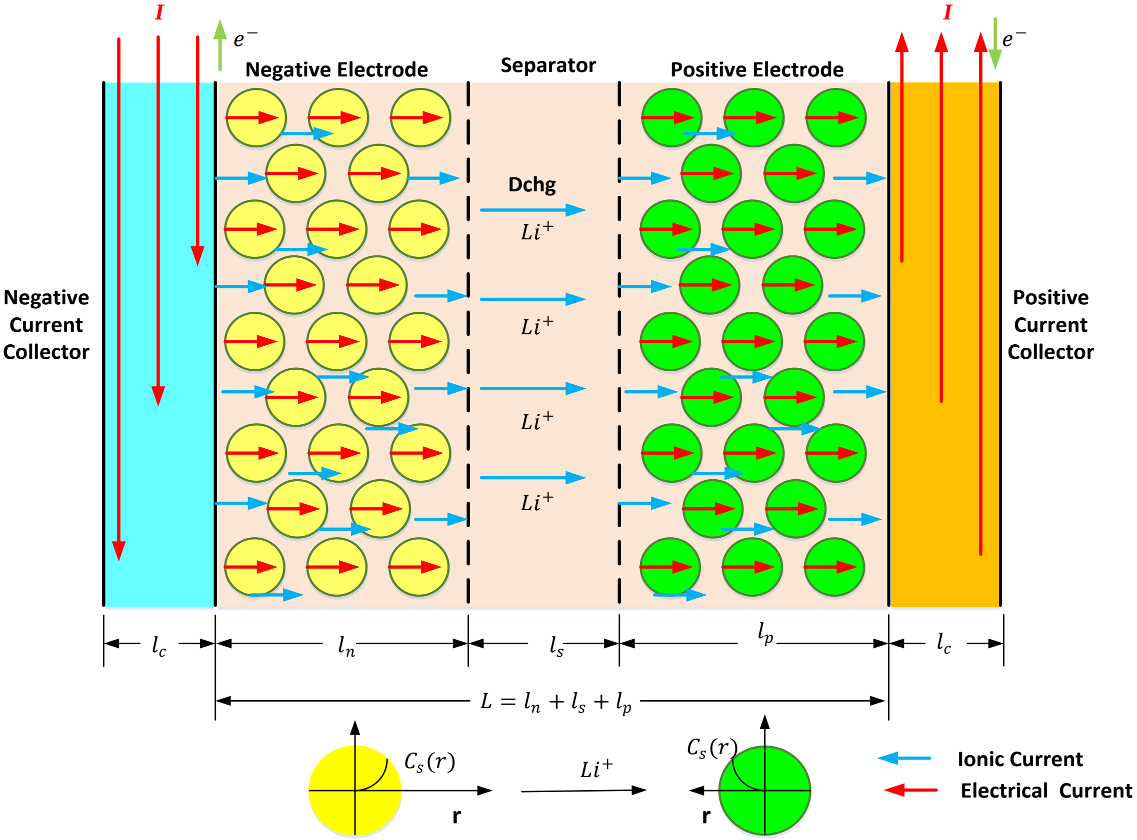

Figure 4.7: Schematic diagram of lithium-ion battery cell configuration for the pseudo-two dimensional multi-particle model (modified from [154]).

During the discharge process, Lithium diffuses to the surface of the negative-electrode particles and undergoes an electrochemical reaction. This reaction releases an electron and transfers lithium to the electrolyte phase. The lithium ions diffuse and conduct through the electrolyte solution to the positive electrode, where a similar reaction transfers lithium to the positive solid phase. Lithium is stored inside the positive electrode particles until the cell is later recharged. The lithium-ion transport phenomena in the porous electrode and active particle material can be described by the charge and mass conservation laws. Charge conservation governs the electrolyte phase potential and the solid phase potential, $\emptyset_e$ and $\emptyset_s$, while mass conservation governs the electrolyte phase concentration and the solid phase concentration, C_e and C_s.

4.2.2 Governing Equations and Boundary Conditions

In this section, all governing equations for charge conservation in solid phase, charge conservation in electrolyte phase, lithium conservation in solid phase, lithium conservation in electrolyte phase, and the Butler-Volmer equation are described with their boundary conditions.

4.2.2.1 Charge conservation in solid phase

The charge conservation equation in the solid electrode material is governed by Ohm's law [151, 204]:

$$\nabla(\sigma^{eff}\,\nabla\emptyset_s) - j^{Li} = 0 \tag{4.22}$$

in other words,

$$\frac{\partial}{\partial x}\left(\sigma^{eff}\,\frac{\partial\emptyset_s}{\partial x}\right) = j^{Li} \tag{4.23}$$

$$-\sigma_{-}{}^{eff}\left(\frac{\partial\emptyset_s}{\partial x}\right)_{x=0} = \frac{I}{A} \quad \text{and} \quad +\sigma_{+}{}^{eff}\left(\frac{\partial\emptyset_s}{\partial x}\right)_{x=L} = \frac{I}{A} \tag{4.24}$$

$$\left(\frac{\partial\emptyset_s}{\partial x}\right)_{x=l_n} = 0 \quad \text{and} \quad \left(\frac{\partial\emptyset_s}{\partial x}\right)_{x=l_n+l_s} = 0 \tag{4.25}$$

where σ^{eff} is the effective conductivity of the solid phase. j^{Li} is the transfer current resulting from Lithium insertion/de-insertion at the electrode/electrolyte interface. σ_+ and σ_- are effective electrical conductivity for the positive and negative electrodes. $\emptyset_+$ and $\emptyset_-$ are the phase potential positive and negative electrodes. l_n is the length of the negative electrode, l_s is the length of the separator, l_p is the length of the positive electrode. $L = l_n + l_s + l_p$ is the overall length.

4.2.2.2 Charge conservation in electrolyte phase

The charge conservation in the electrolyte solution is expressed as [151, 204]:

$$\nabla(k^{eff}\nabla\emptyset_e) + \nabla\left(k_D^{eff}\nabla\ln c_e\right) + j^{Li} = 0 \tag{4.26}$$

in other words,

$$\frac{\partial}{\partial x}\left(k^{eff}\,\frac{\partial\emptyset_e}{\partial x}\right)+\frac{\partial}{\partial x}\left(k_D^{eff}\,\frac{\partial\ln c_e}{\partial x}\right)=-\,j^{Li} \qquad (4.27)$$

$$\left(\frac{\partial\emptyset_e}{\partial x}\right)_{x=0}=0 \qquad \text{and} \qquad \left(\frac{\partial\emptyset_e}{\partial x}\right)_{x=L}=0 \qquad (4.28)$$

where k^{eff} is the effective diffusional conductivity called the Burggeman relation and is given by $k^{eff}=k{\epsilon_e}^{\beta}$, where β is the Burggeman porosity exponent. ${k_D}^{eff}$ is the effective ionic conductivity, given by:

$$ {k_D}^{eff}=\frac{2RTk^{eff}}{F}\,({t_+}^0-1)\left(1+\frac{d\ln f_{\pm}}{d\ln C_e}\right) \qquad (4.29)$$

where $f_{\pm}$ is the molecular activity coefficient of the electrolyte, also called the electrolyte activity coefficient. ϵ_e is the volume fraction of the electrolyte phase in the electrode, R is the universal gas constant with a value of 8.3143 kJ/kg mole. K. F is the Faraday's constant and its value is 96485 Columb/mole. ${t_+}^0$ is the transfer number of lithium-ion. C_e is the concentration of lithium in the electrolyte phase.

4.2.2.3 Lithium conservation in solid phase (Phase transition and ion transport)

The material balance for lithium ions in an active solid material particle is governed by Fick's second law in spherical coordinate [151, 205]:

$$\frac{\partial C_s}{\partial t}-\frac{D_s}{r^2}\frac{\partial}{\partial r}\left(r^2\frac{\partial C_s}{\partial r}\right)=0 \qquad (4.30)$$

with boundary conditions:

$$D_s\left(\frac{\partial C_s}{\partial r}\right)_{r=0}=0 \qquad \text{and} \qquad -D_s\left(\frac{\partial C_s}{\partial r}\right)_{r=R_s}=\frac{j^{Li}}{a_sF} \qquad (4.31)$$

where C_s is the concentration of lithium in solid phase. D_s is the mass diffusion coefficient of lithium-ion in the electrolyte, r is the radial coordinate along the active material particle, R_s is the radius of the solid active material particle, j^{Li} is the transfer current resulting from Lithium insertion/de-insertion at the electrode/electrolyte interface, which consumes/generates the species Li$^+$,

$$j^{Li} = a_s i_o \begin{cases} a_{s,a}\, i_{n,a} \\ 0 \\ a_{s,c}\, i_{n,c} \end{cases} \text{in the anode, separator and cathode} \tag{4.32}$$

4.2.2.4 Lithium conservation in electrolyte phase

The lithium-ion balance in the liquid phase is described as follows [151]:

$$\frac{\partial(\epsilon_e\, c_e)C_s}{\partial t} - \nabla\left(D_e{}^{eff}\nabla\, c_e\right) - \frac{1 - t_+{}^0}{F} j^{Li} + \frac{i_e\, \nabla t_+}{F} = 0 \tag{4.33}$$

in other words,

$$\frac{\partial(\epsilon_e\, c_e)C_s}{\partial t} = \frac{\partial}{\partial x}\left(D_e{}^{eff}\frac{\partial C_e}{\partial x}\right) + \frac{1 - t_+{}^0}{F} j^{Li} + \frac{i_e\, \nabla t_+}{F} \tag{4.34}$$

$$\left(\frac{\partial C_e}{\partial x}\right)_{x=0} = 0 \quad \text{and} \quad \left(\frac{\partial C_e}{\partial x}\right)_{x=L} = 0 \tag{4.35}$$

where ϵ_e is the volume fraction/porosity of the electrolyte, $D_e{}^{eff}$ is the effective diffusion coefficient (Burggeman relation, $D_e{}^{eff} = D_e \epsilon_e{}^{\beta}$), $t_+{}^0$ is the transfer number of Li$^+$ with respect to the velocity of the solvent (a function of electrolyte concentration, if assuming constant, $\frac{i_e\, \nabla t_+}{F} = 0$). Also, ϵ_s is the volume fraction of solid particle (active material) in the electrode. ϵ_f is the volume fraction of filler material in the electrode.

4.2.2.5 Electrochemical Kinetics: Reaction Rate (Butler-Volmer Equation)

The electrochemical reaction rate on the surface of electrode particles is usually governed by the Butler-Volmer equation [154, 156, 158]; i.e the Butler-Volmer equation is used to couple a charge-species governing equation and is given by:

$$j^{Li} = a_s i_o \left\{\exp\left[\frac{\propto_a F}{R\, T}\, \eta\right] - \exp\left[\frac{\propto_c F}{R\, T}\, \eta\right]\right\} \tag{4.36}$$

where η is the local surface over potential which is given by [172]:

$$\eta = \emptyset_s - \emptyset_e - U \tag{4.37}$$

and the exchange current density is given by [204]:

$$i_0 = k_m(C_e)^{\propto_a}(C_{s,max} - C_{s,e})^{\propto_a}(C_{s,e})^{\propto_c} \tag{4.38}$$

where a_s is the active surface area per electrode unit volume for electron transfer reactions (1/cm), i_0 is the exchange current density (a function of lithium concentrations in both electrolyte and solid active materials), $\propto_a$ is the transfer coefficient of the anode, T is the temperature (K), η is the over potential (V), $\propto_c$ is the transfer coefficient of the cathode, U is thermodynamics OCV, $C_{s,max}$ is the maximum concentration of lithium in solid phase and $C_{s,e}$ is the concentration of lithium at the surface of solid particles, and $\emptyset_s$ and $\emptyset_e$ are the phase potential for solid and electrolyte phase.

For coupling the model, temperature dependent physicochemical properties, such as diffusion coefficient (D_s) and ionic conductivity of an electrolyte (k) are needed and dependence can be generally described by Arrhenius Equation [204]:

$$D_s = D_{s,ref} \exp\left[\frac{-E_d}{R\left(\frac{1}{T} - \frac{1}{T_{ref}}\right)}\right] \tag{4.39}$$

$$k_m = k_{m,ref} \exp\left[\frac{-E_r}{R\left(\frac{1}{T} - \frac{1}{T_{ref}}\right)}\right] \tag{4.40}$$

also diffusion coefficient in electrolyte phase, D_e, is given by:

$${D_e}^{eff} = D_e {\epsilon_e}^{\beta} \tag{4.41}$$

$$a_s = 3\,\frac{\epsilon_s}{r_s} \tag{4.42}$$

where a_s is the solid/electrolyte interfacial area per unit volume, D_s is the diffusion coefficient in solid phase, $D_{s,ref}$ is the reference solid diffusion coefficient, $k_{m,ref}$ is the reference reaction rate coefficient, D_e is the diffusion coefficient in the electrolyte phase, E_d is the activation energy that controls temperature sensitivity of $\mathrm{D_s}$, E_r is the activation energy that controls the temperature sensitivity of k_m, and T_{ref} is the reference temperature = 298 K.

4.2.3 Energy Equation

The energy balance equation is given by [151]:

$$\nabla^2 T + \frac{\dot{q}}{k} = \frac{1}{\alpha}\frac{\partial T}{\partial t} \tag{4.43}$$

in other words,

$$\frac{\partial^2 T}{\partial x^2} + \frac{\partial^2 T}{\partial y^2} + \frac{\partial^2 T}{\partial z^2} + \frac{\dot{q}}{k} = \frac{1}{\alpha}\frac{\partial T}{\partial t} \tag{4.44}$$

The above equation is further modified to

$$\dot{q} = \frac{\partial(\rho c_p T)}{\partial t} - \nabla\,(k\,\nabla T) \tag{4.45}$$

also,

$$\nabla\left(\sigma_+ \nabla_{\emptyset_+}\right) = -\,j \tag{4.46}$$

$$\nabla\left(\sigma_- \nabla_{\emptyset_-}\right) = +\,j \tag{4.47}$$

$$\dot{q} = \left(\sigma_+\,\nabla^2{}_{\emptyset_+}\right) + \left(\sigma_-\,\nabla^2{}_{\emptyset_-}\right) + \dot{q}_{ECH} \tag{4.48}$$

where $\dot{q}_{ECH}$ is the electro chemical heat and is given by [151]:

$$\dot{q}_{ECH} = \frac{i_p(\emptyset_+ - \emptyset_-) + \left(\sigma_-\,\nabla^2{}_{\emptyset_-}\right) + \int_0^L j^{Li}\left(T_{ref}\frac{\partial U}{\partial t} - U_{ref}\right)dx}{L} \tag{4.49}$$

also,

$$i_p = \int_0^{l_p} j^{Li}\,dx \tag{4.50}$$

$$j = -\,a\,i_p \tag{4.51}$$

where $\dot{q}$ is the heat generation rate during battery operation which includes joule heating, electrochemical reaction heating and entropic heating, ρ is the density, c_p is the specific heat. The parameters used for the modeling are shown in Table 4.2.

Table 4.2: Parameters used in the 2D Model [151, 152, 45, 154, 206, 155, 207, 208].

Parameter	Notation	Value	Unit
Thickness of +ve electrode	l_p	183	µm
Thickness of separator	l_s	52	µm
Thickness of -ve electrode	l_n	100	µm
Particle radius for +ve electrode	$R_{s,p}$	1.6e-05/2	µm
Particle radius for -ve electrode	$R_{s,n}$	2.5e-05/2	µm
Maximum solid Li^+ Concentration for +ve electrode	$C_{s,p,max}$	22806	mol/m^3
Maximum solid Li^+ Concentration for -ve electrode	$C_{s,n,max}$	31370	mol/m^3
Initial solid Li^+ concentration for +ve electrode	$C_{s,p,0}$	3886.2	mol/m^3
Initial solid Li^+ concentration for -ve electrode	$C_{s,n,0}$	14870.76	mol/m^3
Initial electrolyte Li^+ concentration for +ve electrode	C_o	2000	mol/m^3
Initial electrolyte Li^+ concentration for -ve electrode	C_o	2000	mol/m^3
Initial electrolyte Li^+ concentration for separator	C_o	2000	mol/m^3
Volume fraction for +ve electrode	ϵ_p	0.444	-
Volume fraction for -ve electrode	ϵ_n	0.357	-
Volume fraction for separator	ϵ_s	1	-
Filler fraction for +ve electrode	$\epsilon_{f,p}$	0.259	-
Filler fraction for -ve electrode	$\epsilon_{f,n}$	0.172	-
Reference diffusivity for +ve electrode	$D_{s,p}$	1e-13	m^2/s
Reference diffusivity for -ve electrode	$D_{s,n}$	3.9e-14	m^2/s

Activation energy for +ve electrode	$E_{d,p}$	8.6e4	
Activation energy for -ve electrode	$E_{d,n}$	2e4	
Conductivity for +ve electrode	σ_p	3.8	S/m
Conductivity for -ve electrode	σ_n	100	S/m
Reference rate constant for +ve electrode	k_p	2.072818e-11	mol/m^{2}s/(mol/m^3)$^{1.5}$
Reference rate constant for -ve electrode	k_n	2.072818e-11	mol/m^{2}s/(mol/m^3)$^{1.5}$
Activation energy for +ve electrode	$E_{r,p}$	9e3	
Activation energy for -ve electrode	$E_{r,n}$	2e4	
Electrolyte diffusivity for +ve electrode	D_e	7.5e-11	m^2/s
t_+ factor for +ve electrode	t_+	0.363	-
Nominal capacity of cell	C	20	Ah
Minimum stop voltage	V_{min}	2.0	V
Maximum stop voltage	V_{max}	4.1	V
Reference temperature	T_{ref}	298	K
Universal gas constant	R	8.3143	kJ/kg mole K
Faraday's constant	F	96485	Columb/mole

The material properties are also presented in Table 4.3. These properties are used in the simulation.

Table 4.3: Material Properties used in the simulation [151, 152, 207].

Property	Symbol	Value	Unit
Density for positive tab	ρ_p	2719	kg/m^3
Density for negative tab	ρ_n	8978	kg/m^3
Density for active zone	ρ_a	2092	kg/m^3
Specific heat for positive tab	$C_{p,p}$	871	J/kg-K
Specific heat for negative tab	$C_{p,n}$	381	J/kg-K
Specific heat for active zone	$C_{p,a}$	678	J/kg-K
Thermal conductivity for positive tab	K_p	202	W/m-K
Thermal conductivity for negative tab	K_n	387.6	W/m-K
Thermal conductivity for active zone	K_a	18.2	W/m-K

4.3 Model 3: Numerical Model for Mini Channel Cold Plates

In this section, ANSYS CFD modeling for mini-channel cold plates placed on the top and bottom of a large sized prismatic $LiFePO_4$ lithium-ion battery is presented along with governing equations, geometry created in ICEM-CFD, boundary conditions, meshing, and finally grid independence study. The results obtained from simulation are also compared with experimental data. This kind of study provides an insight into improvement of design of cold plates for thermal management of a lithium-ion battery pack for automotive applications.

4.3.1 Governing Equations

The flow in this study is turbulent. Although analytical solutions for these flows are not accurate, on the basis of the continuum fluid assumption, the dynamics of turbulence is adequately described by the continuity and Navier-Stokes equations. The solutions of the Navier-Stokes equations are solved numerically. The solution is implemented by generating a mesh of the region of interest or domain. The governing equations are then discretized yielding a system of algebraic equations which can be solved at each point within the domain. In this section, the goal of this CFD study is to obtain trends that can be validated with the experimental measurements. In addition, because the experimental technique obtained only point-wise data, the CFD technique provides the whole field and comprehensive data to complement the experimental data.

As previously mentioned, the water flow in the cold plates is turbulent and therefore the flow is modeled using the Reynolds-Averaged Navier-Stokes Equations (RANS·). Since the temperature field is also of interest, the Reynolds-Averaged Energy equation is also solved. The governing equations are:

$$\nabla \cdot \vec{V} = 0 \tag{4.52}$$

$$\rho \left[\frac{\partial \bar{V}}{\partial t} + \left(\vec{V} \cdot \nabla \bar{V} \right) \right] = -\nabla \bar{p} + \left(\mu \nabla^2 \bar{V} - \lambda \right) \tag{4.53}$$

$$\frac{\partial \rho \bar{T}}{\partial t} + \rho \overrightarrow{V} \nabla T = \nabla \cdot \left[\left(\frac{\mu}{Pr} + \frac{\mu_t}{Pr_t} \right) \nabla \bar{T} \right] \tag{4.54}$$

where ∇ is the gradient operator, $\bar{V}$ is the average velocity (m/s), V is the speed (m/s), ρ is the density (kg/m^3), P is the pressure (Pa), μ is the viscosity (Pas), λ is the gradient of Reynold's stress, Pr is the Prandtl number, and Pr_t is the turbulent Prandtl number.

Since the flow in the problem is assumed to be turbulent, an appropriate turbulence model is required. In this study, the standard k-ε turbulence model was used, given the robustness of the model, reasonable accuracy for a wide range of flows and its proven capability in heat transfer and flow analysis. The equations in ANSYS Fluent for turbulent kinetic energy and rate of dissipation are as shown below [204]:

$$\frac{\partial \rho k}{\partial t} + \nabla * \left[\rho \vec{V} k\right] = \nabla * \left[\left(\mu + \frac{\mu_t}{\sigma_k}\right)\nabla k\right] + G_k + G_b - \rho\varepsilon - Y_M + S_k \tag{4.55}$$

$$\frac{\partial \rho \varepsilon}{\partial t} + \nabla * \left[\rho \vec{V} \varepsilon\right] = \nabla * \left[\left(\mu + \frac{\mu_t}{\varepsilon_k}\right)\nabla \varepsilon\right] + C_{1\varepsilon}\frac{\varepsilon}{k}(G_k + C_{3\varepsilon}G_b) - C_{2\varepsilon}\,\rho\,\frac{\varepsilon^2}{k} + S_\varepsilon \tag{4.56}$$

where $C_{1\varepsilon}$, $C_{2\varepsilon}$, $C_{3\varepsilon}$ are the model constants, σ_k and ε_k are the turbulent Prandtl numbers for k and ε. G_k represents the generation of turbulence kinetic energy due to the mean velocity gradients, G_b is the generation of turbulence kinetic energy due to buoyancy. Y_M represents the contribution of the fluctuating dilatation in compressible turbulence to the overall dissipation rate. S_k and S_ε are user-defined source terms. The turbulent (or eddy) viscosity is computed by combining k and ε as follows:

$$\mu_t = C_\mu\,\rho\,\frac{k^2}{\varepsilon} \tag{4.57}$$

where C_μ is a constant. The ANSYS Fluent was used in this study because of its flexibility and availability. Starting from an initial condition, the solution strides towards a steady-state. Convergence was judged against the normalized continuity, momentum and energy residuals and is considered converged when these residuals have been reduced to 1×10^{-6}.

4.3.2 Geometry and Boundary Conditions

The full geometry, with the top and bottom cold plates along with lithium-ion battery in NX 8.5, is depicted in Figure 4.8.

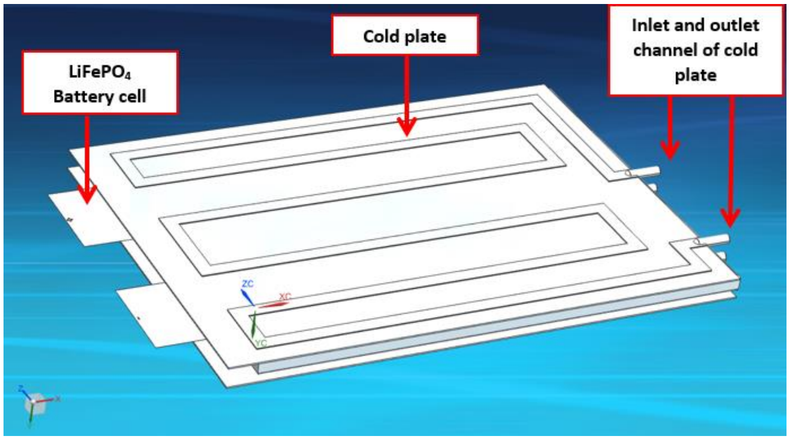

Figure 4.8: Top and bottom cold plate with lithium-ion battery in NX 8.5.

In a CFD simulation, the term "wall" refers to any solid surface that the flow cannot penetrate and thus includes the walls, floor, ceiling, and surfaces of the test battery.

The following parameters are selected for model development:

1) Viscous model: R_e = 8.7 x 10^3. The wall distance was 1.1 x 10^{-4}. C_1= 1.44, C_2 = 1.92, TKE Prandtl number =1, TDR Prandtl number =1.3, Energy Prandtl number =0.85, Wall Prandtl number =0.85.
2) In the turbulent specification method: Turbulent intensity of 5%, and turbulent viscosity ratio of 10.
3) Solver: Type: pressure based; Time: steady state; Velocity formulation: absolute velocity
4) Residuals convergence variables: X-velocity, Y-velocity, Z-velocity, energy, k-epsilon, continuity equation.
5) wall treatment (y^+=5)
6) Number of elements: approximately 20 million
7) Method for meshing: unstructured tetrahedral with prism wall layers
8) Convergent criteria: 0.000001 residuals
9) 1st or 2nd order: 2nd order
10) Type of flow: turbulent

Prism meshing parameters:

1) Growth law: exponential; Initial height: 0.1; Height ratio: 1.1; Number of layers: 3; Total height: 0.331; Minimum prism quality: 0.0099999998; Ortho weight: 0.50; Fillet ratio: 0.1

Global mesh size:

1) Global element scale factor: 1; Global element seed size: 1; Curvature/proximity based refinement minimum size limit: 1.

Assumption:

1) Symmetry about the center of the battery, and 2) adiabat on outside the surface of the cooling plate

Different turbulence models in ANSYS Fluent were used to simulate the above flow conditions to obtain the reattachment lengths using the experimental results for validation. In order to have a good agreement between the numerical results and experimental data, it was ensured that the computational domain is sufficiently long. The flow was considered incompressible, steady state and turbulent. Water was chosen as the working fluid with a density of 998.2 kg/m^3 and dynamic viscosity of 1.002 x 10^{-3} N s/m^2. The computational grid consists of around 20 million elements. A uniform free stream velocity inlet boundary condition for incompressible flow was applied upstream of the step. Average velocity was applied at the inlet using a derived relation valid for channel flows. The inlet and outlet boundary conditions were set based on the turbulent intensity and turbulent length scale. A turbulent intensity of 5%, to be consistent with the value obtained by the experimental study, was used. The velocity was 0.5784 m/s. The pressure outlet boundary condition was applied at the outflow plane, which was positioned far downstream of the step to reduce the influence of the outflow conditions and on all other surfaces the no-slip boundary condition was applied. The RANS models available in ANSYS Fluent were used with enhanced wall treatment (y^+=1) as the near wall function.

4.3.3 Mesh Generation

The meshing of the domain is a very important step since various meshing parameters, such as the number of nodes and the shape of the elements, have a significant impact on the accuracy of the results and the numerical behavior of the solution. A fine unstructured tetrahedral mesh was generated using ANSYS ICEM to resolve all flow features of interest. The mesh resolution at various locations within the geometry is shown in Figure 4.9. This meshing is at the inlet and the outlet channels of the cold plates placed on the top and bottom of the lithium-ion battery cell. The overall meshing generated in a small portion of channel is shown in Figure 4.10. It shows the meshing in the inlet channel to the cold plate along with battery surface.

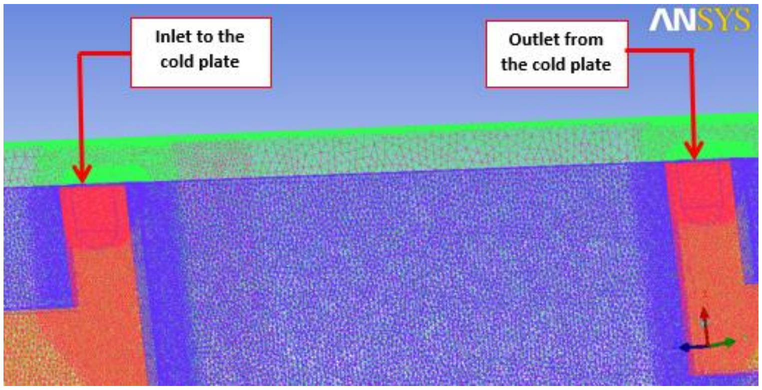

Figure 4.9: Inlet and outlet channel with meshing of cold plate in ICEM-CFD.

The flow along the various surfaces in the space is resolved by using a finer mesh size around those obstacles while the boundary layers along all surfaces are resolved by clustering 3 layers of prismatic elements near the walls. The prismatic layers are also adjusted such that the first node is 0.1 mm away from the wall. This wall node spacing yields a dimensionless wall distance of y^+ ~1, where y^+ was chosen to be 5. This value is consistent with the recommended value for near wall flows while being closer to acceptable values for the standard k-ε turbulence model. It trades off extreme resolution with lower y^+ values while still maintaining some approximation of the boundary layer. Using the recommended values of $y^+ \geq 30$ resulted in the first layer thickness being larger than the channel height itself, thus necessitating compromises.

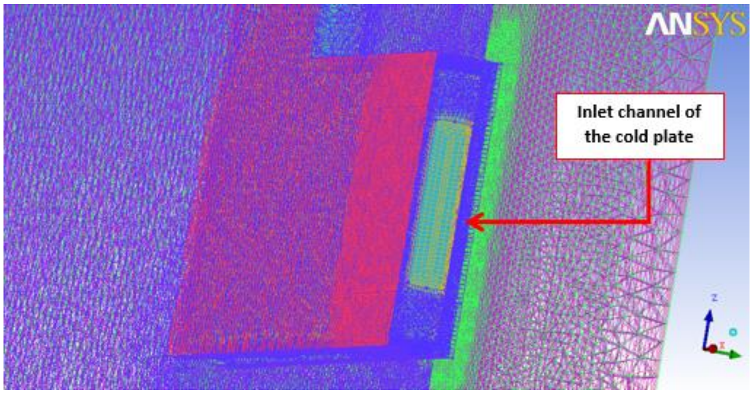

Figure 4.10: Meshing in small portion of channel in ICEM-CFD.

The total number of elements used for the mesh is approximately 20 million. It was ensured that the numerical results are mesh independent by conducting grid independence tests. A negligible effect in the reattachment points was observed for mesh elements greater than 10 million. It was assured that the numerical residuals were in the order of magnitude 10^{-6} and solution was considered converged as numerical residuals reached the convergence criteria. The solution did not significantly change after this criteria was achieved. The analysis was also performed at different planes in the channel. Figure 4.11 shows the vertical planes within the cold plates for CFD analysis, where 1 is inlet to the cold plate and 4 is the outlet from the cold plate.

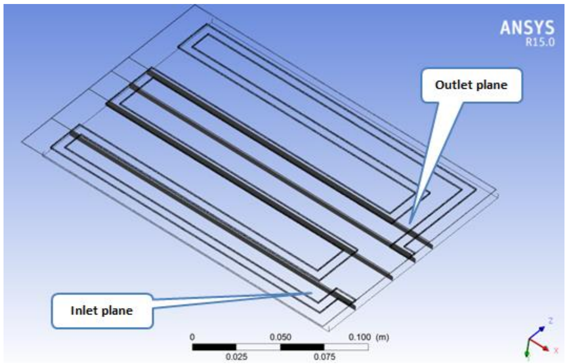

Figure 4.11: Vertical planes 1, 2 3, 4 (1 is inlet and 4 is outlet) within mini-channel cold plates.

4.3.4 Grid Independence Study

A grid independence study was undertaken in order to verify that the solutions generated by the numerical analysis were not reliant on the resolution of the meshes generated. As a result, a coarser mesh of 20 million cells and a finer mesh of 40 million cells were made. Solutions were computed from the 4C discharge 15°C boundary conditions. This was compared to the standard 33 million cell medium-detail mesh used for the rest of the simulations. Table 4.4 and Table 4.5 present the grid independence data for the temperature and velocity taken across the width of the outlet, as shown in Figure 4.12, Figure 4.13, and Figure 4.14.

Figure 4.12: Temperature and velocity grid independence test data taken at the yellow line across with width of the outlet, as shown above.

Table 4.4: Grid independence data for temperature contours.

[Data] Chart Count	20 million cells 50% Larger Temperature [K]	33 million cells Nominal Temperature [K]	40 million cells Next Inlet Channel Finer (0.2mm) Temperature [K]	% coarse to nominal	% fine to nominal
0	288.35	291.11	291.27	0.94	-0.05
0.1	288.42	291.39	291.36	1.01	0.01
0.2	288.42	291.42	291.38	1.02	0.01
0.3	288.43	291.43	291.37	1.02	0.01
0.4	288.43	291.40	291.34	1.01	0.02
0.5	288.44	291.38	291.34	1.00	0.01
0.6	288.44	291.37	291.35	1.00	0.00
0.7	288.43	291.40	291.37	1.01	0.01
0.8	288.41	291.42	291.37	1.03	0.01
0.9	288.35	291.18	291.29	0.97	-0.03

Table 4.5: Grid independence data for velocity contours.

[Data] Chart Count	20 million cells 50% Larger Velocity [m/s]	33 million cells Nominal Velocity [m/s]	40 million cells Next Inlet Channel Finer (0.2mm) Velocity [m/s]	% coarse to nominal	% fine to nominal
0	0.09	0.01	0.00	30.76	46.15
0.1	0.57	0.57	0.57	1.21	0.17
0.2	0.66	0.66	0.66	0.15	0.60
0.3	0.72	0.72	0.72	0.27	-0.13
0.4	0.76	0.76	0.76	0.13	-0.13
0.5	0.77	0.78	0.77	0.12	0.25
0.6	0.78	0.78	0.78	-0.12	0
0.7	0.78	0.78	0.78	0.63	0
0.8	0.76	0.76	0.76	1.04	0
0.9	0.04	0.01	0.01	-152.63	21.05

The velocity data is a near match across the coarse, medium and fine detail meshes, showing that the solution calculated was not dependent on the mesh resolution. The temperature data again shows very high correlation, with the maximum variance between the coarse and medium detail mesh being 1.03%. This is far less than the 10% accepted range of error for CFD solutions [209], again validating the mesh resolution. Given the difference in computational times for the meshes – approximately 10 hours for the coarse mesh, 12 hours for the medium mesh and 18 hours for the fine mesh – it was decided that the medium detail mesh was a good balance between computational time and accuracy.

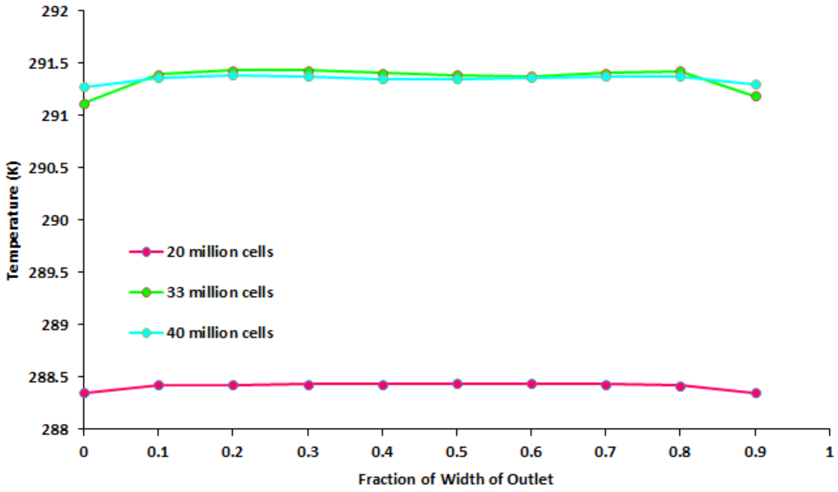

Figure 4.13: Temperature grid independence data at the specified outlet location at 4C discharge & 15 °C BC.

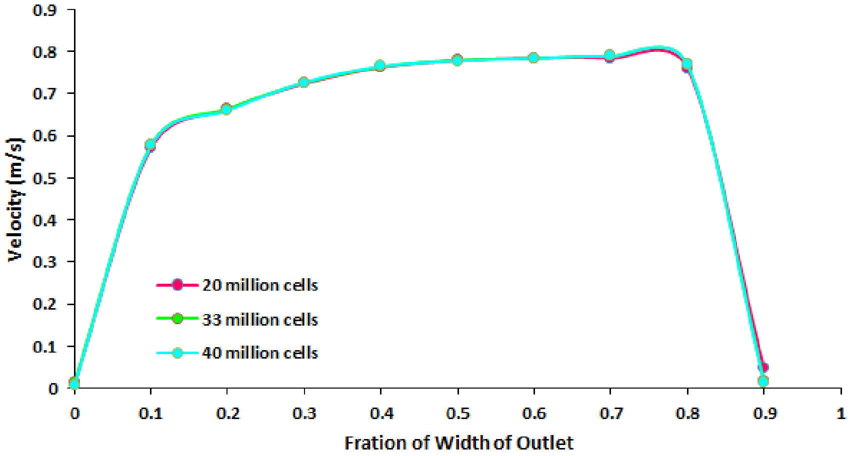

Figure 4.14: Velocity grid independence data at the specified outlet location at 4C discharge & 15°C BC.

4.4 Model 4: Battery Degradation Model

In this section, a degradation model is presented with regards to the real world drive cycles obtained from an EV with different ambient temperatures of -6°C, 2°C, 10°C, and 23°C, in order to assess the performance of the battery. Battery behavior varies highly non-linearly with respect to current and state-of-charge among other variables and a wide range of modeling strategies of varying complexities exist to capture this. The approach chosen in this study is the application of an equivalent circuit model (ECM), in which the behavior of the battery is modeled using a combination of ideal circuit elements. More specifically, the Thevenin model was chosen due to its simplicity and effectiveness in capturing the voltage behavior of batteries.

As shown in Figure 4.15, the internal resistance of the battery is captured by the resistor R_1 while the transient voltage response to the changing current is captured by the RC pair. The ideal voltage source V_{oc} represents the open-circuit voltage (OCV) of the cell, which was correlated to the cell SOC. The voltage of the circuit (V_L) is given as the solution to equations (4.58), (4.59), and (4.60). An additional incentive for the choice of the Thevenin model is its extensive use and application in battery modeling in the literature [210] .

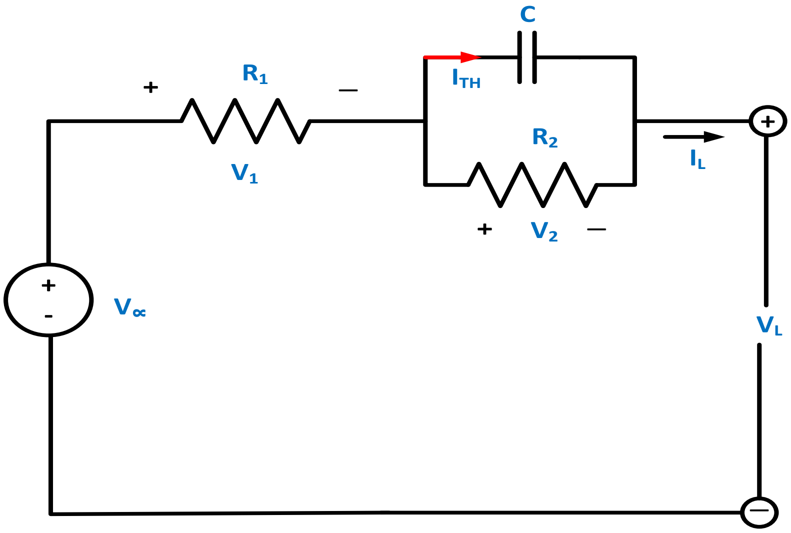

Figure 4.15: Degradation model.

$$V_L = V_{oc} - V_1 - V_2 \tag{4.58}$$

$$V_1 = I\,R_1 \tag{4.59}$$

$$\frac{dV_2}{dt} = \frac{I}{C} - \frac{V_2}{R_2 C} \tag{4.60}$$

The model parameters of the Thevenin model were experimentally determined using a charge-discharge test at a current rate of C/25 (0.8A) as well as a hybrid pulse power characterization (HPPC) test at various known SOC values. The C/25 cycle was used to correlate SOC and OCV. The HPPC procedure was a 1C (20A) discharge for 10 seconds, followed by 40 seconds of rest and then a 0.75C (15A) charge for 10 seconds. The circuit parameters R_1, R_2 and C were fit to the HPPC data using a genetic algorithm in MATLAB. HPPC was conducted at intervals of 10% SOC, and the correlations between the parameters and SOC are shown in equations (4.61), (4.62), and (4.63). Figure 4.16 shows the current profile and fitting results of an HPPC test at 50% SOC. Furthermore, a number of cells were characterized to account for stochastic variation in cell manufacturing quality.

$$R_1 = -0.000513\,(SOC) + 0.002733 \tag{4.61}$$

$$R_2 = 0.001426\,(SOC)^{-0.771947} \tag{4.62}$$

$$C = 3297.55\,\log\,(SOC) + 13481.96 \tag{4.63}$$

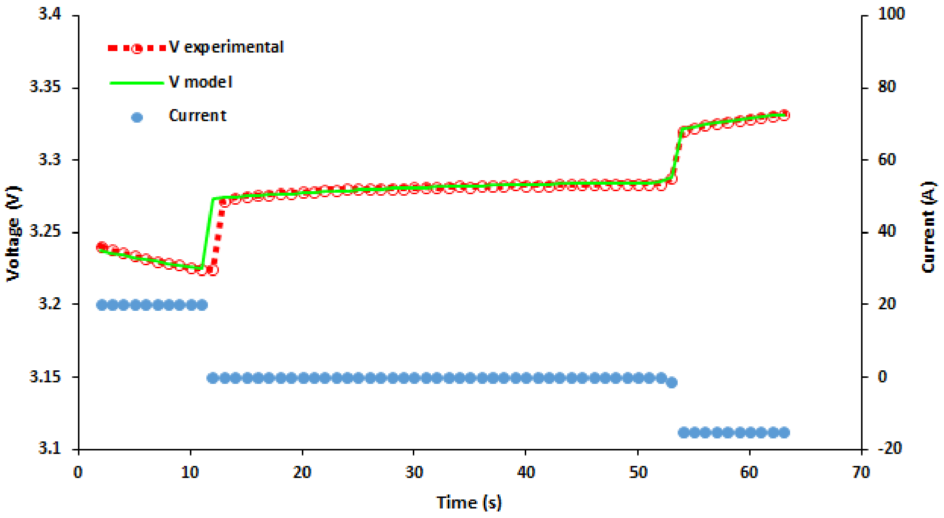

Figure 4.16: Voltage and current profiles of an HPPC test at 50% SOC.

The cell model was constructed in a MATLAB object-oriented environment, for ease of use and computational speed. In the drive cycles recorded, the majority of the current was less than 1C in magnitude [211]. Therefore, the model behavior was compared with charge and discharge curves at 1C and C/2 for model validation. The results of these comparisons for 1C charge and 1C discharge are shown in Figure 4.17, and those for C/2 charge and C/2 discharge are shown in Figure 4.18. The model was deemed suitably accurate to be used with model real-world drive-cycles.

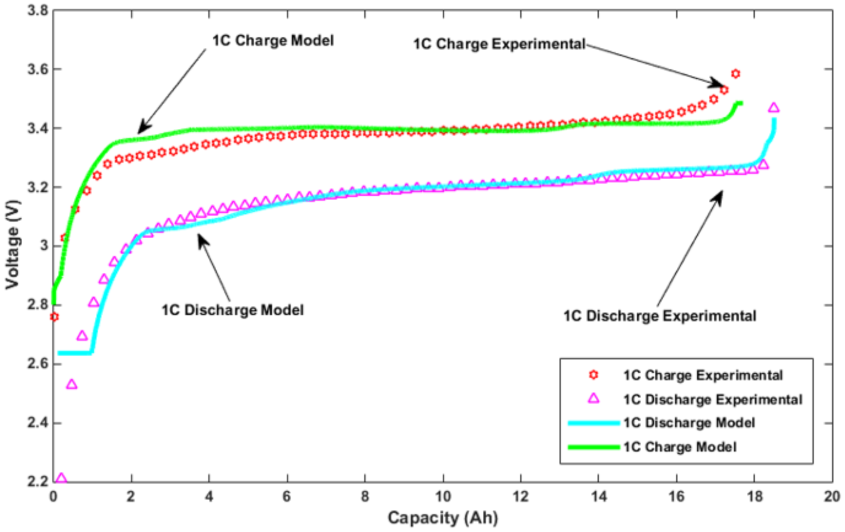

Figure 4.17: Model and experimental comparison at 1C charge and discharge.

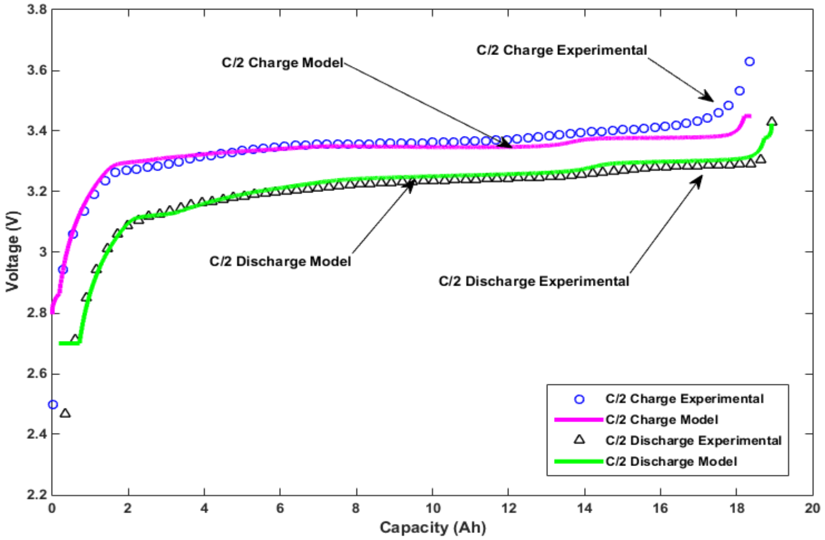

Figure 4.18: Model and experimental comparison at C/2 charge and discharge.

With regards to battery degradation, the degradation model proposed by [212] was chosen to reflect the degradation behavior of the battery. It has been established that cycling aging is governed most significantly by depth-of-discharge (*DOD*), charge throughput and the average SOC during cycling [213, 214, 215]. The degradation model used accounts for these variables, with average voltage (V_{avg}) taking the place of average SOC but essentially being equivalent. Equations (4.64) and (4.65) govern this degradation model.

$$C_t = C_0 \, (1 - \beta\sqrt{Q}) \tag{4.64}$$

$$\beta = A \, (V_{avg} - B)^2 + C + D \cdot DOD \tag{4.65}$$

where C_t is the current battery capacity, C_0 is its initial capacity, Q is the amount of charge processed in ampere-hours and *A*, *B*, *C* and *D* are fitted parameters.

Chapter 5

Results and Discussion

In this, Section 5.1 presents the experimental results obtained from a particular battery cell and pack at different discharge rates and varying boundary conditions. The results are presented in terms of the battery surface temperature distributions, tab temperature distributions, heat flux profiles, and heat generation profiles obtained from the analysis method explained in Section 3.4. IR images, which were captured during the experiments, are also presented and discussed. In Section 5.2, for the first model developed using the neural network approach, validation is completed from the simulation with the results obtained from an experimental data in terms of the surface temperature and discharge voltage at all C-rates and BCs. In Section 5.3, for the second model developed (ECT model), validation of the simulated results obtained from an ANSYS CFD is performed with IR images obtained for this particular lithium-ion battery. In Section 5.4, for the third model developed (ANSYS turbulence model), validation is presented for mini-channel cold plates designed for water flow inside the cold plates in terms of temperature and velocity contours. In Section 5.5, for the fourth model developed (battery degradation model), validation is presented for individual drive cycles in terms of voltage and SOC distributions along with capacity fade over three months.

5.1 Experimental Results on Cell and Pack Testing

This section presents the experimental results obtained from a particular battery cell and pack at different discharge rates and various boundary conditions are presented.

5.1.1 Battery Cell Surface and Tab (Electrode) Temperature Profile

Figure 5.1 shows the surface temperature distribution on the principle surface of the battery at 1C, 2C, 3C, and 4C discharge rates and an ambient condition of 22°C (boundary condition). Here, the battery surface temperature profile recorded by ten thermocouples is plotted as a function of time. It can be observed that the response of the thermocouple at location TC-1, 1, TC-1, 2, and TC-1, 3 has the faster rate of increase over the entire period. These thermocouples are nearest the negative (anode) and the positive (cathode) electrodes of the battery and indicate the location of highest heat accumulation, and the rates of heat generation are likely highest near the electrodes. It can be also seen that the thermocouples placed on +ve tab (cathode) and –ve tab (anode) are always higher than at any other locations on the surface of the battery. In Table 5.1, the maximum surface temperature measured by the ten thermocouples at all operating temperatures (5°C, 15°C, 25°C, and 35°C) for water cooling and air cooling (~22°C) are given against discharge rates of 1C, 2C, 3C, and 4C.

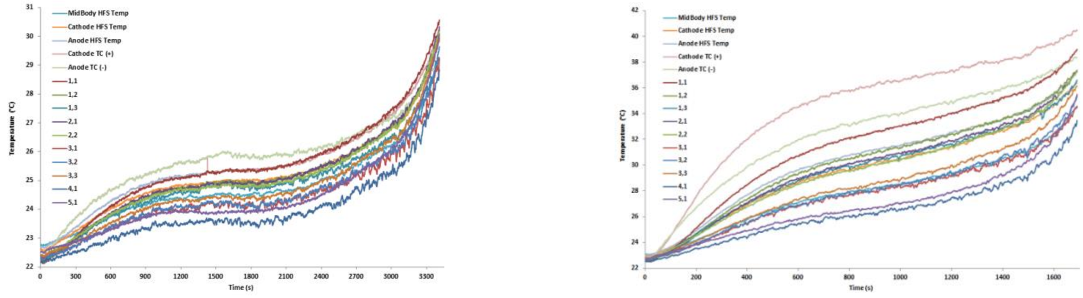

(a) 1C at 22°C

(a) 2C at 22°C

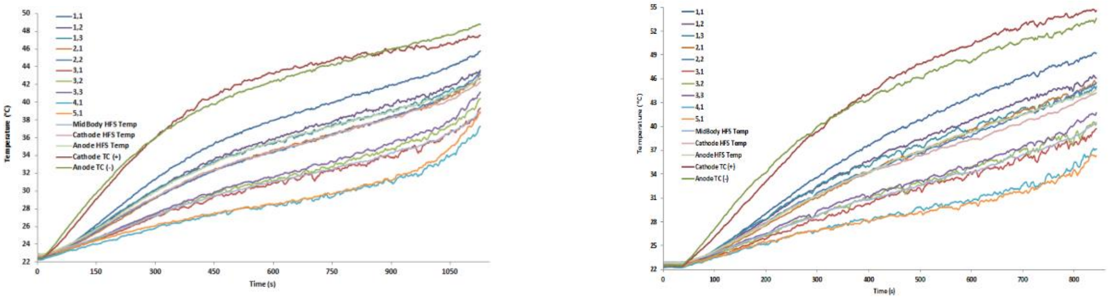

(a) 3C at 22°C

(a) 4C at 22°C

Figure 5.1: Battery cell surface temperature profile at 1C, 2C, 3C, and 4C at 22°C BC.

Table 5.1: Summary of battery cell peak surface temperature at four discharge rates and five boundary conditions.

Cooling Type	Boundary Condition [°C]	Maximum surface temperature [°C]			
		1C	2C	3C	4C
Water	5	7.1176	12.7432	15.1435	18.1927
	15	19.0899	20.817	25.0103	26.4309
	25	27.1619	29.2420	32.1083	34.6552
	35	35.4805	37.7887	35.6479	41.4498
Air	~22	29.71	36.2802	41.4325	46.4781

Figure 5.2 shows the surface temperature distribution on the principle surface of the battery at 1C, 2C, 3C, and 4C discharge rates with water cooling at 5°C BC. Figure 5.3 shows the surface temperature distribution on the principle surface of the battery at 1C, 2C, 3C, and 4C discharge rates with water cooling at 35°C BC. For 1C-5°C and 1C-35°C, the discharge time is 3600s and for 4C-5°C and 4C-35°C, the discharge time is 900s. Similar plots are also generated for 2C and 3C discharge rates at 15°C and 25°C BCs. In Table 5.2, the average surface temperature measured by the ten thermocouples at all operating temperatures (5°C, 15°C, 25°C, and 35°C) for water cooling and air cooling (~22°C) are given against discharge rates of 1C, 2C, 3C, and 4C.

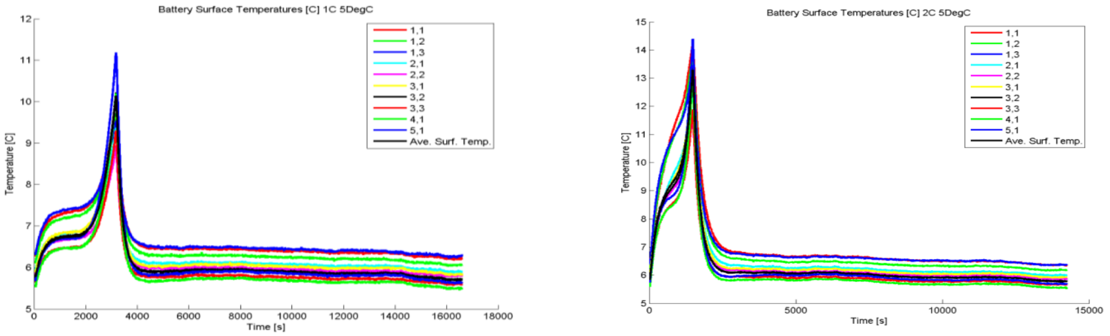

(a) Temperature_1C at 5°C **(b) Temperature_2C at 5°C**

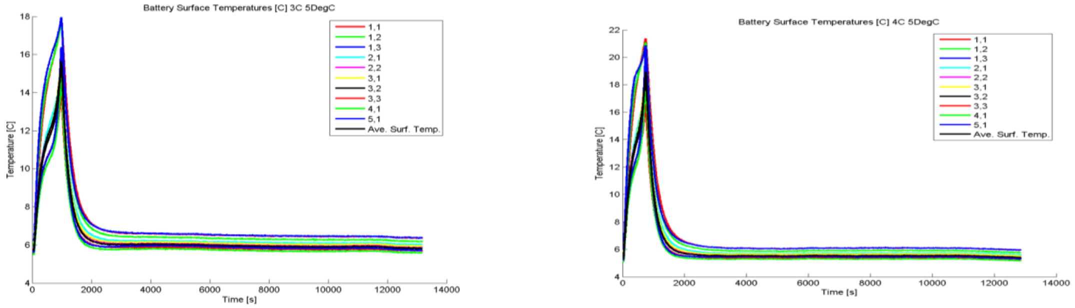

(c) Temperature_3C at 5°C **(d) Temperature_4C at 5°C**

Figure 5.2: Battery cell surface temperature profile at 1C, 2C, 3C, 4C at 5°C BC.

Finally, in the above discussion, the effect of cooling plates is seen since the surface temperature does not proceed beyond 44°C for the water cooling method because of the circulating water inside the top and bottom cold plates. Basically, this circulating water takes heat which is generated by the battery. This is of particular concern for the development of EV, HEV, and PHEV because the vehicle range is directly affected by the battery temperature. Overall, by comparing all plots it is noted that the lowest temperature value is 7.11°C observed at the end of discharge for the 1C-5°C and the highest temperature value is observed to be 41.44°C at the end of discharge for 4C-35°C for the water cooling method. The overall trend observed is that increased discharge rates (between 1C, 2C, 3C, and 4C) and increased operating temperatures (between 5°C, 15°C, 25°C, and 35°C) result in increased temperatures at all the locations measured.

Table 5.2: Summary of battery cell average surface temperature at four discharge rates and five boundary conditions.

Cooling Type	Boundary Condition [°C]	Average surface temperature [°C]			
		1C	2C	3C	4C
Water	5	9.7491	9.3341	11.3141	12.9050
	15	16.9011	18.1048	20.3254	21.5003
	25	25.4630	26.8112	27.5401	30.1444
	35	34.6655	35.9051	37.3724	38.3437
Air	~22	24.7419	28.7582	31.8774	34.8339

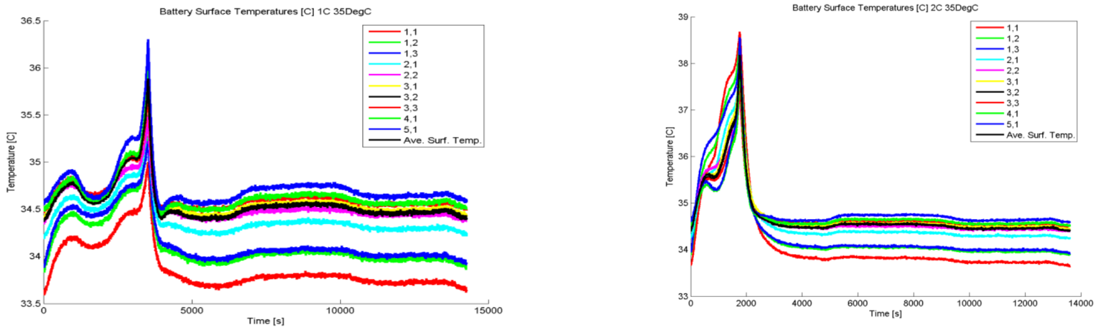

(e) Temperature_1C at 35°C

(f) Temperature _2C at 35°C

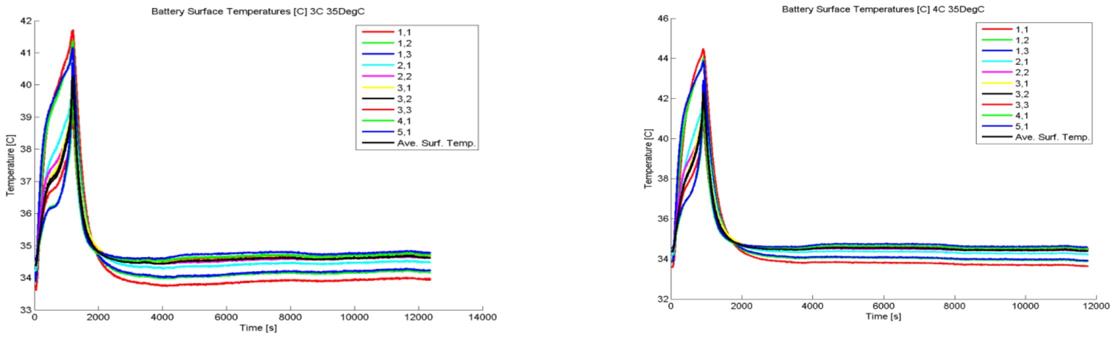

(g) Temperature _3C at 35°C

(h) Temperature _4C at 35°C

Figure 5.3: Battery cell surface temperature profile at 1C, 2C, 3C, 4C at 35°C BC.

5.1.2 Battery Cell Discharge Voltage Profile

Figure 5.4 shows the battery cell discharge voltage profile as a function of discharge capacity at C/10, C/5, C/2, 1C, 2C, 3C, and 4C at an ambient temperature of 22°C. To evaluate the impact of the discharge rate, seven experiments were performed on a newly purchased lithium-ion battery cell (20Ah capacity) with 1C charge rate and different discharge rates of C/10, C/5, C/2, 1C, 2C, 3C, and 4C at an ambient temperature of 22°C. It was found that with an ambient condition of 22°C, the battery capacity was observed to be closer (19.3 Ah) as reported by the manufacturer's data sheet (20 Ah) at all discharge rates. For the low discharge rate, the discharge voltage is higher and it decreases with an increase in C-rate; i.e. the voltage plateau of the battery cycles at higher discharge rates (3C and 4C) is shorter than the one cycled at the lower discharge rates (C/5 and C/10).

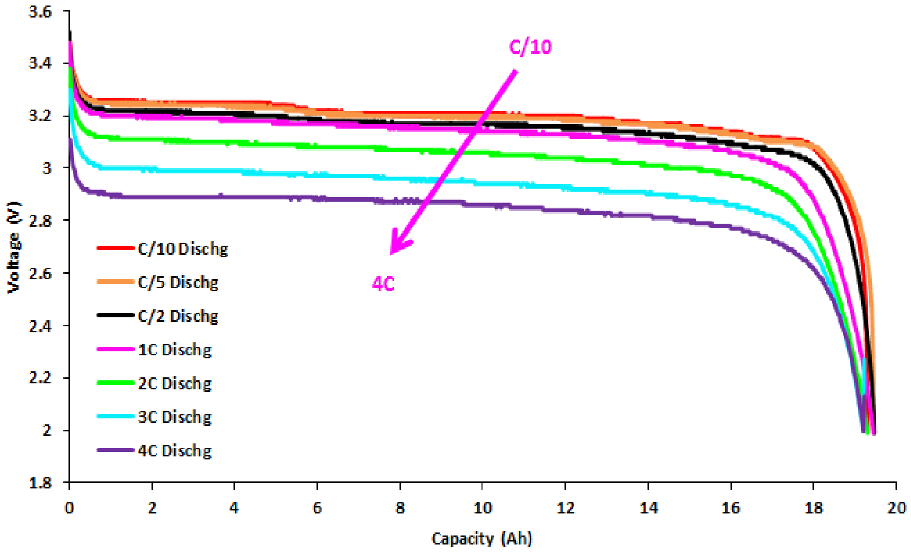

Figure 5.4: Discharge voltage profile as a function of discharge capacity at C/5, C/2, 1C, 2C, 3C, and 4C at an ambient temperature of 22°C.

Figure 5.5 (a, b, c, and d) shows a comparison of the measured discharged terminal voltage obtained at 1C, 2C, 3C, and 4C discharge rates and varying BCs of 5°C, 15°C, 25°C, and 35°C for water cooling. The plots are made against the discharge capacity in order to see the effect of boundary conditions on the discharge capacity. Here, the battery is charged with constant current-constant voltage (CC-CV) protocol until the voltage reaches 3.6V and discharged with the constant current (CC) until the voltage drops to 2.0V. At lower discharge rates, the cell potential stays close to the cell's open circuit potential (OCP). As discharge rates increase, the cell voltage deviates significantly from the OCP due to ohmic, activation, and mass transport losses. In Figure 5.5 (a), there is drastic drop in voltage at 3C and 4C discharge because of the cold conditions.

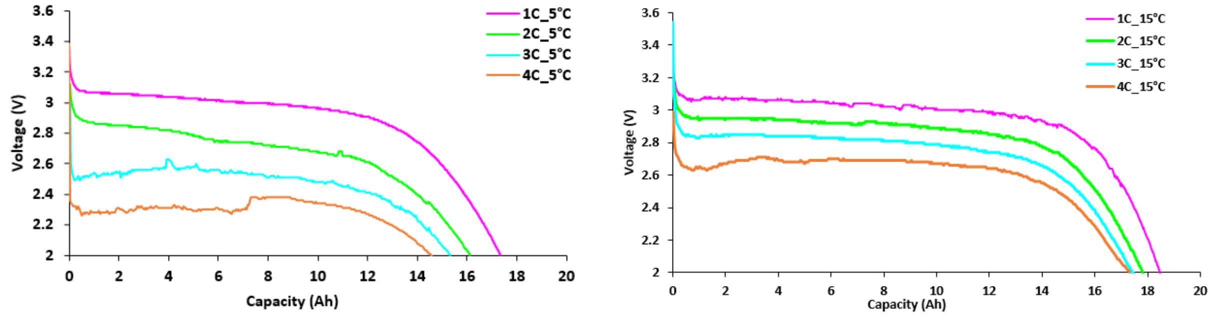

(a) 1C, 2C, 3C, and 4C at 5°C BC

(b) 1C, 2C, 3C, and 4C at 15°C BC

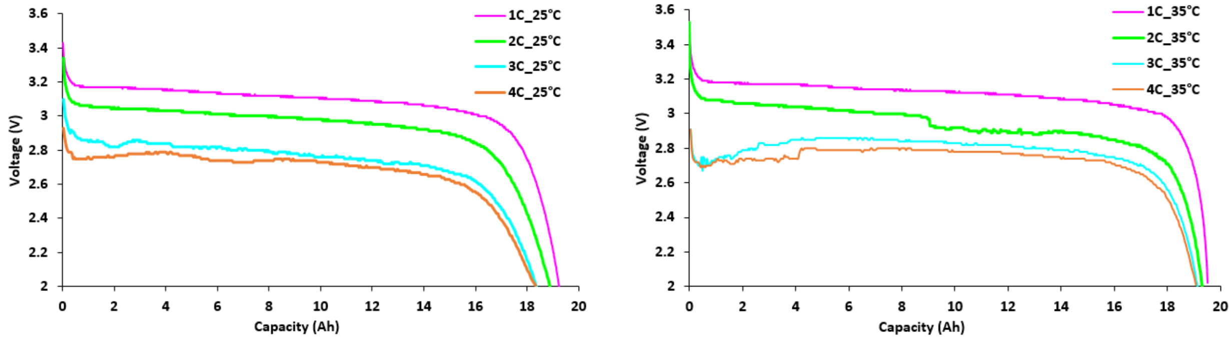

(c) 1C, 2C, 3C, and 4C at 25°C BC

(d) 1C, 2C, 3C, and 4C at 35°C BC

Figure 5.5: Battery cell discharge voltage profile at 1C, 2C, 3C, and 4C at 5°C, 15°C, 25°C, and 35°C BCs.

5.1.3 Heat Flux Profile for Battery Cell

Figure 5.6 shows the heat flux profiles at 4C discharge rate for the air cooling method (an ambient 22°C BC). It should be noted that HFS 1 is located near the positive electrode or cathode, HFS 2 is located near the negative electrode or anode, and HFS 3 is located in the middle of the cell (mid body) along the height of the cell as shown in Figure 3.8. For the particular case of 4C discharge and 22°C BC of air cooling, the peak heat flux values are 586.72 W/m^2 near the cathode, 667.88 W/m^2 near the anode, and 303.09 W/m^2 near the mid body. It is observed that the values are higher near the electrodes (cathode and anode) as compared to the mid body. Figure 5.7 shows the heat flux profiles at 1C, 2C, 3C, and 4C discharge rates against the discharge capacity for the air cooling method (an ambient 22°C BC) and water cooling method (BCs of 5°C, 15°C, and 25°C). For water cooling, the highest heat flux is 3300.50 W/m^2 obtained at 4C-25°C BC and the lowest heat flux value is 508.67 W/m^2 obtained at 1C-5°C BC.

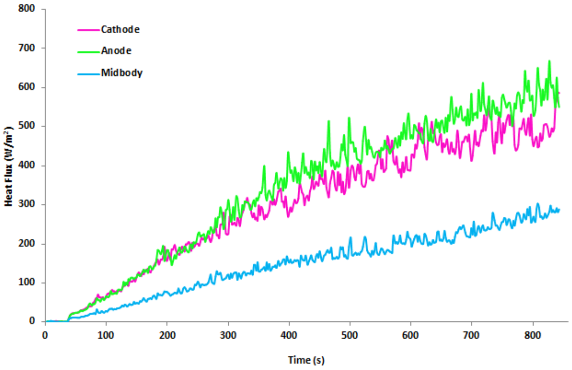

Figure 5.6: Heat flux profiles at 4C discharge rate and 22°C BC (ambient air cooling).

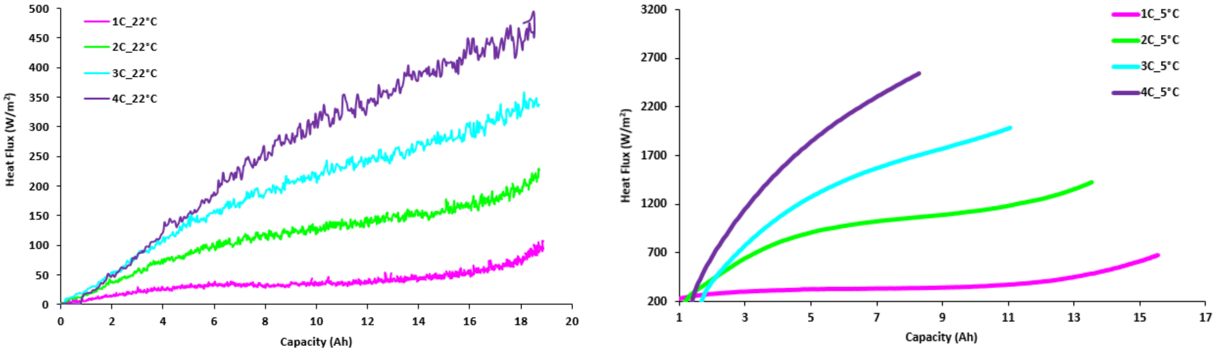

(a) 1C, 2C, 3C, and 4C at 22°C BC

(b) 1C, 2C, 3C, and 4C at 5°C BC

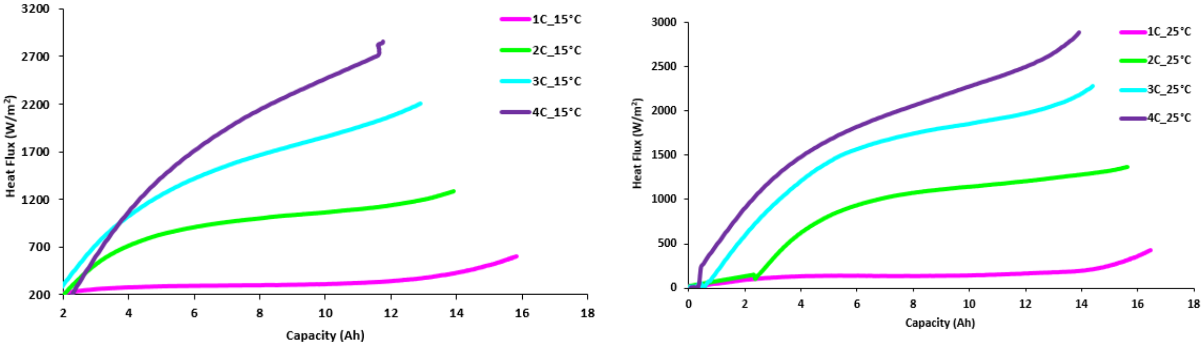

(c) 1C, 2C, 3C, and 4C at 15°C BC

(d) 1C, 2C, 3C, and 4C at 25°C BC

Figure 5.7: Heat flux profile at 1C, 2C, 3C, and 4C at 22°C BC (air cooling) and 5°C, 15°C, 25°C BCs (water cooling).

In Table 5.3, the average heat flux as measured by all three heat flux sensor operating temperatures (5°C, 15°C, and 25°C) for water cooling and air cooling (22°C) are given against discharge rates of 1C, 2C, 3C, and 4C. For air cooling cases, the average heat flux of HFS 2, near the negative electrode, is always highest. Water cooling cases do not show a definitive pattern between HFS 1 and 2. This is likely due to the slightly uneven cooling gradient across the cold plate. The coolant temperature, and thus plate temperature, increases across the width of the battery surface as heat is absorbed. This is in contrast to the air cooling case, where the vertical orientation of the battery provided a condition where cooling potential is approximately equal across the width of the surface. It could be inferred that the air cooling cases are a better representation of the differences in heat generation between the three locations. The trend observed is that increased discharge rates (between 1C, 2C, 3C, and 4C) results in increased average heat fluxes at the three locations measured.

Table 5.3: Summary of average heat flux at four discharge rates and four boundary conditions.

Cooling Type	Boundary Condition [°C]	Average Heat Flux [W/m^2]				
		Position	**1C**	**2C**	**3C**	**4C**
Water	5	Cathode	334.23	661.73	976.03	1267.61
		Anode	556.92	1522.257	1766.22	1921.61
		Mid Body	193.07	504.26	789.70	1061.93
	15	Cathode	454.83	1237.42	1656.41	1882.98
		Anode	359.44	913.17	1667.82	2014.69
		Mid Body	113.68	283.27	512.41	710.18
	25	Cathode	199.63	1226.89	2279.34	1988.01
		Anode	180.42	1170.87	2071.78	2391.31
		Mid Body	71.08	198.19	423.69	605.61
Air	~22	Cathode	41.80	131.30	237.91	301.84
		Anode	47.10	146.73	239.17	340.077
		Mid Body	25.12	72.10	107.37	147.60

5.1.4 IR Images of Battery Cells

Figure 5.8 shows the thermal images of two different lithium-ion battery cells during 4C (80A) discharge rate at the beginning, middle and end of the discharge cycle.

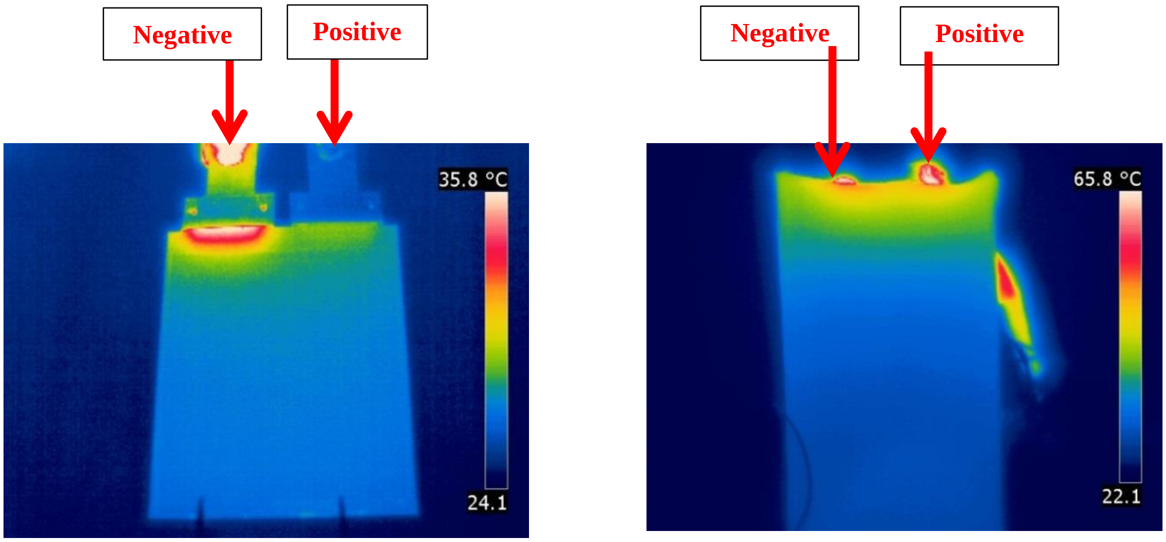

Beginning of the discharge cycle

Beginning of the discharge cycle

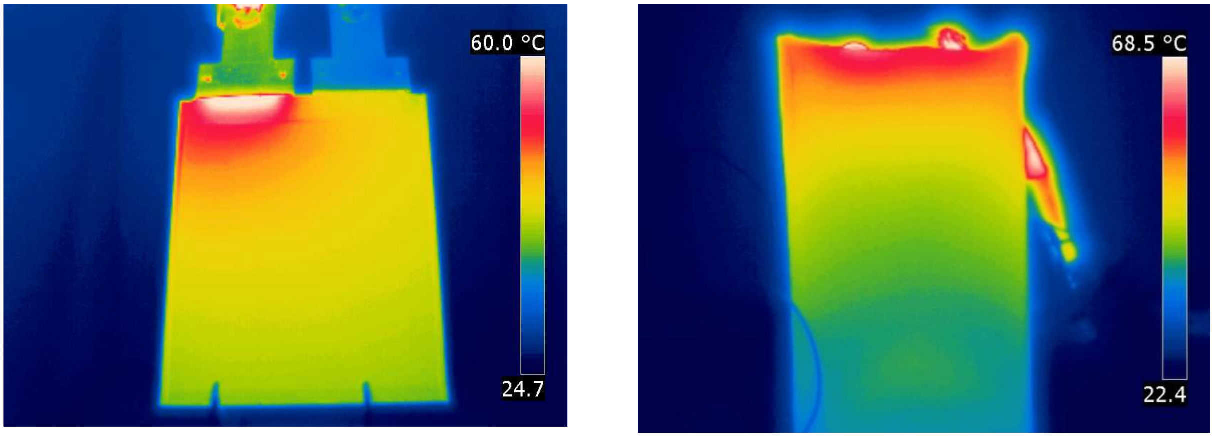

Middle of the discharge cycle

Middle of the discharge cycle

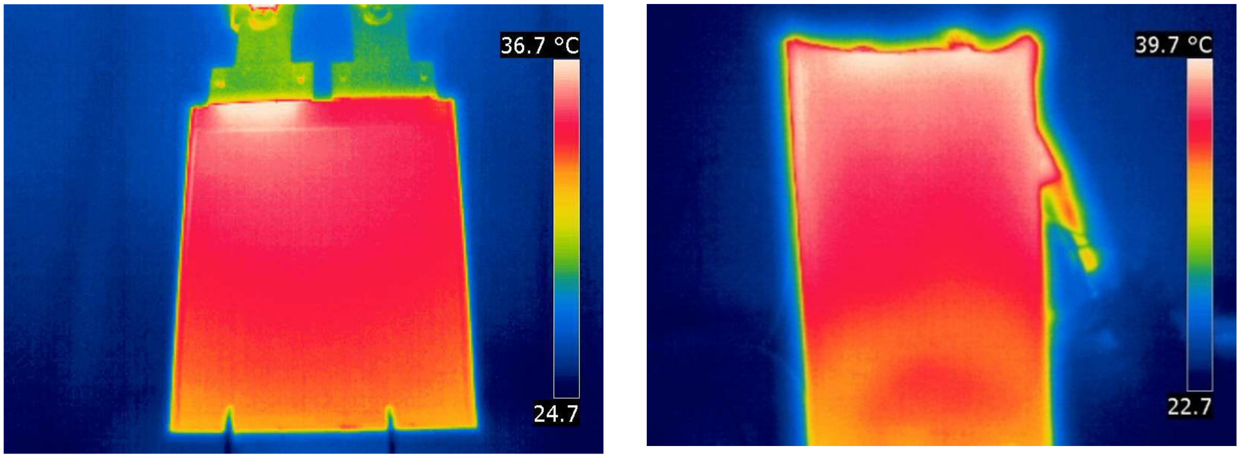

End of the discharge cycle

End of the discharge cycle

Figure 5.8: Thermal images at the beginning, middle and at the end of discharge of 20Ah and 16Ah battery cell.

Infrared (IR) equipment is generally used to obtain thermal images of the surface of any object. A camera equipped with an IR detector can capture different energies radiating from different surface temperatures of an object. The IR equipment converts the energy back to the temperature. This is a great tool for finding temperature distribution or hot spots on the surface of an object without using any intrusive temperature sensors. From IR imaging, the temperature gradient along the height of the pouch cell can be seen. It is observed that the gradient stratifies down the height with little effect from the geometry change at the edges. The brightest white parts of the image show where the highest temperatures are seen and correspondingly where the highest heat flux is expected. This is the expected result when joule heating is the dominant heat generation process. This is due to the concentration of current as it collects on the "current collector" tabs of the anode and cathode. This technique is very helpful for assessing thermal behaviour and could be used to point out trouble areas and provide insight to improve the design.

5.1.5 Battery Pack Temperature Profiles

Figure 5.9 shows the experimental average surface temperature profiles for a battery pack at 1C, 2C, 3C, and 4C and 5°C, 15°C, 25°C, and 35°C BCs for the water cooling method. Here, the battery surface temperature profile recorded by 18 thermocouples is plotted as a function of time. It can be observed that the thermocouple locations near the negative (anode) and the positive (cathode) electrodes of the battery indicate the location of highest heat accumulation, and the rates of heat generation are likely highest near the electrodes. Here, in this experimental work, the cycle represents first 1C charge, then 1-hour rest, followed by 1C discharge, after which the same cycle is repeated but, for discharging, instead of 1C it is 2C, 3C, and 4C discharge and total time for all charge/discharge cycle is 18 hours. To refresh the reader, TC 1 is located near the positive electrode or cathode, TC 2 is located near the negative electrode or anode, and TC 3 is located in the middle of the cell along the height of the cell. The highest value of the average surface temperature is obtained for 4C and 35°C BC (36.36°C) and the lowest value is obtained for 1C and 5°C BC (7.22°C). The trend observed is that the increased C-rates and increased boundary conditions result in an increase in average surface temperature for all cells 1, 2, and 3 (or stack). For the air cooling method, the values are higher at all discharge rates as compared to the water cooling method. The highest value of the average surface temperature for the air cooling method obtained at 4C discharge rate is 41.38°C. Table 5.4 summarizes the average surface temperatures for all C-rates and various BCs for both the water cooling as well as air cooling methods. Similarly, in Table 5.5, the peak surface temperatures for all C-rates and various BCs for both the water cooling as well as air cooling methods are presented.

Table 5.4: Summary of battery pack average surface temperature at four discharge rates and five boundary conditions.

Cooling Type	Boundary Condition [°C]	Average surface temperature [°C]			
		1C	2C	3C	4C
Water	5	7.22	8.49	10.43	11.58
	15	16.58	17.30	18.81	19.83
	25	25.30	26.15	27.44	28.25
	35	35.17	35.34	36.35	36.36
Air	~22	27.86	34.18	36.86	41.38

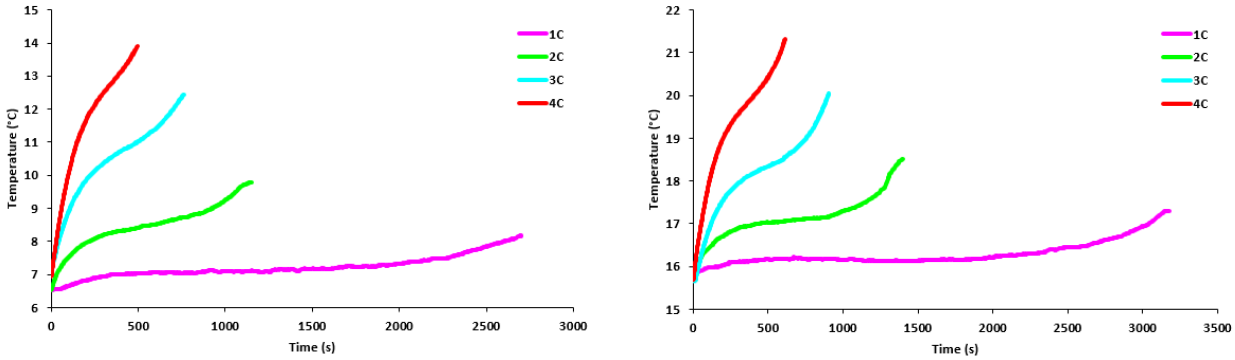

(a) Temperature at 1C,2C,3C,4C and 5 °C BC **(b) Temperature at 1C,2C,3C,4C and 15 °C BC**

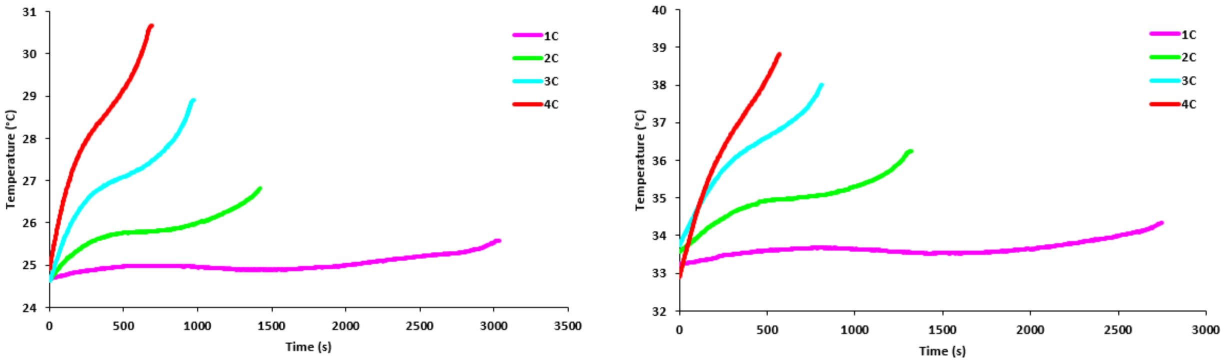

(c) Temperature at 1C,2C,3C,4C and 25 °C BC **(d) Temperature at 1C,2C,3C,4C and 35 °C BC**

Figure 5.9: Battery pack average discharge surface temperature profiles at 1C, 2C, 3C, and 4C and 5°C, 15°C, 25°C, and 35°C BCs.

Table 5.5: Summary of battery pack peak surface temperature at four discharge rates and five boundary conditions.

Cooling Type	Boundary Condition [°C]	Maximum surface temperature [°C]			
		1C	2C	3C	4C
Water	5	8.17	9.78	12.44	13.89
	15	17.30	18.51	20.05	21.35
	25	25.58	26.82	28.90	30.66
	35	35.34	36.24	38.01	38.82
Air	~22	32.99	42.72	48.61	56.49

5.1.6 Battery Pack Voltage Profiles

Figure 5.10 shows stack voltage profiles obtained during all discharge rates of 1C, 2C, 3C, and 4C and different BCs of 5°C, 15°C, 25°C, and 35°C for water cooling.

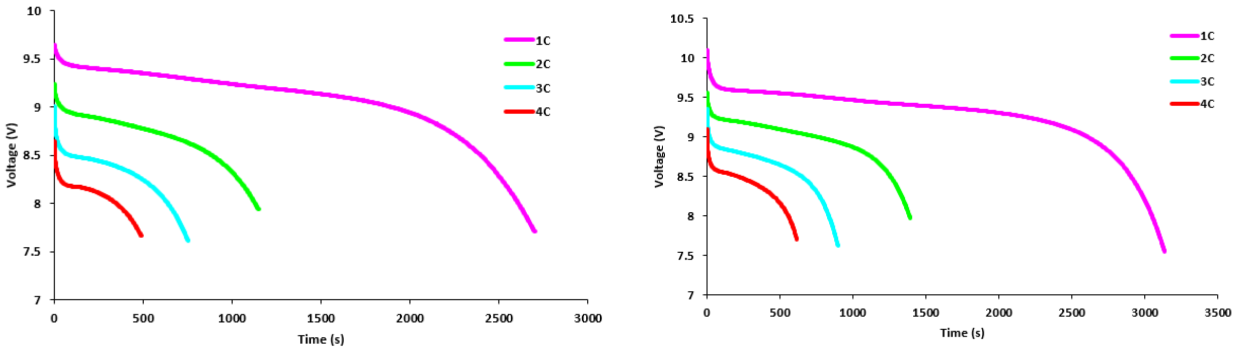

(a) Stack voltage at 1C,2C,3C,4C and 5°C BC **(b) Voltage at 1C,2C,3C,4C and 15°C BC**

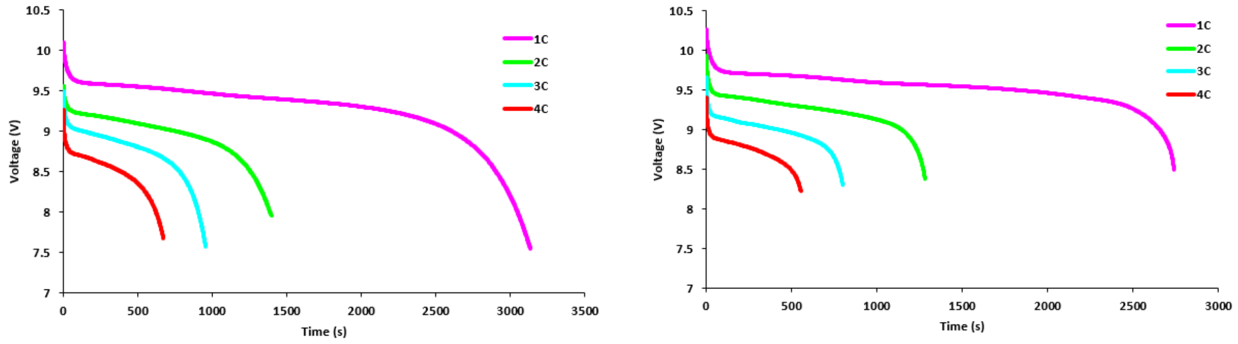

(c) Voltage at 1C,2C,3C,4C and 25°C BC **(d) Voltage at 1C,2C,3C,4C and 35°C BC**

Figure 5.10: Battery pack discharge voltage profiles at 1C, 2C, 3C, 4C at 5°C, 15°C, 25°C, and 35°C BCs.

The voltage window for cell 1, cell 2, and cell 3 is between 4.0 V to 2.0V and for the stack, as they are connected in series, the voltage is between 11.0 to 6V. Here, all three cells are charged with a constant current (CC) protocol until the voltage reaches 3.6V and discharged with the constant current (CC) until the voltage drops to 2.0V. There is a great impact of boundary conditions (5°C, 15°C, 25°C, and 35°C) on the discharge capacity of the cells. It is observed that, as the C-rate increases, the discharge capacity of all cells increases.

5.2 Model 1 : Battery Thermal Model Validation

In this section, the validation of the temperature distributions on the principle surface of the battery are presented and discussed in detail, with different discharge rates and various boundary conditions. The actual and simulated temperature and voltage profiles are also discussed in detail. The developed neural network model is later used to validate the real world drive cycle. They are discussed in detail in the following subsections. The proposed battery thermal model can be used for any kind of lithium-ion battery and an example of this use is demonstrated by validating the thermal performance of the drive cycle collected from an EV.

5.2.1 Battery Surface Temperature Profile Validation

Figure 5.11 (a, b, c, and d) and Figure 5.12 (a, b, c, and d) show a comparison of average battery surface temperature recorded by ten thermocouples with the profiles predicted by the neural network at 1C, 2C, 3C, and 4C discharge rates and 5°C and 15°C water cooling BCs. Overall, it shows good agreement between data and model (curve fit). Here, the predicted values follow expected trends but slight discrepancies are observed. The model tends to slightly over predict temperature increase at the higher discharge rate of 4C for all BCs. The model temperature response depends on the heat generated by losses in the cell, the thermal mass of the cell, and the heat transfer to the environment. Within the limits of the ability to estimate the input values, the agreement between the measured and computed temperature seems to be quite reasonable. Access to more definitive information on the battery cell properties would lead to better agreement between the model and measurement. Similar plots are also created for 1C, 2C, 3C, and 4C discharge rates at 25°C and 35°C water cooling BCs, and are presented in Figure 5.13 (a, b, c, and d) and Figure 5.14 (a, b, c, and d).

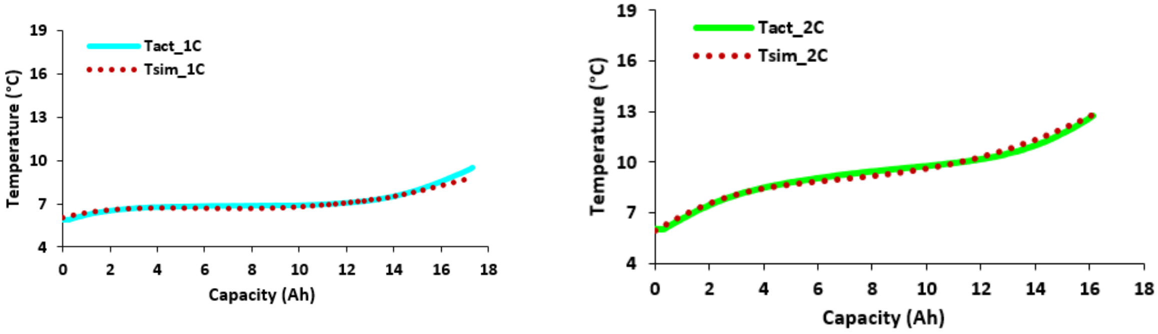

(a) Temperature validation_1C at 5°C

(b) Temperature validation__2C at 5°C

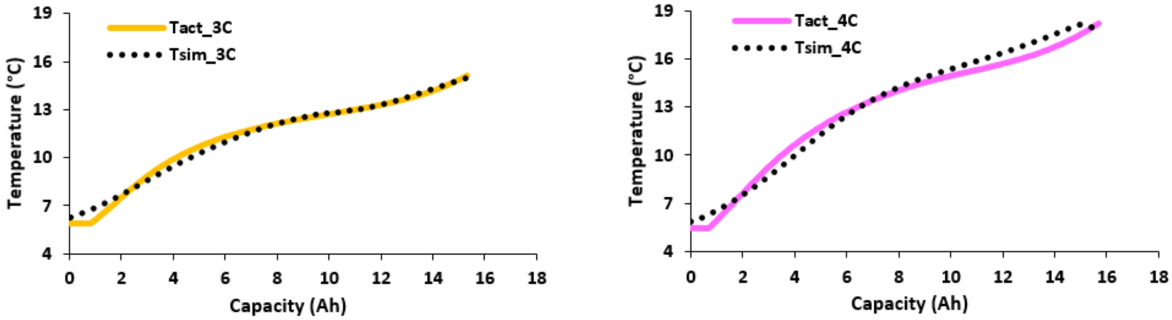

(c) Temperature validation__3C at 5°C

(d) Temperature validation_ 4C at 5°C

Figure 5.11: Comparison of actual and simulated battery cell discharge temperature profiles at 1C, 2C, 3C, 4C at 5°C BC.

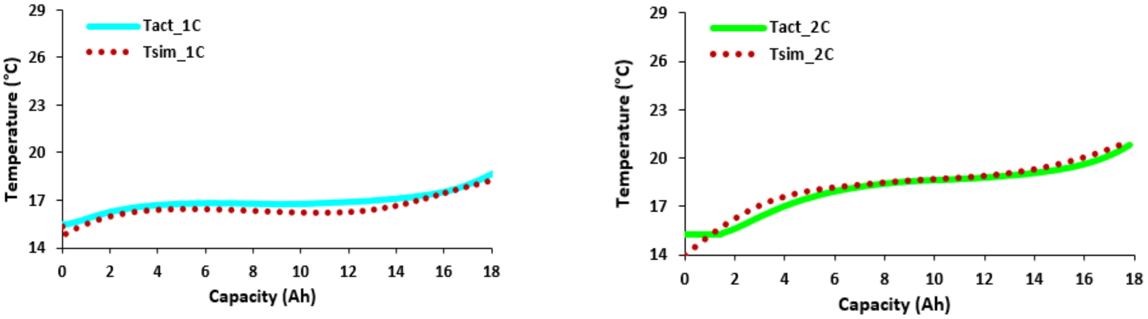

(a) Temperature validation_1C at 15°C

(b) Temperature validation_2C at 15°C

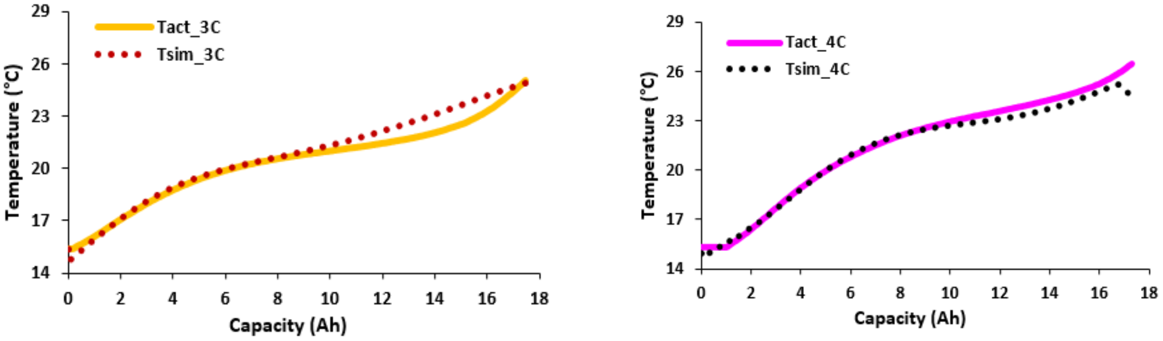

(c) Temperature validation_3C at 15°C

(d) Temperature validation_4C at 15°C

Figure 5.12: Comparison of actual and simulated discharge temperature profiles at 1C, 2C, 3C, 4C at 15°C BC.

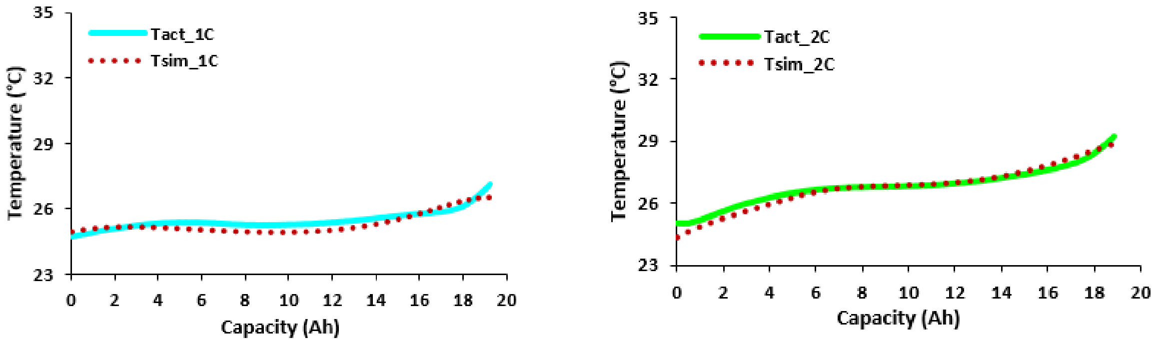

(a) Temperature validation_1C at 25°C

(b) Temperature validation_2C at 25°C

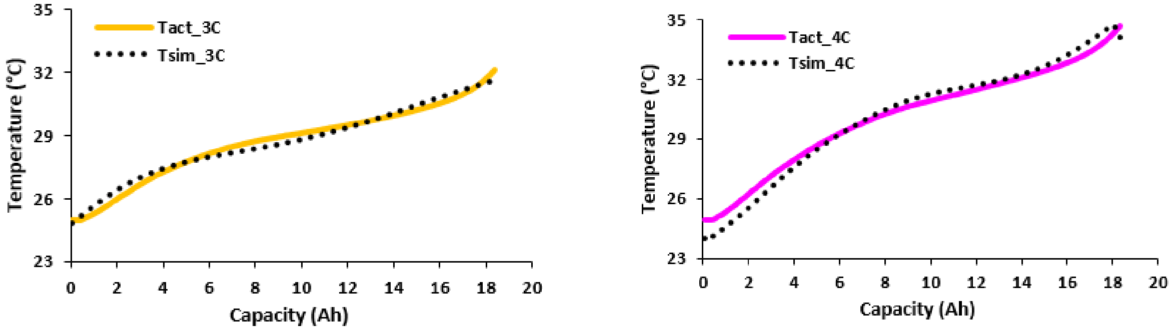

(c) Temperature validation_3C at 25°C

(d) Temperature validation_4C at 25°C

Figure 5.13: Comparison of actual and simulated discharge temperature profiles at 1C, 2C, 3C, 4C at 25°C BC.

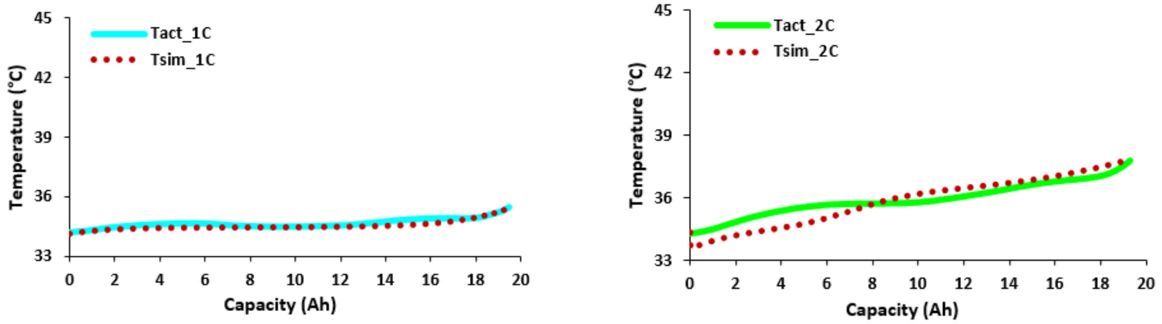

(a) Temperature validation_1C at 35°C

(b) Temperature validation_2C at 35°C

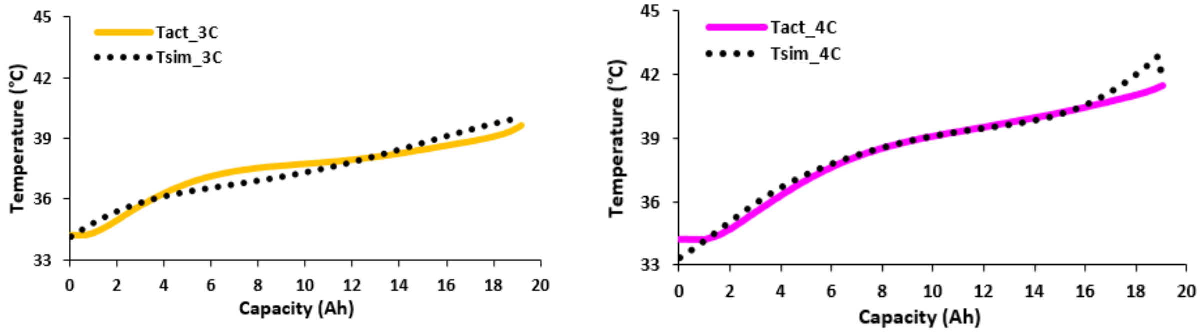

(c) Temperature validation_3C at 35°C

(d) Temperature validation_ 4C at 35°C

Figure 5.14: Comparison of actual and simulated battery cell discharge temperature profiles at 1C, 2C, 3C, 4C at 35°C BC.

5.2.2 Drive Cycle Validation

The developed neural network battery thermal model from controlled BCs lab experiments, as discussed in the previous section, is later used to validate the thermal profiles obtained from an EV under a real world drive cycle. Figure 5.15 shows the validation between measured temperature profiles for all three battery packs from an EV with the profiles predicted by neural network. It is seen that the overall trend matches at the higher temperature side but, at the lower temperature side, some discrepancies are observed. One of the reasons for this is that the EV has a thermal controller which automatically activates fans and is designed to maintain pack temperature below 38°C regardless of ambient temperature. It can also be observed that there is a drastic change in temperature in the range 1100-3000s, because the vehicle was continuously in operation and all three battery packs continuously generate heat. In addition to this, when the drive cycle was collected at that time the ambient temperature was quite low. Finally, this gives the performance of NN model against unseen data.

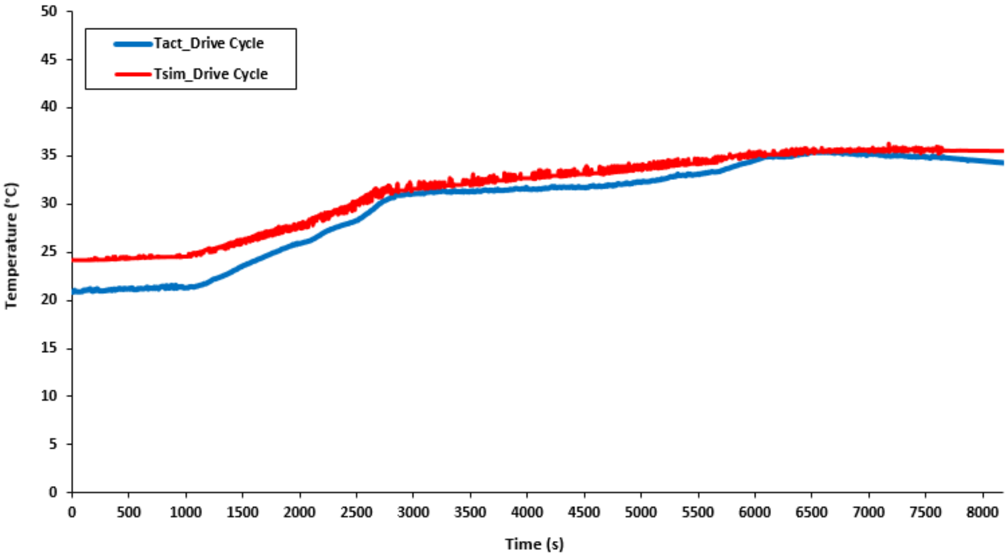

Figure 5.15: EV drive cycle validation.

5.2.3 Discharge Voltage Profile Validation

Figure 5.16 (a, b, c, and d) and Figure 5.17 (a, b, c, and d) show a comparison of the measured discharged terminal voltage obtained at 1C, 2C, 3C, and 4C discharge rates with 5°C and 15°C BCs with the values predicted by the neural network model. Here, the strong agreement between the experimental and simulation data demonstrates the robustness and accuracy of the model. The cell is charged with constant current-constant voltage (CC-CV) protocol until the voltage reaches 3.8V and discharged with the constant current (CC) until the voltage drops to 2.0V. In Figure 5.16 (c and d), the initial immediate drop-off in voltage is due to cold conditions, but quick recovery of voltage after some time is due to rapid increase in the battery cell temperature, which leads to enhanced performance.

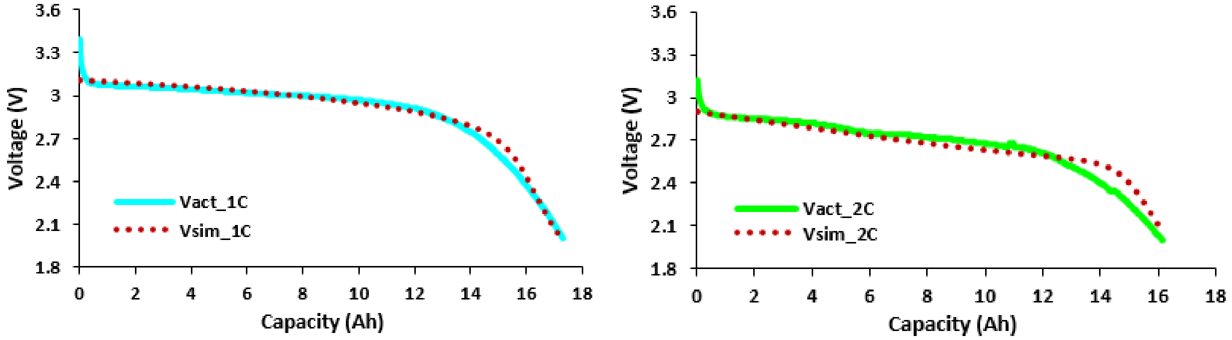

(a) Voltage validation_1C at 5°C **(b) Voltage validation_2C at 5°C**

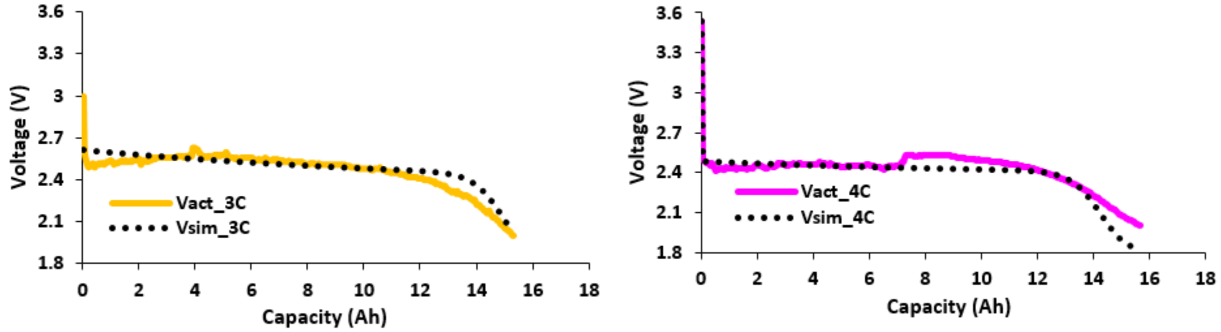

(c) Voltage validation_3C at 5°C **(d) Voltage validation_ 4C at 5°C**

Figure 5.16: Comparison of actual and simulated battery cell discharge voltage profiles at 1C, 2C, 3C, 4C at 5°C BC.

By comparing images, it is seen that the predictions quite well match the experimental data for a wide range of C-rates. At lower discharge rates, the cell potential stays close to the cell's open circuit potential (OCP). As discharge rates increase, the cell voltage significantly deviates from the OCP due to ohmic, activation, and mass transport losses. The developed neural network model is useful with all kinds of lithium-ion batteries. Similar plots were created for 1C, 2C, 3C, and 4C discharge rates at 25°C and 35°C water cooling BCs, and are presented in Figure 5.18 (a, b, c, and d) and Figure 5.19 (a, b, c, and d).

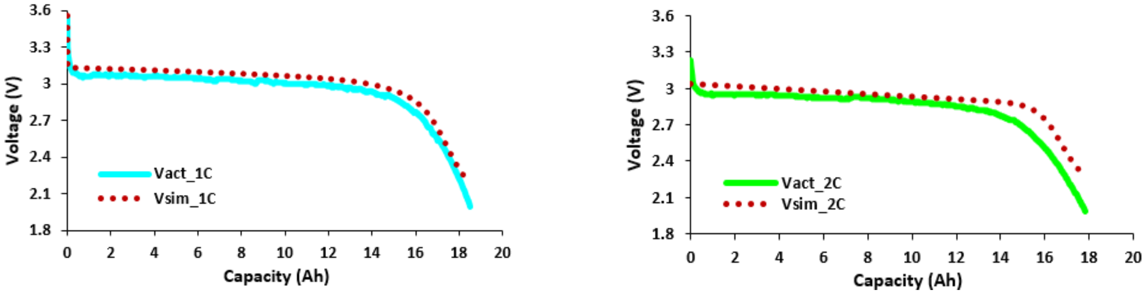

(a) Voltage validation_1C at 15°C

(b) Voltage validation_2C at 15°C

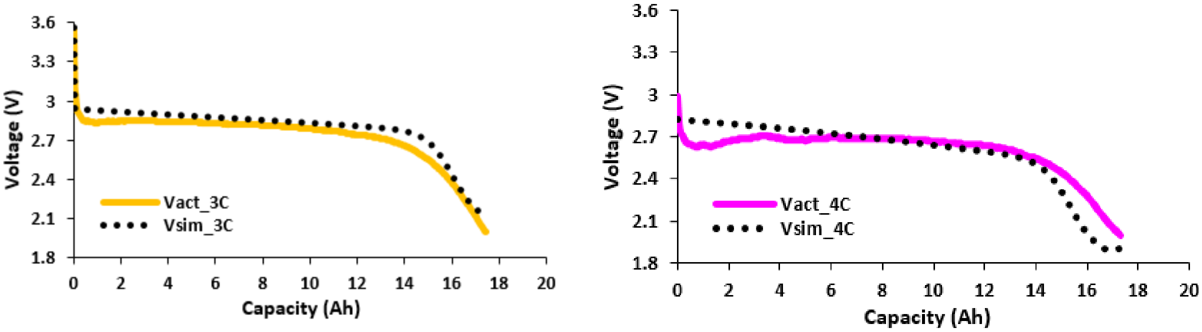

(c) Voltage validation_3C at 15°C

(d) Voltage validation_ 4C at 15°C

Figure 5.17: Comparison of actual and simulated discharge voltage profiles at 1C, 2C, 3C, 4C at 15°C BC.

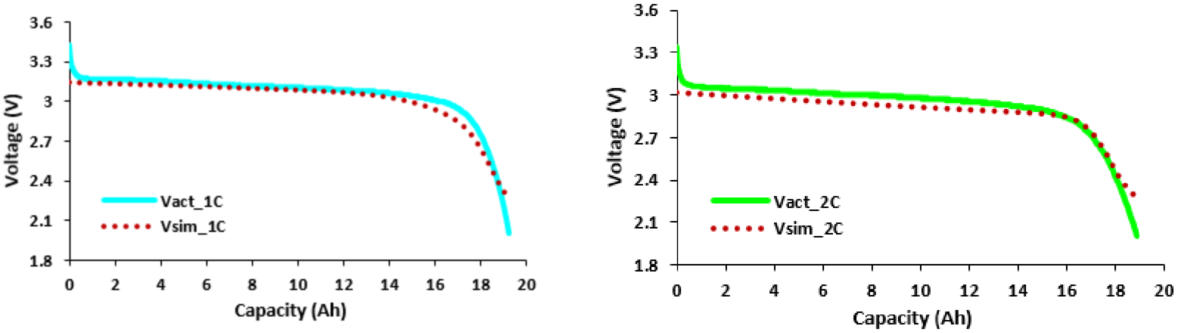

(a) Voltage validation_1C at 25°C

(b) Voltage validation_2C at 25°C

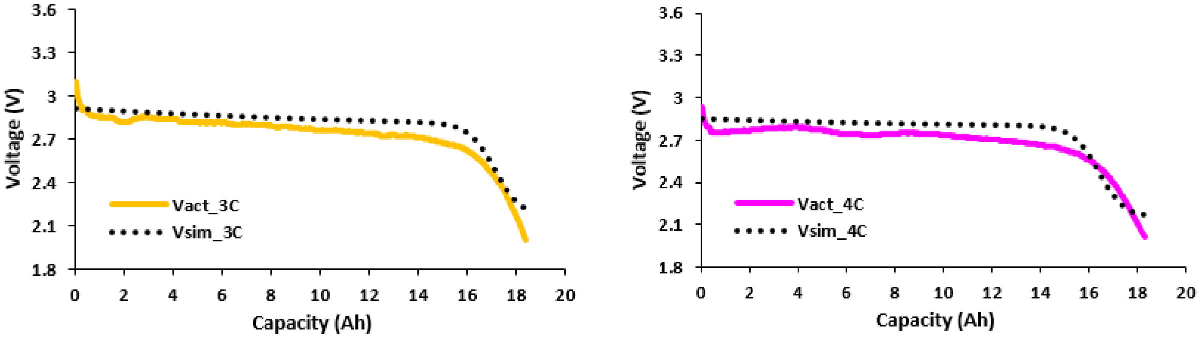

(c) Voltage validation_3C at 25°C

(d) Voltage validation_ 4C at 25°C

Figure 5.18: Comparison of actual and simulated discharge voltage profiles at 1C, 2C, 3C, 4C at 25°C BC.

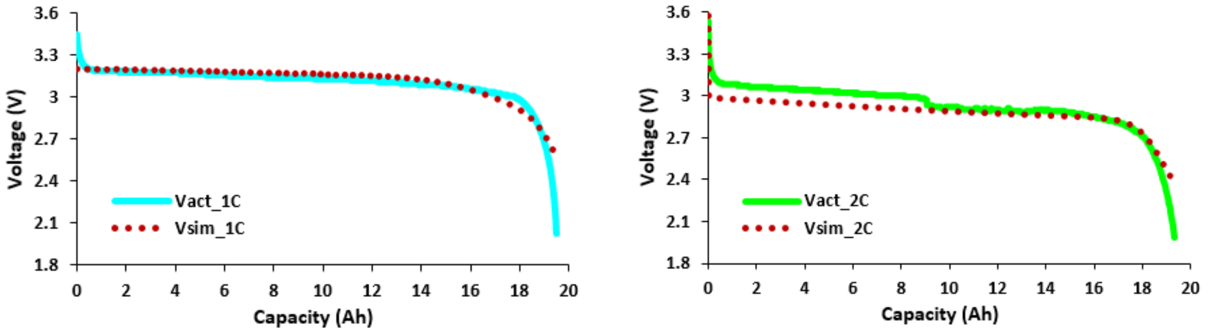

(a) Voltage validation_1C at 35°C

(b) Temperature validation_2C at 35°C

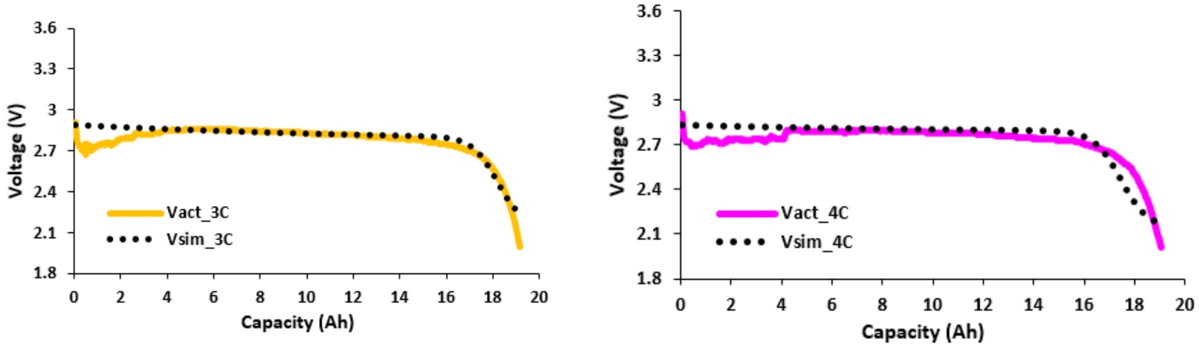

(c) Temperature validation_3C at 35°C

(d) Voltage validation_ 4C at 35°C

Figure 5.19: Comparison of actual and simulated battery cell discharge voltage profiles at 1C, 2C, 3C, 4C at 35°C BC.

5.2.4 Heat Generation Validation

Another NN model, created for the rate of heat generation measurement from a particular lithium-ion battery, was validated with the experimental heat generation rate calculated by using Equation (3.4). Figure 5.20 and Figure 5.21 show comparisons of the actual and simulated rates of heat at 1C, 2C, 3C and 4C discharge rates at 5°C and 15°C BCs. Here, the heat generation is plotted as a function of discharge capacity (Ah). Similarly, Figure 5.22 and Figure 5.23 show a comparison of the actual and simulated rates of heat generation at 1C, 2C, 3C and 4C discharge rates at 25°C and 35°C BCs. At the lower discharge rate of 1C, the rate of heat generation remains approximately constant from the beginning to almost 80% of the discharge. Overall, the simulated data agrees well with the experimental data, demonstrating the robustness and accuracy of the model. However, a small degree of discrepancy is still observed between the simulated and experimental data in the fine structure occurring at the initial periods of the discharge process, appearing most evident for 3C and 4C. A steep rise in the rate of heat generation at the beginning of the discharge

(1 Ah) was also observed, at which point the heat generation rate tends to reach a steady state until approximately 60% of the discharge rate when a steady increase is observed. The increase in the heat generation rate becomes steeper as the discharge progresses and highest near the end of discharge.

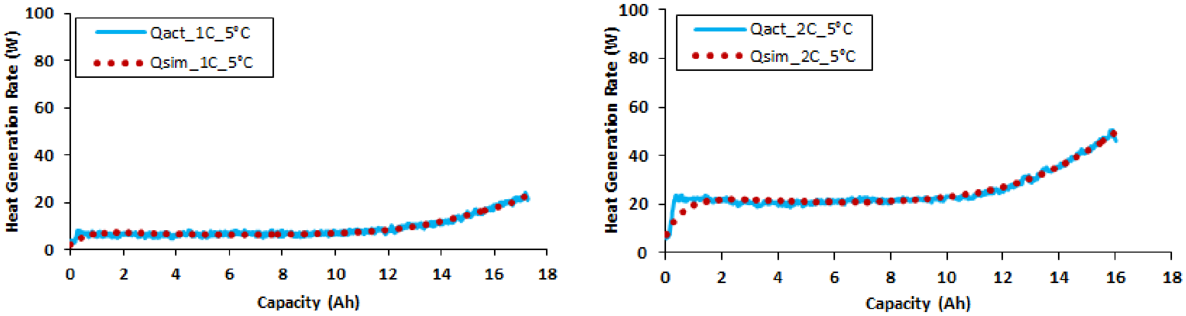

(a) Heat Generation Rate_1C at 5°C **(b) Heat Generation Rate_2C at 5°C**

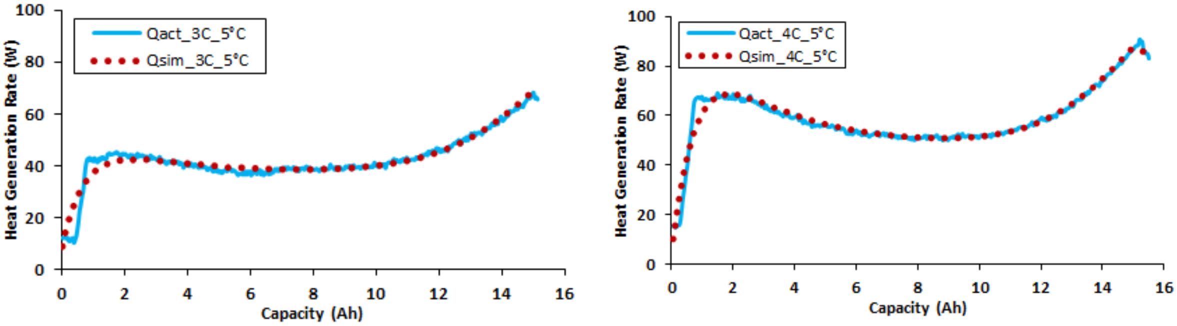

(c) Heat Generation Rate_3C at 5°C **(d) Heat Generation Rate_4C at 5°C**

Figure 5.20: Comparison of actual and simulated heat generation rate at 1C, 2C, 3C and 4C at 5°C BC.

It was also found that the highest rate of heat generation was 91 W, measured at 4C discharge rate and 5°C BC and the minimum value was 11W, measured at 1C discharge rate and 35°C BC. The trend observed is that increased discharge rates (between 1C, 2C, 3C, and 4C) and decreased operating temperatures (between 35°C, 25°C, 15°C, and 5°C), result in increased rates of heat generation. The increased heat generation can be accounted for by looking at Equations (2.10) and (2.12). As the current is increased with the discharge rate, the irreversible ohmic heating term becomes larger. From Equation (2.12), the current collector heat generation increases with the square of current. From this, it follows that more heat is generated at higher discharge rates. The variations in the BCs from 5°C to 35°C and increase in C-rates also have a great effect on discharge capacity. It was found that as the C-rate increased, the discharge capacity (Ah) of the battery decreases and the discharge capacity increases when the BCs increase from 5°C to 35°C. In general, increased C-rates and decreased BCs result in decreased discharge capacity. The proposed battery heat generation model can be used for any kind of lithium-ion battery.

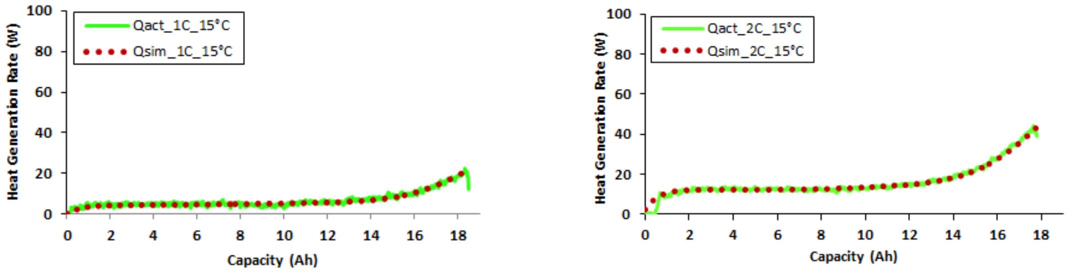

(a) Heat Generation Rate_1C at 15°C **(b) Heat Generation Rate_2C at 15°C**

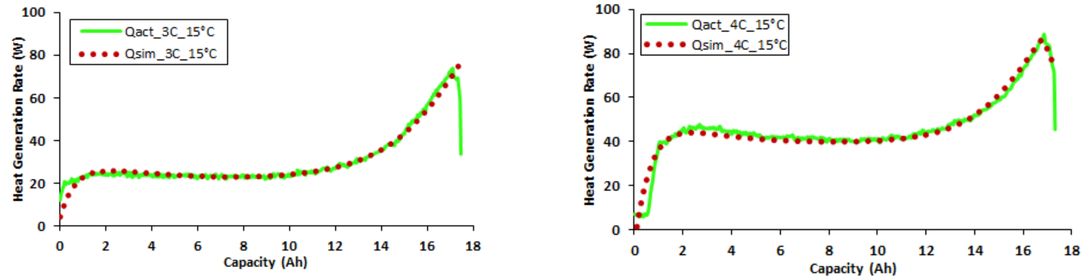

(c) Heat Generation Rate_3C at 15°C **(d) Heat Generation Rate_4C at 15°C**

Figure 5.21: Comparison of actual and simulated heat generation rate at 1C, 2C, 3C and 4C at 15°C BC.

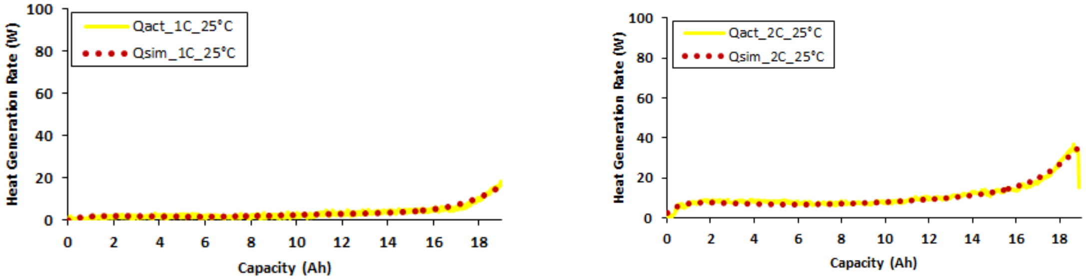

(a) Heat Generation Rate_1C at 25°C **(b) Heat Generation Rate_2C at 25°C**

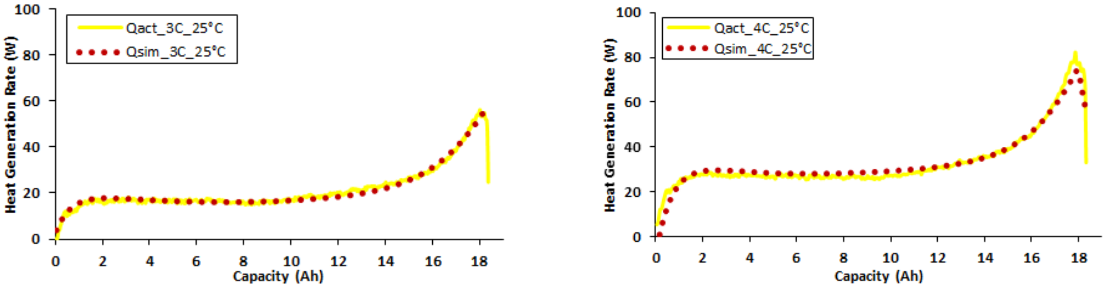

(c) Heat Generation Rate_3C at 25°C **(d) Heat Generation Rate_4C at 25°C**

Figure 5.22: Comparison of actual and simulated heat generation rate at 1C, 2C, 3C and 4C at 25°C BC.

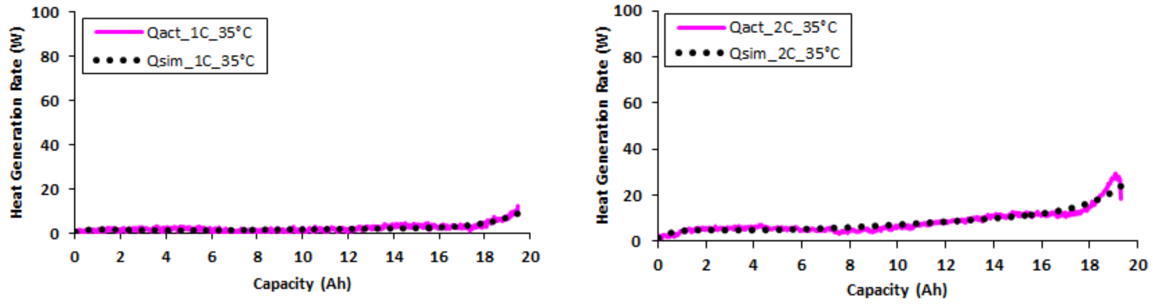

(a) Heat Generation Rate_1C at 35 °C **(b) Heat Generation Rate_2C at 35 °C**

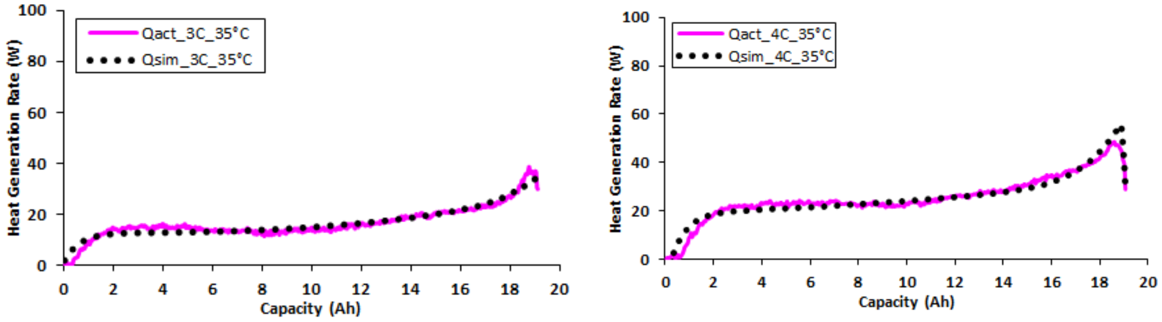

(c) Heat Generation Rate_3C at 35 °C **(d) Heat Generation Rate_4C at 35 °C**

Figure 5.23: Comparison of actual and simulated heat generation rate at 1C, 2C, 3C and 4C at 35°C BC.

5.3 Model 2 : Electrochemical Thermal Model Validation

Figure 5.24 shows a comparison of the temperature contour of a battery at 4C discharge rate with IR image and simulation by the numerical model, as created with ANSYS Fluent software. It can be seen that, with simulation, the temperature at the end of the discharge rate is 67°C while with the IR image the temperature is 70°C, which is quite close. It was also noted that the highest temperature distribution was observed near the tabs (positive and negative electrode) as compared to the middle and the end on the principle surface of the battery along the height of the battery. The lowest spread in temperature is observed at the end on the surface of the battery along the height of the battery. Figure 5.25 shows the validation of experimental and simulated temperature field results at 2C, 3C, and 4C discharge rates. The operating condition for the battery under different C-rates (2C, 3C, and 4C) is at an initial temperature of 22°C. As shown in Figure 5.25, the average surface temperature increases by 14°C, 24°C, and 36°C above the ambient temperature for the discharge rates of 2C, 3C, and 4C. It can also be seen that the surface temperature increases faster at a higher discharge rate. The variation of temperature profile with discharge time may be due to the internal heat generation. The advantage of the MSMD numerical model is its relatively high calculation speed, which ranges in order of minutes, with relatively high accuracy results. The quality of the computational mesh has the higher influence on the actual computational time. The simulation can give more accurate results if the computational mesh is finer and better quality.

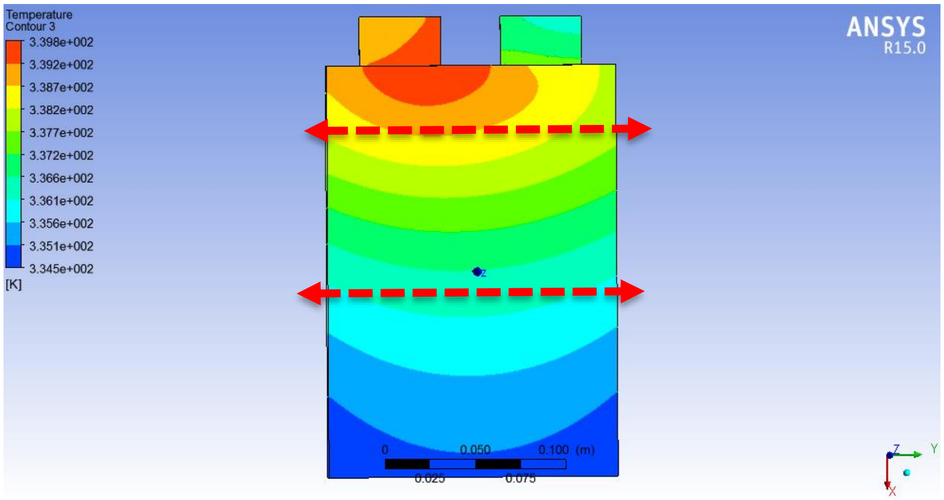

(a) Simulated result at 4C discharge rate

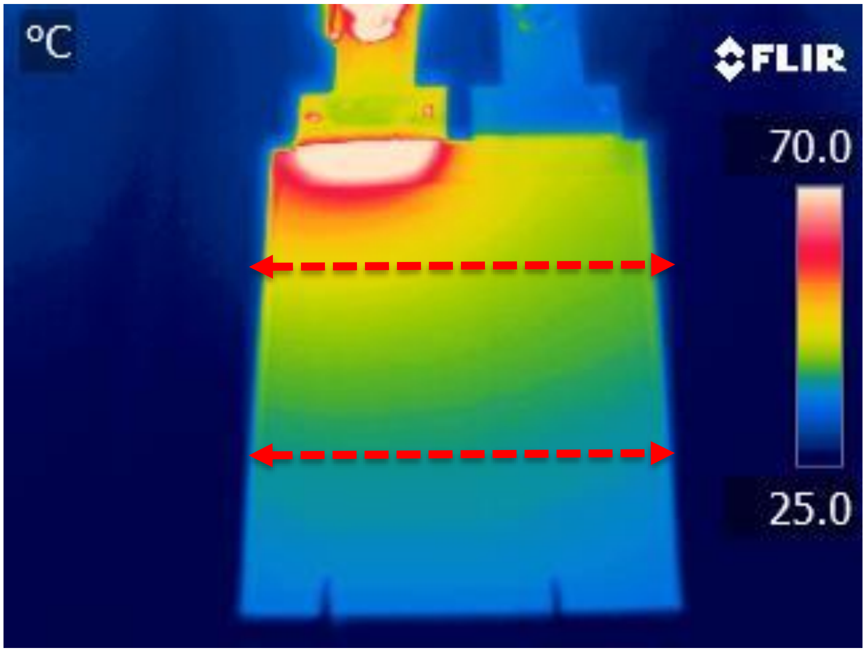

(b) IR imaging result at 4C discharge rate

Figure 5.24: Comparison of temperature contour of battery at 4C discharge rate (simulated and real image).

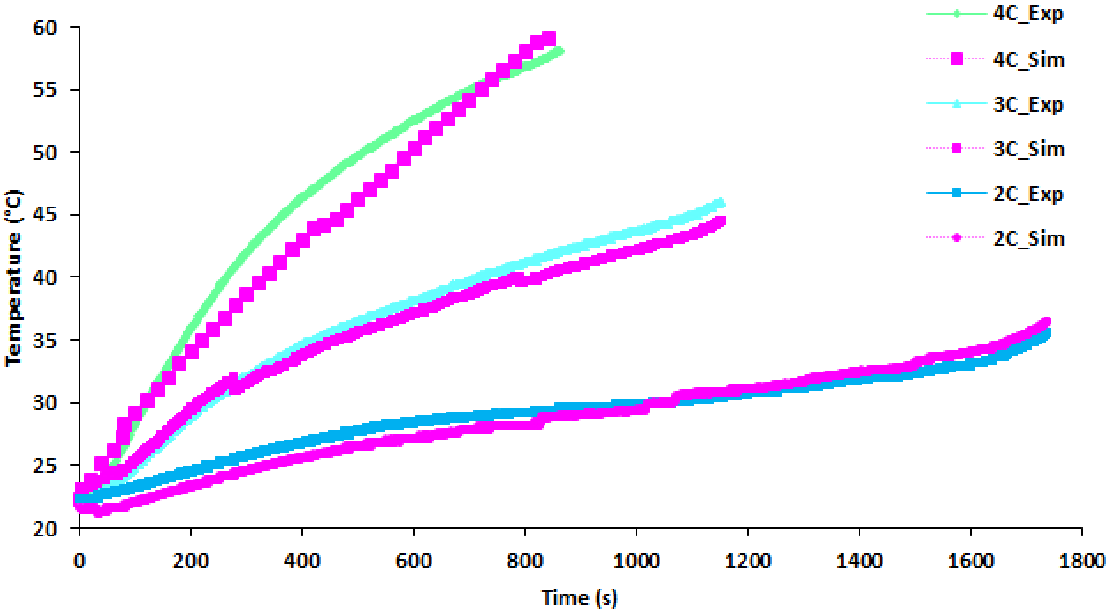

Figure 5.25: Validation of experimental and simulated results at 2C, 3C, and 4C discharge rate.

5.4 Model 3 : Numerical Model Validation

In this section, the results obtained from ANSYS CFD for mini channel cold plates with different discharge rates of 1C, 2C, 3C and 4C and water cooling BCs of 5°C, 15°C, and 25°C are presented. They are discussed in detail in following subsections. This study provides the results showing the temperature and velocity distributions using experimental and computational approaches at different C-rates and boundary conditions (BCs). The physical insight of this kind of study will provide more information to automotive manufacturing companies in order to improve the design of an effective battery cooling system.

5.4.1 Temperature & Velocity Contours at 2C and 5°C, 15°C, and 25°C BCs

Figure 5.26 (a, b, and c) shows the temperature contours obtained from ANSYS CFD at 1C discharge rate and 5°C, 15°C, and 25°C BCs (water cooling). Similarly, Figure 5.27 (a, b, and c) shows the temperature contours obtained from ANSYS CFD at 2C discharge rate and 5°C, 15°C, and 25°C BCs (water cooling). These contours were obtained at the midplane of the cooling plate. It is observed that there is a great impact of BC on battery performance as well as cold plates and that, as the BC increases between 5°C to 25°C for a particular discharge rate of 2C, the temperature contour values also increase. The general cooling patterns are the same, showing greater temperature differences at the inlet of the cooling plate when the water is coldest. There, temperatures vary with the inlet temperature boundary condition, but the overall pattern remains roughly the same.

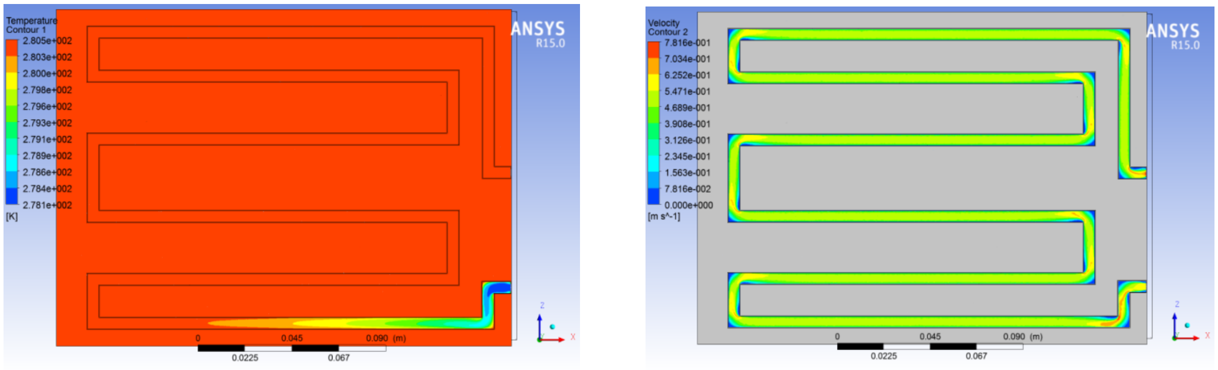

(a) Temperature contour at 1C discharge & 5°C BC **(d) Velocity contour at 1C discharge & 5°C BC**

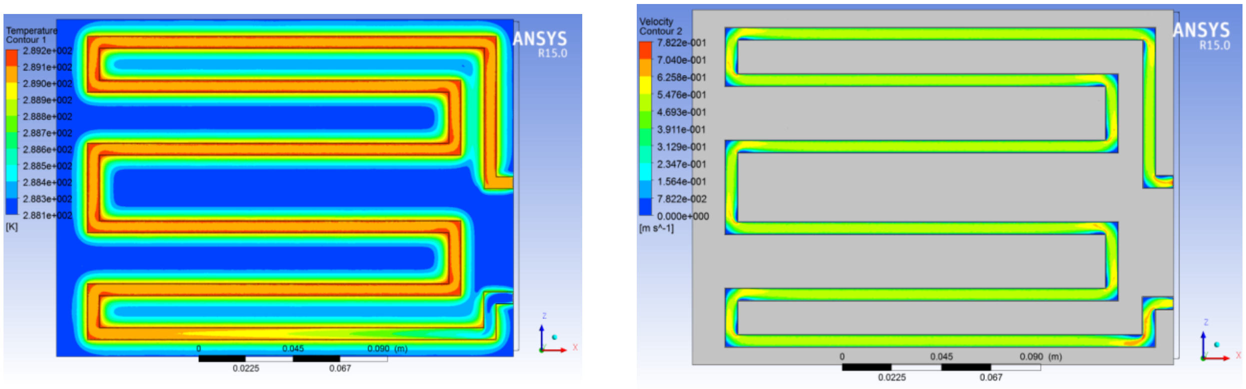

(b) Temperature contour at 1C discharge & 15°C BC **(e) Velocity contour at 1C discharge & 15°C BC**

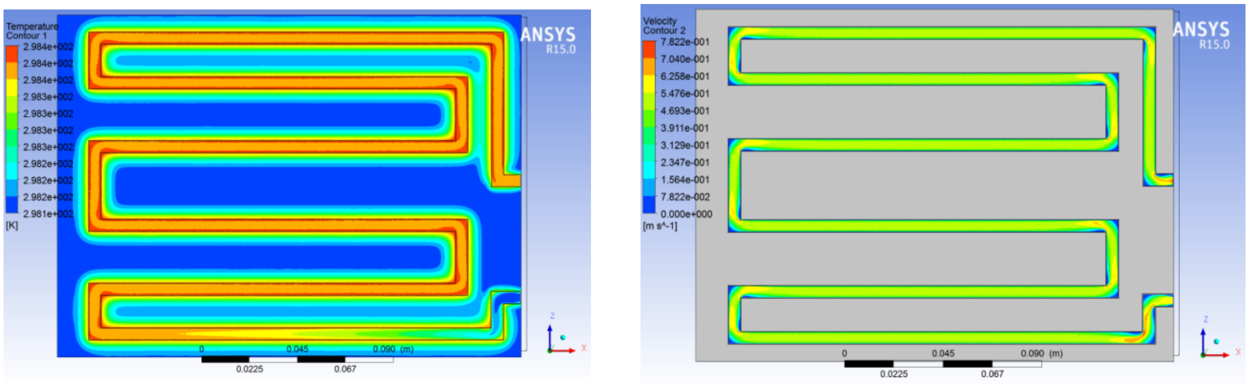

(c) Temperature contour at 1C discharge & 25°C BC **(f) Velocity contour at 1C discharge & 25°C BC**

Figure 5.26: Temperature and velocity contours at 1C and 5°C, 15°C, and 25°C BCs.

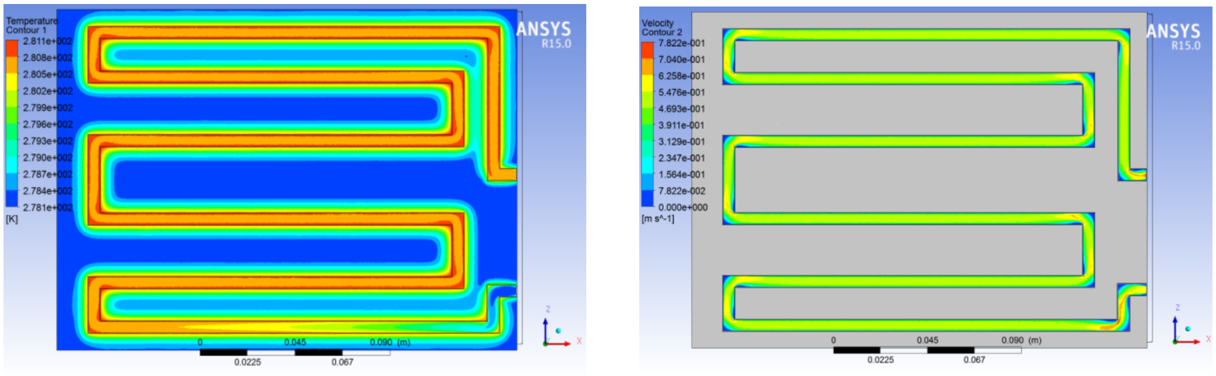

(a) Temperature contour at 2C discharge & 5°C BC **(d) Velocity contour at 2C discharge & 5°C BC**

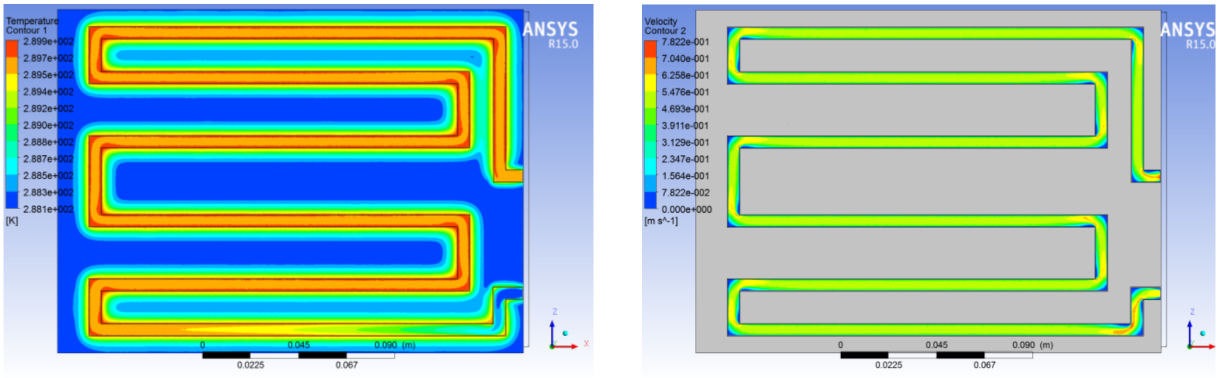

(b) Temperature contour at 2C discharge & 15°C BC **(e) Velocity contour at 2C discharge & 15°C BC**

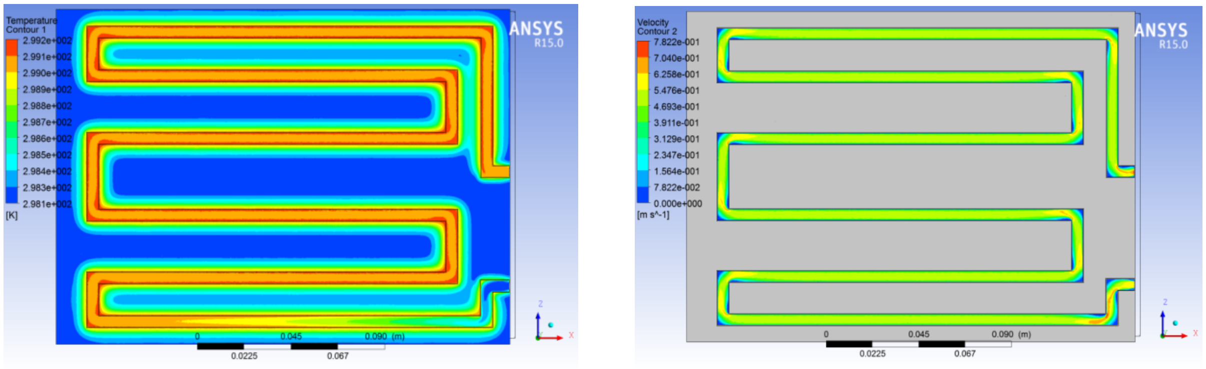

(c) Temperature contour at 2C discharge & 25°C BC **(f) Velocity contour at 2C discharge & 25°C BC**

Figure 5.27: Temperature and velocity contours at 2C and 5°C, 15°C, and 25°C BCs.

There was an exception for the 1C discharge rate and 5°C BC, likely due to the low temperature differences and low discharge rate involved. The cooling patterns follow what is seen on the batteries experimentally, with the outlet being of a higher temperature than the inlet. The velocity contours are identical in all cases. This is expected, given the low temperatures involved in the simulations that would have little to no effect on the density of the water. These results may be affected by the low y$^+$ value, wall functions and turbulence model used. The corresponding velocity contours at 1C and 2C discharge rates and 5°C, 15°C, and 25°C BCs appear in Figure 5.26 (d, e, and f) and Figure 5.27 (d, e, and f).

5.4.2 Temperature & Velocity Contours at 3C and 5°C, 15°C, and 25°C BCs

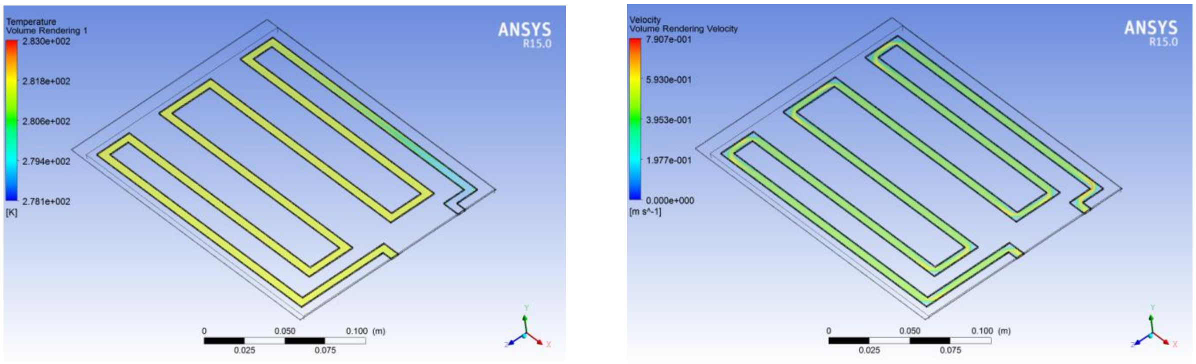

(a) Temperature contour at 3C discharge & 5°C BC **(d) Velocity contour at 3C discharge & 5°C BC**

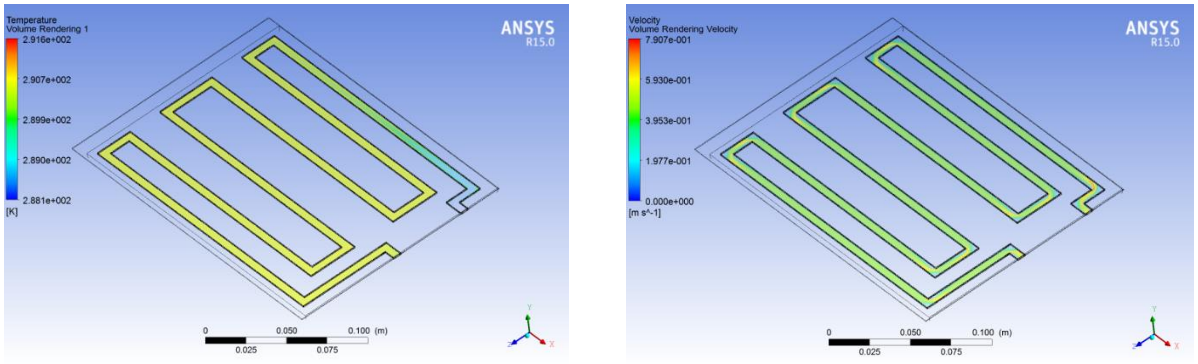

(b) Temperature contour at 3C discharge & 15°C BC **(e) Velocity contour at 3C discharge & 15°C BC**

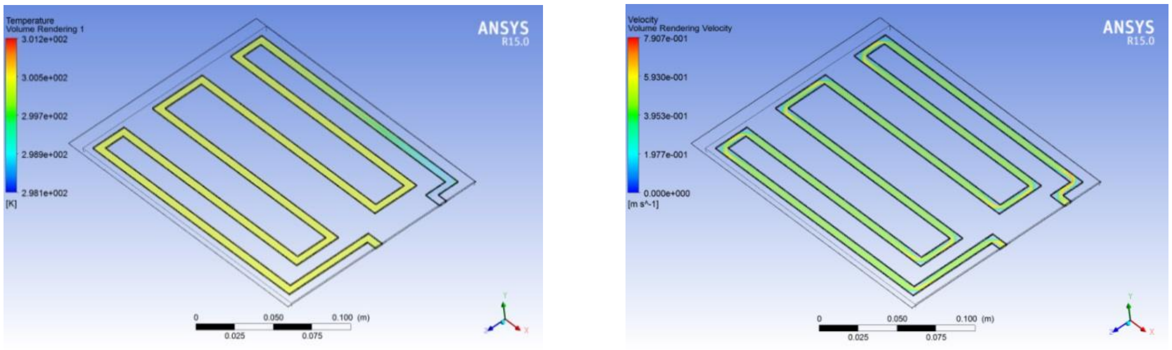

(c) Temperature contour at 3C discharge & 25°C BC **(f) Velocity contour at 3C discharge & 25°C BC**

Figure 5.28: Temperature and velocity contours at 3C and 5°C, 15°C, and 25°C BCs.

Figure 5.28 (a, b, and c) shows the temperature contours at 3C discharge rate and 5°C, 15°C, and 25°C BCs. These contours were obtained at the midplane of the cooling plate. Here, the temperature and velocity contours are presented in 3D form. It is observed that, as the battery discharges, the circulating water is heated, therefore the temperature contours values are increased at the outlet of the cold plate. It is clearly seen that the inlet to the cold plate is colder and the outlet is hotter. The velocity contours for 3C are presented in Figure 5.28 (d, e, and f).

5.4.3 Temperature & Velocity Contours at 4C and 5°C, 15°C, and 25°C BCs

Figure 5.29 (a and b) shows the temperature contours at 4C discharge rate and 5°C BC. It should be noted that Figure 5.29 (a) presents the temperature contour at the inlet plane 1 and Figure 5.29 (b) shows the temperature contour at outlet plane 4. In order to refresh readers, the planes are shown in Figure 4.11. The corresponding velocity contours for inlet plane 1 and outlet plane 4 are shown in Figure 5.29 (c and d). These velocity contours are specifically presented in order to see the effect of flow inside the mini channel cold plates.

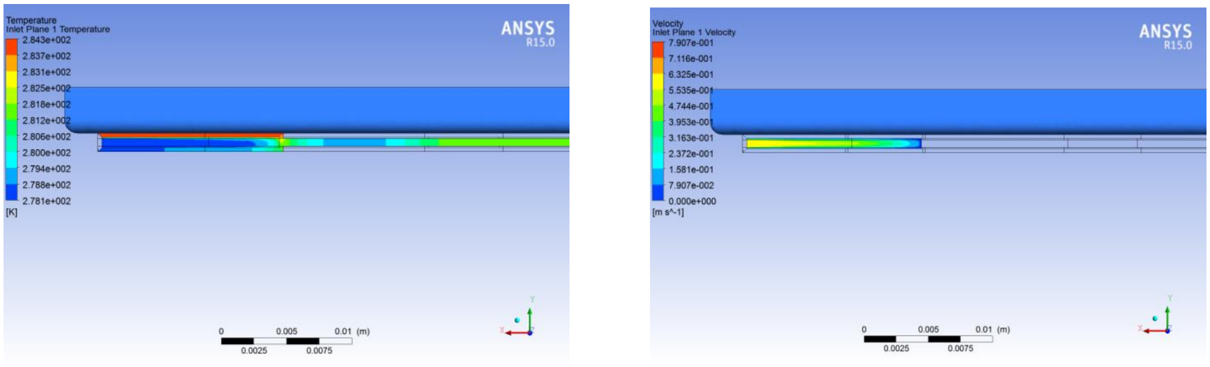

(a) Temperature contour at inlet plane 1 for 4C & 5°C **(c) Velocity contour at inlet plane 1 for 4C & 5°C**

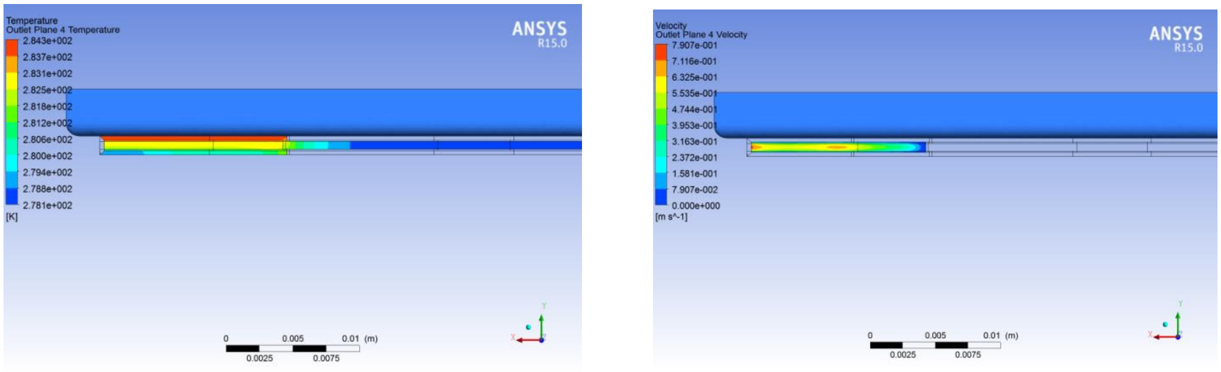

(b) Temperature contour at outlet plane 4 for 4C & 5°C **(d) Velocity contour at outlet plane 4 for 4C & 5°C**

Figure 5.29: Temperature and velocity contours at inlet and outlet planes at 4C and 5°C BC.

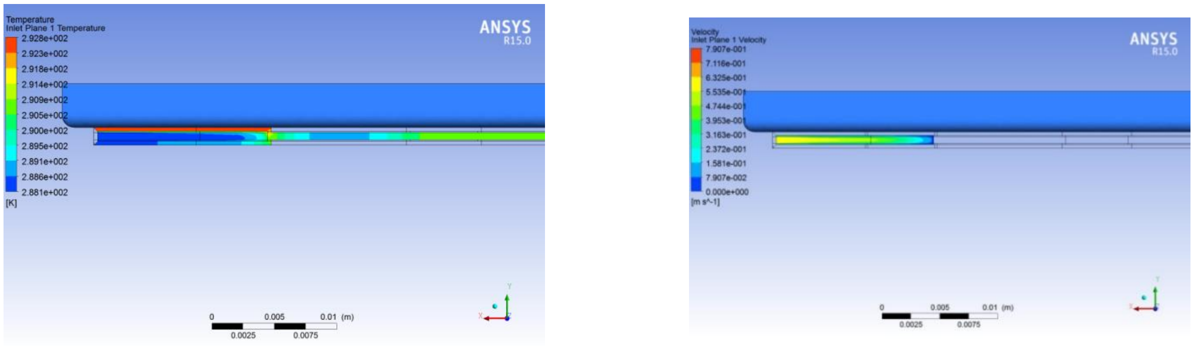

(a) Temperature contour at inlet plane 1 for 4C & 15°C **(c) Velocity contour at inlet plane 1 for 4C & 15°C**

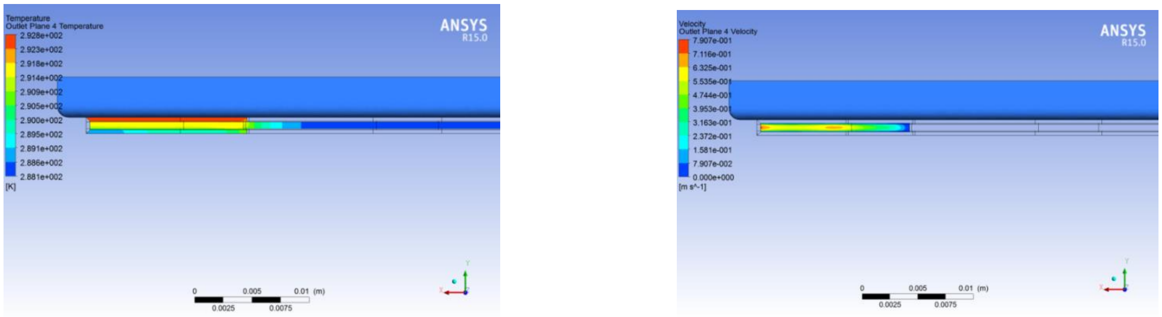

(b) Temperature contour at outlet plane 4 for 4C & 15°C **(d) Velocity contour at outlet plane 4 for 4C & 15°C**

Figure 5.30: Temperature and velocity contours at inlet and outlet planes at 4C and 15°C BC.

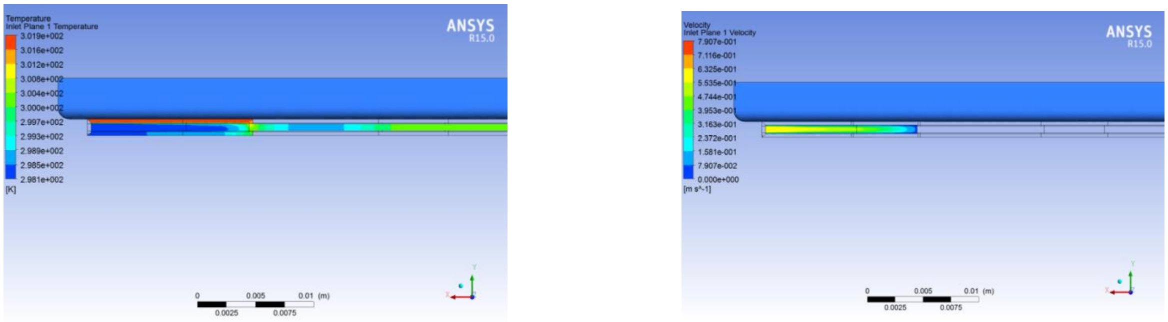

(a) Temperature contour at inlet plane 1 for 4C & 25°C **(c) Velocity contour at inlet plane 1 for 4C & 25°C**

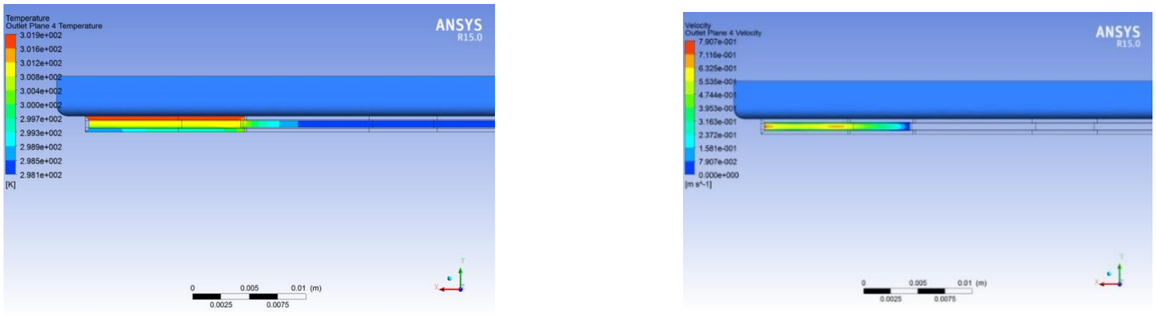

(b) Temperature contour at outlet plane 4 for 4C & 25°C **(d) Velocity contour at outlet plane 4 for 4C & 25°C**

Figure 5.31: Temperature and velocity contours at inlet and outlet planes at 4C and 25°C BC.

Similarly, Figure 5.30 (a and b) and Figure 5.31 (a and b) show the temperature contours at 4C discharge rate and 15°C and 25°C BCs. It is observed that as the discharge rate increases from 1C to 4C, there is also an increase in temperature values. The trend observed is that increased discharge rates and increased BCs result in increased temperatures in the cold plate. Again, the general cooling patterns are the same, similar to the results in the previous Section 5.4.1. There are greater temperature differences between the outlet and the inlet of the cooling plate when the water is coldest. There, temperature values vary with the inlet temperature boundary condition, but the overall pattern remains roughly the same. Similarly, the velocity contours are the same in all cases. The corresponding velocity contours at 4C discharge rate and 15°C and 25°C BCs are shown in Figure 5.30 (c and d) and Figure 5.31 (c and d). Table 5.6 provides a summary of water inlet and outlet temperatures at 1C, 2C, 3C, and 4C discharge rates and different BCs of 5°C, 15°C, and 25°C. It can be seen that the inlet water temperature to the cold plate is constant and the outlet temperature of the water from the cold plate is heated due to heat transfer from the battery to the cold plates. The joule heating is the dominant factor for this heating. As C-rate increases, the water outlet temperature also increases and for the lower C-rate (1C) there is not much change in water temperature. In addition, the effect of the boundary conditions can be seen.

Table 5.6: Summary of water inlet and outlet temperature at 1C, 2C, 3C, and 4C discharge rates and different boundary conditions.

Cooling Type	Boundary Condition [°C]	Position	Water inlet and outlet temperature [K]			
			1C	2C	3C	4C
Water	5	Inlet	278.15	278.15	278.15	278.15
		Outlet	280.94	281.55	283.05	284.31
	15	Inlet	288.42	288.42	288.15	288.15
		Outlet	289.33	289.93	291.60	292.81
	25	Inlet	297.45	298.15	298.10	298.10
		Outlet	298.45	299.22	301.21	301.91

5.5 Model 4 : Battery Degradation Model Validation

Given the drive cycle data, bench testing data and model development described in former sections, this section clarifies the results acquired for individual cycles and on a degradation scale.

5.5.1 Drive Cycle # 1 Results

Figure 5.32 (a) demonstrates the drive cycle # 1 acquired from the EV and the statistics of the same drive cycle are introduced in Table 5.7. The vehicle was driven for 1 hour 4 minutes with a cumulative distance of 126.72 km and a battery state-of-charge range of 94% to 35%. The peak speed was seen as 119.80 km/h and occurred while driving on the highway. The average speed was 71.53 km/h. During this trip, the outside temperature was +2°C. This drive cycle incorporates both city and highway driving. In Figure 5.32 (a), the drive cycle #1 portion between 500 -1700s is identified as aggressive driving on the highway and, in the same way, the segment between 3400-3800s represents city driving. All electrical accessories were operating during this trip.

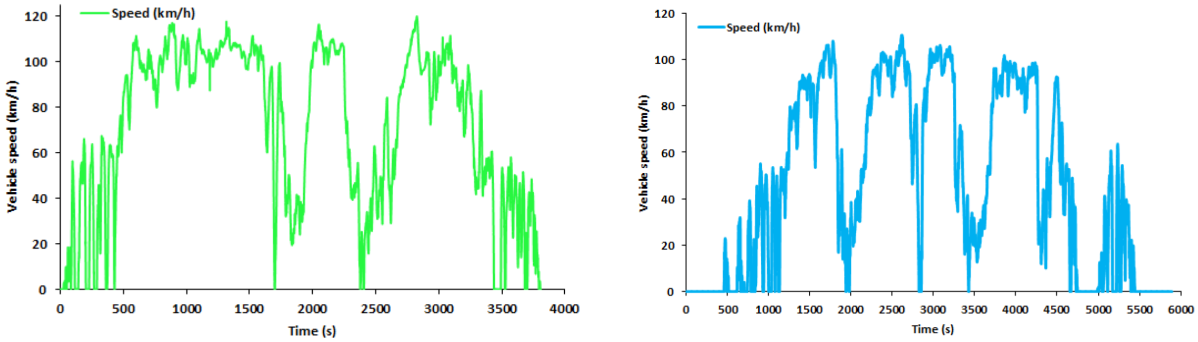

a) Drive cycle # 1 **b) Drive cycle # 2**

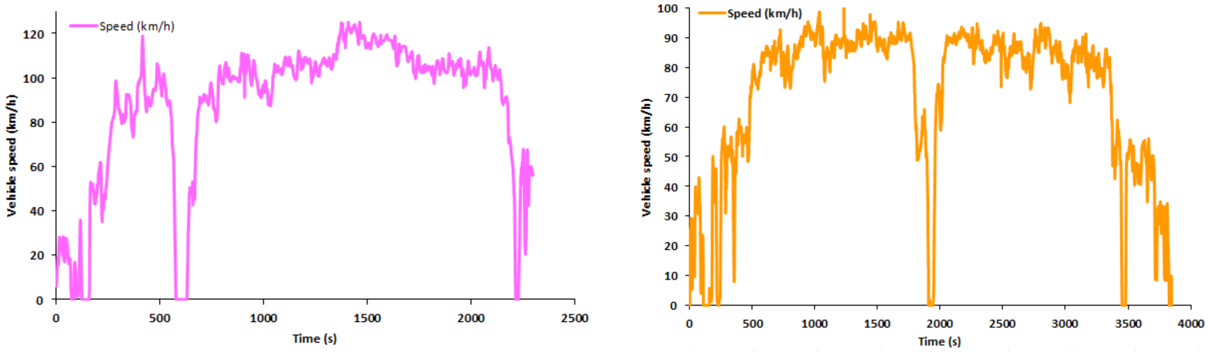

c) Drive cycle # 3 **d) Drive cycle # 4**

Figure 5.32: Details of drive cycles 1, 2, 3, and 4.

5.5.2 Battery Voltage for Drive Cycle # 1

Figure 5.33 (a) demonstrates the comparison of the battery voltage profile obtained from drive cycle # 1 (green colored line) of an EV with the data from the model (red colored line). Overall,

Figure 5.33 (a) shows fair agreement between the experimental and model data, which is indicative of the accuracy of the present model. However, slight discrepancies are observed as the simulated values are slightly higher than the experimental. These discrepancies may be due to regenerative braking and the effect of ambient temperature because the ambient temperature was +2°C when this drive cycle was collected.

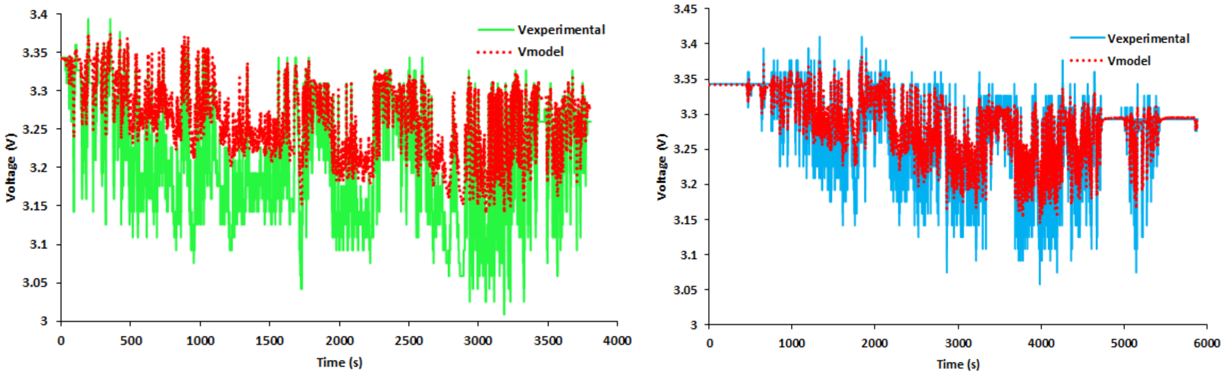

a) Vexp and Vmodel for drive cycle # 1 **b) Vexp and Vmodel for drive cycle # 2**

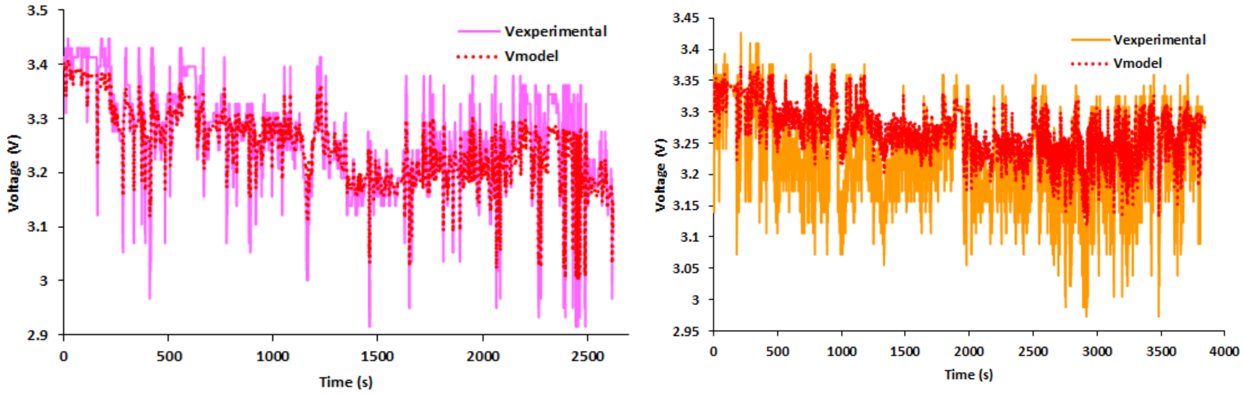

c) Vexp and Vmodel for drive cycle # 3 **d) Vexp and Vmodel for drive cycle # 4**

Figure 5.33: Experimental/Model comparison for battery voltage profile for drive cycles 1, 2, 3, and 4.

5.5.3 Battery SOC for Drive Cycle # 1

Figure 5.34 (a) demonstrates the SOC profile obtained from the EV for drive cycle # 1. Here, we can see an SOC range from 94 to 35%. Figure 5.34 (a) additionally demonstrates a comparison of the measured (experimental) SOC (green colored line) with the values predicted by the model (red colored line). Overall, Figure 5.34 (a) shows good agreement between the experimental and model data, which is characteristic of the accuracy of the present model. There is a great reduction in the

SOC profile from 94% to around 55% because of highway driving. Each of the three battery packs consistently withdrew power, after which an increase and a decrease in the SOC curve are observed due to the regenerative braking in city driving, which involves frequent starts and stops at intersections.

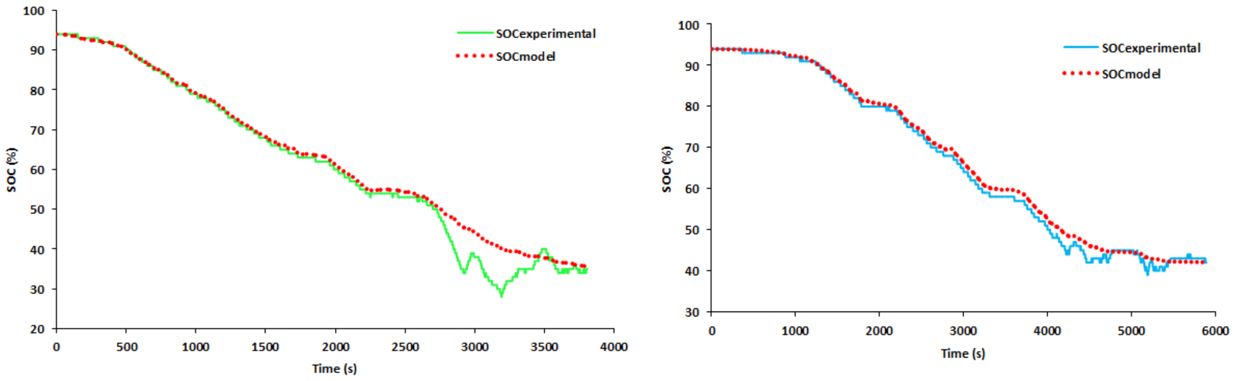

a) SOCexp and SOCmodel for drive cycle # 1 **b) SOCexp and SOCmodel for drive cycle # 2**

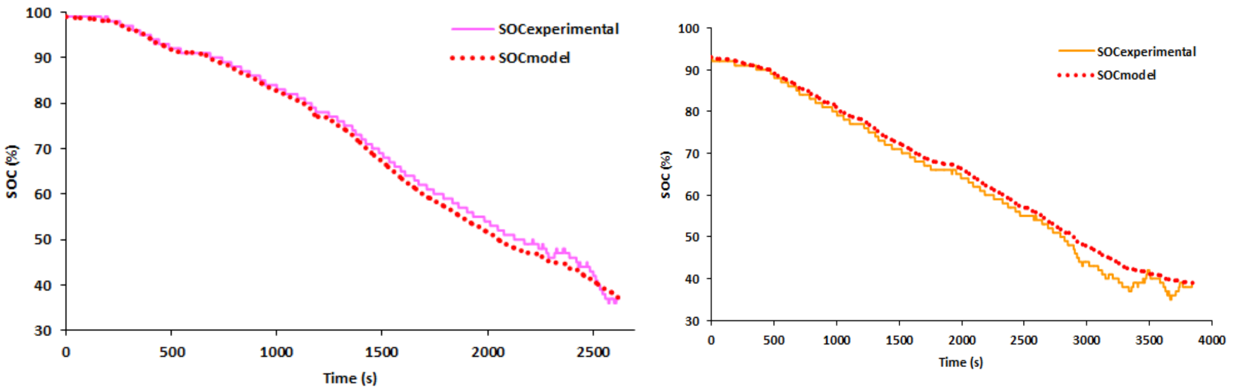

c) SOCexp and SOCmodel for drive cycle # 3 **d) SOCexp and SOCmodel for drive cycle # 4**

Figure 5.34: Experimental/Model comparison for battery SOC profile for drive cycles 1, 2, 3, and 4.

5.5.4 Drive Cycle # 2 Results

Figure 5.32 (b) demonstrates drive cycle # 2 acquired from the EV and the statistics of the same drive cycle are exhibited in Table 5.7. The vehicle was driven for 1 hour 39 minutes with a trip distance of 76 km and a battery state-of-charge of 94- 42%. The peak speed was observed as 110.5 km/h and the average speed was 46.43 km/h. During this trip, the outside temperature was 23°C.This drive cycle # 2 includes aggressive driving on highway 401 in the province of Ontario. The corresponding voltage and SOC validations are shown in Figure 5.33 (b) and Figure 5.34 (b).

5.5.5 Drive Cycle # 3 Results

Figure 5.32 (c) demonstrates drive cycle # 3 acquired from the EV and the statistics of the same drive cycle are displayed in Table 5.7. The vehicle was driven for 44 minutes with a trip distance of 43 km and a range of battery state-of-charge of 99-36%. The peak speed recorded was 125.09 km/h while driving on the highway. The average speed was 59.89 km/h. During this trip, the outside temperature was -6°C. This drive cycle # 3 incorporates both aggressive and gentle driving. The corresponding voltage validation is shown in Figure 5.33 (c), while the SOC profile validation for drive cycle # 3 is displayed in Figure 5.34 (c).

Table 5.7: Details of drive cycles # 1, 2, 3 and 4.

Specification	Drive cycle # 1	Drive cycle # 2	Drive cycle # 3	Drive cycle # 4
Trip Duration (min)	63.46	98.18	43.72	64.13
Trip Distance (km)	126.72	75.68	43.63	75.96
Starting SOC (%)	94	94	99	93
Ending SOC (%)	35	42	36	39
Cycle Average Speed (km/h)	71.53	46.43	59.89	71.07
Cycle Peak Speed (km/h)	119.80	110.5	125.09	102.3
Average Positive Acceleration (m/s^2)	0.59	0.55	1.05	0.63
Peak Positive Acceleration (m/s^2)	3.22	3.35	4.18	3.99
Outside Temperature (°C)	+2	+23	-6	+10

5.5.6 Drive Cycle # 4 Results

Figure 5.32 (d) demonstrates drive cycle # 4 acquired from the EV and the statistics of the same drive cycle are displayed in Table 5.7. The vehicle was driven for 1 hour 4 minutes with a trip distance of 76 km and a range of battery state-of-charge of 93- 39%. The peak speed was observed as 102.3 km/h while driving on the highway. The average speed was 71.07 km/h. During this trip, the outside temperature was 10°C. This drive cycle # 4 incorporates both aggressive and gentle driving. The corresponding voltage validation is shown in Figure 5.33 (d), while the SOC profile validation for drive cycle # 4 is displayed in Figure 5.34 (h).

5.5.7 Degradation Measurement and Modeling

Drive cycle #4 was repeated almost daily for 3 months from July 2nd to September 30th. Day-to-day variations in travel time and battery demand existed due to factors such as traffic and were quantified in Figure 5.35 and Figure 5.36. Figure 5.35 is a histogram showing the variation in daily charge throughput, and Figure 5.36 makes the same comparison for depth-of-discharge. Battery capacity was measured intermittently until September 13th, and the results of these tests are summarized in Table 5.8. Over three months, a capacity fade of 4.60% was observed.

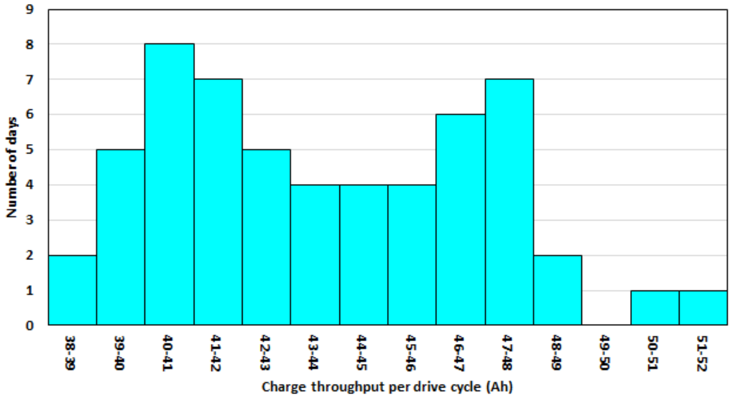

Figure 5.35: Charge throughput histogram.

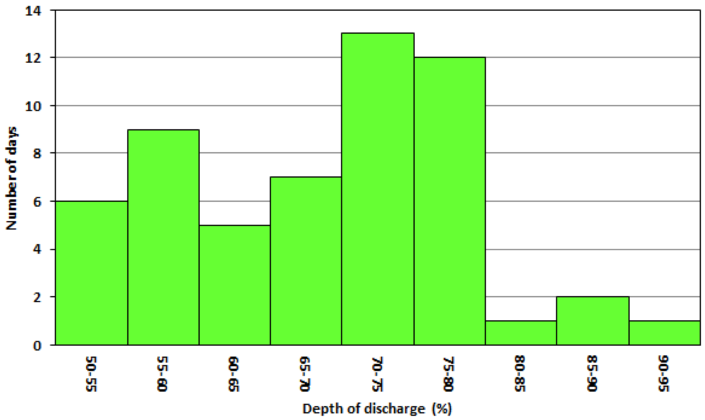

Figure 5.36: Depth of discharge histogram.

This degradation data was used to fit the degradation model in Equations (4.64) and (4.65). DOD, average voltage and charge throughput were calculated for each day of driving and charging to obtain an accurate fit. The parameters were again found using a genetic algorithm in MATLAB, and the result of the fit is shown in Figure 5.37. The model parameters that fitted were as follows:

$$A = -\,2.2439 \times 10^{-8}$$

$$B = 5.2790$$

$$C = 0.0010$$

$$D = 0.0043$$

Table 5.8: Degradation data over three months.

Date	Pack capacity (Ah)	Charge throughput to date (Ah)	Capacity fade %
July 2	60.19	0	0
July 12	59.69	562	0.83
July 23	59.34	1115	1.44
Aug 1	58.61	1600	2.69
Aug 15	57.83	2351	4.04
Aug 28	57.75	3140	4.23
Sept 13	57.54	4025	4.60

Extrapolation of the model using these parameters gives the result that 20% capacity fade would be reached after about 900 cycles, given the charge throughput, DOD and average voltage of the typical drive cycle. These kinds of information will be helpful for vehicle model developers. In addition, the collected data from the vehicles as well as experimental test apparatus will also be provided for the validation of electrochemistry based battery thermal models.

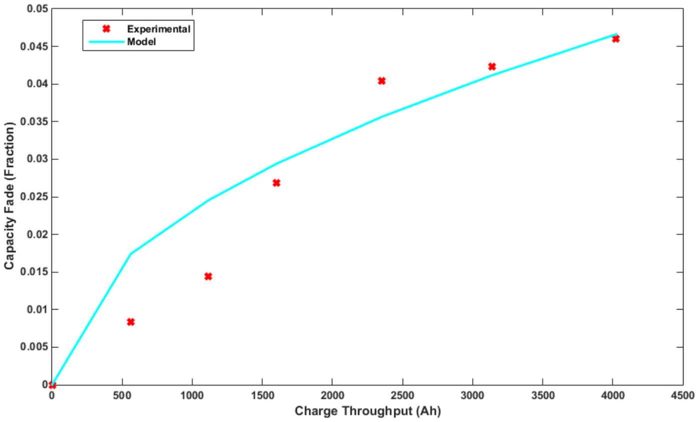

Figure 5.37: Experimental capacity fade measurement and empirically fit model.

Chapter 6

Conclusions and Recommendations

6.1 Conclusions

In this thesis, an experimental thermal characterization of a lithium-ion battery cell and pack (with three $LiFePO_4$ batteries connected in series), thermal imaging, four different models (including the battery thermal model, battery electrochemical thermal model, numerical model for mini channel cold plates for water cooling for large sized $LiFePO_4$ battery, and battery degradation model for an EV) have been performed according to the objectives of the study outlined above. The following conclusions are drawn from the results of this study:

- Thermal characterization of the lithium-ion battery cell showed that the surface temperature distributions of a prismatic lithium-ion battery increased with the discharge rate (1C, 2C, 3C, to 4C) and operating temperature (5°C, 15°C, 25°C, to 35°C). The highest value of the maximum surface temperature for the air cooling method obtained at 4C discharge rate is 46.47°C, while for the liquid cooling method it is 41.44°C at 4C discharge rate and 35°C BC. The effect of BCs on battery cell discharge capacity was also studied and it was found that the battery discharge capacity decreased as the operating temperature (BC) is decreased and also as battery discharge rate is increased.
- From the surface temperature measurements at ten different locations on the principle surface of the battery and heat generation rate, it was clearly shown that the rate of heat generation was not uniform across the principal surface of the battery. Specifically, the thermocouples mounted nearest to the electrodes sensed temperature increases that were larger than at other locations. Measurements of heat flux near the electrodes confirm the high value of heat flux in that area (as high as 2391.31 W/m^2).
- Thermal characterization of the lithium-ion battery pack showed that the surface temperature distributions of the prismatic lithium-ion battery pack increased with the discharge rate (1C, 2C, 3C, to 4C) and operating temperature (5°C, 15°C, 25°C, to 35°C). The highest value of the

maximum surface temperature for the air cooling method obtained at 4C discharge rate is 56.49°C, while for the water cooling method it is 38.82°C at 4C discharge rate and 35°C BC.

- The developed battery thermal model for the prismatic lithium-ion battery using a neural network approach showed good agreement between the actual and simulated values in terms of thermal (average surface temperature) and electrical (voltage distribution) performance. The proposed battery thermal model can be used for any kind of lithium-ion battery. An example of this use was demonstrated by validating the thermal performance of a realistic drive cycle collected from an EV at different environment temperatures.
- The non-uniformity of temperature was visually observed by using an IR image experiment which is an indication of heat generation non-uniformity on a surface. As such, it can be concluded that the area of highest temperature and non-uniformity is the location where heat generation is largest. For the large sized prismatic lithium-ion battery, the area of maximum heat generation appears to be at the external tab to the current collector interface along the top edge of the battery.
- The simulated data from the ECT model showed good validation with the experimental data and IR image for this large sized prismatic lithium-ion battery. It was noted that the highest temperature distribution was observed near the tabs (positive and negative electrodes) compared to the middle and end on the principle surface of the battery along the height of the battery.
- The temperature and velocity distributions were investigated using experimental and computational approaches at different C-rates and boundary conditions using ANSYS. The observed trend is that increased discharge rates and increased BCs result in increased temperatures in the cold plates for a large sized water cooled $LiFePO_4$ battery (the highest value of temperature at cold plate is 301.91K at at 4C-25°C BC).
- From the degradation study, the developed Thevenin battery model utilizing MATLAB along with an empirical degradation model showed good validation in terms of the battery SOC and voltage profiles for different drive cycles collected from an EV at a wide range of ambient conditions of -6°C, 2°C, 10°C, and 23°C. The capacity fade over three months was found experimentally to be 4.60% and when fit to a degradation model and extrapolated, 20% capacity fade was predicted to occur after 900 daily driving cycles (about 2.5 years).

6.2 Recommendations

Several recommendations can be made for future research as listed below:

- The battery test bench should be thermally isolated. The temperature of the battery during cycling is largely influenced by the ambient temperature of the room. Since both the capacity of the battery and the degradation rate are functions of temperature, the results obtained from the test stand contains noise due to the fluctuations in ambient temperature. These fluctuations are caused by the cycle of day and night and by day-to-day changes in temperature. In order to eliminate this noise and obtain more accurate results, the stand should be properly insulated to ensure that temperature fluctuations are only caused by the heat generated during charging/discharging of the battery.
- More thermal testing of the batteries should be carried out at negative coolant/ambient/operating temperatures of -5°C, -15°C, -25°C, and -35°C, in order to evaluate cold climate performance and the resultant heat generation rates. In addition to this, the charge/discharge testing with different cooling fluids should be carried out in order to obtain more thermal data.
- The number of heat flux sensors should be increased to cover the entire battery cell surface. This will enable accurate measurement of the heat flux distribution on the battery cell. This approach can also be used for pack level testing.
- Different cold plate designs, with different cooling flow channel patterns, inlet/outlet conditions, and SOC ranges, could be investigated as potential thermal management systems. Further testing using such systems will enable the effectiveness of possible thermal management systems to be compared.
- Changes in battery design could result in reduced non-uniformity in heat generation and decreased temperature, such as moving external current tabs to opposite ends of the battery. Even, an increase in external tab size has a larger area of contact between the external tabs and current collectors of the electrodes.
- The developed electrochemical-thermal model can be extended to simulate a module or even a pack. However, since the computational time is in the order of an hour, extending this work to higher levels consisting of even 300 cells may result in a very long simulating time.

- The developed two dimensional electrochemical-thermal model can also be modified and extended to a three dimensional battery thermal model. It can be modified by changing the battery geometry from prismatic to cylindrical so that the battery thermal and electrical performance can be studied.

References

[1] A. Babapoor , M. Azizi and G. Karimi, "Thermal management of a Li-ion battery using carbon fiber-PCM," Applied Thermal Engineering, vol. 82, pp. 281-290, 2015.

[2] Y. Lai, S. Du, L. Ai, A. Lihua, Y. Cheng, Y. Tang and J. Ming, "Insight into heat generation of lithium ion batteries based on the electrochemical-thermal model at high discharge rates," International Journal of Hydrogen Energy, vol. 40, pp. 3039-3049, 2015.

[3] K. M. Tan, V. K. Ramachandaramurthy and Y. J. Yong, "Integration of electric vehicles in smart grid: A review on vehicle to grid technologies and optimization techniques," Renewable and Sustainable Energy Reviews, vol. 53, pp. 720-732, 2016.

[4] "National Inventory Report 1990-2012 - Greenhouse Gas Sources and Sinks in Canada," Environment Canada, Gatineau, 1910-7064, 2012.

[5] D. Chakraborty, W. Vaz and A. K. Nandi, "Optimal driving during electric vehicle acceleration using evolutionary algorithms," Applied Soft Computing, vol. 34, pp. 217-235, 2015.

[6] A. K. Nandi, D. Chakraborty and W. Vaz, "Design of a comfortable optimal driving strategy for electric vehicles using multi-objective optimization," Journal of Power Sources, vol. 283, pp. 1-18, 2015.

[7] A. Lajunen and T. Lipman, "Lifecycle cost assessment and carbon dioxide emissions of diesel, natural gas, hybrid electric, fuel cell hybrid and electric transit buses," Energy, vol. 106, pp. 329-342, 2016.

[8] K. Yeow, M. Thelliez, H. Teng and E. Tan, "Thermal analysis of a Li-ion battery system with indirect liquid cooling using finite element analysis approach," SAE International Journal, vol. 1, no. 1, pp. 65-78, 2012.

[9] S. Peck and M. Pierce, "Developement of a temperature dependent Li-ion battery thermal model, ThermoAnalytics Inc.," in SAE International, 2012.

[10] Q. Wang, Q. Sun, P. Ping, X. Zhao, J. Sun and Z. Lin, "Heat transfer in the dynamic cycling of lithium–titanate batteries," International Journal of Heat and Mass Transfer, vol. 93, pp. 896-905, 2016.

[11] Z. Ling, F. Wang, X. Fang, X. Gao and Z. Zhang, "A hybrid thermal management system for lithium ion batteries combining phase change materials with forced-air cooling," Applied Energy, no. 148, pp. 403-409, 2015.

[12] H. Ge, J. Huang, J. Zhang and Z. Li, "Temperature-adaptive alternating current preheating of lithium-ion batteries with lithium deposition prevention," Journal of The Electrochemical Society, vol. 163, no. 2, pp. A290-A299, 2016.

[13] A. Ritchie and W. Howard, "Recent developments and likely advances in lithium-ion batteries," Journal of Power Sources, vol. 162, pp. 809-812, 2006.

[14] Y. Ye, L. H. Saw, Y. Shi and A. A. Tay, "Numerical analyses on optimizing a heat pipe thermal management system for lithium-ion batteries during fast charging," Applied Thermal Engineering, vol. 86, pp. 281-291, 2015.

[15] Y. Xing, Q. Miao, K.-L. Tsui and M. Pecht, "Prognostics and health monitoring for lithium-ion battery," in IEEE International Conference on, 2011.

[16] X. Feng, M. Fang, X. He, M. Ouyang, L. Lu, H. Wang and M. Zhang, "Thermal runaway features of large format prismatic lithium ion battery using extended volume accelerating rate calorimetry," Journal of Power Sources, vol. 255, pp. 294-301, 2014.

[17] L. Lu, X. Han, J. Hua, M. Ouyang and J. Li, "A review on the key issues for lithium-ion battery management in electric vehicles," Journal of Power Sources, vol. 226, pp. 272-288, 2013.

[18] I. Husain, Electric and hybrid vehicles: Design fundamentals, Second edition, Boca Raton, FL, USA: CRC Press, Taylor and Francis Group, 2011.

[19] D. Varma, R. Vaishnana and A. Mittal, "A review of energy sources and power converters for electrified vehicles," International Journal of Renewable Energy and Environmental Engineering, vol. 3, no. 1, pp. 2348-0157, 2015.

[20] M. Brain, "How Electric Cars Work. How Stuff Works 2008 [cited 2014 15 Sept]," Available from: http://www.howstuffworks.com/electric-car.htm., 2014.

[21] M. F. M. Sabri, K. A. Danapalasingam and M. F. Rahmat, "A review on hybrid electric vehicles architecture and energy management strategies," Renewable and Sustainable Energy Reviews, vol. 53, pp. 1433-1442, 2016.

[22] J. Wang, Z. Yang, S. Liu, Q. Zhang and Y. Han, "A comprehensive overview of hybrid construction machinery," Advances in Mechanical Engineering, vol. 8, no. 3, pp. 1-15, 2016.

[23] O. Hegazy, R. Barrero, P. Van den Bossche, M. E. Baghdadi, J. Smekens, J. V. Mierlo, W. Vriens and B. Bogaerts, "Modeling, analysis and feasibility study of new drivetrain architectures for off-highway vehicles," Energy, vol. 109, pp. 1056-1074, 2016.

[24] K. Bergsson, "Hybrid Vehicle Design,The next step in the evolution of the Automobile.," Available from: http://www.hybrid-vehicle.org/hybrid-vehicle-design.html., 2014 [cited 2014 18 Sept]; .

[25] T. A. Burress, S. L. Campbell, C. Coomer, C. W. Ayers, A. A. Wereszczak, J. P. Cunningham, L. D. Marlino, L. E. Seiber and H.-T. Lin, "Evaluation of the 2010 Toyota prius hybrid synergy drive system," Oak Ridge National Laboratory (ORNL), Chicago, 2011.

[26] I. Rahman, P. M. Vasant, B. M. Singh, M. Abdullah-Al-Wadud and N. Adnan, "Review of recent trends in optimization techniques for plug-in hybrid, and electric vehicle charging infrastructures," Renewable and Sustainable Energy Reviews, vol. 58, pp. 1039-1047, 2016.

[27] J. Aghaei, A. Esmaeel Nezhad, A. Rabiee and E. Rahimi, "Contribution of plug-in hybrid electric vehicles in power system uncertainty management," Renewable and Sustainable Energy Reviews, vol. 59, pp. 450-458, 2016.

[28] T. H. Bradley and A. A. Frank, "Design, demonstrations and sustainability impact assessments for plug-in hybrid electric vehicles," Renewable and Sustainable Energy Reviews, vol. 13, no. 1, pp. 115-128, 2009.

[29] R. C. Green II, L. Wang and M. Alam, "The impact of plug-in hybrid electric vehicles on distribution networks: A review and outlook," Renewable and Sustainable Energy Reviews, vol. 15, no. 1, pp. 544-553, 2011.

[30] Transitions to alternative transportation technologies-plug-in hybrid electric vehicles, The National Academies Press, 2010.

[31] M. Mahmoud, R. Garnett, M. Ferguson and P. Kanaroglou, "Electric buses: A review of alternative powertrains," Renewable and Sustainable Energy Reviews, vol. 62, pp. 673-684, 2016.

[32] D. B. Richardson, "Electric vehicles and the electric grid: A review of modeling approaches, impacts, and renewable energy integration," Renewable and Sustainable Energy Reviews, vol. 19, pp. 247-254, 2013.

[33] U. Eberle and R. V. Helmolt, "Sustainable transportation based on electric vehicle concepts: a brief overview," Energy & Environmental Science, vol. 3, no. 6, pp. 689-699, 2010.

[34] J. Y. Yong, V. K. Ramachandaramurthy, K. M. Tan and N. Mithulananthan, "A review on the state-of-the-art technologies of electric vehicle, its impacts and prospects," Renewable and Sustainable Energy Reviews, vol. 49, pp. 365-385, 2015.

[35] "History of electric cars," Edison Tech Center, The miracle of electricity and engineering, New York, 2013.

[36] USEPA, "Vehicle and fuel emissions testing (EPA vehicle chassis dynamometer driving schedules (DDS))," US Environmental Protection Agency, Ann Arbor,MI,USA, 2016.

[37] P. Ramadass, B. Haran, R. White and B. N. Popov. , "Capacity fade of Sony 18650 cells cycled at elevated temperatures: Part I. Cycling performance," Journal of Power Sources, vol. 112, pp. 606-613, 2011.

[38] R. Spotnitz and J. Franklin, "Abuse behaviour of high power Lithium-ion cells," Journal of Power Sources, vol. 113, pp. 81-87, 2011.

[39] C. R. Pals and J. Newman, "Thermal modeling of the lithium/polymer battery," Journal of the Electrochemical Society, vol. 142, no. 10, pp. 3274-3281, 1995.

[40] M. Doyle, T. F. Fuller and J. Newman, "Modeling of galvanostatic charge and discharge of the lithium/polymer/insertion cell," Journal of The Electrochemical Society, vol. 140, no. 6, pp. 1526-1533, 1993.

[41] G.-H. Kim, K. Smith, K.-J. Lee, S. Santhanagopalan and A. Pesaran, "Multi-domain modeling of lithium-ion batteries encompassing multi-physics in varied length scales," Journal of The Electrochemical Society, vol. 158, no. 8, pp. A955-A969, 2011.

[42] L. Rao and J. Newman, "Heat-generation rate and general energy balance for insertion battery systems," Journal of The Electrochemical Society, vol. 144, no. 8, pp. 2697-2704, 1997.

[43] K. E. Thomas and J. Newman, "Thermal modeling of porous insertion electrodes," Journal of the Electrochemical Society, vol. 150, no. 2, pp. A176-A192, 2003.

[44] V. Srinivasan and C. Y. Wang, "Analysis of electrochemical and thermal behavior of Li-ion cells," Journal of The Electrochemical Society, vol. 150, no. 1, pp. A98-A106, 2003.

[45] W. Fang, O. J. Kwon and C.-Y. Wang, "Electrochemical–thermal modeling of automotive Li-ion batteries and experimental validation using a three-electrode cell," International Journal of Energy Research, vol. 34, no. 2, pp. 107-115, 2009.

[46] F. R. Kalhammer, B. M. Kopf, D. H. Swan, V. P. Roan and M. P. Walsh, "Status and prospects for zero emissions vehicle technology, Report of the ARB independent expert panel," Sacramento, California, 2007.

[47] Z. G. Qu, W. Q. Li and W. Q. Tao, "Numerical model of the passive thermal management system for high-power lithium-ion battery by using porous metal foam saturated with phase change material," International Journal of Hydrogen Energy, vol. 39, no. 8, pp. 3904-3913, 2014.

[48] P. Van den Bossche, F. Vergels, J. Van Mierlo, J. Matheys and W. Van Autenboer, "SUBAT: An assessment of sustainable battery technology," Journal of Power Sources, vol. 162, no. 2, pp. 913-919, 2006.

[49] M. Mehrens, P. Axmann and M. Wachtler, "Electrochemical energy storage systems for car applications," HYSA Systems Business Seminar, Capetown, 2009.

[50] R. Lache, P. Nolan, D. Galves, G. Toulemonde, J. Gehrke, K. Sanger, V. Ha, S. Rao and J. Crane, "Electric Cars: Plugged In. Batteries Must Be Included," Deutsche Bank AG, 2008.

[51] "Types of Lithium-ion batteries, Battery University," Available: http://batteryuniversity.com/learn/article/types_of_lithium_ion, 2011.

[52] MIT Electric Vehicle Team, "A guide to understanding battery specifications," December 2008. [Online]. Available: http://web.mit.edu/evt/summary_battery_specifications.pdf.

[53] "Endless-sphere.com (Electric Vehicle and Technology Forum)," Endless Sphere Technology, 13 December 2009. [Online]. Available: https://endless-sphere.com/forums/viewtopic.php?f=14&t=14719&start=30.

[54] "GM-Volt (A123 and Hitachi release energy density for newest batteries)," A123 and Hitachi, 15 June 2008. [Online]. Available: http://gm-volt.com/forum/showthread.php?2940-A123-and-Hitachi-release-energy-density-for-newest-batteries.

[55] J.-K. Park, Principles and applications of lithium secondary batteries, Boschstr. 12, 69469 Weinheim, Germany: Wiley-VCH Verlag & Co. KGaA, 2012.

[56] D. Linden and T. B. Reddy, "Handbook of Batteries, 3rd ed.," McGraw-Hill, 2001.

[57] A. Dinger, R. Martin, X. Mosquet, M. Rabl, D. Rizoulis and G. Sticher, "Batteries for electric cars,challenges,opportunities, and the outlook to 2020," The Boston Consulting Group, 2010.

[58] L. Y. Shao-Horn, C. Delmas, C. E. Nelson and M. A. O'Keefe, "Atomic resolution of lithium ions in LiCoO2," Nature Materials, vol. 2, pp. 464-467, 2003.

[59] C. Julien, "Local structure of lithiated manganese oxides," Solid State Ionics, vol. 177, pp. 11-19, 2006.

[60] J. T. Bloking, S. Y. Chung and Y. M. Chiang, "Electrically conductive phospho-olivines as lithium storage electrodes," Nature Materials, vol. 1, pp. 123-128, 2002.

[61] D. Anderson, "Lowering cost of lithium-ion batteries for EV trains," Sustainable manufacturer network, 2010.

[62] P. Vyroubal, T. Kazda, J. Maxa and J. Vondrák, "Analysis of temperature field in lithium-ion battery by discharging," ECS Transactions, vol. 70, no. 1, pp. 269-273, 2015.

[63] L. Zou, X. Li, Y. P. Zheng, W. Shen and J. Zhang, "Investigations on the modified natural graphite as anode materials in lithium-ion battery," Journal of Physics and Chemistry of Solids, vol. 69, pp. 1265-1271, 2008.

[64] R. J. Brodd and A. Kozawa, Lithium-ion Batteries, New York: Springer Science LLC, 2009.

[65] B. Gao, C. Bower, J. Lorentzen, L. Fleming, A. Kleinhammes, X. P. Tang, L. McNeil, Y. Wu and O. Zhou, "Enhanced saturation lithium composition in ball-milled single-walled carbon nanotubes," Chemical Physics Letters, vol. 327, no. 1-2, pp. 69-75, 2000.

[66] A. R. Kamali and D. J. Fray, "Review on carbon and silicon based materials as anode materials for lithium-ion batteries," Journal of New Materials for Electrochemical Systems, vol. 13, pp. 147-160, 2010.

[67] J. Cho, T.-G. Kim, C. Kim, J.-G. Lee, Y.-W. Kim and B. Park, "Comparison of Al2O3 and AlPO4 coated LiCoO2 cathode materials for a li-ion cell," Journal of Power Sources, vol. 146, no. 1-2, pp. 58-64, 2005.

[68] J. W. Fergus, "Recent developments in cathode materials for lithium ion batteries," Journal of Power Sources, vol. 195, no. 4, p. 939–954, 2010.

[69] B. Xia, H. Cao, Z. Zhang and N. Xu, "LiAlO2-coated LiCoO2 as cathode material for lithium ion batteries," Solid State Ionics, vol. 176, pp. 911-914, 2005.

[70] A. F. Hollenkamp, A. P. Lewandowski, S. W. Donne and A. S. Best, "Cycling and rate performance of Li-LiFePO4 cells in mixed FSI-TFSI room temperature ionic liquids," Journal of Power Sources, vol. 195, pp. 2029-2035, 2010.

[71] G. X. Wang, S. A. Needham, H. K. Liu and V. A. Drozd, "Synthesis and electrochemical performance of doped LiCoO2 materials," Journal of Power Sources, vol. 174, no. 13th International Meeting on Lithium Batteries., pp. 828-831, 2007.

[72] J. Park, S. Lee, J. Kim, S. Ahn, J.-S. Park and Y. Jeong, "Effect of conducting additives on the properties of composite cathodes for lithium-ion batteries," Journal of Solid State Electrochemistry, vol. 14, no. 4, pp. 593-597, 2010.

[73] X. He, J. Li, Y. Cai, Y. Wang, J. Ying, C. Jiang and C. Wan, "Preparation of co-doped spherical spinel LiMn2O4 cathode materials for Li-ion batteries," Journal of Power Sources, vol. 150, pp. 216-222, 2005.

[74] J. P. Tu, Y. Z. Yang and W. K. Zhang, "Spray-drying technology for the synthesis of nanosized LiMn2O4 cathode material," Materials Letters, vol. 61, pp. 864-867, 2007.

[75] H. W. Lee, P. Muralidharan, R. Ruffo, C. M. Mari, Y. Cui and D. K. Kim, "Ultrathin spinel LiMn2O4 nanowires as high power cathode materials for Li-ion batteries," NANO Letters, vol. 10, no. 10, p. 3852–3856, 2010.

[76] R. M. Torresi and F. F. C. Bazito, "Cathodes for lithium-ion batteries: the benefits of using nanostructured materials," Journal of the Brazilian Chemical Society, vol. 17, pp. 627-642, 2006.

[77] H. Chen, Y. Chen, W. Gong, K. Xiang, B. Sun and J. Liu, "Preparation and electrochemical performance of LiFePO4/C composite with network connections of nano-carbon wires," Materials Letters, vol. 65, no. 3, pp. 559-561, 2011.

[78] S. S. Zhang, "A review on the separators of liquid electrolyte Li-ion batteries," Journal of Power Sources, vol. 164, no. 1, pp. 351-364, 2007.

[79] J. Dahn and G. M. Ehrlich, "Lithium-ion batteries," in Linden's Handbook of Batteries, New York, McGraw Hill, 2011, pp. 26.1-26.79.

[80] J. M. Tarascon and M. Armand., "Issues and challenges facing rechargeable lithium batteries," Nature, 414 : 359-367, 2001.

[81] B. Wu, V. Yufit, M. Marinescu, G. J. Offer, R. F. Martinez-Botas and N. P. Brandon, "Coupled thermal–electrochemical modelling of uneven heat generation in lithium-ion battery packs," Journal of Power Sources, vol. 243, pp. 544-554, 2013.

[82] A. A. Pesaran, G. H. Kim and M. Keyser, "Integration issues of cells into battery packs for plug-in and hybrid electric vehicles," in EVS-24 International Battery, Hybrid and Fuel Cell Electric Vehicle Symposium, Stavanger, Norway, 2009.

[83] M. Klein, S. Tong and J. W. Park, "In-plane nonuniform temperature effects on the performance of a large-format lithium-ion pouch cell," Applied Energy, vol. 165, pp. 639-647, 2016.

[84] R. Zhao, S. Zhang, J. Liu and J. Gu, "A review of thermal performance improving methods of lithium ion battery: Electrode modification and thermal management system," Journal of Power Sources, vol. 299, pp. 557-577, 2015.

[85] A. A. Pesaran, "Battery thermal models for hybrid vehicle simulations," Journal of Power Sources, vol. 110, no. 2, pp. 377-382, 2002.

[86] K. Y. Oh and B. I. Epureanu, "A novel thermal swelling model for a rechargeable lithium-ion battery cell," Journal of Power Sources, vol. 303, pp. 86-96, 2016.

[87] C. Lin, S. Xu, G. Chang and J. Liu, "Experiment and simulation of a LiFePO4 battery pack with a passive thermal management system using composite phase change material and graphite sheets," Journal of Power Sources, vol. 275, pp. 742-749, 2015.

[88] Q. Wang, B. Jiang, B. Li and Y. Yan, "A critical review of thermal management models and solutions of lithium-ion batteries for the development of pure electric vehicles," Renewable and Sustainable Energy Reviews, vol. 64, pp. 106-128, 2016.

[89] J. Smith, M. Hinterberger, C. Schneider and J. Koehler, "Energy savings and increased electric vehicle range through improved battery thermal management," Applied Thermal Engineering, vol. 101, pp. 647-656, 2016.

[90] G. H. Kim, A. Pesaran and R. Spotnitz, "A three-dimensional thermal abuse model for lithium-ion cells," Journal of Power Sources, vol. 170, no. 2, pp. 476-489, 2007.

[91] H. Sun, X. Wang, B. Tossan and R. Dixon, "Three-dimensional thermal modeling of a lithium-ion battery pack," Journal of Power Sources, vol. 206, pp. 349-356, 2012.

[92] K. Yeow and H. Teng, "Reducing temperature gradients in high-power, large-capacity lithium-ion cells through ultra-high thermal conductivity heat spreaders embedded in cooling plates for battery systems with indirect liquid cooling," in SAE Technical Paper, Detroit, 2013.

[93] G. Karimi and A. Dehghan, "Thermal management analysis of a lithium-ion battery pack using flow network approach," International Journal of Mechanical Engineering and Mechatronics, vol. 1, no. 1, 2012.

[94] A. Pesaran, G. Kim, K. Smith, S. Santhanagopalan and K. Lee, "Overview of computer-aided engineering of batteries and introduction to multi-scale, multi-dimensional modeling of lithium-ion batteries," U.S. DOE Hydrogen Program and Vehicle Technologies Program, Arlington, Virginia, 2012.

[95] K. Shah, S. J. Drake, D. A. Wetz, J. K. Ostanek, S. P. Miller, J. M. Heinzel and A. Jain, "An experimentally validated transient thermal model for cylindrical Li-ion cells," Journal of Power Sources, vol. 271, pp. 262-268, 2014.

[96] K. Shah, S. J. Drake, D. A. Wetz, J. K. Ostanek, S. P. Miller, J. M. Heinzel and A. Jain, "Modeling of steady-state convective cooling of cylindrical Li-ion cells," Journal of Power Sources, vol. 258, pp. 374-381, 2014.

[97] S. Panchal, I. Dincer, M. Agelin-Chaab, R. Fraser and M. Fowler, "Experimental temperature distributions in a prismatic lithium-ion battery at varying conditions," International Communications in Heat and Mass Transfer, vol. 71, pp. 35-43, 2016.

[98] S. Panchal, I. Dincer, M. Agelin-Chaab, R. Fraser and M. Fowler, "Experimental and simulated temperature variations in a LiFePO4-20 Ah battery during discharge process," Applied Energy, vol. 180, pp. 504-515, 2016.

[99] Z. Rao, Y. Huo, X. Liu and G. Zhang, "Experimental investigation of battery thermal management system for electric vehicle based on paraffin/copper foam," Journal of the Energy Institute, vol. 88, no. 3, pp. 241-246, 2015.

[100] P. Taheri, M. Yazdanpour and M. Bahrami, "Transient three-dimensional thermal model for batteries with thin electrodes," Journal of Power Sources, vol. 243, pp. 280-289, 2013.

[101] C. Forgez, D. V. Do, G. Friedrich, M. Morcrette and C. Delacourt, "Thermal modeling of a cylindrical LiFePO4/graphite lithium-ion battery," Journal of Power Sources, vol. 195, no. 9, pp. 2961-2968, 2010.

[102] W. B. Ye, "Thermal simulation and evaluation for non-uniformity detection of electrode," Applied Thermal Engineering, vol. 96, pp. 583-592, 2016.

[103] Y. Ye, Y. Shi, N. Cai, J. Lee and X. He, "Electro-thermal modeling and experimental validation for lithium-ion battery," Journal of Power Sources, vol. 199, pp. 227-238, 2012.

[104] C. Mi, B. Li, D. Buck and N. Ota, "Advanced electro-thermal modeling of lithium-ion battery system for hybrid electric vehicle applications," IEEE, 2007.

[105] R. E. Williford, V. V. Viswanathan and J. G. Zhang, "Effects of entropy changes in anodes and cathodes on the thermal behavior of lithium-ion batteries," Journal of Power Sources, vol. 189, pp. 101-107, 2009.

[106] S. Garimella, T. M. Bandhauer and T. F. Fuller, "A critical review of thermal issues in lithium-ion batteries," Journal of the Electrochemical Society, vol. 158, pp. R1-R24, 2011.

[107] H. Maleki, J. S. Hong, Al Hallaj and L. Redey, "Electrochemical-calorimetric studies of lithium-ion cells," Journal of the Electrochemical Society, vol. 145, pp. 1489-1591, 1998.

[108] Al Hallaj and J. R. Selman, "Characterization of commercial li-ion batteries using electrochemical-calorimetric measurements," Journal of Power Sources, vol. 87, pp. 186-194, 2000.

[109] Al-Hallaj, H. Maleki, J. S. Hong and J. R. Selman, "Thermal modeling and design consideration of lithium-ion batteries," Journal of Power Sources, vol. 83, pp. 1-8, 1999.

[110] J. S. Kim, J. Prakash and J. R. Selman, "Thermal characteristics of LiMn204 spinel," Electrochemical and Solid-state Letters, vol. 4, no. 9, pp. A141-A144, 2001.

[111] Y. Kobayashi, K. Kumao, T. Takei and K. Iwahori, "Precise electrochemical calotimetry of liCoO2/graphite lithium-ion cell," Journal of the Electrochemcial Society, vol. 149, no. 8, pp. A978-A982, 2002.

[112] A. Keller and G. Whitehead, "Thermal characteristics of electric vehicle batteries.," Electric Vehicle R & D: Technical Report No. 1560911727., 1991.

[113] C. M. Kuper, M. Hoh, G. Houchin-Miller and J. Fuhr, "Thermal management of hybrid vehicle battery systems," EVS24, Stavanger, Norway, pp 1-10., 2009.

[114] H. Fathabadi, "High thermal performance lithium-ion battery pack including hybrid active–passive thermal management system for using in hybrid/electric vehicles," Energy, vol. 70, pp. 529-538, 2014.

[115] R. Liu, J. Chen, J. Xun, K. Jiao and Q. Du, "Numerical investigation of thermal behaviors in lithium-ion battery stack discharge," Applied Energy, vol. 132, pp. 288-297, 2014.

[116] C. Lin, S. Xu, Z. Li, B. Li, G. Chang and J. Liu, "Thermal analysis of large-capacity LiFePO4 power batteries for electric vehicles," Journal of Power Sources, vol. 294, pp. 633-642, 2015.

[117] M. C. Niculuta and C. Veje, "Analysis of the thermal behavior of a LiFePO4," Journal of Physics, vol. 395, 2012.

[118] M. Streza, C. Nuţ, C. Tudoran, V. Bunea, A. Calborean and C. Morari, "Distribution of current in the electrodes of lead-acid batteries: a thermographic analysis approach," Journal of Physics D : Applied Physics, vol. 49, no. 5, pp. 55503-55510, 2016.

[119] M. A. Keyser, A. Pesaran and M. Mihalic, "Thermal characterization of advanced lithium-ion polymer cells," in Third Advanced Automotive Battery Conference, 2003.

[120] S. J. Bazinski and X. Wang, "Predicting heat generation in a lithium-ion pouch cell through thermography and the lumped capacitance model," Journal of Power Sources, vol. 305, pp. 97-105, 2016.

[121] Y. Chen and J. Evans, "Thermal analysis of lithium-ion batteries," Journal of Electrochemical Society, vol. 141, pp. 2947-2952, 1994.

[122] G. Wierschem, B. McKinney and E. Nrotek, "Thermal management of lead-acid batteries for electric vehicles," in Research and developement testing, Detroit, 1993.

[123] Y. Abdul-Quadir, T. Laurila, J. Karppinen and M. Paulasto-Kröckel, "Thermal simulation of high-power Li-ion battery with LiMn1/3Ni1/3Co1/3O2 cathode on cell and module levels," International Journal of Energy Research, vol. 38, pp. 564-572, 2014.

[124] Y. Abdul-Quadir, T. Laurila, J. Karppinen, K. Jalkanen, K. Vuorilehto, L. Skogström and M. Paulasto-Kröckel, "Heat generation in high power prismatic Li-ion battery cell with LiMnNiCoO2 cathode material," International Journal of Energy Research, vol. 38, pp. 1424-1437, 2014.

[125] S. J. Drake, M. Martin, D. A. Wetz, J. K. Ostanek, S. P. Miller and A. Jain, "Heat generation rate measurement in a Li-ion cell at large C-rates through temperature and heat flux measurements," Journal of Power Sources, vol. 285, pp. 266-273, 2015.

[126] X. Feng, J. Sun, M. Ouyang, F. Wang, X. He, L. Lu and H. Peng, "Characterization of penetration induced thermal runaway propagation process within a large format lithium ion battery module," Journal of Power Sources, vol. 275, pp. 261-273, 2015.

[127] X. Feng, X. He, M. Ouyang, L. Lu, P. Wu, C. Kulp and S. Prasser, "Thermal runaway propagation model for designing a safer battery pack with 25 Ah LiNixCoyMnzO2 large format lithium ion battery," Applied Energy, vol. 154, pp. 74-91, 2015.

[128] P. T. Coman, S. Rayman and R. White, "A lumped model of venting during thermal runaway in a cylindrical lithium cobalt oxide lithium-ion cell," Journal of Power Sources, vol. 307, pp. 56-62, 2016.

[129] H. Fathabadi, "A novel design including cooling media for Lithium-ion batteries pack used in hybrid and electric vehicles," Journal of Power Sources, vol. 245, pp. 495-500, 2014.

[130] W. B. Gu and C. Y. Wang, "Thermal-electrochemical modeling of battery systems," Journal of The Electrochemical Society, vol. 147, no. 8, pp. 2910-2922, 2000.

[131] U. S. Kim, C. B. Shin and C.-S. Kim, "Effect of electrode configuration on the thermal behavior of a lithium-polymer battery," Journal of Power Sources, vol. 180, no. 2, pp. 909-916, 2008.

[132] U. S. Kim, C. B. Shin and C. S. Kim, "Modeling for the scale-up of a lithium-ion polymer battery," Journal of Power Sources, vol. 189, pp. 841-846, 2009.

[133] A. A. Pesaran, A. Vlahinos and S. D. Burch, "Thermal performance of EV and HEV battery modules and packs," National Renewable Energy Laboratory, Golden, Colorado, 1997.

[134] S. Panchal, I. Dincer, M. Agelin-Chaab, R. Fraser and M. Fowler, "Experimental and theoretical investigation of temperature distributions in a prismatic lithium-ion battery," International Journal of Thermal Sciences, vol. 99, pp. 204-212, 2016.

[135] S. Panchal, I. Dincer, M. Agelin-Chaab, R. Fraser and M. Fowler, "Thermal modeling and validation of temperature distributions in a prismatic lithium-ion battery at different discharge rates and varying boundary conditions," Applied Thermal Engineering, vol. 96, pp. 190-199, 2016.

[136] S. Panchal, I. Dincer, M. Agelin-Chaab, R. Fraser and M. Fowler, "Experimental and theoretical investigations of heat generation rates for a water cooled LiFePO4 battery," International Journal of Heat and Mass Transfer, vol. 101, pp. 1093-1102, 2016.

[137] S. Panchal, I. Dincer, M. Agelin-Chaab, R. Fraser and M. Fowler, "Experimental investigation and simulation of temperature distributions in a 16Ah-LiMnNiCoO2 battery during rapid discharge rates," Heat and Mass Transfer, vol. 52, no. 12, pp. 1-10, 2016.

[138] A. Pruteanu, B. V. Florean, G. Maria Moraru and R. C. Ciobanu, "Development of a thermal simulation and testing model for a superior lithium-ion-polymer battery," in Optimization of Electrical and Electronic Equipment (OPTIM), IEEE, pages 947–952, 2012.

[139] J. Yi, U. S. Kim, C. B. Shin, T. Han and S. Park, "Three-dimensional thermal modeling of a lithium-ion battery considering the combined effects of the electrical and thermal contact resistances between current collecting tab and lead wire," Journal of the Electrochemical Society, vol. 160, no. 3, pp. 437-443, 2013.

[140] C. Alaoui, "Solid-state thermal management for lithium-ion EV batteries," IEEE Transactions on Vehicular Technology, vol. 62, no. 1, pp. 98-107, 2013.

[141] X. Hu, S. Asgari, S. Lin, S. Stanton and W. Lian, "A linear parameter-varying model for HEV/EV battery thermal modeling," in Energy Conversion Congress and Exposition (ECCE), IEEE, pages 1643-1649, 2012.

[142] A. Smyshlyaev, M. Krstic, N. Chaturvedi, J. Ahmed and A. Kojic, "PDE model for thermal dynamics of a large Li-ion battery pack," in American Control Conference (ACC), IEEE, pages 959-964, 2011.

[143] J. Li, L. Wang, C. Lyu, H. Wang and X. Liu, "New method for parameter estimation of an electrochemical-thermal coupling model for LiCoO2 battery," Journal of Power Sources, vol. 307, pp. 220-230, 2016.

[144] O. Erdinc, B. Vural and M. Uzunoglu, "A dynamic lithium-ion battery model considering the effects of temperature and capacity fading," IEEE Clean Electrical Power, pp. 383-386, 2009.

[145] L. Lam, P. Bauer and E. Kelder, "A practical circuit-based model for lithium-ion battery cells in electric vehicle applications," in In Telecommunications Energy Conference (INTELEC), IEEE 33rd International, pp. 1–9., 2011.

[146] A. Ostadi, M. Kazerani and S. K. Chen, "Optimal Sizing of the Energy Storage System (ESS) in a Battery-Electric Vehicle," Transportation Electrication Conference and Expo (ITEC), IEEE, pp. 1-6, 2013.

[147] J. Newman and W. Tiedemann, "Porous-electrode theory with battery application," AIChE, vol. 21, pp. 25-41, 1975.

[148] T. F. Fuller, M. Doyle and J. Newman, "Simulation and optimization of the dual lithium-ion insertation cell," Journal of Electrochemical Society, vol. 141, pp. 1-10, 1994.

[149] C. Y. Wang, W. B. Gu and B. Y. Liaw, "Micro-macroscopic coupled modeling of batteries and fuel cells: Part II: Applications to Ni-Cd and Ni-MH cells," Journal of Electrochemical Society, vol. 145, pp. 3418-3427, 1998.

[150] W. B. Gu and C. Y. Wang, "Thermal and electrochemical coupled modeling of a lithium-ion cell," Journal of Electrochemical Society, vol. 99, pp. 748-762, 2000.

[151] G. Li and S. Li, "Physics-based CFD simulation of lithium-ion battery under the FUDS driving cycle," ECS Transactions, vol. 64, no. 33, pp. 1-14, 2015.

[152] M. M. Majdabadi, S. Farhad, M. Farkhondeh, R. Fraser and M. Fowler, "Simplified electrochemical multi-particle model for LiFePO4 cathodes in lithium-ion batteries," Journal of Power Sources, vol. 275, no. 1, pp. 633-543, 2015.

[153] M. Mastali , M. Farkhondeh, S. Farhad, R. Fraser and M. Fowler, "Electrochemical modeling of commercial LiFePO4 and graphite electrodes: kinetic and transport properties and their temperature dependence," Journal of The Electrochemical Society, vol. 163, no. 13, pp. A2803-A2816, 2016.

[154] M. Xu, Z. Zhang, X. Wang, L. Jia and L. Yang, "A pseudo three-dimensional electrochemical thermal model of a prismatic LiFePO4 battery during discharge process," Energy, vol. 80, pp. 303-317, 2015.

[155] N. Yang, X. Zhang, B. Shang and G. Li, "Unbalanced discharging and aging due to temperature differences among the cells in a lithium-ion battery pack with parallel combination," Journal of Power Sources, vol. 306, pp. 733-741, 2016.

[156] W. Huo, H. He and F. Sun, "Electrochemical–thermal modeling for a ternary lithium ion battery during discharging and driving cycle testing," RSC Advances, vol. 71, no. 5, pp. 57599-57607, 2015.

[157] H. He, R. Xiong and J. Fan, "Evaluation of lithium-ion battery equivalent circuit models for state of charge estimation by an experimental approach," Energies, vol. 4, pp. 582-598, March 2011.

[158] A. Fotouhi, D. J. Auger, K. Propp, S. Longo and M. Wild, "A review on electric vehicle battery modelling : From Lithium-ion toward Lithium–Sulphur," Renewable and Sustainable Energy Reviews, vol. 56, pp. 1008-1021, 2016.

[159] I. Sharma, "Operation of distribution systems with PEVs and smart loads," Ph.D thesis, Electrical and Computer Enginering, Waterloo, 2014.

[160] K. Hornik, M. Stinchcombe and H. White, "Multilayer feedforward networks are universal approximators," Journal on Neural Networks, vol. 2, no. 5, pp. 359-366, 1989.

[161] F. Scarselli and A. Chung Tsoi, "Universal approximation using feedforward neural networks: A survey of some existing methods, and some new results," Journal on Neural Networks, vol. 11, no. 1, pp. 15-37, 1998.

[162] Q. J. Zhang, C. Gupta and C. Kuldip, "Neural Network Structure," http://www.ieee.cz/knihovna/Zhang/Zhang100-ch03.pdf.

[163] A. Raghurajan, "Optimal demand response of controllable loads in isolated microgrids," University of Waterloo, Waterloo, 2014.

[164] "Divide Data for Optimal Neural Network Training," MATLAB, 2016. [Online]. Available: http://www.mathworks.com/help/nnet/ug/.

[165] A. Samba, N. Omar, H. Gualous, Y. Firouz, P. V. d. Bossche, J. V. Mierlo and T. I. Boubekeur, "Development of an advanced two-dimensional thermal model for large size lithium-ion pouch cells," Electrochimica Acta, vol. 117, pp. 246-254, 2014.

[166] C. H. Wang, T. Lin, J. T. Huang and Z. H. Rao, "Temperature response of a high power lithium-ion battery subjected to high current discharge," Materials Research Innovations, vol. 19, pp. 156-160, 2015.

[167] L. W. Jin, P. S. Lee, X. X. Kong, Y. Fan and S. K. Chou, "Ultra-thin minichannel LCP for EV battery thermal management," Applied Energy, vol. 113, pp. 1786-1794, 2014.

[168] A. Jarrett and I. Y. Kim, "Design optimization of electric vehicle battery cooling plates for thermal performance," Journal of Power Sources, vol. 196, no. 23, pp. 10359-10368, 2011.

[169] J. Zhao, Z. Rao and Y. Li, "Thermal performance of mini-channel liquid cooled cylinder based battery thermal management for cylindrical lithium-ion power battery," Energy Conversion and Management, vol. 103, pp. 157-165, 2015.

[170] L. H. Saw, Y. Ye, A. A. Tay, W. T. Chong, S. H. Kuan and M. C. Yew, "Computational fluid dynamic and thermal analysis of lithium-ion battery pack with air cooling," Applied Energy, vol. 177, pp. 783-792, 2016.

[171] S. Mohammadian, Y. L. He and Y. Zhang, "Internal cooling of a lithium-ion battery using electrolyte as coolant through microchannels embedded inside the electrodes," Journal of Power Sources, vol. 293, pp. 458-466, 2015.

[172] Y. Huo, Z. Rao, X. Liu and J. Zhao, "Investigation of power battery thermal management by using mini-channel cold plate," Energy Conversion and Management, vol. 89, pp. 387-395, 2015.

[173] B. Y. Liaw and M. Dubarry, "From driving cycle analysis to understanding battery performance in real-life electric hybrid vehicle operation," Journal of Power Sources, vol. 174, no. 1, pp. 76-88, 2007.

[174] Y. Zhang, C. Y. Wang and X. Tang, "Cycling degradation of an automotive LiFePO4 lithium-ion battery," Journal of Power Sources, vol. 196, pp. 1513-1520, 2011.

[175] M. Dubarry, V. Svoboda, R. Hwu and B. Y. Liaw, "A roadmap to understand battery performance in electric and hybrid vehicle operation," Journal of Power Sources, vol. 172, no. 2, pp. 366-372, 2007.

[176] Y. Merla, B. Wu, V. Yufit, N. P. Brandon, R. F. Martinez-Botas and G. J. Offer, "Novel application of differential thermal voltammetry as an in-depth state-of-health diagnosis method for lithium-ion batteries," Journal of Power Sources, vol. 307, pp. 308-319, 2016.

[177] A. M. Andersson, D. P. Abraham, R. Haasch, S. MacLaren, J. Liu and K. Amine, "Surface characterization of electrodes from high power lithium-ion batteries," Journal of The Electrochemical Society, vol. 149, no. 10, pp. A1358-A1369, 2002.

[178] I. Buchmann, "How to store batteries," Battery University, 2015.

[179] R. Spotnitz, "Simulation of capacity fade in lithium-ion batteries," Journal of Power Sources, vol. 113, no. 1, pp. 72-80, 2003.

[180] W. C. Limited, "Cell chemistries - How batteries work, Electropaedia-battery and energy technologies," 2011. [Online]. Available: http://www.mpoweruk.com/chemistries.htm.

[181] Q. Zhang and R. E. White, "Capacity fade analysis of a lithium ion cell," Journal of Power Sources, vol. 179, no. 2, pp. 793-798, 2008.

[182] J. Jaguemont, L. Boulon and Y. Dubé, "A comprehensive review of lithium-ion batteries used in hybrid and electric vehicles at cold temperatures," Applied Energy, vol. 164, pp. 99-114, 2016.

[183] T. Gustafsson, K. Edström and J. O. Thomas, "The cathode–electrolyte interface in the Li-ion battery," Electrochimca Acta, vol. 50, no. 2-3, pp. 397-403, 2004.

[184] M. Dubarry and B. Y. Liaw, "Identify capacity fading mechanisms in a commercial LiFePO4 cell," Journal of Power Sources, vol. 194, no. 1, pp. 541-549, 2009.

[185] C. Rosenkranz, "Plug In Hybrid Batteries," Pres EVS20, 2003.

[186] J. Vetter,, M. R. Wagner, C. Veit, K. C. Möller, J. O. Besenhard, M. Winter, M. Wohlfahrt-Mehrens, C. Vogler and A. Hammouche, "Ageing mechanisms in lithium-ion batteries," Journal of Power Sources, vol. 147, no. 1-2, pp. 269-281, 2005.

[187] J. Apt, S. B. Peterson and J. F. Whitacre, "Lithium-ion battery cell degradation resulting from realistic vehicle and vehicle-to-grid utilization," Journal of Power Sources, vol. 195, no. 8, pp. 2385-2392, 2010.

[188] H. Teng, Y. Ma, K. Yeow and M. Thelliez, "An analysis of a lithium-ion battery system with indirect air cooling and warm-up," SAE International Journal of Passenger Cars-Mechanical Systems, vol. 4, no. 3, pp. 1343-1357, 2011.

[189] F. He and L. Ma, "Thermal management in hybrid power systems using cylindrical and prismatic battery cells," Heat Transfer Engineering, vol. 37, no. 6, pp. 581-590, 2016.

[190] I. Bayraktar, "Computational simulation methods for vehicle thermal management," Applied Thermal Engineering, vol. 36, pp. 325-329, 2012.

[191] J. H. Feikert, T. D. Tran and R. W. Pekala, "Rate effect on lithium-ion graphite electrode performance," Journal of Applied Electrochemistry, vol. 26, no. 11, pp. 1161-1167, 1996.

[192] Electropaedia, "Lithium Battery Failures.," February 2011. [Online]. Available: Available: http://www.mpoweruk.com/lithium_failures.htm.

[193] J. Liu, . K. Anime and I. Belharouak, "High-temperature storage and cycling of C-LiFePO4/ graphite lithium-ion cells," Electrochemistry Communications, vol. 7, no. 7, pp. 669-673, 2005.

[194] M. Broussely, "Aging mechanisms and calendar-life predictions in lithium-ion batteries," Adv. in Li-ion batteries, pp. 293-432, 2002.

[195] G. Abbas, Nazri and Pistoia, "Lithium Batteries, Science and Technology," in Kluwer Academic Publishers, 2004.

[196] M. Doyle, R. E. White and P. Arora, "Capacity fade mechanisms and side reactions in lithium-ion batteries," Journal of electrochemical society, vol. 145, no. 10, pp. 3647-3666, 1998.

[197] H. Maleki and J. N. Howard, "Effects of overdischarge on performance and thermal stability of a Li-ion cell," Journal of Power Sources, vol. 160, no. 2, pp. 1395-1402, 2006.

[198] M. Nagata, C. Kishiyama, J. Dodd, P. Lam and H. Tsukamoto, "Improvement of deep discharge capability for lithium-ion batteries," Proc. Electrochemical Society, vol. 28, pp. 252-259, 2004.

[199] A123 Systems, "Nanophosphate® Lithium Ion Prismatic Pouch Cell-AMP20M1HD-A," Jan 2016. [Online]. Available: http://www.a123systems.com/prismatic-cell-amp20.htm.

[200] R. J. Moffat, "Describing the uncertainties in experimental results," Experimental Thermal and Fluid Science, vol. 1, pp. 3-17, 1988.

[201] Keithley, "Model 2700 Multimeter/Switch System User's Manual," November 2002. [Online]. Available: http://www.ee.bgu.ac.il/~acl/Equip/2700_900_01fnl.pdf. [Accessed 10 October 2013].

[202] L. Cai and R. E. White, "Mathematical modeling of a lithium-ion battery with thermal effects in COMSOL Inc. Multiphysics (MP) software," Journal of Power Sources, vol. 196, no. 14, pp. 5985-5989, 2011.

[203] M. Farkhondeh, M. Safari, M. Pritzker, M. Fowler, T. Han, J. Wang and C. Delacourt, "Full-range simulation of a commercial LiFePO4 electrode accounting for bulk and surface effects: A comparative analysis," Journal of The Electrochemical Society, vol. 161, no. 3, pp. A201-A212, 2014.

[204] A. Inc., "ANSYS Fluent Advanced Add-On Modules," ANSYS, Inc., November 2013. [Online]. Available: http://www.ansys.com. [Accessed November 2013].

[205] N. Yang, X. Zhang, G. Li and D. Hua, "Assessment of the forced air-cooling performance for cylindrical lithium-ion battery packs: A comparative analysis between aligned and staggered cell arrangements," Applied Thermal Engineering, vol. 80, pp. 55-65, 2015.

[206] M. M. Majdabadi Kohneh, E. Samadani, S. Farhad, R. Fraser and M. Fowler, "Three-dimensional electrochemical analysis of a Graphite/LiFePO4 lithium-ion cell to improve its durability," SAE International, 2015.

[207] W. Zhao, G. Luo and C. Y. Wang, "Modeling nail penetration process in large-format Li-ion cells," Journal of The Electrochemical Society, vol. 162, no. 1, pp. A207-A217, 2015.

[208] K. Smith and C.-Y. Wang, "Power and thermal characterization of a lithium-ion battery pack for hybrid-electric vehicles," Journal of Power Sources, vol. 160, no. 1, pp. 662-673, 2006.

[209] G. Karniadakis and S. Sherwin, Introduction in spectral/hp element methods for CFD: Second edition, New York, USA: Oxford University Press, 2005.

[210] X. Hu, S. Li and H. Peng, "A comparative study of equivalent circuit models for Li-ion batteries," Journal of Power Sources, vol. 198, pp. 359-367, 2012.

[211] E. Samadani, M. Mastali, S. Farhad, R. Fraser and M. Fowler, "Li-ion battery performance and degradation in electric vehicles under different usage scenarios," International Journal of Energy Research, vol. 40, pp. 379-392, 2015.

[212] J. Schmalstieg, S. Käbitz, M. Ecker and D. U. Sau, "A holistic aging model for Li(NiMnCo)O2 based 18650 lithium-ion batteries," Journal of Power Sources, vol. 257, pp. 325-334, 2014.

[213] E. Samadani, S. Farhad, W. Scott, M. Mastali, L. E. Gimenez, M. Fowler and R. Fraser, "Empirical modeling of lithium-ion batteries based on electrochemical impedance spectroscopy tests," Electrochimica Acta, vol. 160, pp. 169-177, 2015.

[214] A. Millner, "Modeling lithium-ion battery degradation in electric vehicles," 2010 IEEE Conference on Innovative Technologies for an Efficient and Reliable Electricity Supply, pp. 349-356, 2010.

[215] L. Ahmadi, M. Fowler, S. B. Young, R. A. Fraser, B. Gaffney and S. B. Walker, "Energy efficiency of Li-ion battery packs re-used in stationary power applications," Sustainable Energy Technologies and Assessments, vol. 8, pp. 9-17, 2014.